Vortex-Induced Vibrations of a Cylinder in the Streamwise Direction

Neil Cagney

Department of Mechanical Engineering

University College London

A thesis submitted for the degree of

Doctor of Philosophy

April 2013

Declaration

I declare that the work presented in this thesis is entirely my own, and to the best of my knowledge is original. Where work has been derived from other sources, this has been indicated in the thesis.

Neil Cagney

April 2013

Acknowledgements

There are a number of people I am deeply indebted to, without whom this thesis would not have been possible.

Firstly, I would like to thank my supervisor, Dr. Stavroula Balabani, who has given up so much of her time to ensure that my time in King's and University College London was as fulfilling as possible. She was been a great support throughout the three and a half years we have worked together, both as a colleague and as a friend. None of this work would have been possible without her.

I would also like to thank Mr. Julian Greenberg, who has been exceptionally generous with his time both while I was studying in King's, and after moving to UCL. He has always been helpful with all of requests I have made, no matter how much equipment I broke or did not return.

I would like to acknowledge the help of a number of other people; my second supervisor, Prof. Michael Yianneskis, for his comments and advice throughout this work; Dr. Jon Dusting and soon-to-be-Dr. Joe Sherwood, who were always generous with their time; and the staff in the workshop at UCL whose help made the transfer as painless as could I could have hoped.

Throughout this work I have been funded by a Doctoral Training Award from King's College London.

Lastly I would like to thank my family who have always encouraged me throughout my studies, and the friends I have made at King's and UCL, who made my time here so enjoyable.

Abstract

Vortex-induced vibration (VIV) of a circular cylinder has been the focus of extensive research, as it can lead to fatigue damage in a wide range of industrial applications. When the forces induced by the periodic shedding of vortices from a structure in crossflow coincide with one of its natural frequencies, the structure can exhibit large amplitude vibrations. The majority of the work performed in this area has focused exclusively on transverse vibration, while relatively little is known about VIV acting in the streamwise (flow) direction, although this is known to have a strong effect on the overall response of structures with multiple degrees-of-freedom (DOFs). This work aims to characterise the behaviour of the wake and the structural response of a cylinder throughout the streamwise VIV response regime, which is crucial if the wealth of information on the transverse-only case is to be extended to the more practical and complex case of multi-DOF structures. Experiments were performed on a cylinder free to move in the streamwise direction for a range of reduced velocities in a closed-loop water tunnel. Particle-Image Velocimetry (PIV) was used to simultaneously measure the cylinder displacement and the velocity field in the wake, in the Reynolds number range 400 - 5500.

The response regime was characterised by two branches, separated

by a region of low amplitude vibration, as reported in the literature. Five distinct regions were identified, each of which was discussed in terms of the dominant wake mode, structural response characteristics, velocity profiles and estimates of the strength and trajectories of the shed vortices. In the first branch the mode was found to switch intermittently between the symmetric S-I mode (in which two vortices were shed simultaneously from either side of the cylinder) and the alternate A-II mode (which is similar to the von Kármán vortex street observed behind stationary bodies). A criterion was developed which could determine which mode was dominant in a given instantaneous PIV field, and the effect of both modes on the cylinder response and wake characteristics was examined.

Multi-modal behaviour was also observed in the second branch. At one value of reduced velocity, the wake could exhibit one of three modes; the A-II, the SA (similar to the A-II mode, with the vortices forming closer to the cylinder base) or the A-IV mode (which was characterised by the shedding of two pairs of counter-rotating vortices). Each mode was associated with a different cylinder response amplitude. The stability of the cylinder response while each mode dominated was examined using phase-portraits, which indicated that the system behaved as a hard oscillator.

The forces acting on the cylinder were estimated using two methods, based on the measurements of the cylinder displacement signal and the flow field, respectively. The results found using both methods

were in agreement, and the accuracy of the estimates was discussed. It was found that the amplitude of the unsteady drag force was very low between the two response branches, which was thought to be the cause of the reduction in the cylinder vibrations in this region. Finally, the effect of the various wake modes on the amplitude of the fluid forces throughout the response regime was examined.

The results presented in this study provide a comprehensive description of the behaviour of the wake and the associated fluid forces throughout the streamwise response regime. The work reveals the inherent differences between the extensively studied case of transverse-only VIV and the streamwise-only case, which is crucial if the wealth of information available on transverse VIV is to be extended to the more practical multi-DOF case.

Contents

List of Figures

Nomenclature

Roman Symbols

$\mathbf{a}$	Matrix of amplitude coefficients of POD modes, [m/s]
$\mathbf{C}$	Cross-correlation matrix of velocity fields, [m^2/s^2]
$\mathbf{F}$	Force vector, [N]
$\mathbf{G^{2D}}$	Two-dimensional velocity gradient tensor, [1/s]
$\mathbf{H}$	Matrix of eigenvectors of $\mathbf{C}$, [m^2/s^2]
$\mathbf{n}$	Normal vector, [-]
$\mathbf{T}$	Viscous stress tensor, [s]
$\mathbf{u_s}$	Velocity vector of control surface, [m/s]
$\mathbf{u}$	Velocity vector, [m/s]
$\mathbf{x}$	Position vector, [m]
St_i	Strouhal number calculated, neglecting i^{th} data point, [-]
$\widetilde{C_{d,num}}$	Amplitude of section drag coefficient in numerical simulations, [-]

$\widetilde{C}_{l,num}$ Amplitude of section lift coefficient in numerical simulations, [-]

A Amplitude response of cylinder, [m]

a_i Temporal coefficient of the i^{th} POD mode, [m/s]

A_0 Initial disturbance of cylinder, [m]

A_c Area of cylinder cross-section, [m^2]

A_{iw} Area of interrogation window, [m^2]

c_e Total damping of a system, [Ns/m]

C_n Combined mass-damping parameter, [-]

$C_{d,o}$ Arbitrary offset value of the sectional drag coefficent, [-]

C_{ea} Effective added-mass coefficient, [-]

C_{PIV} Number of columns in a PIV field, [-]

D Cylinder diameter, [m]

f Frequency, [Hz]

f_e External forcing frequency, [Hz]

f_n Natural frequency in water, [Hz]

F_x Streamwise component of force vector, [N]

f_x Cylinder response frequency in streamwise direction, [Hz]

F_y Transverse component of force vector, [N]

$f_{n,a}$ Natural frequency in air, [Hz]

f_{St} Vortex-shedding frequency from a fixed body, [Hz]

f_{vs} Frequency of velocity fluctuations in the wake, [Hz]

k Stiffness, [N/m]

L Cylinder length, [m]

l_{rc} Recirculation length, [m]

l_{vf} Vortex formation length, [m]

m Cylinder mass, [kg]

m_e Effective cylinder mass, [kg]

N Number of points, [-]

N_b Number of integration boundaries, [-]

N_p Number of tap test peaks, [-]

N_x Number of points in x-direction, [-]

N_y Number of points in y-direction, [-]

p Pressure, [N/m^2]

R_f Percentage of noise added to velocity fields, [-]

R_{PIV} Number of rows in a PIV field, [-]

S Surface surrounding a control volume, [m^2]

s Laser sheet thickness, [m]

T Period, [s]

t time, [s]

t_i i^{th} timestep, [s]

$t_{p,i}$ time of i^{th}peak in tap test displacement signal, [s]

u Streamwise velocity component, [m/s]

U_0 Freestream velocity, [m/s]

V Control volume, [m^3]

v Transverse velocity component, [m/s]

V_{iw} Volume of interrogation window, [m^3]

w Axial velocity component, [m/s]

x Streamwise position, [m]

x_b Streamwise position of integration boundary, [m]

x_c Streamwise position of vortex core, [m]

x_{bin} Size of binning window in x-direction, [pixels]

y Transverse position, [m]

y_c Transverse position of positive vortex core, [m]

y_c^+ Transverse position of positive vortex core, [m]

y_c^- Transverse position of negative vortex core, [m]

y_{bin} Size of binning window in y-direction, [pixels]

z Spanwise position, [m]

Greek Symbols

$\Delta\mathbf{x}$ Displacement vector of particles between PIV images, [pixels]

Δm Added mass, [kg]

Δt Timestep, [s]

Δu Pulsation amplitude, [m/s]

ΔV_{iw} Volume of interrogation window which leaves laser sheet between PIV images, [m^3]

δ Logarithmic decrement, [-]

Γ Circulation of vortex, [m^2/s]

$\Lambda_{ci,peak}$ Maximum of absolute modified swirling parameter in a vortex, [1/s]

Λ_{ci} Modified swirling parameter, [1/s]

λ_{ci} Complex component of eigenvalue of velocity gradient tensor, [1/s]

Λ_{ci}^+ Positive-only modified swirling parameter, [1/s]

Λ_{ci}^- Negative-only modified swirling parameter, [1/s]

γ_{imp} Term in Impulse Equation, [m^2/s^2]

γ_{mom} Term in Momentum Equation, [m^2/s^2]

$\mathbf{\Lambda}$ Matrix of eigenvalues of $\mathbf{C}$, [m^2/s^2]

ω Vorticity vector, [1/s]

$\mathbf{\Phi}$ Spatial POD modes, [-]

$\mathbf{\Upsilon}$ Matrix containing all velocity fields, [m/s]

μ Dynamic viscosity, [kg/ms]

ν Kinematic viscosity, [m^2/s]

ω_z Out-of-plane vorticity, [1/s]

ϕ Phase Angle, [radians]

$\phi_{x,d}$ Phase difference between cylinder displacement and drag force, [radians]

ρ Fluid density, [kg/m^3]

σ Standard deviation

$\varepsilon(u)$ Uncertainty in measurement of velocity field, [-]

ε_{bin} Error in displacement signal calculated from binned images, [pixels]

ε_d Error in estimate of sectional drag coefficient, [-]

ε_l Error in estimate of sectional lift coefficient, [-]

ε_{St} Error in estimate of Strouhal number, [-]

ε_u Residual of continuity equation evaluated in the wake, [-]

ζ Structural damping ratio, [-]

ζ_w Combined structural and hydrodynamic damping ratio, [-]

Other Symbols

$\mathcal{H}$ Hilbert transform

$\mathcal{N}$ Number of spatial dimensions [-]

Abbreviations

DNS Direct Numerical Simulation

DOF Degree-of-freedom

FFT Fast Fourier Transform

LIF Laser-Induced Florescence

PIV Particle-Image Velocimetry

POD Proper-Orthogonal Decomposition

PSD Power-Spectral Density

R1, R2, . . . Response Regime 1, 2, . . .

rms root-mean-square

VIV Vortex-Induced Vibrations

Dimensionless Groups

Re	Reynolds number, $\mathrm{Re} = \frac{U_0 D}{\nu}$
St	Strouhal number, $\mathrm{St} = \frac{f_{\mathrm{St}} D}{U_0}$
U_r	Conventional reduced velocity, $Ur = \frac{U_0}{f_n D}$
f^*	Frequency ratio, $f^* = f_x / f_n$
$U_r\mathrm{St}/f^*$	'True' reduced velocity, $U_r\mathrm{St}/f^* = f_{St}/f_x$
AR	Aspect ratio, $AR = L/D$
C_a	Added mass coefficient, $C_a = \frac{\Delta m}{\rho D^2 L/4}$
C_d	Sectional drag coefficient, $C_d = \frac{F_x(z)}{0.5\rho U_0^2 D}$
C_D	Overall drag coefficient, $C_D = \frac{F_x}{0.5\rho U_0^2 DL}$
C_l	Sectional lift coefficient, $C_l = \frac{F_y(z)}{0.5\rho U_0^2 D}$
C_L	Overall lift coefficient, $C_L = \frac{F_y}{0.5\rho U_0^2 DL}$
$\mathbf{C_f}$	Sectional force coefficient vector, $\mathbf{C_f} = \frac{\mathbf{F}(z)}{0.5\rho U_0^2 D}$
$\mathbf{C_F}$	Overall force coefficient vector, $\mathbf{C_F} = \frac{\mathbf{F}}{0.5\rho U_0^2 DL}$

Additional Notation

$\dot{q}$	Temporal derivative of variable, q
$\ddot{q}$	Second order temporal derivative of variable, q
q'	Fluctuating component of variable, q
$\overline{q}$	Mean value of variable, q
$\widetilde{q}$	Unsteady component of variable, q
q_{rms}	Root-mean-square of variable, q
$\langle q \rangle$	Phase-averaged value of variable, q
$\lvert q \rvert$	Absolute value of variable, q
$\lvert\lvert \mathbf{q} \rvert\rvert$	Magnitude of a vector, $\mathbf{q}$

Chapter 1

Introduction

1.1 Background

Vortex-Induced Vibration (VIV) occurs throughout both industry and nature, affecting bodies as diverse as nuclear reactors, vegetation [Levy et al., 2011] and whiskers of marine creatures [Hanke et al., 2010]. VIV caused by the wind was utilised by the ancient Greeks to create music with Aoelian harps, while more recently, VIV has been proposed as a potential source of renewable energy [Bernitsas et al., 2008]. VIV can also cause significant damage in many industrial applications, such as bridges, chimneys, marine structures, riser cables and heat-exchangers; detailed descriptions of two instances in which VIV caused severe damage in a nuclear reactor are presented by Païdoussis [2006].

Despite the wide range of areas affected by VIV, it was not until the mid-twentieth century that the physical mechanism causing it was identified. Feng [1963] performed measurements in a wind tunnel of the fluid forces and vortex-shedding frequency of a cylinder which was free to move normal to the flow, and

attributed the structural vibrations to resonance between the forces induced by the vortex-shedding and the natural frequency of the cylinder. The majority of subsequent VIV studies have also examined the case of cylinder free to move only in the transverse direction, as the vibrations and unsteady fluid forces in this direction tend to be an order of magnitude larger than those in the drag direction (see reviews by Bearman [1984]; Sarpkaya [2004]; Williamson and Govardhan [2004]). However, in recent years there has been a renewed interest in streamwise VIV. This has been motivated in part by the failure of a thermowell in the 'Monju' nuclear reactor in Japan; design engineers had accounted for VIV acting in the transverse direction, but not in the streamwise direction, which occurs at lower flowrates [Okajima et al., 2001]. The recent interest has also been motivated by the work of Williamson and Jauvtis [2004], who showed that the freedom of a cylinder to move in both the streamwise and transverse directions can have a dramatic effect on the overall response regime, compared to the transverse-only case. However, there remains relatively little work in the literature concerning the response of a cylinder free to move in the streamwise direction. Many of the recent investigations of cylinders with multiple degrees-of-freedom (DOFs) have focused on the effects of the streamwise motion on the transverse response [Flemming and Williamson, 2005; Williamson and Jauvtis, 2004], rather than the region of the response regime where the cylinder vibrations occur primarily in the streamwise direction.

The freedom of a structure to move in the streamwise direction also has significant implications for the prediction of VIV. Chaplin et al. [2005] measured the streamwise and transverse response along the span of a long tension riser in uniform crossflow, and compared the results to the predictions of 11 numerical

models. The set of modes included algorithms presented in the literature as well as commercial design codes, which were based on either numerical simulation of the flow field or empirical relations derived from experiments performed on rigid cylinders. It was found that predictions of the response of the riser produced by the models based on numerical simulations were poor, particularly in the streamwise direction. The empirical models were found to provide more accurate estimates of the transverse response. However, they were unable to predict the streamwise response due to a lack of experimental data. While the variation in the wake mode throughout the response regime of a cylinder free to move transversely to the flow has been well-documented [Govardhan and Williamson, 2000; Morse and Williamson, 2009], comparatively little is known about the behaviour of the wake in the streamwise-only case due to a lack of experimental data. Chaplin et al. [2005] noted that the inability of the models to predict to the streamwise response will have significant implications for the design of structures vulnerable to VIV, because, in practice, the fatigue damage caused by streamwise vibrations may exceed that caused by vibrations in the transverse direction. Detailed information on streamwise VIV is needed if the design codes are to be improved to accurately represent the structural motion and fatigue damage experienced by multi-DOF bodies, which occur in practice.

The aim of this study is to characterise the structural response and wake characteristics of a cylinder free to move in the streamwise direction. Simultaneous measurements of the cylinder displacement and the surrounding velocity field throughout the streamwise response regime were performed using Particle-Image Velocimetry (PIV). The measurements were used to examine the variation in both the dominant and transient wake modes, to relate the modes to the cylinder

motion, and to estimate the fluid forces associated with VIV.

1.2 Literature Review

The aim of this review is to provide an overview of the previous work in the literature which relates to the experimental results and discussions presented in the following chapters. The review is divided into four sections, which provide a description of the phenomenon of VIV, and summarise the various studies of the flow around cylinders which are forced to oscillate, freely oscillating cylinders and cylinders with multiple degrees-of-freedom (DOFs).

A number of books and extensive reviews of VIV occurring in the transverse direction are available in the literature [Bearman, 1984; Blevins, 1977; Gabbai and Benaroya, 2005; Sarpkaya, 2004; Williamson and Govardhan, 2004]. This literature review focuses on experimental studies of VIV of rigid circular cylinders which are free to move either in the streamwise or both the streamwise and transverse directions.

1.2.1 Phenomenon of VIV

Flow Around Stationary Cylinders

A cylinder in crossflow is a classical case of fluid-structure interaction. As the freestream velocity, U_0, is increased above a critical value (which depends on the fluid properties and cylinder geometry), flow separation occurs at the cylinder surface, which can lead to the periodic formation and shedding of vortices. The vortices shed from a stationary cylinder form the well-known von Kármán vortex street in the wake, which is shown in Figure 1.1. The frequency at which

the vortices are shed from a stationary body, f_{St}, is non-dimensionalised as the Strouhal number, $\mathrm{St} = f_{\mathrm{St}}D/U_0$, (where D is the cylinder diameter) which is approximately equal to 0.2. The structure of the von Kármán street and the value of the Strouhal number are stable over a large Reynolds number range, $\mathrm{Re} = U_0 D/\nu$, where ν is the kinematic viscosity of the fluid [Blevins, 1977].

Fluid Forces

The periodic vortex-shedding induces unsteady fluid forces on the cylinder in the drag and lift directions (parallel and perpendicular to the flow direction, respectively). Due to the symmetry of the cylinder and the wake, the vortices shed from either side of the cylinder have an identical effect on the drag force; therefore the unsteady drag force occurs at $2f_{\mathrm{St}}$, while the lift force occurs at f_{St}. When the forcing frequency occurs near one of the natural frequencies of the structure, it can excite large amplitude oscillations, a phenomenon known as Vortex-Induced Vibrations (VIV). The structural motion in turn can affect the wake, causing the vortex-shedding frequency to occur at the vibration frequency or a sub-harmonic rather than the Strouhal frequency (a condition known as *lock-in*), as well as altering the arrangement of the shed vortices in the wake (the *wake mode*).

Forced and Free Studies

The majority of investigations of VIV can be classed as either free or forced studies; in the former, typically the freestream velocity is varied and the effect on the non-dimensional amplitude response of the cylinder, A/D, is examined, while in the latter the cylinder is forced to oscillate at a range of amplitudes and frequencies which allows the effect of the structural motion on the wake to be isolated and examined. The freestream velocity is typically non-dimensionalised

as the reduced velocity, $U_r = U_0/f_n D$, where f_n is the natural frequency of the structure in still fluid. However, in order to account for variations in the Strouhal number between studies and changes in the cylinder vibration frequency, f_x, the so-called 'true' reduced velocity, $U_r \mathrm{St}/f^*$, where $f^* = f_x/f_n$, can be employed instead [Govardhan and Williamson, 2000]. This parameter, henceforth referred to simply as the reduced velocity, is equal to the ratio of the Strouhal frequency and the vibration frequency, f_{St}/f_x. As the lift force occurs at the vortex-shedding frequency and the unsteady drag force at twice this value, resonance between the fluid forces and the structural motion will occur in the streamwise and transverse directions at $U_r \mathrm{St}/f^* = 0.5$ and 1, respectively.

1.2.2 Flow Past Cylinders Forced to Oscillate

Transverse Forced Ocsillation Studies

Several studies have been performed in which a cylinder was forced to oscillate in steady flow, the majority of which have examined transverse oscillations, e.g. Carberry et al. [2005]; Morse and Williamson [2009]. Williamson and Roshko [1988] forced a cylinder to oscillate in the transverse direction over a wide range of amplitudes and reduced velocities and developed a 'mode map', shown in Figure 1.2, which presented the dominant wake mode as a function of $U_r \mathrm{St}/f^*$ and A/D (in this case the natural frequency is given by the forcing or oscillation frequency, f_x, and by definition $f^* = 1$). Subsequent free-vibration studies indicated that the mode map in Figure 1.2 can be used to accurately predict the dominant wake mode throughout the response regime of a cylinder free to move in the transverse direction [Flemming and Williamson, 2005; Fujarra et al., 2001]. A more recent

study of the variation of the wake characteristics throughout the $U_r\mathrm{St}/f^* - A/D$ plane for transverse vibrations was performed by Morse and Williamson [2009], who used PIV to measure the velocity fields in the wake and a force balance to measure the lift force acting on a cylinder forced to oscillate. By relating the measurements of the force to the cylinder displacement signals, they were able to accurately predict the response of a freely oscillating cylinder, and could relate the various excitation mechanisms to the different wake modes observed. The work of Williamson and Roshko [1988] and Morse and Williamson [2009] demonstrates the potential of forced oscillation studies to provide insight into the dynamics and flow behaviour of a freely moving body.

Streamwise Forced Studies

The fluid forces and wake modes associated with a cylinder oscillating in the streamwise direction have also been the focus of a number of studies [Griffin and Ramberg, 1976; Nishihara et al., 2005; Ongoren and Rockwell, 1988]. Several studies have also examined the case of a fixed cylinder in pulsating flow, which is equivalent to the case of a cylinder vibrating in the streamwise direction in steady flow, providing the wavelength of the pulsations is large with respect to the cylinder diameter. In this case, the equivalent forcing amplitude is given by:

$$A/D = \frac{\Delta u}{U_0}\frac{1}{2\pi f_e D}, \tag{1.1}$$

where Δu and f_e are the amplitude and frequency of the pulsations, respectively. In the following discussion, the results of studies in pulsating flow are presented in terms of the equivalent forcing amplitude, and the reduced velocity is defined

with respect to pulsation frequency, i.e. $f_n = f_e$ and $f^* = 1$.

Table 1.1: Summary of various experimental studies which examine the effect of streamwise oscillations on lock-in, and are presented in Figure 1.3.

Researcher	Method of excitation	Re	Symbol
Armstrong and Barnes [1986]	Flow pulsations	21500	Closed blue ⋆
Barbi et al. [1986]	Flow pulsations	3000	Closed red □
Barbi et al. [1986]	Flow pulsations	40000	Closed green ◊
Griffin and Ramberg [1976]	Cylinder oscillations	190	Open blue □
Konstantinidis et al. [2003]	Flow pulsations	2150	Closed cyan ◯
Tanida et al. [1973]	Cylinder oscillations	80	Open red ▽
Tanida et al. [1973]	Cylinder oscillations	4000	Open green ◊
Tatsuno [1972]	Cylinder oscillations	100	Open cyan ◯

Lock-in

When the forcing frequency is near $f_{\mathrm{St}}/2$, and the amplitude is sufficiently large, the vortex-shedding locks-in to the excitation frequency. The reduced velocity range over which lock-in occurs has been examined in a number of studies, some of which are summarised in Table 1.1 and Figure 1.3. The lock-in range is roughly centred at $U_r\mathrm{St}/f^* = 0.5$, and increases with A/D. Konstantinidis et al. [2003] noted that the lock-in range appears to increase with Re, based on a similar graph to that shown in Figure 1.3; this is particularly clear in the results of Tanida et al. [1973], at $A/D = 0.028$, and Re = 80 and 4000. This trend was also noted in the numerical simulations of Marzouk and Nayfeh [2009], which they attributed to the influence of viscous effects; at low Re, the effect of the

structural motion on the flow field is weaker due to greater viscous dissipation, and a larger A/D is required to maintain lock-in.

The fluid force measurements of Griffin and Ramberg [1976] (which were used to determine the presence of lock-in) indicated that the frequency of the forcing did not change abruptly at the boundary of the lock-in region, but instead varied smoothly as the reduced velocity was increased. The lack of a sudden step-change in the vortex-shedding frequency may also be responsible for some of the scatter in the estimated boundary of the lock-in region shown in Figure 1.3.

Armstrong and Barnes [1986] found that lock-in corresponded to an increase in the mean drag coefficient, and caused the wake to become more two-dimensional. Konstantinidis et al. [2003] observed that lock-in was also associated with a contraction of the recirculation region (the region in the near wake in which the streamwise velocity component is reversed) and the vortex formation length (the position along the wake centreline at which the transverse velocity fluctuations reach a maximum).

Nishihara et al. [2005] measured the forces acting on a cylinder forced to oscillate in the streamwise direction at $A/D = 0.05$ for a range of reduced velocities. By examining the phase of the drag force with respect to the displacement signal, they showed that there was positive energy transfer to the cylinder in the ranges $U_r\mathrm{St}/f^* \approx 0.3 - 0.5$ and $0.52 - 0.67$. Outside these ranges the unsteady drag force opposed the cylinder motion (i.e. it acted as a damping force), including at $U_r\mathrm{St}/f^* \approx 0.51$, which corresponded to the centre of the lock-in range.

Wake Modes

The streamwise motion of the cylinder also affects the wake, resulting in a number of different wake modes, some of which are sketched in Figure 1.4. Except

where otherwise stated, the modes are referred to using the notation of Ongoren and Rockwell [1988], where 'A' and 'S' indicate modes in which the vortices are shed *alternately* and *symmetrically*, respectively. The A-II mode is similar to the von Kármán vortex street observed in the wake of a stationary body, and is observed when the amplitude of the cylinder oscillations is low. A similar mode was observed by Jauvtis and Williamson [2003] in the wake of a cylinder free to move in both the streamwise and transverse directions, in which the vortices were formed very close to the cylinder base and remained close to the wake centreline as they were shed downstream. They referred to this mode as the 'Streamwise Antisymmetric' or SA mode. As the SA mode consists of two vortices shed alternately per wake cycle, it maybe viewed as a special case of the A-II mode. In order to aid discussion, in this work the distinction between the A-II and SA modes is maintained, despite the two modes typically being treated as one. Griffin and Ramberg [1976] noted that the transverse spacing between the shed vortices decreased with A/D. As the SA mode is characterised by negligible transverse vortex-spacing with respect to the A-II mode, the SA mode can be expected to occur when the amplitude is large.

Ongoren and Rockwell [1988] also observed the A-IV mode, which was characterised by the formation of four vortices per wake cycle. The vortices were shed into the wake as two counter-rotating pairs. When the cylinder oscillations contained a streamwise component (i.e. the motion was not purely in the transverse direction), the S-I mode was either dominant or appeared intermittently in the wake. This mode was characterised by the simultaneous shedding of vortices from either side of the cylinder. The vortex-shedding occurred at the frequency of the cylinder motion, unlike the A-II, SA and A-IV modes, in which one shedding

cycle corresponded to two cylinder oscillation cycles (during lock-in).

Other modes observed include the A-III and S-II modes [Ongoren and Rockwell, 1988; Xu et al., 2006]; these have not been observed at reduced velocities and amplitudes relevant to VIV of freely oscillating cylinders, and thus are not shown in Figure 1.4. The former mode is characterised by the shedding of three vortices per wake cycle; a single vortex is shed from one side of the cylinder and a counter-rotating pair from the other. The S-II mode was observed by Xu et al. [2006] at very high forcing frequencies and amplitudes, when the maximum velocity of the cylinder throughout its vibration cycle exceeded U_0. This caused the local flow at the cylinder surface to become reversed and a vortex-pair to be shed simultaneously from either side of the cylinder at the oscillation frequency.

Previous forced oscillation studies in which the wake mode was identified are summarised in Table 1.2. The reported wake modes are shown in Figure 1.5 as a function of the reduced velocity and forcing amplitude, in a similar manner to the mode map measured for transverse VIV by Williamson and Roshko [1988] (Figure 1.2). There are few regions in which one mode can be said to be clearly dominant. This uncertainty may be caused by the variation in the experimental conditions (Re, blockage ratio etc.) used in the reported studies, and 'mode-switching', in which the wake was observed to switch randomly between different modes, making the classification of the dominant mode difficult.

The A-II mode tends to occur outside the lock-in range (as indicated in Figure 1.3), while the SA mode is observed at higher values of A/D, as was noted previously, and tends to occur near $U_r\mathrm{St}/f^* \approx 0.5$.

Mode Switching

The S-I mode is observed at $U_r\mathrm{St}/f^* \approx 0.25$. Naudascher [1987] described this

Table 1.2: Review of experimental forced streamwise oscillation studies in which wake modes were clearly identified.

Researcher	$U_r\mathrm{St}/f^*$	A/D	Visualisation Method	Modes	Symbol (Figure 1.5)
Griffin and Ramberg [1976]	$0.45-0.57$	$0.06-0.24$	DEHP[a]	A-II, A-III, A-IV, SA	★
Kim et al. [2006][b]	0.5	0.02	PIV	SA	◊
Konstantinidis et al. [2005][b]	$0.45-0.57$	$0.04-0.05$	PIV	A-IV, SA	□
Konstantinidis et al. [2007][b]	$0.53-0.57$	$0.01-0.03$	PIV	A-IV, SA	□
Konstantinidis and Balabani [2007][b]	$0.25-0.33$	$0.02-0.04$	PIV	A-II, S-I	□
Konstantinidis and Balabani [2008][b]	0.5	$0-0.09$	PIV	A-II, SA	□
Nishihara et al. [2005]	$0.25-2$	0.05	LIF	A-II, A-IV, S-I, SA	△
Ongoren and Rockwell [1988]	$0.23-2$	0.15	Hydrogen Bubbles	A-II, A-III, S-I	▽
Xu et al. [2006]	$0.32-2$	$0.5-0.67$	LIF	A-III, A-IV, S-I, S-II	+

[a] Bis(2-ethylhexyl) phthalate.
[b] Studies were performed using a fixed cylinder in pulsating flow.

mode as a 'wake-breathing' mechanism, in which the fluid entrained by the cylinder motion causes the shear layers to periodically move close together and then separate (to 'breath'); this causes the layers to roll up and the resulting vortices to separate from the cylinder simultaneously, as shown in Figure 1.6. As a result of the symmetry of the wake, the lift force induced by the S-I mode is negligible [Nishihara et al., 2005]. However, this symmetrical structure tends to rearrange downstream into an alternate pattern (i.e. the A-II mode) [Griffin and Ramberg, 1976; Konstantinidis and Balabani, 2007; Ongoren and Rockwell, 1988]. Ongoren and Rockwell [1988] found that the breakdown of the S-I mode was affected by the amplitude of the cylinder oscillations and transient conditions; the sudden excitation of the cylinder from rest caused the appearance of the S-I mode in the wake, which reverted to the alternate mode after a number of cycles. They attributed this rearrangement to the competing effects of the structural motion and the far wake; the symmetrical motion of the cylinder promotes a symmetric arrangement of vortices (which they referred to as the 'downstream influence' of the cylinder), while the stability of the von Kármán vortex street which occurs downstream promotes an alternate arrangement (the 'upstream influence'). Konstantinidis and Balabani [2007] examined the wake of a cylinder in pulsating flow at $U_r\mathrm{St}/f^* = 0.25 - 0.33$ and at lower forcing amplitudes, $A/D = 0.02 - 0.04$, and found that the downstream position at which the breakdown occurred was a probabilistic function of both the forcing amplitude and the reduced velocity. They also observed mode switching between the S-I and A-II modes in the near wake.

In a similar study, Konstantinidis et al. [2007] observed mode competition between the SA and the A-IV modes at slightly higher reduced velocities, $U_r\mathrm{St}/f^* =$

$0.55 - 0.57$, $A/D = 0.01 - 0.03$. In this case the modes were found to occur consistently over long periods (of the order of 10^2 cycles), before randomly switching.

1.2.3 Flow Past Freely Oscillating Cylinders

Effect of Mass-Damping

The response of a cylinder free to move in the streamwise direction was measured by Aguirre [1977] (summarised by Naudascher [1987]), and subsequently by Okajima et al. [2003] and Blevins and Coughran [2009]. The amplitude response measured by Aguirre [1977] for three cylinders with different damping coefficients is shown in Figure 1.7. The response regime is characterised by two branches which have peak amplitudes of approximately $A/D \sim 0.1$, separated by a region of low amplitude vibration at $U_r\mathrm{St}/f^* \approx 0.5$. The peak amplitude is affected by the structural damping ratio, ζ, and the mass ratio, m^* = (vibrating mass)/(displaced fluid mass). Okajima et al. [2003] found that the peak amplitude was controlled by the combined mass-damping parameter, which he expressed as $C_n = 2m^*\delta$, where δ is the logarithmic decrement, $\delta = 2\pi\zeta/\sqrt{1-\zeta^2}$. They found that the streamwise response was negligible when $C_n = 2.12$. Similarly, Blevins and Coughran [2009] found that the response was negligible when $C_n = 2.6$ ($m^* = 4.14, \zeta = 0.05$).

Added Mass Effects

The mass ratio of the cylinder also affects the structural response in a distinct and more complex manner which is related to the '*added mass*'. The apparent mass of a body moving in a fluid differs from that measured in a vacuum, as it includes not only the mass of the body, but also the mass of the fluid which

is permanently displaced by the structural motion, as well as the effects of the fluid forcing which is in phase with the structural acceleration [Sarpkaya, 2004]. The added mass of the body, Δm, is non-dimensionalised as the added mass coefficient:

$$C_a = \frac{\Delta m}{\pi \rho D^2 L/4}, \tag{1.2}$$

where ρ is the fluid density and L is the cylinder length. The added mass of a two-dimensional cylinder is commonly taken as $C_a = 1$ [Leonard and Roshko, 2001]. However, as Sarpkaya [2004] notes, C_a is dependent on the cylinder motion, and the ideal value of $C_a = 1$ will only hold at very low vibration amplitudes.

The added mass of the cylinder has significant implications for the response frequency of the structure and the lock-in range. The natural frequency of the structure measured in a vacuum (or in a light fluid such as air, in which case the added mass is negligible) is inversely proportional to the square root of the mass, $f_{n,a} \propto m^{-1/2}$. However, when the body is vibrating in a dense fluid, the response frequency is dependent on the total effective mass; $f_x \propto (m + \Delta m)^{-1/2}$. Previous researchers (e.g. Khalak and Williamson [1999]; Sarpkaya [2004]) have shown that the added mass coefficient can be derived *a posteriori* from the displacement signal:

$$C_a = m^* \left(\left(\frac{f_x}{f_{n,a}} \right)^2 - 1 \right). \tag{1.3}$$

The added mass can be negative [Sarpkaya, 2004; Vikestad et al., 2000; Williamson and Govardhan, 2004], which raises the response frequency of the cylinder, thus extending the range of U_r over which lock-in will occur. In contrast to the classical case of lock-in of cylinders with large mass ratios, in which the vortex-shedding frequency changes to match the response frequency, in the case of low m^* cylinders, the response frequency also varies to match the shedding frequency [Williamson and Govardhan, 2004]. This effect can be accounted for by expressing the cylinder response as a function of the 'true' reduced velocity (i.e. $U_r\mathrm{St}/f^*$), which is dependent on the actual response frequency, rather than the natural frequency in a still fluid. Thus, in this thesis the results of previous studies are presented in terms of $U_r\mathrm{St}/f^*$, which facilitates the direct comparison between studies that employed different mass ratios.

Amplitude Response Branches

The first amplitude response branch occurs in the range $U_r\mathrm{St}/f^* \approx 0.3 - 0.45$ [Aguirre, 1977; Okajima et al., 2003], as can be seen in Figure 1.7, and is generally associated with the S-I mode [Jauvtis and Williamson, 2003; Okajima et al., 2003]. However, Aguirre [1977] found that the A-II mode was dominant for $U_r\mathrm{St}/f^* \gtrsim 0.4$. There is also some disagreement regarding the frequency of vortex-shedding during the first branch. Jauvtis and Williamson [2003] estimated the shedding frequency using measurements of the fluid forces, and found that lock-in occurred for the entirety of the first branch, while Aguirre [1977] found that the onset of lock-in occurred at a slightly higher reduced velocity, based on flow visualisation of the wake. Finally, Okajima et al. [2003] measured the velocity fluctuations six diameters downstream of the cylinder using a hot-film probe, and found that the wake continued to follow the Strouhal relation throughout this

region, i.e. lock-in was not occurring. The cause of this disagreement, as well as the effects of the different methods of estimating the presence of lock-in, have not been examined.

The SA mode is dominant in the second branch [Aguirre, 1977; Okajima et al., 2003], and the vortex-shedding is locked-in to the cylinder motion. Aguirre [1977] found that the second branch occurred over the range $U_r\mathrm{St}/f^* \approx 0.52-0.65$. This range of reduced velocity and amplitude response ($A/D \lesssim 0.1$) corresponds to the region of the $U_r\mathrm{St}/f^*-A/D$ plane in which Nishihara et al. [2005] observed the A-IV mode and Konstantinidis et al. [2007] observed mode competition between the A-IV and SA modes; however, the A-IV mode has not previously been recorded in the wake of a freely oscillating cylinder. Aguirre [1977] found that the reduced velocity range over which the second branch extended was significantly shorter when the reduced velocity was decreased, i.e. the response regime was affected by hysteresis in this region. He also noted that the second branch extended over a wider range of $U_r\mathrm{St}/f^*$ when the structural damping was reduced, as can be seen in Figure 1.7.

Low Amplitude Region at $U_r\mathbf{St}/f^* \approx 0.5$

The counter-intuitive nature of the low amplitude region separating the two response branches at $U_r\mathrm{St}/f^* \approx 0.5$ has been noted by previous researchers (e.g. Konstantinidis et al. [2005]; Naudascher [1987]; Okajima et al. [2003]); for transverse VIV and classical resonance, the synchronisation between the forcing and the structural response causes the vibrations to increase in amplitude and become steadier [Govardhan and Williamson, 2000], while for streamwise VIV the opposite is observed. Various hypotheses have been proposed to explain the reduction in A/D in this region.

Okajima et al. [2003] installed a splitter-plate in the cylinder wake, which prevented the alternate shedding of vortices, as demonstrated schematically in Figure 1.8. The amplitude response of the cylinder measured with and without the splitter-plate attached is shown in Figure 1.9 in terms of the conventional reduced velocity, U_r. When the splitter-plate was attached, the low amplitude region at $U_r\mathrm{St}/f^* \approx 0.5$ (which corresponds to $U_r \approx 2.5$) was not observed; the amplitude response continued to increase throughout this region, before dropping off at approximately the same reduced velocity at which the original cylinder (without a splitter-plate) began to exhibit the second response branch. Aguirre [1977] performed similar experiments and observed the same response. Based on these results, Naudascher [1987] proposed that the low amplitude region was caused by the incompatibility between the symmetric S-I and the alternate SA modes which dominate in the first and second branches, respectively; in the low amplitude region, symmetric vortex-shedding is required to excite large amplitude cylinder vibration, but as the reduced velocity is increased the wake has an increased tendency to form an alternate structure. At $U_r\mathrm{St}/f^* \approx 0.5$ the alternate arrangement dominates at the expense of the S-I mode, and the fluid excitation becomes negligible. However, this hypothesis does not explain why the SA mode is capable of providing positive energy transfer to the cylinder in the second branch, but not at $U_r\mathrm{St}/f^* \approx 0.5$.

The forced oscillation experiments of Nishihara et al. [2005] indicated that the unsteady drag force was in phase with the cylinder displacement in the region $U_r\mathrm{St}/f^* \approx 0.5$ (for $A/D = 0.05$), which corresponded to negligible fluid excitation. They suggested that there was a change in the phase of vortex-shedding (and therefore the unsteady fluid forces) with respect to the cylinder motion in

this region, which reduced the levels of fluid excitation and was responsible for the low amplitude response observed for freely oscillating cylinders. Similarly, Konstantinidis et al. [2005] observed a change in the phase of vortex-shedding with respect to the external forcing (i.e. the pulsations in the freestream velocity) between $U_r\mathrm{St}/f^* = 0.5$ and 0.57 and argued that this was likely to cause a change in the fluid forcing and excitation acting on a freely oscillating cylinder. However, the transverse forced vibration study of Morse and Williamson [2009] indicated that the fluid excitation was negative *whenever* the forcing amplitude was larger than the amplitude of a freely oscillating cylinder (with negligible damping) at the same reduced velocity. Therefore, the results of Nishihara et al. [2005] regarding the negative fluid excitation observed at $U_r\mathrm{St}/f^* \approx 0.5$ for $A/D = 0.05$ may simply indicate that the non-dimensional amplitude response of a freely oscillating cylinder will not exceed 0.05 at this reduced velocity, rather than indicating the physical mechanism causing the reduction in amplitude at this point.

Fluid Forces

Knowledge of the fluid forces acting on a freely oscillating cylinder is crucial if the excitation and structural dynamics throughout the VIV response regime are to be fully understood. Govardhan and Williamson [2000] used simultaneous measurements of the structural displacement, fluid forces and velocity fields the wake of a cylinder free to oscillate in the transverse direction to examine the hysteretic switching between the 'Initial' and 'Upper' response branches. The Initial branch is associated with the '2S' mode (shown in Figure 1.10(a)), while the '2P' mode (Figure 1.10(b)) occurs during the Upper branch. These two modes are similar in appearance to the SA and A-IV modes, respectively [Konstantinidis et al., 2007]. Govardhan and Williamson observed that, despite the 2P mode

causing significantly higher levels of cylinder vibration, it did not correspond to greater fluid forces. However, they found that at the transition between the two branches, there was a change in the phase of the forcing with respect to the cylinder motion; when the 2P mode occurred the forcing was largely in phase with the cylinder velocity and more energy was transmitted to the structure than when the 2S mode was dominant.

As far as the author is aware, no previous study in the literature has attempted to measure the fluid forces acting on a cylinder freely oscillating in the streamwise direction. Therefore, it is not known whether the mode competition observed in streamwise VIV will also correspond to a change in the amplitude and phase of the fluid forces, as Govardhan and Williamson [2000] observed for the transverse case. Similarly, it is unclear how the drag force behaves throughout the response regime; in particular, whether there is a change in its phase with respect to the cylinder motion near $U_r \mathrm{St}/f^* = 0.5$, as hypothesised by Nishihara et al. [2005] and Konstantinidis et al. [2005].

1.2.4 Flow Past Cylinders with Multiple Degrees-of-Freedom

Cylinders with Large Mass Ratios

In practice, the majority of structures which are vulnerable to VIV will be free to move in more than one direction, i.e. they will have multiple degrees-of-freedom. Sarpkaya [1995] and Jauvtis and Williamson [2003] compared the amplitude response of cylinders which had mass ratios above 6, and were free to move in both the streamwise and transverse directions, to those of cylinders free to move only transversely to the flow. Both studies found that the additional

DOF caused an increase in the peak transverse amplitude of approximately 10%, but concluded that the streamwise motion did not significantly alter the overall cylinder response. Jauvtis and Williamson [2003] observed the S-I and the SA modes at the peaks of the first and second response branches, respectively, in agreement with the results of Okajima et al. [2003], for a single-DOF cylinder.

Cylinders with Low Mass Ratios

A subsequent series of experiments performed by Williamson and Jauvtis [2004] indicated that when the mass ratio of the cylinder was below 6, the streamwise freedom significantly altered the cylinder response; the response regime contained a new branch at $U_r\mathrm{St}/f^* \approx 1.2 - 1.5$, which they referred to as the 'Super Upper' branch. The streamwise frequency doubled (i.e. $f_x \approx 2f_n$) and the cylinder followed a figure-of-eight trajectory, with peak amplitudes of approximately $A/D = 0.3$ and 1.5 in the streamwise and transverse directions, respectively. A new mode was observed in the wake, which involved the shedding of two triplets of vortices per cycle (the '2T' mode). Throughout the response regime examined, $U_r\mathrm{St}/f^* \approx 1 - 2$, it was found that the additional DOF caused an increase in the transverse amplitude response compared to the single DOF case.

Blevins and Coughran [2009] examined the fluid forces acting on a series of cylinders with $m^* < 6$ which could be constrained to move in only the streamwise or transverse directions, or allowed to move in both. They found that the the streamwise amplitude response of the multi-DOF cylinder was similar to that measured for the streamwise-only case (as was also found by Jauvtis and Williamson [2004]). In the first response branch the multi-DOF cylinder vibrated only in streamwise direction, which is consistent with the results of Nishihara et al. [2005], who found that the amplitude of the lift force was negligible in this

region. In the second branch the cylinder followed a figure-of-eight trajectory, in which the cylinder vibrated in the streamwise and transverse directions at f_x and $f_x/2$, respectively; the amplitude was slightly larger in the streamwise direction compared to the transverse vibrations.

1.3 Main Findings

The main findings of the literature review are summarised below:

- Vortex-Induced Vibrations occur when the fluid forces caused by the vortices shed from a bluff body coincide with one of its natural frequencies. The resulting vibrations can cause the vortex-shedding to lock-in to the frequency of the structural motion.
- VIV can occur in both the streamwise and transverse directions, although the former case has received comparatively little attention.
- For the case of a cylinder oscillating in the streamwise direction, the lock-in range is centred at $U_r\mathrm{St}/f^* = 0.5$ and increases with A/D.
- The wake of a cylinder oscillating in the streamwise direction can exhibit a number of modes, including the A-II, SA, A-IV and S-I modes (shown in Figure 1.4).
- The S-I mode induces a negligible lift force, and tends to decay into an alternate structure downstream. The point at which breakdown occurs is affected by the vibration amplitude and reduced velocity, as well as transient conditions.

- The response regime of a cylinder free to move in the streamwise direction is characterised by two branches, separated by a low amplitude region at $U_r\mathrm{St}/f^* \approx 0.5$. The mass-ratio and structural damping control the peak amplitude observed. The reduced velocity range over which VIV occurs is affected by the mass ratio (due to added mass effects), the structural damping and hysteresis.

- The first branch occurs over the range $U_r\mathrm{St}/f^* \approx 0.3 - 0.45$. There are conflicting results in the literature in terms of the reduced velocity range over which the S-I mode dominates and the existence of lock-in in this region.

- The second branch is observed for $U_r\mathrm{St}/f^* \approx 0.5 - 0.6$ and is associated with the SA wake mode. The A-IV mode has also been observed at similar values of $U_r\mathrm{St}/f^*$ and A/D in forced oscillation studies, but to the best of the author's knowledge, it has not been recorded in the wake of a freely oscillating cylinder.

- The low amplitude region in the response regime at $U_r\mathrm{St}/f^* \approx 0.5$ coincides with the centre of the lock-in range. It has been suggested that this counter-intuitive reduction in amplitude is caused by the incompatibility of the S-I and SA modes which dominate at lower and higher reduced velocities, respectively [Naudascher, 1987], or a change in the phase of the vortex-shedding with respect to the cylinder motion [Konstantinidis et al., 2005; Nishihara et al., 2005]. However, no studies have attempted to measure the fluid forces acting on a cylinder freely oscillating in the streamwise direction and thus explain the presence of low amplitude vibrations at $U_r\mathrm{St}/f^* \approx 0.5$.

1.4 Objectives of Current Study

The literature review has shown that while VIV in the transverse direction has been well-studied, comparatively little in known about the streamwise case. A number of areas in which the results of previous investigations of streamwise VIV have been lacking or conflicting results exist are listed below:

- No previous studies have presented simultaneous, quantitative measurements of the structural response and the wake of a cylinder experiencing VIV in the streamwise direction.
- There are conflicting results regarding the dominant wake mode and the existence of lock-in in the first response branch.
- The A-IV mode and unsteady mode-competition has been observed in the region of the second response branch in previous forced oscillation studies, but no such behaviour has been reported in the wake of a freely oscillating cylinder in the same region.
- There has been no attempt to estimate the fluid forces acting on a freely oscillating cylinder throughout the streamwise response regime.

Based on these observations the objectives of the thesis are outlined as:

1. Design a system in which the wake and the structural motion of a cylinder exhibiting VIV in the streamwise direction can be measured simultaneously using time-resolved Particle-Image Velocimetry.
2. Characterise the variation in the structural response and dominant wake mode throughout the streamwise response regime.

3. Examine the behaviour of the wake in the first response branch, focusing on the conflicting results in the literature regarding the presence of the S-I mode and lock-in.

4. Examine the effects of hysteresis on the wake and structural response near the second branch, and investigate the stability of the system in this region.

5. Estimate the fluid forces acting on the cylinder throughout the response regime and relate the estimates of the forcing to the dominant wake modes observed.

1.5 Outline of Thesis

The remainder of this thesis is divided into six chapters. The following chapter outlines the experimental facilities and techniques used throughout this study. Chapter 3 describes the dominant wake modes and cylinder response characteristics throughout the response regime. The presence of multiple wake modes and their effect on the structural motion in the first and second response branches are discussed in Chapters 4 and 5, respectively. Chapter 6 presents estimates of the fluid forces acting on the cylinder, while the final chapter summarises the work presented throughout the entire thesis and makes some suggestions for future work.

1.6 Figures

Figure 1.1: Flow visualisation presented in Van Dyke [1982], showing the von Kármán vortex street in the wake of a stationary cylinder (Re = 140).

Figure 1.2: Mode map, adapted from Williamson and Roshko [1988], showing the wake modes observed throughout the $U_r\mathrm{St}/f^* - A/D$ plane. The cylinder was forced to oscillate in the transverse direction.

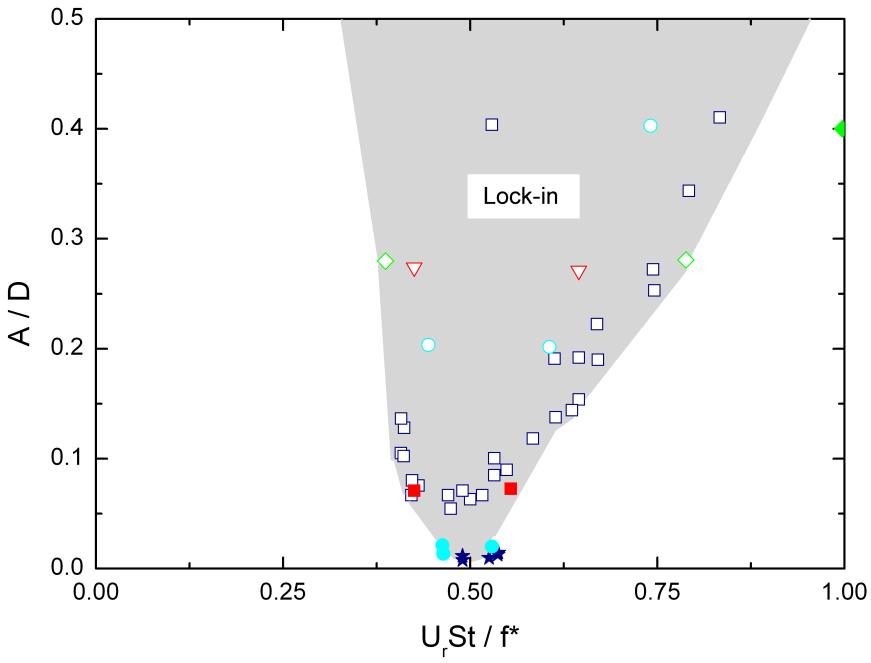

Figure 1.3: Minimum forcing amplitude required to induce lock-in as a function of reduced velocity, compiled from various studies in the literature. The details of the studies and the symbols are listed in Table 1.1. The shaded region corresponds to the approximate lock-in range.

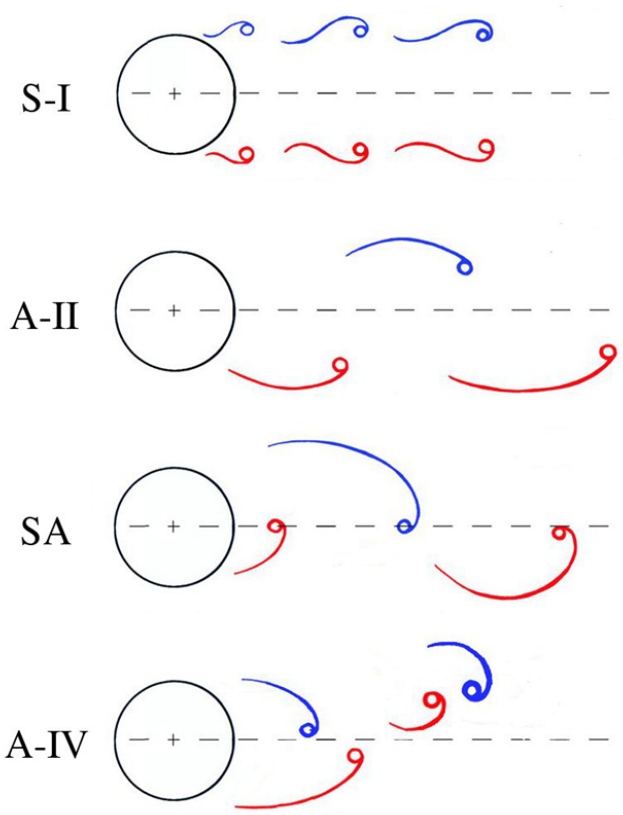

Figure 1.4: Sketch representing the S-I, A-II, SA and A-IV wake modes.

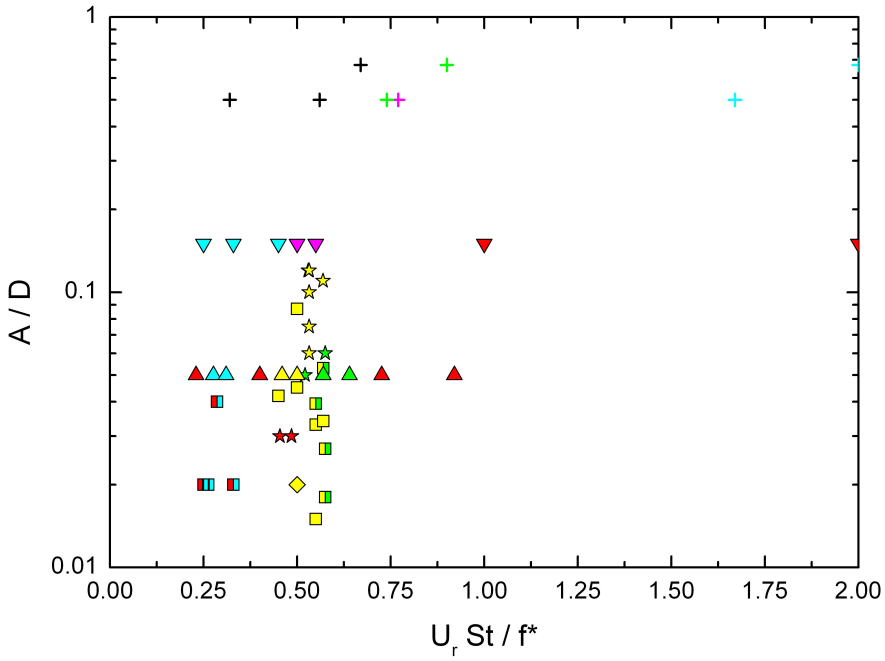

Figure 1.5: Summary of published forced studies of streamwise VIV in which the wake modes have been identified. The symbol colour denotes the wake mode observed at each point; S-I (cyan); S-II (black); A-II (red); A-III (magenta); A-IV (green); and SA (yellow). The study is indicated by the symbol used, as detailed in Table 1.2. Symbols with two colours (i.e. the studies of Konstantinidis et al. [2005, 2007] and Konstantinidis and Balabani [2007]) indicate points at which mode-switching was observed.

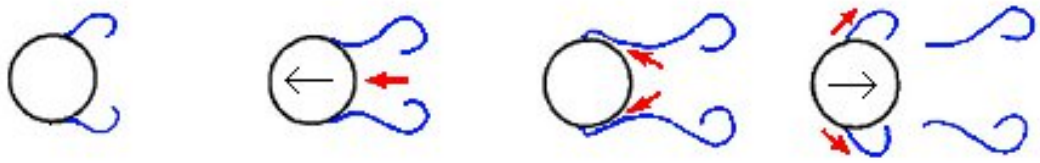

Figure 1.6: Sketch representing the stages of the wake-breathing process (i.e. the S-I wake mode). The black and red arrows indicate the direction of the cylinder motion and the fluid entrainment, respectively. Adapted from Aguirre [1977].

Figure 1.7: Amplitude response of three cylinders with different levels of damping. The mass ratio was 1.2, and ζ_w was measured in water, i.e. it included the effects of both the structural and the hydrodynamic damping. Adapted from Aguirre [1977].

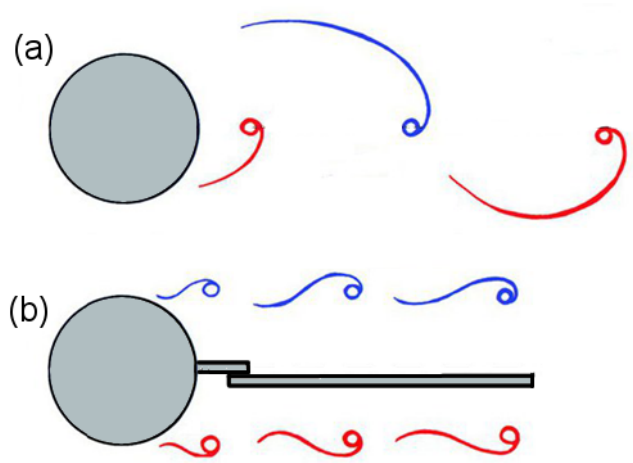

Figure 1.8: Schematic showing the splitter-plate used by Okajima et al. [2003] and Aguirre [1977]; when the plate is absent the vortices are shed alternately (a); however, when the splitter-plate is present this shedding mode is not possible and the S-I mode is observed (b).

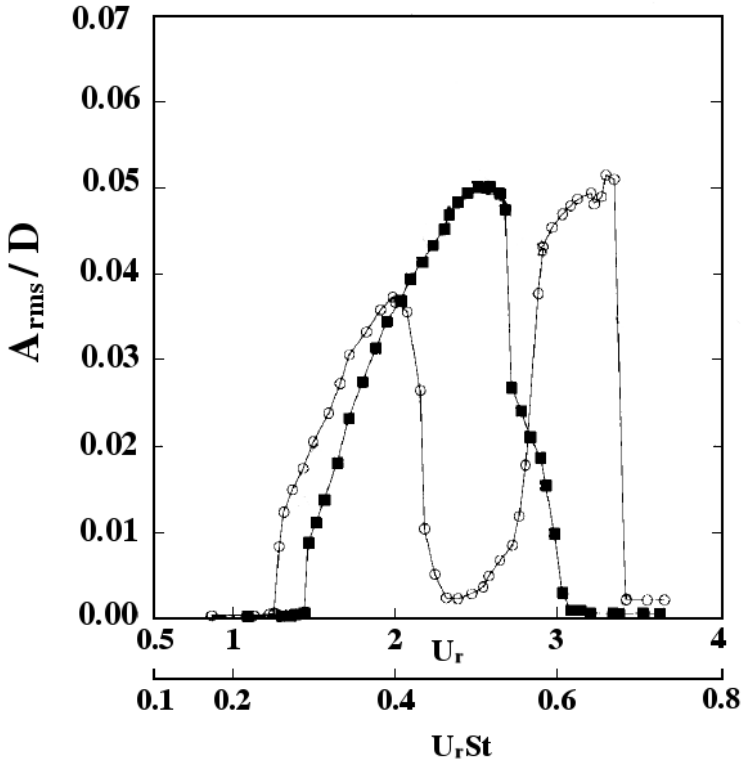

Figure 1.9: Amplitude response of a circular cylinder with and without a splitter-plate (closed and open symbols, respectively), adapted from Okajima et al. [2003]. The cylinder had a combined mass-damping parameter of $C_n = 0.7$ (the values of the mass ratio and damping were not identified), and the Reynolds number range was $8000 - 40000$. The cylinder response frequency was not presented, and the results are not shown in terms of the true reduced velocity. The low amplitude region occurs at $U_r \approx 2.5$.

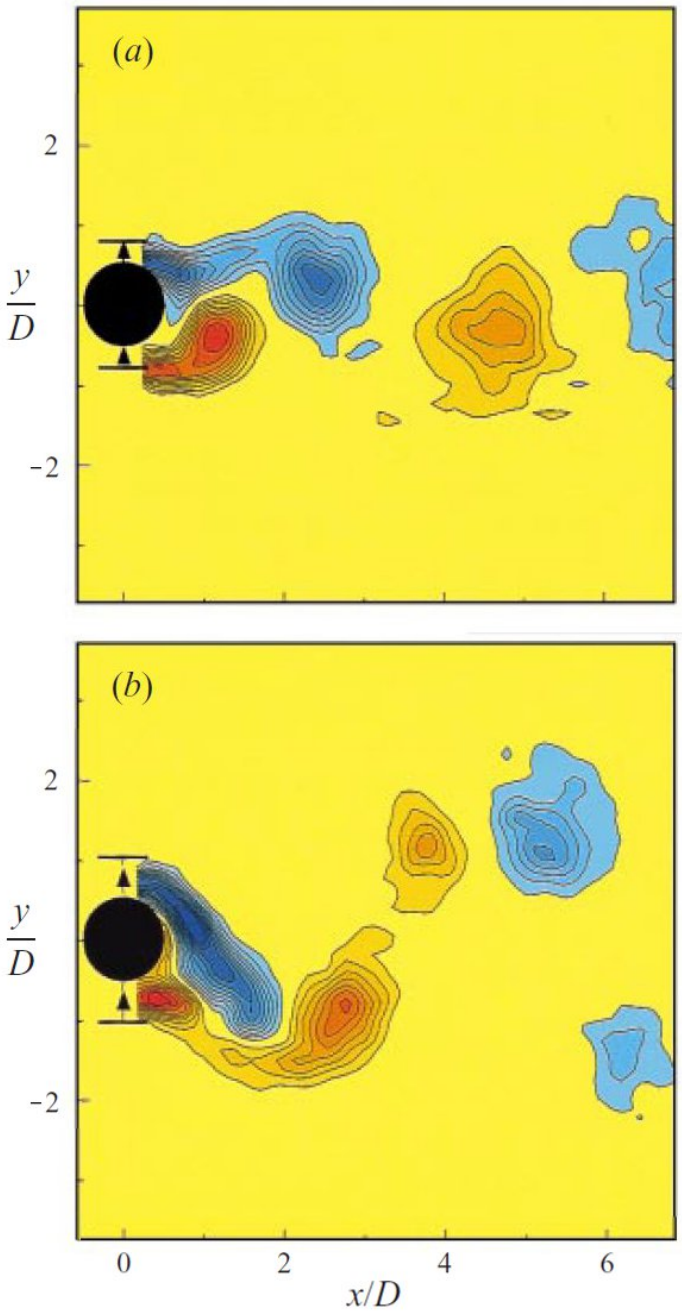

Figure 1.10: Vorticity distributions indicating the '2S' (a) and '2P' modes (b), adapted from Govardhan and Williamson [2000]. The cylinder is vibrating in the transverse direction at $A_y/D = 0.33$, $U_r/f^* = 5.4$ (a) and $A_y/D = 0.6$, $U_r/f^* = 5.82$ (b). Contour levels for each case are $\omega_z D/U_0 = \pm 0.4, \pm 0.8, \ldots$

Chapter 2

Experimental Details

2.1 Introduction

The experimental facilities and techniques as well as the various post-processing algorithms used to obtain the results presented throughout this thesis are described in this chapter.

The experiments involved the simultaneous measurement of the displacement signal of a cylinder undergoing VIV in the streamwise direction and the surrounding velocity field using Particle-Image Velocimetry (PIV). The measurements were performed in two stages; the results presented in Chapter 3 and Sections 4.2 to 4.6 were performed in the first stage, while those discussed in Sections 4.7 to 4.8 and Chapters 5 and 6 were performed in the second stage. The same experimental facilities and cylinder were used in both stages; however, the cylinder had a higher natural frequency in the second stage (due to changes in the stiffness of the supports) and the experimental procedures employed in both stages differed slightly, as will be outlined in the following sections. For convenience, the mea-

surements used to obtain the results presented in Chapter 3 and Sections 4.2 to 4.6 are referred to as Test Stage 1, while those presented in Sections 4.7 to 4.8 and Chapters 5 and 6 are referred to as Test Stage 2.

2.2 Water Tunnel Facility

The experiments were performed in a closed-loop water tunnel, which is shown schematically in Figure 2.1. A pump is used to generate the flow, and the flowrate can be adjusted using two valves (labeled 'A' and 'B' in Figure 2.1). The maximum flowrate was approximately 290L/min, which corresponded to a freestream velocity of approximately 1m/s. The water tunnel is also capable of generating pulsating flow using a rotating valve and motor, which was employed in the work of Konstantinidis and Balabani [2007, 2008] and Konstantinidis et al. [2003, 2005, 2007], who investigated unsteady flow past a fixed cylinder. However, the current experiments were performed under steady-flow conditions and the section of the tunnel containing the rotating valve was not used. A magnetic flowmeter was used to monitor the flowrate (but not to estimate the freestream velocity, which was performed using PIV). A chiller unit was connected to the reservoir, which was used to control the water temperature to within $22 \pm 0.5°C$. Bleeds were installed at the top of the tunnel and in the reservoir to remove any air in the system.

The test-section had a cross-sectional area of 72mm×72mm, and the walls were made of Perspex to allow optical access. A hexagonal honeycomb, screens and a 9:1 contraction were used to condition the flow upstream of the test-section. The profiles of the mean and fluctuating components of the velocity were mea-

sured using PIV. The details of the measurements are presented in Section 2.4.2. The fluctuating velocity was calculated as:

$$u'(y) = \frac{1}{N}\sum_{i=1}^{N}\left|u(y,t_i) - \overline{u}(y,t_i)\right|, \tag{2.1}$$

where u is the streamwise velocity component, N is the number of fields examined ($N = 1000$), and t_i is the time-step of the measurements.

The symmetry of the flow in the test-section is indicated in Figure 2.2, which shows the profiles of the mean and fluctuating components of the streamwise velocity measured at three values of Reynolds number (Re = 1540, 2910 and 4340). The profiles were measured approximately eight cylinder diameter upstream of the mean cylinder position. The magnitude of the fluctuating velocity was found to be less than 2% of the U_0 and $\overline{u}/U_0$ was uniform to within 1% 1.5 cylinder diameters (10.7mm) from the test-section walls.

2.3 Test Section and Cylinder Supports

It was necessary to design a test-section such that the cylinder could be supported within the flow and vibrate in the streamwise direction. A number of constraints existed; the structural damping had to be sufficiently low so as to allow relatively large streamwise oscillations; the cylinder supports should not prevent optical access to the flow surrounding the cylinder; and any motion of the cylinder other than translation in the streamwise direction (e.g. transverse motion or pitching) was required to be negligible. The cylinder was also required to have a sufficiently low natural frequency, such that the entire streamwise response regime could be examined in the water tunnel. As the maximum freestream velocity attainable

was approximately 1m/s, in order to reach a reduced velocity of $U_r\mathrm{St}/f^* = 0.8$ (which is beyond the second response branch), the maximum response frequency was required to be below $f_x \sim 35\mathrm{Hz}$.

The cylinder was supported at either end using fishing wires, which were perpendicular to both the flow direction and the cylinder axis, as shown in Figure 2.3. Fishing wire was found to be a suitable choice of material, as it allowed the system to have a natural frequency in a suitable range ($f_n \approx 15\mathrm{Hz} - 25\mathrm{Hz}$), provided low structural damping, was thin (and therefore had negligible blockage effects) and did not snap at high flowrates. The cylinder was secured in place along the wires using rubber sealant glue, which prevented it from moving in the transverse direction. The ends of the wire were passed through small holes in the test-section walls, which were then sealed with sealant glue to prevent leakage.

Figure 2.3 also indicates the coordinate system; the origin was defined as the mean position of the centre of the cylinder, x and y were measured in the streamwise and transverse directions, respectively, and z was measured along the cylinder axis from its midspan. As the mean drag coefficient and the mean cylinder position varied with the flowrate, the origin of the coordinate system was also defined separately for each reduced velocity examined. The change in the mean cylinder position throughout any of the experiments performed (i.e. the difference in the mean position between the lowest and the highest flowrates examined) was less than $0.14D$.

The tension in the wires was maintained by suspending weights outside the test-section. The stiffness of the supports was found to weakly depend on the magnitude of the weight applied. The weights could therefore be adjusted to ensure that the stiffness at both ends of the cylinder was approximately equal,

and the cylinder motion was approximately symmetrical about its midspan. In order to ensure that the levels of non-translational motion were negligible, tests were performed in which the cylinder motion was tracked by illuminating it along its axis and taking images at various flow rates. The maximum change in angle of the cylinder axis was less than 1°, and the maximum displacement at the cylinder tip due to rotational motion was found to be less than 5% of that due to translational motion. For all flowrates examined in which the cylinder experienced VIV, the spectra of the displacement signals indicated that any energy contained in any sub- or super-harmonics was less than 1% of that occurring at the primary response frequency (i.e. f_x). This indicated that the cylinder displacement signals did not contain significant non-linear components, and that the stiffness of the cylinder supports was essentially linear.

The cylinder was made of solid Perspex and had a mass ratio of $m^* = 1.17$ (neglecting the mass of the support wires). It had a diameter and length of 7.1mm and 71mm, respectively, which corresponded to an aspect ratio of $AR = 10$ and a blockage ratio of 9.9%. As the aspect ratio is relatively low, the wake at the cylinder mid-span (where the velocity field is measured) may be subject to end-effects which increase the three-dimensionality of the flow field. In order to assess the effects any three-dimensional flow structures present would have on the current set of experiments, prior work was performed using laser-Doppler anemometry in which the fluctuating and mean velocity components in the streamwise and transverse directions were measured at 1mm intervals along the axial direction of the cylinder for a range of reduced velocities. It was found that the magnitude of the streamwise and transverse velocity fluctuations were approximately constant two diameters from either end of the cylinder. This is consistent with the results

of Konstantinidis et al. [2003], who also performed laser-Doppler anemometry measurements in the same water tunnel.

While a very large aspect ratio would be ideal, in practice this was not possible in the current test facilities. The aspect ratio of 10 is of the same order of magnitude of the majority of the experimental work cited in this paper; in particular, Aguirre [1977] used an AR of 10, while Jauvtis and Williamson [2003] used aspect ratios of 7.5 and 10. It is also worth noting, Govardhan and Williamson [2000] compared the amplitude response of a cylinder free to move in transverse direction for the case of $AR = 10$ and $AR = 20$ (the two cases also had different mass-damping values), and found a very good matching. This suggests that in spite of the three-dimensional flow structures associated with finite-length cylinders, the results of studies with cylinders having an $AR \sim 10$ are in general applicable to cases with larger AR values.

The damping and natural frequency of the cylinder were found to depend on the tension within the wires as they were sealed in place, i.e. the structural parameters were not the same each time the cylinder was installed. The structural parameters were estimated prior to each set of experiments from a series of 'free-decay' or 'tap' tests. The displacement signal of a single-DOF, lightly damped body following an applied perturbation is given by:

$$x(t) = A_0 \sin(2\pi f_n t)\, e^{-2\pi f_n \zeta t}, \tag{2.2}$$

where A_0 is the amplitude of the initial disturbance, and f_n and ζ are the natural frequency and the damping ratio in the fluid in which the tap test was performed. The natural frequency and damping of the system can be found by 'tapping' the

structure, measuring the resulting displacement signal and fitting the signal to equation 2.2.

A series of tap tests were performed in both air and water, in order to identify the structural parameters with and without the added mass effects. A sample displacement signal is shown in Figure 2.4(a). The cylinder was displaced a number of times in each set of measurements. To ensure that the signal was oscillating about zero, the mean was estimated from a small segment of the signal, prior to the first time that the cylinder was perturbed ($t < 0.25$s in Figure 2.4(a)), and was deducted from the signal. The resulting signal was then divided into segments, each corresponding to one tap test, as shown in Figure 2.4(b). The peaks in each segment were identified (red circles in Figure 2.4(b)), and the time difference between the first and last peak ($t_{p,1}$ and $t_{p,N}$, respectively) were used to estimate the natural frequency:

$$f_n = \frac{N_p - 1}{t_{p,N} - t_{p,1}}, \tag{2.3}$$

where N_p is the number of peaks identified. Finally, a least-squares optimisation algorithm was used to fit the exponential decay curve $A_0 e^{-2\pi f_n \zeta t}$ to the peaks (green line in Figure 2.4(b)), which was used to find the damping ratio. This method of estimating f_n and ζ was found to provide more consistent estimates than identifying the peak in the frequency spectra of the segments of the displacement signal or applying the logarithmic decrement method.

The values of the natural frequency and the damping ratio found from each test were averaged and the standard deviation was used to estimate the accuracy of the estimates. The natural frequency was found from tests performed

in still water (in which case the effective mass of the system included the added mass). Assuming an ideal mass coefficient of $C_a = 1$, and the density of air to be 1.225kg/m^3, the total added mass of the system in air is $\Delta m = 3.49 \times 10^{-6}$kg, which is approximately 0.1% of the cylinder mass, and will have a negligible effect on the structural response. Therefore, the natural frequency measured in air, $f_{n,a}$, could be used as an estimate of the natural frequency in the absence of added mass effects, as proposed by Sarpkaya [2004].

Table 2.1: Mean and standard deviation of a series of measurements of the damping and natural frequency of the cylinders used in Test Stages 1 and 2.

Test Stage	Parameter	Mean value	Standard deviation	Working fluid	Number of tests
1	f_n	15.082Hz	0.057Hz(0.38%)	Water	13
1	$f_{n,a}$	27.866Hz	0.074Hz(0.265%)	Air	9
1	ζ_w	0.029	0.0019(6.6%)	Water	13
1	ζ	5.35×10^{-3}	0.426×10^{-3}(7.95%)	Air	9
2	f_n	23.703Hz	0.031Hz(0.13%)	Water	9
2	$f_{n,a}$	33.11Hz	0.09Hz(0.27%)	Air	5
2	ζ_w	0.02	0.9×10^{-3}(4.55%)	Water	9
2	ζ	3.74×10^{-3}	0.182×10^{-3}(4.86%)	Air	5

Similarly, the fluid damping in air is likely to be negligible compared to that in water; therefore, the damping ratio measured in air, ζ, will be approximately equal to the structural damping, while the value measured in water, ζ_w, will be equal to the combined hydrodynamic and structural damping.

The results of the tap tests performed for Test Stages 1 and 2 are presented

in Table 2.1. In both cases, the uncertainty in the estimated natural frequency was less than 0.4%, while the uncertainty in the estimates of ζ was higher, in the range $4\% - 8\%$.

2.4 Particle-Image Velocimetry

Particle-Image Velocimetry is a non-invasive optical flow measurement technique which has become common practice in many areas of fluid mechanics research [Westerweel et al., 2013]. A brief overview of two-component PIV (in which two of the velocity components are measured) is outlined here; a thorough description of the technique can be found in Raffel et al. [2007]. The method requires the flow to be seeded with small particles which are assumed to follow the flow, i.e. the velocity of the particles is assumed to be approximately equal to the local velocity of the fluid. A thin plane of the flow is illuminated with a laser sheet and two images are acquired in quick succession. These images are decomposed into sets of interrogation windows containing a small number of particles (~ 10). The windows from the first image are then cross-correlated with those in the second image, and the maximum of the cross-correlation matrix is used to estimate the mean displacement of the particles, $\Delta\mathbf{x}$. The local fluid velocity can then be estimated as:

$$\mathbf{u} = \frac{\Delta\mathbf{x}}{\Delta t}, \tag{2.4}$$

where Δt is the time difference between acquiring the first and second images.

The technique can be extended to measure the velocity component and gradients normal to the laser sheet and in a three-dimensional volume [Raffel et al.,

2007]. However, in this work only two-component measurements were performed.

The measurements were performed using a pulsed Nd:Yag laser, supplied by Dantec Dynamics, and a high speed IDT X-3 CMOS (Complementary metaloxide-semiconductor) camera which had a resolution of 1024×1280 pixels. The flow was seeded using 14μm silver-coated hollow glass spheres. The laser sheet was approximately $\sim$ 1mm thick, and was positioned at the cylinder midspan, as shown in Figure 2.5. Both the CMOS camera and the light source of the laser were mounted on a mechanical transverse which was controlled using BSA Flow Manager Software (Dantec Dynamics), which had an accuracy of $\pm$0.001mm and moved independently of the water tunnel position.

The image-pairs were acquired using the Dynamic Studio software package (Dantec Dynamics), which was also used to synchronise the camera and the laser pulses. The velocity fields were estimated from the image-pairs using JPIV (http://www.jpiv.vennemann-online.de/). For both test stages a three-pass cross-correlation scheme with 50% window overlap was used. The normalised median test [Westerweel and Scarano, 2005] was applied after each pass, and erroneous vectors were replaced with the local median vector. For Test Stage 1, a 3×3 smoothing filter was also applied to the fields after each pass. The specific details of the cross-correlation scheme employed for Test Stages 1 and 2 are listed in Table 2.2.

2.4.1 Calibration

The PIV images were calibrated by acquiring an image of a grid of circular dots, which were 0.5mm in diameter and had a uniform spacing of 2mm. The images

Table 2.2: Details of the three-pass cross-correlation scheme used to evaluate the velocity fields for Test Stages 1 and 2.

Test Stage	Setting	Pass 1 [pixels]	Pass 2 [pixels]	Pass 3 [pixels]
1	Interrogation Window Size	64	32	24
1	Search Domain Size	12	4	4
1	Vector Spacing	32	16	12
2	Interrogation Window Size	64	32	24
2	Search Domain Size	12	4	4
2	Vector Spacing	32	16	12

were processed in Matlab using a black and white threshold filter, the centroid of each dot was found, and the distance between each centroid was calculated. These values were averaged to find the calibration constant (in units of pixels/mm), and the standard deviation was found in order to approximate the accuracy of the method. The calibration factor was found to be 26.183pixels/mm (with a standard deviation of 0.138pixels/mm) for Test Stage 1, while for Test Stage 2, the calibration factor was estimated as 30.541pixels/mm (with a standard deviation of 0.174pixels/mm). Based on these values, the calibration constants found for Test Stages 1 and 2 were found to be accurate to within 0.53% and 0.57%, respectively.

It should be noted that, as the freestream velocity was also measured using the same PIV system, the errors in the calibration constant will not lead to errors in the non-dimensional velocity and its gradients, e.g. $u/U_0, \omega_z/DU_0$, etc. (as both

the numerator and the denominator are scaled by the same calibration constant). Similarly, while the estimation of groups such as U_r and St (see Section 2.9) will be affected by calibration errors, the combined 'true' reduced velocity, $U_r\mathrm{St}/f^*$, will not.

2.4.2 Freestream Velocity Measurements

The water tunnel contained a magnetic flowmeter which could be used to approximate the freestream velocity. However, it was decided to measure U_0 using PIV, as this method was found to be more accurate, particularly at high flowrates, and reduced the total errors in the calculation of the reduced velocity, as discussed in the previous section.

A series of PIV measurements were acquired of a small region in the centre of the test-section eight diameters upstream of the mean cylinder position. These were processed using JPIV, and the cross-correlation scheme listed in Table 2.3 (the same scheme was used for both test stages). The streamwise velocity component determined from all the fields was averaged to find an estimate of U_0.

Freestream Velocity Profiles

In order to examine the conditions of the flow entering the test-section, the mean and fluctuating streamwise velocity components were measured across the span of the test-section, i.e. $y/D = -5.07$ to 5.07, eight diameters upstream of the cylinder, as shown in Figure 2.2. It was not possible to capture the entire width of the test-section in a single PIV image; therefore the mechanical traverse was used to move the camera and laser source in the transverse direction, and two sets of PIV measurements were acquired; the resulting vector fields spanned

Table 2.3: Details of the two-pass cross-correlation scheme used to evaluate the velocity fields in the freestream for Test Stages 1 and 2, as well as the velocity profiles shown in Figure 2.2.

Measurement Variable	Setting	Pass 1 [pixels]	Pass 2 pixels]
U_0	Interrogation Window Size	128	64
U_0	Search Domain Size	32	12
U_0	Vector Spacing	64	32
$\overline{u}, u'$	Interrogation Window Size	64	64
$\overline{u}, u'$	Search Domain Size	32	12
$\overline{u}, u'$	Vector Spacing	32	32

the ranges $y/D = -4.76$ to -0.28 and $y/D = 0.01$ to 4.83, respectively. These could be combined to form a profile which spanned the width of the section.

At each flowrate, 1000 image-pairs were acquired at 100Hz on either side of the test-section. The velocity vectors were estimated using the PIV settings listed in Table 2.3.

2.4.3 Experimental Procedure

Each time the cylinder was installed in the water tunnel facility, a number of measurements were performed prior to the PIV measurements of the cylinder response and the wake.

Firstly, the tensions within both fishing wires were adjusted and the rotational motion of the cylinder was measured to ensure that any pitching motion was negligible. Series of tap tests were then performed in still water and air to measure

the structural parameters of the system. The flow was subsequently seeded, and a series of PIV measurements were performed at various flowrates to find an optimal range of Δt and a suitable cross-correlation scheme. Finally, the upstream velocity profiles were measured and the measurements of the cylinder response and wake were acquired throughout the response regime.

Prior to acquiring a set of PIV measurements, the flowrate was adjusted and the system was allowed to settle for at least ten minutes to ensure that the cylinder response and wake had reached a steady state (if one existed). The laser and camera was moved in the upstream direction using a mechanical traverse, and the freestream velocity was measured, as outlined in Section 2.4.2. The traversing system was then returned to its original position, such that the cylinder and its wake were within the measurement domain, and PIV image-pairs were acquired.

2.5 Phase-Averaging

The measurements of the cylinder motion and the velocity fields presented throughout this thesis are subject to measurement noise, as well as turbulent fluctuations, which can conceal the large scale, periodic vortical structures present. These effects can be reduced by averaging the results. However, the displacement signal and velocity fields contain periodic phenomena which are of interest and would also be removed by the averaging process. In order to retain information relating to the periodic phenomena, it is necessary to ensemble- or phase-average the measurements. This process involves identifying the phase of each instantaneous measurement using a suitable reference signal, and averaging all the measurements which have a phase within a certain range.

Phase-averaging was used to distinguish the dominant wake mode from background turbulence, and to relate the cylinder position throughout the vortex-shedding cycle to the wake dynamics. In order to perform this for all reduced velocities, including those outside the lock-in range, it was necessary to choose a reference signal from *within* the wake (rather than the cylinder displacement signal). Various methods of finding a suitable reference signal were rigorously tested, such as the time series of the circulation generated in the near wake, the amplitude of the Proper-Orthogonal Decomposition modes [van Oudheusden et al., 2005] and the transverse velocity extracted directly from the PIV fields at various points in the wake. All reference signals were low-pass filtered with a cut-off frequency of twice the peak response frequency. The transverse velocity in the wake was found to provide the most accurate reference signal for the phase averaging process, as it resulted in the least variation within each phase. The transverse velocity was extracted from the wake at $(x/D, y/D) = (3, 0.5), (1, 0.5)$ or $(3, 0)$, depending on what wake mode was dominant, as will be discussed in Chapters 3 - 5.

This method had the advantage of being applicable to situations in which the wake switched intermittently between two modes occurring at different frequencies. By extracting the velocity signal from a suitable location in the wake, it was possible to have a reference signal which contained components occurring at the frequencies of both wake modes. This is discussed in more detail in Section 4.2.

In order to calculate the phase, the reference signal was extracted and filtered, and the times at which peaks in the signal occurred were recorded. In order to reduce the influence of end-effects associated with the filtering process, the segments of the signal before the second peak and after the second last peak were

discarded, and thus the fields in this region were not phase-averaged. For a given field at time t_i, the phase angle was estimated as:

$$\phi(t_i) = 2\pi \left(\frac{t_1 - t_i}{t_1 - t_2} \right), \tag{2.5}$$

where t_1 and t_2 are the times at which the previous and succeeding peaks occurred, respectively, in the reference signal, as shown in Figure 2.6. Cubic spline interpolation was used to increase the temporal resolution of the reference signal (by a factor of 10), which ensured that the phase angle was not biased towards 0; this would occur when the magnitude of the reference signal at time t_i was larger than that at t_{i-1} and t_{i+1}. It was found that the distribution of $\phi(t_i)$ was approximately uniform throughout $[0, 2\pi]$.

The same process was used to phase-average the cylinder displacement signal. The phase-averaged fields were used to estimate the out-of-plane vorticity, $\langle \omega_z \rangle$, where $\langle . \rangle$ denotes a phase-averaged quantity.

2.6 Accuracy of the PIV Measurements

The uncertainty associated with PIV measurements is caused by a wide range of factors, and can be difficult to accurately quantify. In this section, the measurement uncertainty from the laser illumination, three-dimensionality in the flow and bias error are discussed; the uncertainty in the measurements are then quantified by estimating the residual of the continuity equation in the wake.

2.6.1 Laser Sheet Illumination

Sample PIV images are presented in Figure 2.7 for Test Stages 1 and 2. In both cases, the laser illumination is directed from the bottom of the image. There are regions where the illumination is not uniform; the region above the cylinder ($y > 0$), as well as the region near the upstream (left) surface of the cylinder.

The refractive index of the cylinder does not match that of the water; therefore the laser light is diffracted as it passes through the cylinder, resulting in regions of intense illumination and shadow. As the particles in the first image of the acquired pair move into a dark region, they will have lower intensity in the second image, and may not be detected in the cross-correlation process; which will result in errors in the estimated PIV fields. This effect will lead to an under-estimation of the mean streamwise velocity in this region. Figure 2.8 shows the profiles of the mean streamwise velocity measured at $y/D = \pm 1.49$ for $U_0 = 0.76$ for Test Stage 2. This case had the largest Δt time with respect to U_0, and is most likely to be affected by the movement of particles from light to dark regions between images. It is clear that the shadow region ($y/D > 0$) causes the value of $\overline{u}/U_0$ to be under-estimated. It would be possible to account for these errors by interpolating the velocity vectors in this region from neighbouring regions which had uniform illumination; however, as this study focuses on the turbulent wake of the cylinder, the errors in the velocity vectors in this region do not have a significant impact on the results presented in the following chapters, and no interpolation was used.

A similar shadow region is observed slightly upstream of the cylinder in both cases (Figure 2.7); the upstream (left) surface of the cylinder is not visible in either PIV image. As the camera focuses on the wake and is positioned downstream

of the cylinder, the upstream surface of the cylinder is obscured. This will also lead to an under-estimation of the velocity vectors in this region. However, as in the case of the shadow region discussed in the previous paragraph, the region immediately upstream of the cylinder is of little interest to the present study, and the errors will not impact on the results presented.

It should be noted that this problem will not affect the measurements of the freestream velocity, as the traverse is used to move both the laser source and the camera upstream such that the cylinder is not present in the PIV images, and no regions of the images are obscured.

2.6.2 Three-dimensionality in the Flow

The wake of the cylinder is likely to contain velocity fluctuations in the direction of the cylinder span [Williamson, 1996]. The velocity component in this direction, w, acts normal to the PIV measurement plane and cannot be resolved in the current experiments. The spanwise velocity component can decrease the accuracy of the estimated velocity field due to 'particle drop-out', in which the velocity component normal to the laser sheet causes particles which were visible in the first PIV image to be absent in the second. This effect can be minimised by employing small values of Δt, such that the proportion of particles which drop-out during the image-pair acquisition is small. The volume of the fluid in an interrogation window is given by;

$$V_{iw} = sA_{iw}, \tag{2.6}$$

where s is the thickness of the laser sheet and A_{iw} is the area of the window, while the volume of the window which leaves the laser sheet between each image is given by:

$$\Delta V_{iw} = w \Delta t A_{iw}. \tag{2.7}$$

The proportion of particles which drop-out between images (the drop-out ratio) can therefore be expressed as:

$$\frac{\Delta V_{iw}}{V_{iw}} = \frac{w \Delta t}{s}. \tag{2.8}$$

The w velocity component in the wake of a cantilever was found by Adaramola et al. [2006] to be less than 40% of the freestream velocity, and it is likely to be lower in the wake of a two-dimensional cylinder which is exhibiting VIV [Armstrong and Barnes, 1986]. However, a conservative approximation of the drop-out ratio can be found by taking $w = U_0$. Figure 2.9 shows the variation in $\Delta V_{iw}/V_{iw}$ with freestream velocity for Test Stages 1 and 2. As U_0 was increased, Δt was decreased to ensure that the drop-out ratio did not become large. However, below a certain value of Δt (approximately 120μs), the PIV system was unable to maintain a comparable light intensity in both images of a given pair, which reduced the accuracy of the velocity field estimates. As a result, for $U_0 > 0.4$m/s in Test Stage 2, the value of Δt was not changed, and the drop-out ratio increased. The maximum value of $\Delta V_{iw}/V_{iw}$ found in both Test Stages is approximately 0.09.

This indicates that for all measurements at least 90% of the particles observed in the first image of a given pair were also present in the second. Therefore, the accuracy of the PIV measurements is not likely to be significantly affected by the three-dimensionality in the wake.

2.6.3 Bias Error

The errors associated with the PIV measurements can be classed as one of two forms; random errors and bias errors. The effects of the former appear as noise in the velocity estimates and can be accounted for by averaging the results. However, as bias errors are systematic, they cannot be reduced in this way, and will also affect the mean and phase-averaged velocity and vorticity measurements.

The PIV software used to estimate the velocity vectors employs a sub-pixel interpolation algorithm when identifying the location of the peak in the cross-correlation matrix, which allows the displacement vector of the interrogation windows (i.e. $\Delta\mathbf{x}$) to have non-integer values. However, if the seeding of the flow in not optimal (i.e. the seeding density is too low/high, or the particles are too large/small), the estimates of the particle displacement will be biased towards integer values, which is known as 'peak-locking' or bias error [Raffel et al., 2007]. The use of small values of Δt reduces the errors associated with particle drop-out and the shadow regions; however, it also increases the reliance of the estimated velocity vectors on the sub-pixel algorithm employed, and can make the measurements more vulnerable to bias error.

If the PIV measurements are affected by bias error, the components of the velocity vectors will have a tendency to occur at integer values, and the his-

tograms of the velocity components will contain peaks at each integer. This effect was examined for each measurement set acquired in both Test Stages. Histograms of the streamwise velocity component acquired at three reduced velocities ($U_r\mathrm{St}/f^* = 0.187$, 0.388 and 0.574, which correspond to pre-lock-in, and the peaks of the first and second response branches, respectively) in Test Stage 2 are shown in Figure 2.10, which are representative of the results found throughout both stages. In each case, a peak is present at 0pixels, which is likely to be associated with the velocity vectors calculated within the region of the images that was occupied by the cylinder. However, the histograms do not show any sign of peak-locking, and the PIV measurements were not deemed to be affected by bias error. Consequently, the uncertainty associated with the estimates of the velocity field can be attributed to random error, which can be removed by averaging the instantaneous fields.

2.6.4 Estimation of Uncertainty

The uncertainty of the PIV measurements can be estimated by applying the data to a known physical model, such as the continuity equation. As the flow is incompressible, the surface integral of the velocity flux through a control volume (bounded by a surface S) will be equal to zero:

$$\oint \mathbf{u} \cdot \mathrm{d}S = 0. \tag{2.9}$$

By defining a suitable control volume in the PIV domain, the residual of equation 2.9 can be used to approximate the uncertainty in the PIV measurements.

However, as only two velocity components are measured, the magnitude of the residual will also be affected by the three-dimensionality of the wake. The control volume employed in the current work was taken as the boundary of the PIV fields, i.e. x_{min} to x_{max} and y_{min} to y_{max} in the streamwise and transverse directions, respectively.

By neglecting the w velocity component and assuming unit thickness in the spanwise direction, equation 2.9 can be expressed in two-dimensional form as:

$$\int_{y_{min}}^{y_{max}} \Big(u(x_{min}, y, t) - u(x_{max}, y, t)\Big)\mathrm{d}y + \int_{x_{min}}^{x_{max}} \Big(v(x, y_{min}, t) - v(x, y_{max}, t)\Big)\mathrm{d}x = 0. \tag{2.10}$$

By converting equation 2.10 into discrete form, the residual of the continuity equation evaluated for the instantaneous PIV fields can be expressed in non-dimensional form as:

$$\begin{aligned}\varepsilon_u(t) = &\frac{1}{N_y U_0}\sum_{i=1}^{N_y}\Big(u(x_{min}, y_i, t) - u(x_{max}, y_i, t)\Big) \\ &+ \frac{1}{N_x U_0}\sum_{i=1}^{N_x}\Big(v(x_i, y_{min}, t) - v(x_i, y_{max}, t)\Big),\end{aligned} \tag{2.11}$$

where N_x and N_y are the number of vectors summed in the x and y directions, respectively.

A similar method was used to quantify the residual of the continuity equation

applied to phase-averaged velocity fields:

$$\begin{aligned}\langle \varepsilon_u(\phi) \rangle =& \frac{1}{N_y U_0} \sum_{i=1}^{N_y} \Big(\langle u(x_{min}, y_i, \phi) \rangle - \langle u(x_{max}, y_i, \phi) \rangle \Big) \\ &+ \frac{1}{N_x U_0} \sum_{i=1}^{N_x} \Big(\langle v(x_i, y_{min}, \phi) \rangle - \langle v(x_i, y_{max}, \phi) \rangle \Big).\end{aligned} \tag{2.12}$$

The root-mean-square (rms) of $\varepsilon_u(t)$ and $\langle \varepsilon_u(\phi) \rangle$ were calculated at each reduced velocity examined in Test Stages 1 and 2, and were used to quantify the uncertainty in the estimates of the instantaneous and phase-averaged velocity fields, respectively. The phase-averaged fields were calculated using the transverse velocity measured at $(x/D, y/D) = (3, 0.5)$ as a reference signal, and contained 16 phases. The uncertainty in the estimated mean velocity fields was estimated as:

$$\begin{aligned}\overline{\varepsilon_u} =& \frac{1}{N_y U_0} \sum_{i=1}^{N_y} \Big(\overline{u}(x_{min}, y_i) - \overline{u}(x_{max}, y_i) \Big) \\ &+ \frac{1}{N_x U_0} \sum_{i=1}^{N_x} \Big(\overline{v}(x_i, y_{min}) - \overline{v}(x_i, y_{max}) \Big).\end{aligned} \tag{2.13}$$

Figure 2.11 shows the variation in $\varepsilon_{u,rms}$, $\langle \varepsilon_u \rangle_{rms}$ and $\overline{\varepsilon_u}$ for each set of PIV measurements in Test Stages 1 and 2. In both test stages, the errors in the instantaneous measurements tend to be considerably larger than those in the phase-averaged and mean velocity fields, and $\langle \varepsilon_u \rangle_{rms}$ tends to be slightly larger than $\overline{\varepsilon_u}$. The uncertainty in the measurements of the instantaneous velocity fields in Test Stages 1 and 2 was less than 10.4% and 7.3% of the freestream velocity, respectively, while the uncertainty in the phase-averaged fields was 5.5%

and 2.4% of U_0, respectively. These estimates of the uncertainty also include the effect of three-dimensionality flow through the control volume, which has not been measured or accounted for in equations 2.11 - 2.13). Therefore the actual uncertainty is likely to be slightly lower than these values.

The estimates of the uncertainty in the measurement of the instantaneous, phase-averaged and mean velocity fields was taken as the mean value of $\varepsilon_{u,rms}$, $\langle\varepsilon_u\rangle_{rms}$ and $\overline{\varepsilon_u}$, respectively, and are summarised in Table 2.4 for each test stage.

Table 2.4: Measurement uncertainty in the velocity and vorticity estimates performed in Test Stages 1 and 2.

Variable	Uncertainty Test Stage 1	Uncertainty Test Stage 2
$u(t)/U_0$, $v(t)/U_0$	0.104	0.073
$\langle u\rangle/U_0$, $\langle v\rangle/U_0$	0.055	0.024
$\overline{u}/U_0$, $\overline{v}/U_0$	0.049	0.019
$\omega_z(t)D/U_0$	2.28	1.85
$\langle\omega_z D/U_0\rangle$	1.2	0.62

The spatial gradients were estimated using the least-squares method, which is robust with respect to noise in PIV measurements [Raffel et al., 2007], and was found to clearly identify the vortical structures in the wake. The uncertainty in the spatial gradients estimated using the least-squares method are related to the uncertainty in the measurements of the velocity field as:

$$\varepsilon\left(\frac{\partial u}{\partial x}\right) \approx 1.0\frac{\varepsilon(u)}{\Delta x}, \tag{2.14}$$

where $\varepsilon\left(\frac{\partial u}{\partial x}\right)$ and $\varepsilon(u)$ are the uncertainties in $\frac{\partial u}{\partial x}$ and u, respectively, and Δx is the vector spacing [Raffel et al., 2007].

As the two-dimensional vorticity is the sum of two gradients, $\omega_x = \frac{\partial v}{\partial x} - \frac{\partial u}{\partial y}$, the uncertainty in estimates of the vorticity will be given by:

$$\varepsilon\left(\frac{\partial u}{\partial x}\right) \approx \sqrt{2}\frac{\varepsilon(u)}{\Delta x}, \tag{2.15}$$

which can be found by applying the cumulative error formula.

The uncertainty of the instantaneous and phase-averaged measurements of the non-dimensional vorticity found using equation 2.15 are also shown in Table 2.4. While the uncertainty in the instantaneous vorticity fields is relatively large, the uncertainty in the phase-averaged quantities is considerably lower.

Table 2.4 indicates that the measurements performed in Test Stage 2 have a greater accuracy than those of Test Stage 1, and that the phase-averaging process outlined in Section 2.5 succeeds in reducing the uncertainty in the averaged quantities.

2.7 Proper-Orthogonal Decomposition

Proper-Orthogonal Decomposition is increasingly becoming a standard tool in the experimental and numerical analysis of flow fields, and has been applied to

bluff body wakes to analyse large scale flow features by van Oudheusden et al. [2005] and Konstantinidis et al. [2007], amongst others. In the present work, POD is used to define a criterion to determine which wake mode is dominant as a function of time. A brief overview of the method is presented here, while a more extensive review can be found in Berzook et al. [1993].

The method of 'snapshot' POD decomposes a set of N flow fields into a set of orthogonal spatial modes, $\mathbf{\Phi}_i\,(x, y)$, where i denotes the mode number, and a mean flow field, $\overline{\mathbf{u}}$, also known as the zeroth mode. Using amplitude coefficients, $a_i(t)$, the original flow fields can be expressed as:

$$\mathbf{u}\,(x, y, t) = \overline{\mathbf{u}}\,(x, y) + \sum_{i=1}^{N} a_i(t)\mathbf{\Phi}_i\,(x, y)\,. \tag{2.16}$$

In order to perform this decomposition, the mean velocity field is first subtracted from each instantaneous velocity field, which is then expressed as a column vector for computational purposes. These fields are stored in a matrix, $\mathbf{\Upsilon}$, in which each of the N columns corresponds to an instantaneous fluctuating velocity field. A cross correlation matrix $\mathbf{C}$ is found as,

$$\mathbf{C} = \mathbf{\Upsilon}^{\top}\mathbf{\Upsilon}. \tag{2.17}$$

The decomposition can now be expressed as an eigenvector problem:

$$\mathbf{CH} = \mathbf{\Lambda H} \tag{2.18}$$

where $\mathbf{H}$ is a matrix whose columns contain the eigenvectors of $\mathbf{C}$, and $\mathbf{\Lambda}$ is a diagonal matrix in which $\mathbf{\Lambda}_{ii}$ is the i^{th} eigenvalue, λ_i. The POD modes are derived from the eigenvectors:

$$\mathbf{\Phi}_i = \frac{\sum_{n=1}^{N} \mathbf{H}_{in} \mathbf{\Upsilon}_n}{||\sum_{n=1}^{N} \mathbf{H}_{in} \mathbf{\Upsilon}_n||}. \tag{2.19}$$

where $\mathbf{\Upsilon}_n$ is the n^{th} column of $\mathbf{\Upsilon}$. The matrix of amplitude coefficients is found by projecting the matrix of POD modes onto the velocity fields

$$a_k = \mathbf{\Phi}^{\top} \mathbf{\Upsilon}_k. \tag{2.20}$$

The total fluctuating kinetic energy of each mode is proportional to its eigenvalue; the modes can thus be rearranged in order of decreasing energy.

In this work, POD is applied to the instantaneous velocity fields measured using PIV. Both the transverse and the streamwise velocity components were stored in the matrix $\mathbf{\Upsilon}$; thus for a PIV measurement set containing N PIV fields, each with $R_{PIV} \times C_{PIV}$ vectors, $\mathbf{\Upsilon}$ contained $2R_{PIV}C_{PIV}$ rows and N columns.

POD is commonly used to decompose the flow into high energy modes which contain the macroscopic flow features and low energy modes which can be attributed to experimental error and small-scale turbulence, and be discarded. However, in this work the use of POD is restricted to developing a criterion to determine which wake mode is dominant, based on the magnitude of the amplitude

coefficients, a_k, as will be described in Chapter 4.

2.8 Cylinder Motion Tracking Algorithm

The instantaneous cylinder displacement was measured directly from the PIV images using a template-matching algorithm. The process is outlined below:

(i) A small template image of the cylinder was cropped from a single PIV image. A series of points along the cylinder surface were manually selected, and the location of the centre of the cylinder was estimated using trigonometry. In order to reduce the effects of the particles in the template image, it was masked; thus the pixels which were a distance of $0.55D$ or more from the cylinder centre were set to zero. A section of a sample PIV image and a template image after the masking process was applied are shown in Figure 2.12(a) and (b), respectively.

(ii) The template was cross-correlated with each PIV image in a given measurement set. The location of the maximum of the cross-correlation matrix was identified. A sample cross-correlation matrix (found using the images shown in Figure 2.12) is presented in Figure 2.13.

(iii) Spline curves were applied to the region of the matrix which contained the maximum, in order to increase the resolution of the estimated location of the peak (by a factor of 100).

(iv) The location of the peak was transformed into the frame of reference of the PIV image, in order to provide an estimate of the location of the centre of the cylinder within the image.

(v) The process was repeated for every PIV image in a measurement set, and the estimated displacement signals in the transverse and streamwise directions (in units of pixels) were stored.

The displacement signal could then be used to estimate the amplitude response and to find the area of each PIV field which was occupied by the cylinder, allowing the velocity fields to be masked. As the illumination provided by the first and second laser pulses was not identical, two separate template images were used for each PIV image-pair, resulting in two sets of displacement signals for each set. These signals were averaged to estimate the instantaneous cylinder displacement associated with each PIV field. The peaks of the displacement signal were identified, and the mean peak height was used to calculated the non-dimensional cylinder response amplitude, A/D. A flow diagram summarising the process is shown in Figure 2.14.

In order to estimate the accuracy of the method, the cylinder was statically displaced over a range of 3mm, with an interval of 0.25mm, using a manual gauge. Images were taken at each interval and the displacement was estimated. Figure 2.15(a) shows the estimated cylinder displacement, as well as a least-square linear approximation. The difference between the applied and the estimated values is plotted in Figure 2.15(b); it can be seen that the method is accurate to within 0.35pixels.

The robustness of the sub-pixel interpolation method (i.e. the spline fitting used to estimate the location of the peak in the cross-correlation matrix) was investigated by binning (compressing) a series of images, using a range of sizes of binning windows, and examining the effect on the resulting streamwise displacement signal. As the size of the binning window is increased, the resolution of

the cross-correlation matrix (before the spline curves are fitted) is decreased, and the interpolation method is required to perform over a greater range. The errors associated with each signal were estimated as:

$$\varepsilon_{bin} = \frac{1}{N} \sum_{i=1}^{N} |x(t_i) - x_{bin}(t_i)|, \tag{2.21}$$

where t_i is the time step, N is the number of images examined ($N = 500$ in this case), and $x(t_i)$ and $x_{bin}(t_i)$ are the displacement signals estimated for the un-binned and binned images, respectively. Equation 2.21 was evaluated for a series of images acquired near the peak of the first branch ($U_r \mathrm{St}/f^* = 0.403$, Test Stage 2). As this corresponds to the approximately largest amplitude response observed throughout this work ($A/D = 0.08$), the absolute value of the errors are also likely to be the largest. Therefore, at other values of reduced velocity ε_{bin} can be expected to be smaller.

Figure 2.16 shows the variation in ε_{bin} for a range of dimensions of binning windows. The accuracy of the streamwise displacement signal is largely independent of the transverse size of the binning window. Only when the binning window size in the streamwise direction becomes large, $x_{bin} > 4$pixels, does ε_{bin} exceed 0.25pixels. This indicates that the tracking algorithm is reasonably robust with respect to changes in the size of the cylinder within the image (i.e. the calibration factor of the PIV images) and that the sub-pixel interpolation method is unlikely to be affected by the image resolution.

The magnitude of the errors presented in Figure 2.16 when the binning window is small indicates that the errors associated with the sub-pixel interpolation do not contribute significantly to the overall accuracy of the method. The dis-

placement estimates are therefore accurate to within ±0.35pixels, based on the static displacement tests presented in Figure 2.15. The uncertainty of the non-dimensional displacement signal, x/D, will depend on the calibration factor of the PIV measurements (i.e. how many pixels per diameter); for Test Stage 1 the non-dimensional signals are accurate to within $\pm 2.15 \times 10^{-3}$, while for Test Stage 2 the uncertainty is $\pm 1.84 \times 10^{-3}$.

2.9 Strouhal Number Measurements

The Strouhal number, $\mathrm{St} = f_{\mathrm{St}} D/U_0$, of a body is typically found by varying the freestream velocity and estimating the vortex-shedding frequency; a linear correlation can then be fitted to the data to find St. The Strouhal number is strictly defined only for fixed bodies. For bodies which are free to move, the structural motion may cause the vortex-shedding frequency to differ from that measured for a stationary body (due to lock-in).

In order to estimate the Strouhal frequencies of the current system, the vortex-shedding frequency was estimated from the PIV measurements acquired at low reduced velocities, below the onset of lock-in. The shedding frequency was estimated from the dominant frequency of velocity fluctuations in the wake, f_{vs}, which in turn was estimated from the power-spectral density (PSD) of the transverse velocity signal extracted directly from the PIV fields at $(x/D, y/D) = (3, 0.5)$. The PSDs were calculated using Welch's method [Welch, 1967], which was implemented using Matlab. The errors in the measurement of f_{vs} were assumed to be equal to the resolution of the PSD, which was 0.391Hz for Test Stage 1, and 0.781Hz for Test Stage 2, while the uncertainty in U_0 was taken as the

magnitude of the fluctuating velocity in the freestream measurements acquired at each flowrate.

A linear correlation was found between the measured values of $f_{vs}D$ and U_0 using the least squares method, as shown in Figure 2.17. The estimates of St found in both test stages are listed in Table 2.5, along with the corresponding Reynolds number ranges over which the measurements were performed.

Table 2.5: Estimates of the Strouhal number found for Test Stages 1 and 2, using the data presented in Figure 2.17.

Test Stage	St	$\varepsilon_{\mathrm{St}}$	Re
1	0.2014	$\pm$0.0021	450 - 1870
2	0.1999	$\pm$0.0021	750 - 2170

In order to approximate the uncertainty in the estimates of St, the effect of neglecting a single measurement point was examined. For each Test Stage, a series of values, St_i, were found by fitting a linear regression to the values of $f_{vs}D$ and U_0, while neglecting the i^{th} measurement point, i.e. St_1 was found by fitting a regression to $(f_{vs}D)_{2-7}$ and $(U_0)_{2-7}$, and St_2 was found using the values $(f_{vs}D)_{1,3-7}$ and $(U_0)_{1,3-7}$, etc. The uncertainty in the estimates of the Strouhal number, $\varepsilon_{\mathrm{St}}$, was given by the mean absolute difference between St_i and the overall estimate of St:

$$\varepsilon_{St} = \frac{1}{M}\sum_{i=1}^{M} |\mathrm{St} - \mathrm{St}_i|, \tag{2.22}$$

where M is the number of measurement points. The resulting estimates of the uncertainty are also listed in Table 2.5. In both cases, the uncertainty is approx-

imately 1% of St.

2.10 Closure

The test facilities and experimental methods used throughout this thesis have been outlined in this chapter. The water tunnel facility and test-section design have been described, as well as the PIV system used to measure the cylinder motion and the velocity fields in the wake. The main sources of error in the PIV measurements were discussed and the uncertainty was estimated. Details on various post-processing algorithms have also been presented.

The methods and techniques outlined in this chapter were used to examine the wake and structural response of a cylinder free to move in the streamwise direction. The results are presented and discussed in the following chapters.

2.11 Figures

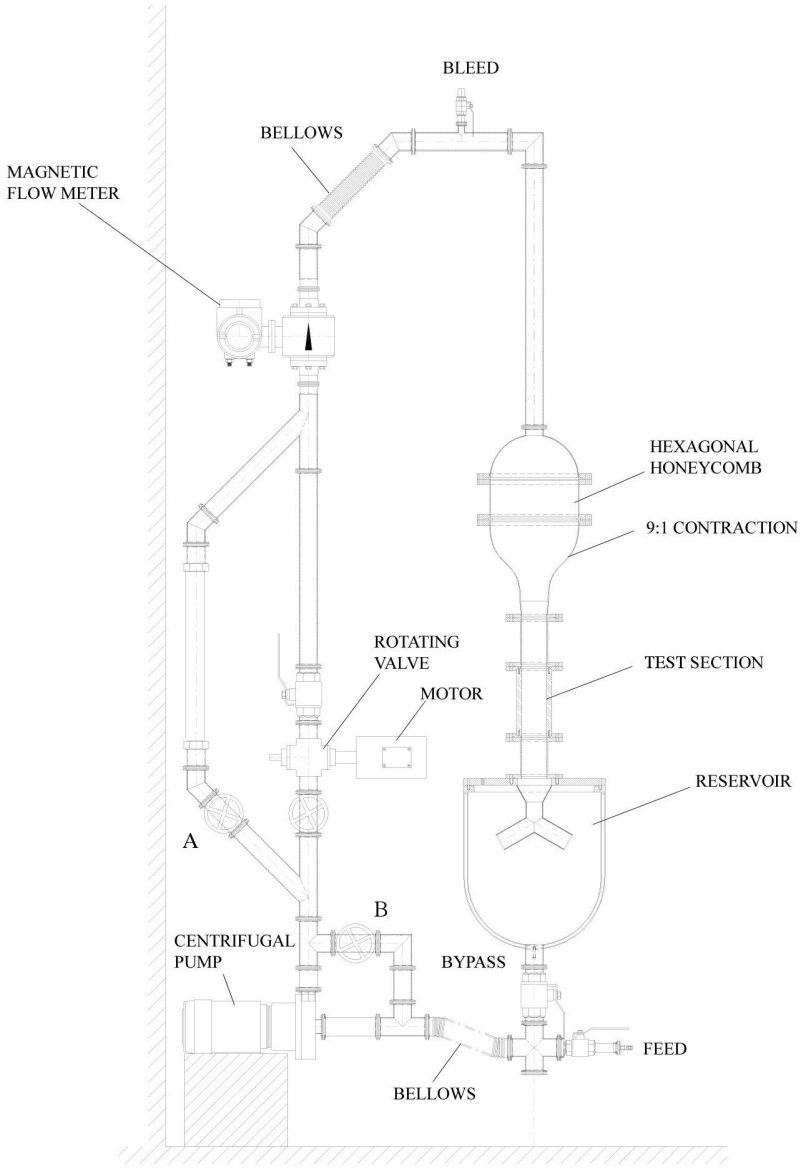

Figure 2.1: Schematic of the water tunnel used to perform the experiments.

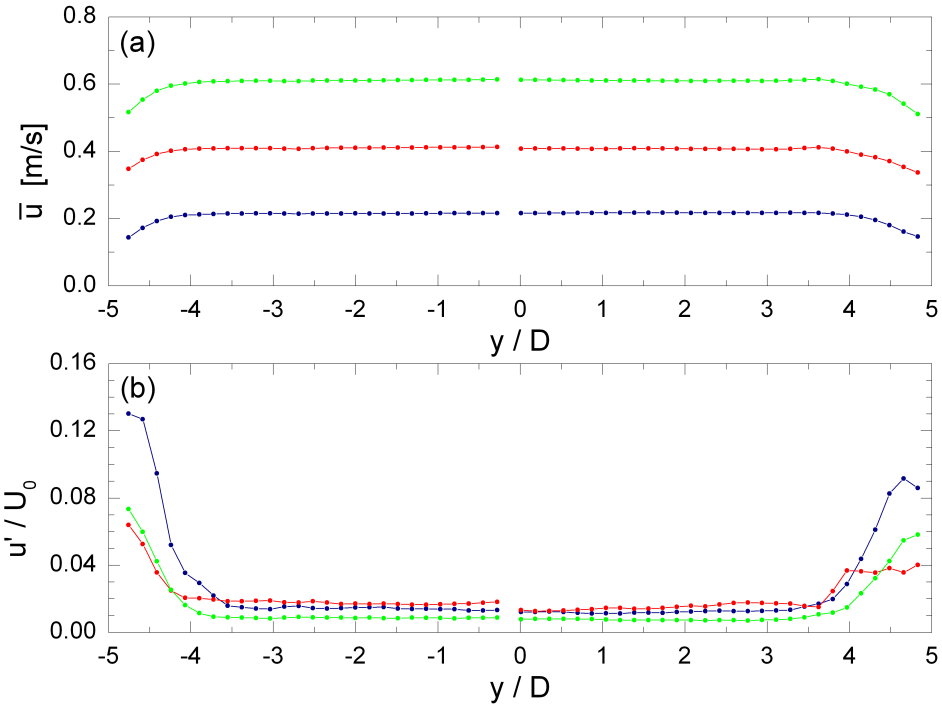

Figure 2.2: Distributions of the mean streamwise velocity (a) and turbulence intensity (b) across the test-section, eight diameters upstream of the cylinder; Re = 1540 (blue); Re = 2910 (red); and Re = 4340 (green).

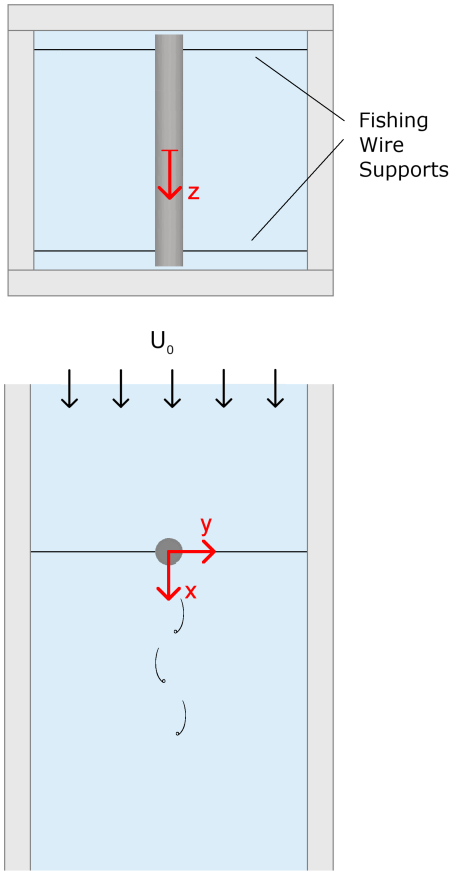

Figure 2.3: Plan and elevation view of the test-section used, including the fishing wire supports and the co-ordinate system employed.

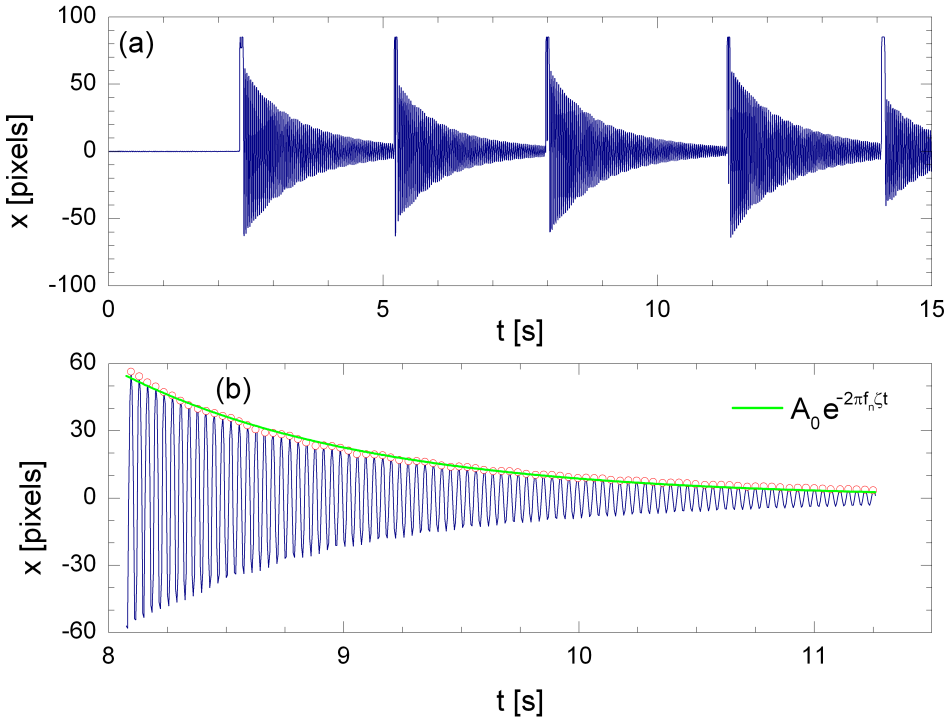

Figure 2.4: Displacement signal measured throughout a series of tap tests performed in air(a), and a segment of the overall signal which was used to estimate the natural frequency and structural damping (b). The displacement signal is shown in blue, the peaks of the signal are indicated by red circles. The peaks were fitted to equation 2.2, $A_0 e^{-2\pi f_n \zeta t}$; in this case $A_0 = 54.56$pixels, $f_n = 27.89$HzHz and $\zeta = 0.0055$.

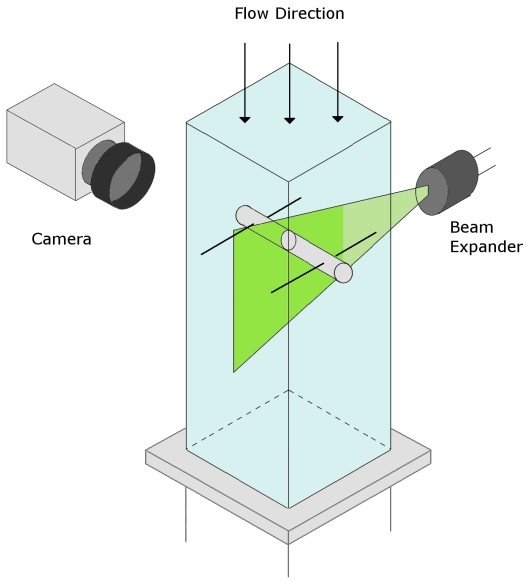

Figure 2.5: Schematic of the test section used, indicating the orientation of the laser and camera used to perform the PIV measurements.

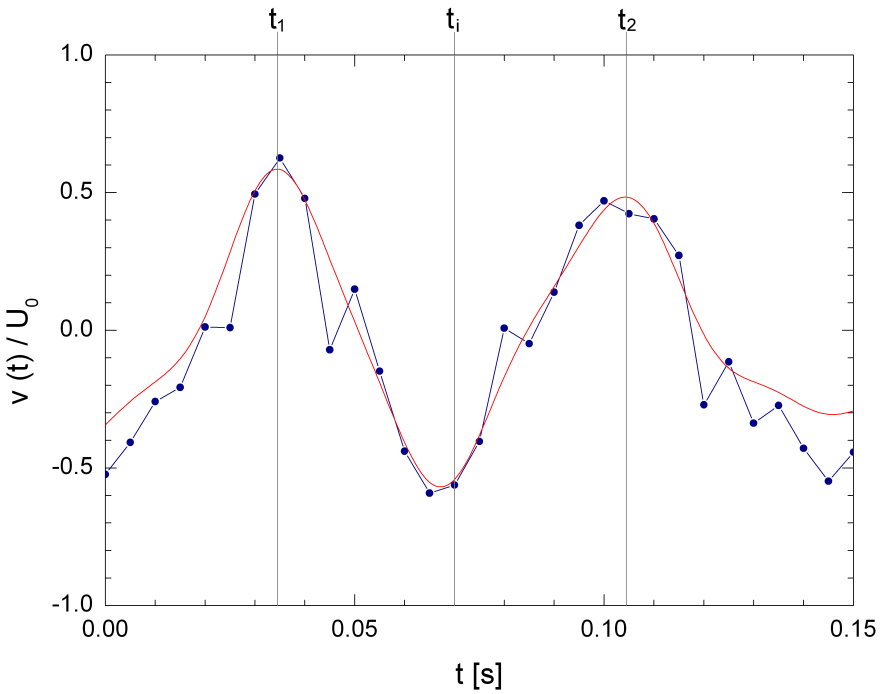

Figure 2.6: Sample of a raw (blue symbols) and filtered (red line) transverse velocity signal extracted at $(x/D, y/D) = (3, 0.5)$, which is used as a reference signal in the phase-averaging process. The times at which the successive peaks in the signal occurred were identified (t_1 and t_2), and the phase at time t_i was identified using equation 2.5.

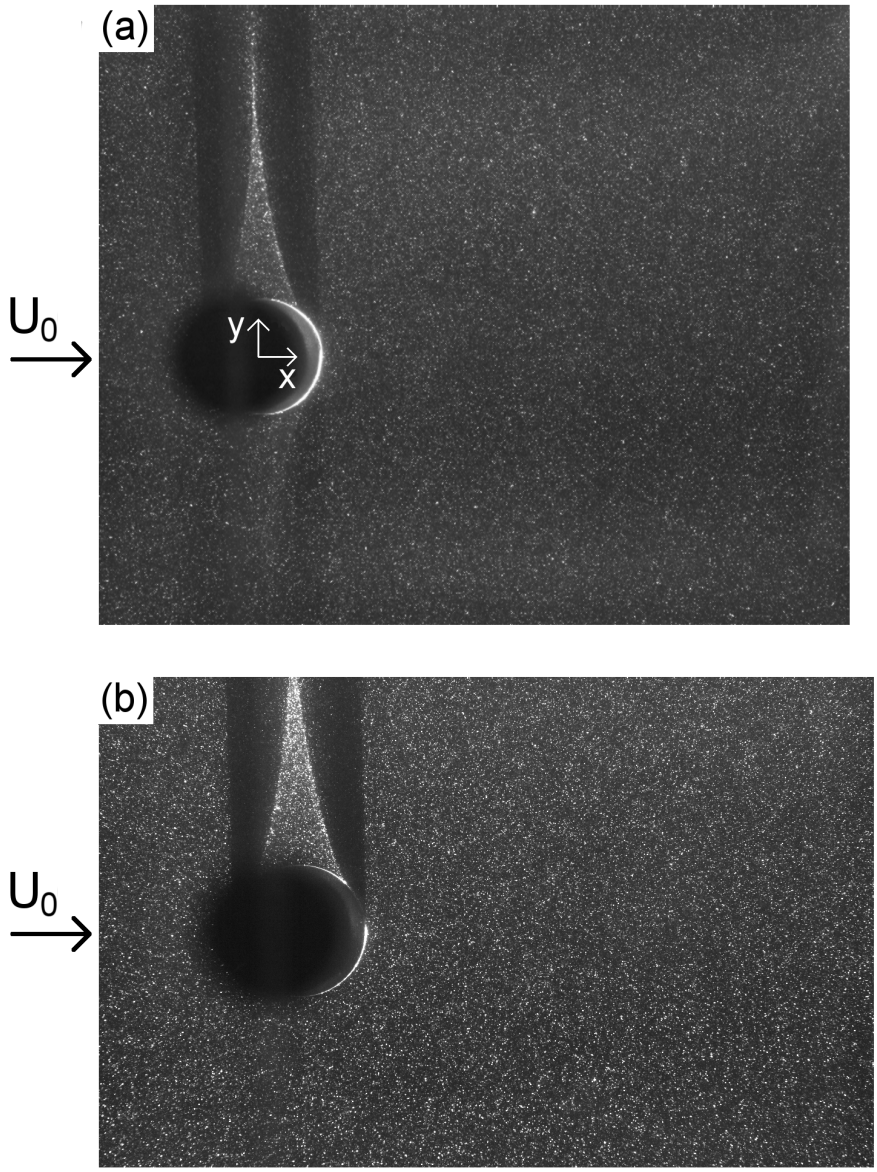

Figure 2.7: Sample PIV images acquired in Test Stages 1 (a) and 2 (b). The flow fields are illuminated from beneath the image.

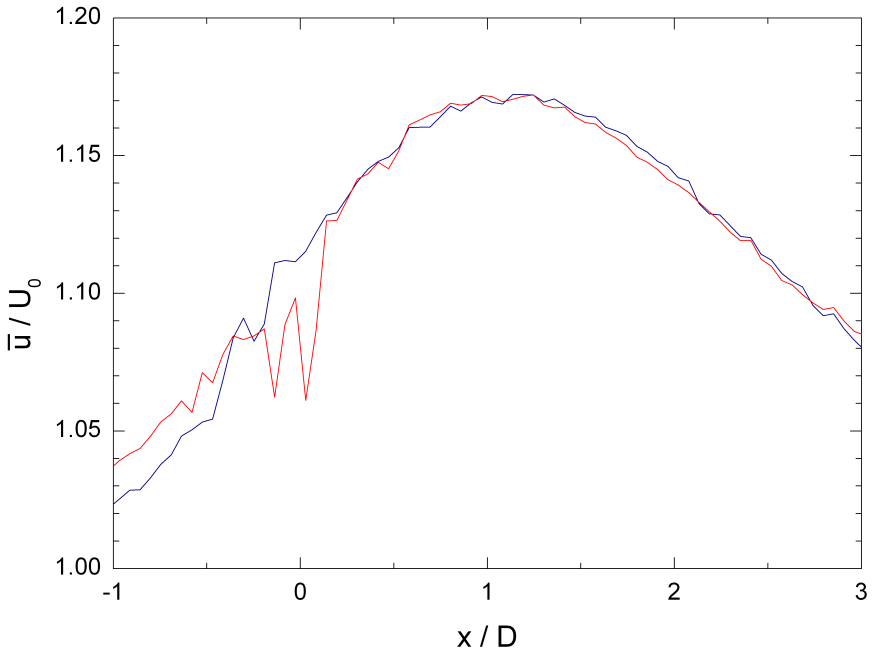

Figure 2.8: Distributions of the mean streamwise velocity along $y/D = -1.49$ (blue) and $y/D = 1.49$ (red line) at $U_0 = 0.75$m/s in Test Stage 2, indicating the effect of the non-uniform laser illumination on the estimates of the velocity fields.

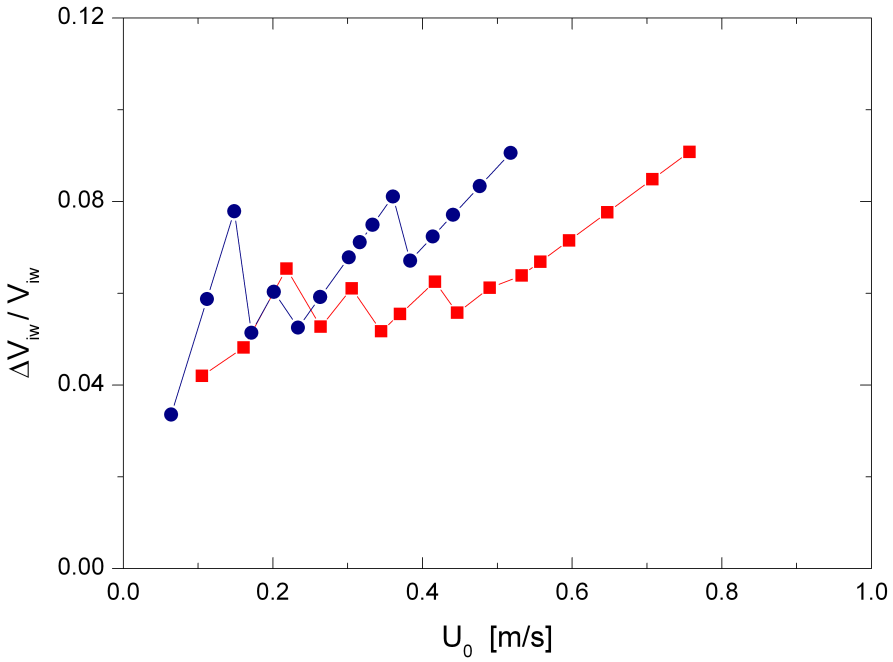

Figure 2.9: Variation in the particle drop-out ratio (defined in equation 2.8) with freestream velocity for Test Stages 1 (blue circles) and 2 (red squares)).

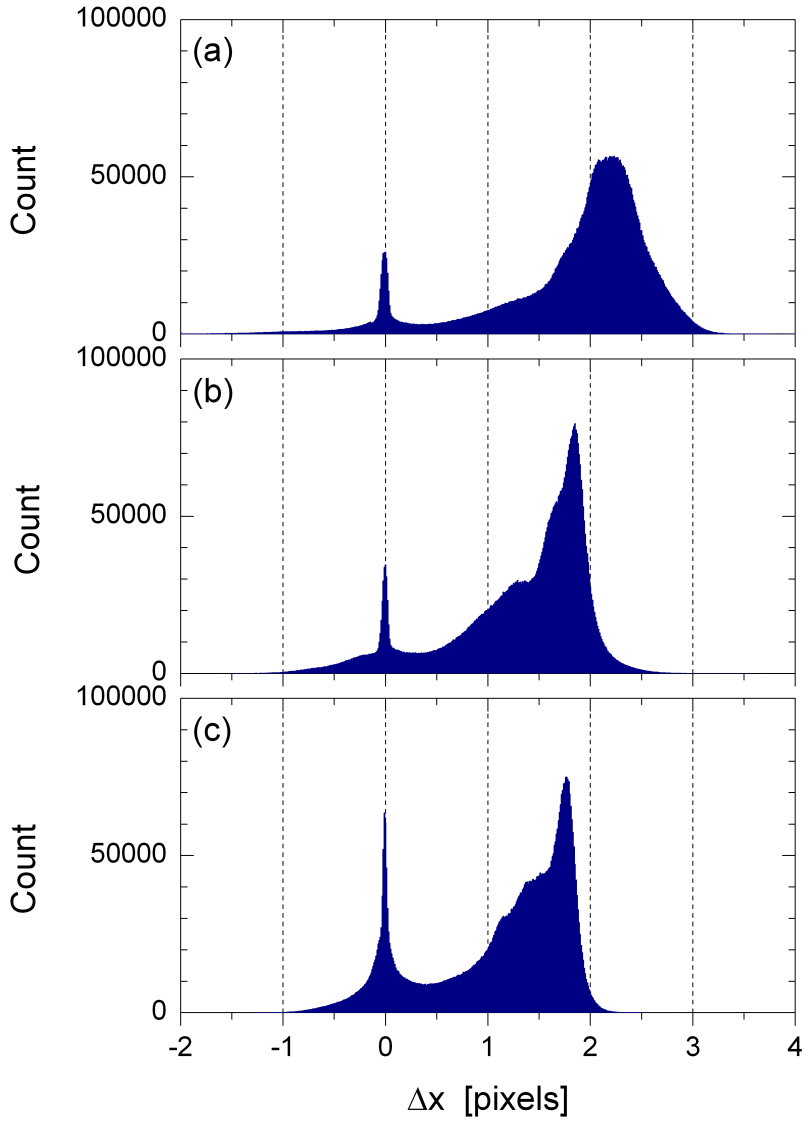

Figure 2.10: Histograms of the streamwise component of the velocity vectors estimated at $U_r\mathrm{St}/f^* = 0.187$ (a), 0.388 (b) and 0.574 (c). These points correspond to pre-lock-in, and near the peak of the first and second response branches, respectively. The histograms were calculated from over 6×10^6 values, and have a resolution of 0.01 pixels.

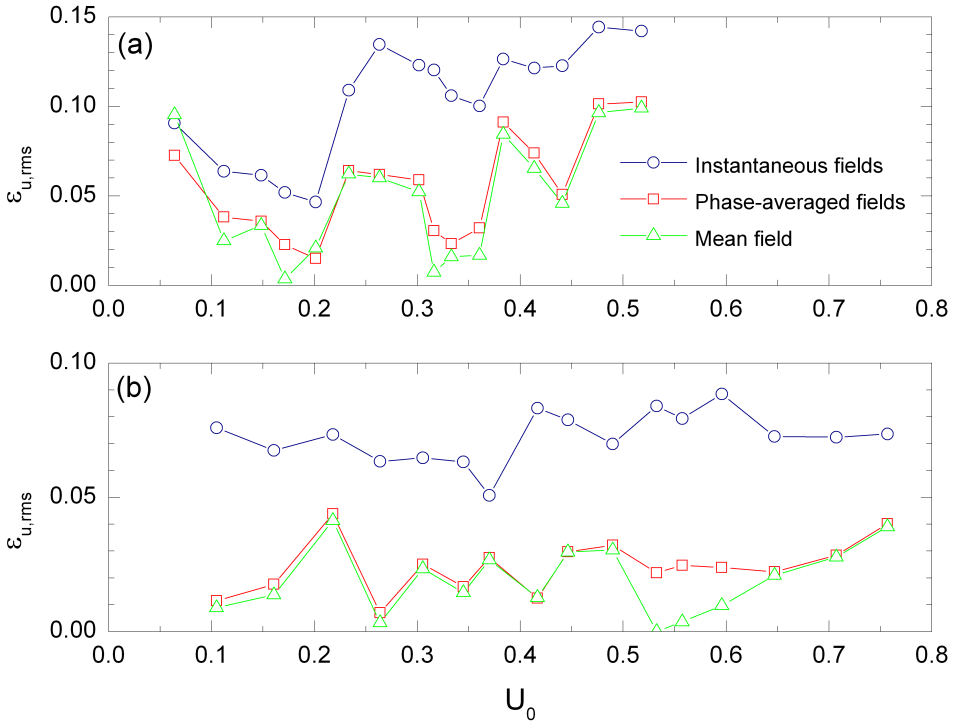

Figure 2.11: Estimates of the uncertainty in the instantaneous, phase-averaged and mean velocity measurements performed in Test Stages 1 (a) and 2 (b). The estimates were found by applying the continuity equation to a boundary surrounding the PIV fields and evaluating equations 2.11-2.13.

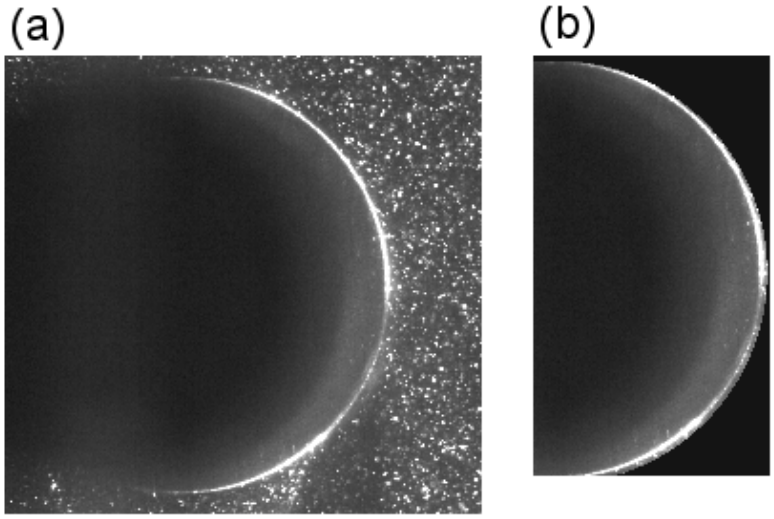

Figure 2.12: Section of a PIV image (a) and a template image (b), acquired in Test Stage 2. The same template image was used for all PIV measurements acquired within a test stage.

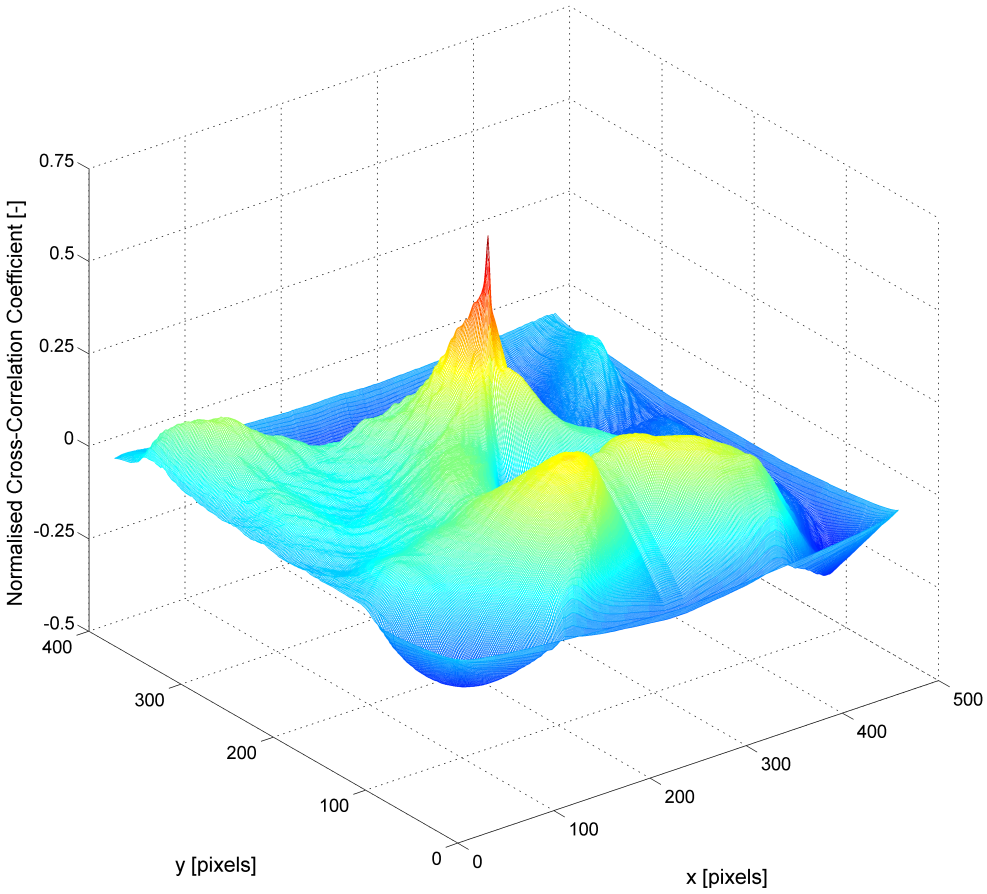

Figure 2.13: Normalised cross-correlation matrix found by cross-correlating the template image and the section of the PIV image shown in Figures 2.12. The resolution of the matrix in the region of the peak could subsequently be increased using interpolated spline curves.

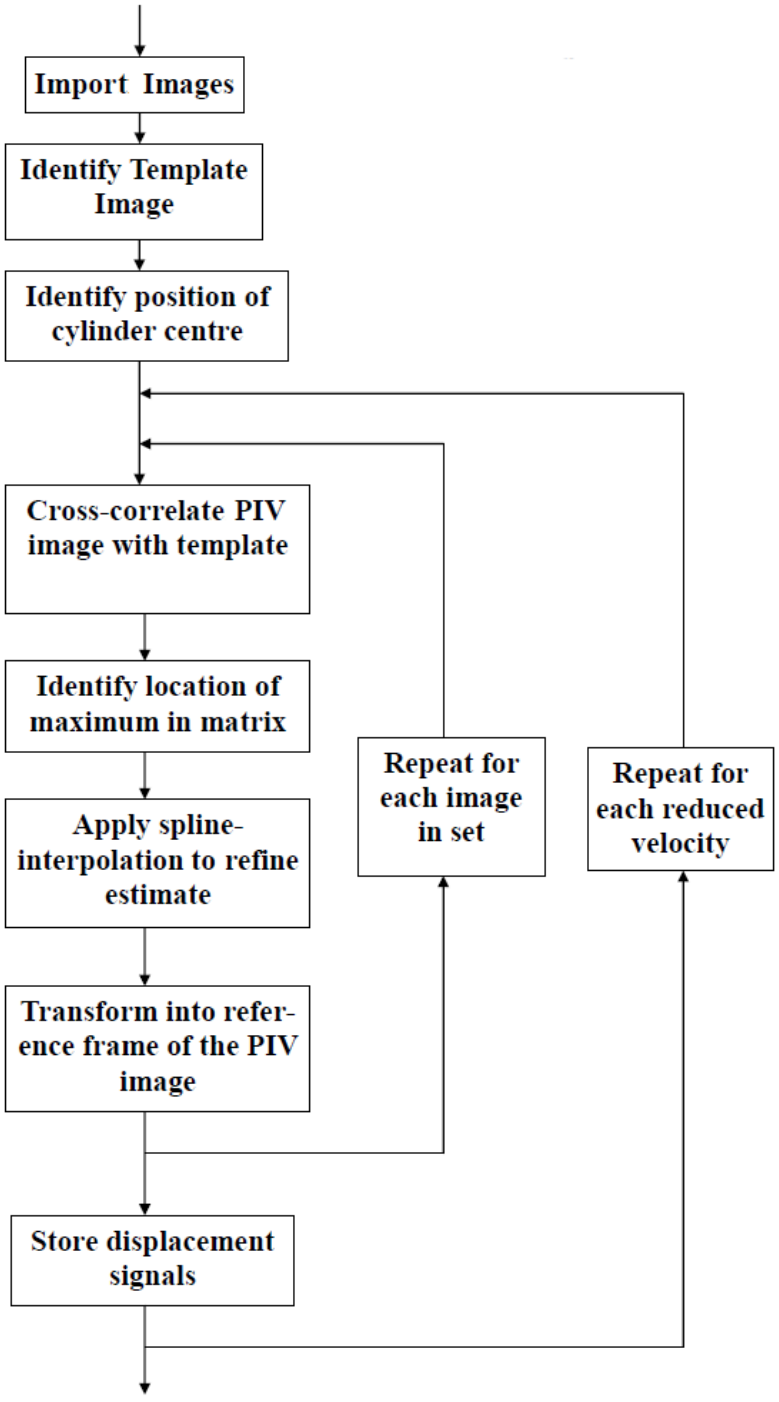

Figure 2.14: Flow diagram representing the cylinder tracking algorithm.

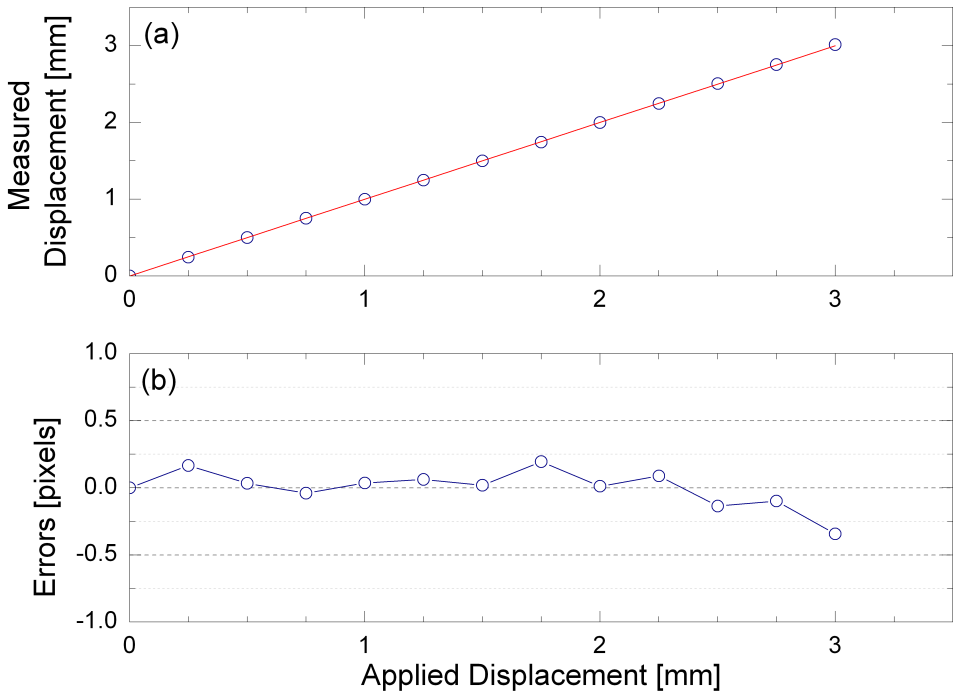

Figure 2.15: Variation in the estimated displacement signal (in mm, blue symbols) with the applied displacement (red line) (a), and the difference between the applied and the estimated displacement. The images had a calibration factor of 24.866 pixels/mm.

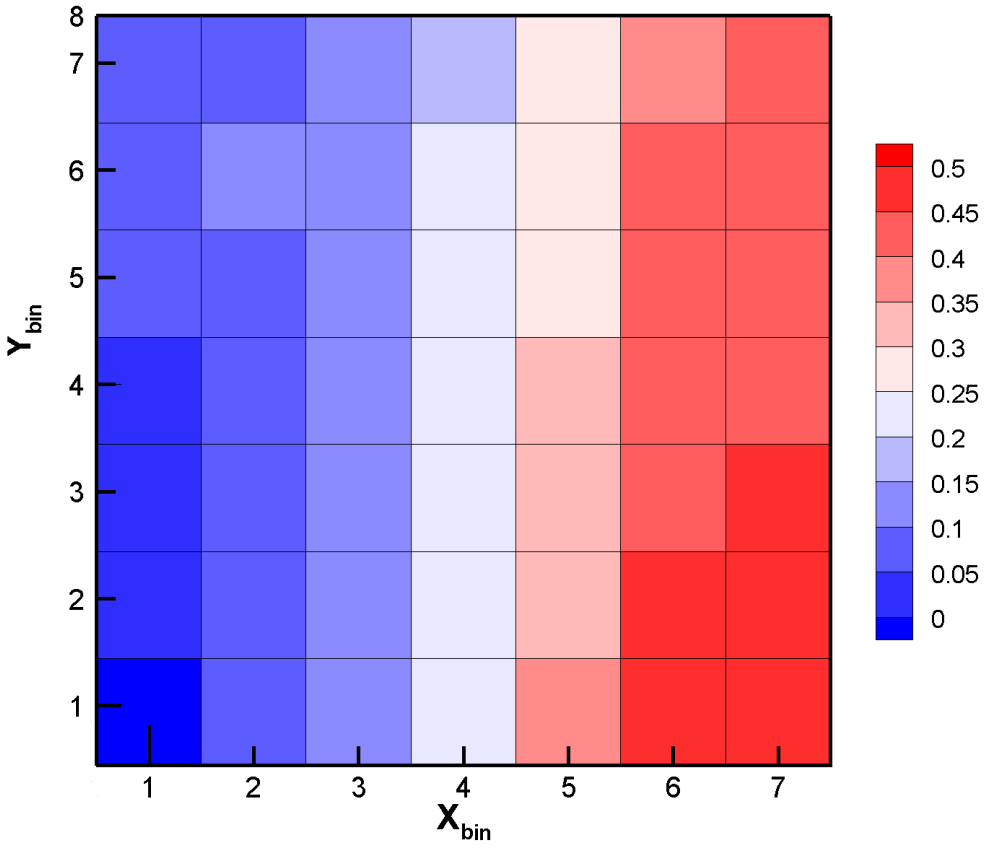

Figure 2.16: Variation in the mean absolute error in the estimated streamwise displacement signal, ε_{bin} for various sizes of binning window. The transverse size of the binning window does not have a significant effect on the accuracy, while the errors increase with the streamwise spacing. However, the magnitude of the errors remains low ($\varepsilon_{bin} < 0.25$pixels for $x_{bin} < 4$pixels), and the sub-pixel interpolation appears to be reasonably robust.

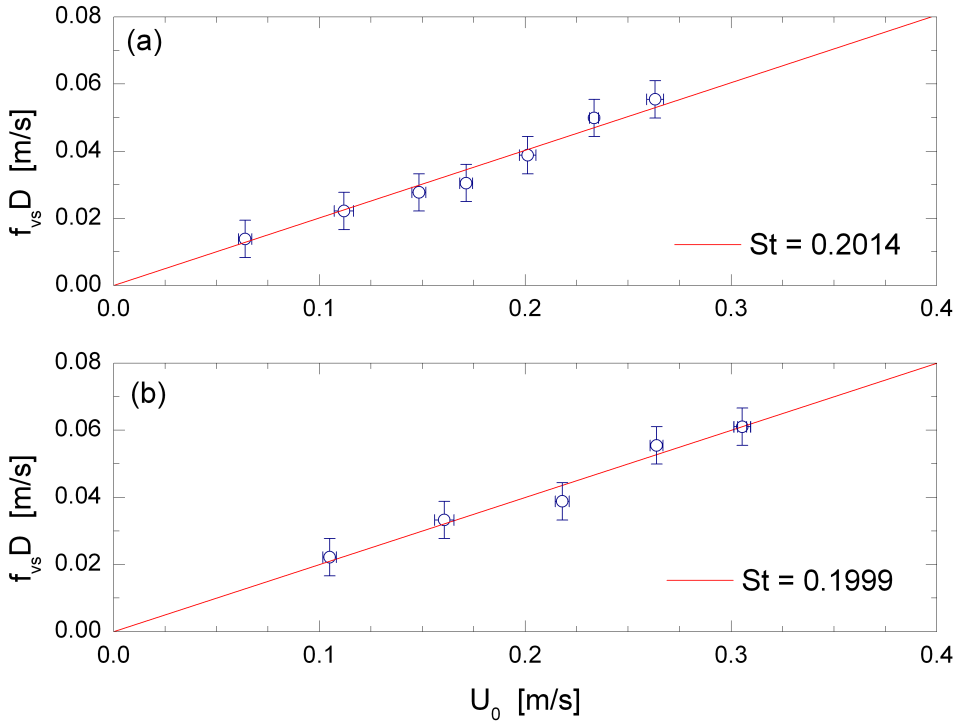

Figure 2.17: Variation in the estimated vortex-shedding frequency with freestream velocity, pre-lock-in, for Test Stages 1 (a) and 2 (b). The lines were correlated to the data points using the least squares method, and the gradient indicated the Strouhal number. The shedding frequency was estimated from the PSD of the transverse velocity signal measured at $(x/D, y/D) = (3, 0.5)$.

Chapter 3

Wake Modes in the Response Regime[1]

3.1 Introduction

The response regime of a fixed body exhibiting VIV is typically characterised by measuring the variation in the cylinder response amplitude with reduced velocity. This has been reported in a number of studies for the case of a cylinder free to move in the transverse direction (e.g. Assi et al. [2006]; Brankovic and Bearman [2006]; Govardhan and Williamson [2000]), as well as the 2DOF case (e.g. Blevins and Coughran [2009]; Dahl et al. [2006]; Flemming and Williamson

[1]The results in this chapter have also been presented/published in:

N. Cagney and S. Balabani. Vortex modes and cylinder response in streamwise-only vortex induced vibration. In *IUTAM Symposium on Bluff Body Flows(BBVIV-7)*, Kanpur, India, 2012.

N. Cagney and S. Balabani. Wake modes of a cylinder undergoing free streamwise vortex-induced vibrations. *Journal of Fluids and Structures* 38, 127-145.

[2005]; Jauvtis and Williamson [2003]). However, while the response regime of a cylinder free to move in the streamwise direction has been measured [Aguirre, 1977; Nakamura et al., 2001; Okajima et al., 2003], to date no study has been performed which provides quantitative measurements of both the cylinder response and the associated flow field in the wake simultaneously.

In this chapter, simultaneous measurements of the wake and structural response of a cylinder free to move only in the streamwise direction are presented for a range of reduced velocities. The flow fields were measured using PIV, and the cylinder displacement signal was estimated directly from the acquired image-pairs.

The test facilities, the structural parameters of the cylinder and the post-processing algorithms employed in the current chapter were presented in Chapter 2. The reduced velocity was controlled by incrementally increasing the flowrate past the cylinder. The specific reduced velocity range was 0.11 - 0.72, which corresponds to a Reynolds number range of 450 - 3700. For $U_r\mathrm{St}/f^* < 0.4$, 500 image-pairs were acquired, spanning the region of x/D from -1.3 to 4.8 and y/D from -2.3 to 2.9. For higher reduced velocities, the separation time between image-pairs was reduced, and the data acquisition software used was capable of reducing the region of interest without affecting the quality of the PIV images acquired. For $U_r\mathrm{St}/f^* > 0.37$, 1000 image-pairs were acquired, with a transverse span of $y/D = -0.75$ - 0.9. The images were acquired at 100Hz, which corresponded to approximately 80 and 160 cylinder oscillation cycles for measurements for $U_r\mathrm{St}/f^* < 0.37$ and > 0.37, respectively. A period of at least ten minutes was left between increasing the reduced velocity and performing the PIV measurements, in order to allow the vortex-shedding and cylinder response to stabilise and to

reduce the impact of any transient behaviour present.

The velocity fields were estimated using JPIV. A three-pass cross-correlation scheme was used, which is summarised in Table 2.2 and had a final vector spacing of 12 pixels (corresponding to approximately 15.5 vectors per cylinder diameter). After each pass the median test was applied, erroneous vectors were replaced by the local median, and the vector fields were smoothed using a 3×3 averaging filter. PIV measurements of a small region of the flow approximately eight diameters upstream of the cylinder were used to estimate the freestream velocity.

In order to reduce the influence of noise and low frequency fluctuations which were not associated with VIV on the measured cylinder displacement signals, the signals were band-pass filtered with cut-off frequencies of a third and 2.5 times the dominant cylinder response frequency.

3.2 Comparison with Previous Studies

In this section, the variation of the cylinder amplitude response with the conventional reduced velocity (i.e. $U_r = U_0/f_nD$) is presented and compared with that found in previous studies, in order to confirm that the present experiments performed capture the main features of the streamwise response regime.

The cylinder amplitude response found in the current work is shown in Figure 3.1, along with that reported by Aguirre [1977]; Jauvtis and Williamson [2003]; Okajima et al. [2003] and Blevins and Coughran [2009]. The experimental details of the various studies are given in Table 3.1. As the Strouhal number was not known for some of the studies presented, the results are presented in terms of U_r/f^*, rather than the 'true' reduced velocity, $U_r\mathrm{St}/f^*$. The response regime

measured in the present study is dominated by two response branches with peak amplitudes of approximately $A/D = 0.08$ and 0.06 respectively. Between these branches, near $U_r/f^* \approx 2.5 \approx 1/2\text{St}$, the amplitude drops to 0.02. Similar trends are also apparent in the response regimes found in the published work, despite differences in the experimental parameters employed. In all studies, the amplitude response is characterised by two branches of comparable height, separated by a region of reduced amplitude.

Table 3.1: Experimental details for previous studies presented in Figure 3.1.

Researcher	m^*	ζ	$m^*\zeta$	Re	AR
Current study	1.17	0.0053	0.0062	450 - 3700	10
Aguirre [1977]	1.229	0.00178	0.00219	1700 - 17000	13.2
Okajima et al. [2003][a]	-	-	0.195	8000 - 40000	8.15
Jauvtis and Williamson [2003][bc]	6.9	0.00145	0.01	1000 - 6000	7.5 - 10
Blevins and Coughran [2009][b]	0.8175	0.01	0.008175	5500 - 50000	17.8

[a] Only the combined mass-damping parameter was presented in this work. The experiments were performed in water using cylinders made of duralumin and stainless steel, which will have mass ratios of around 2.8 and 8, respectively. This would lead to damping ratios of approximately either 0.07 or 0.024.

[b] The cylinder in these studies was free to move in both the streamwise and transverse directions. Only the amplitude in the streamwise direction is presented here.

[c] It is not clear which aspect ratio was used in the data presented in this paper.

Okajima et al. [2003] measured the amplitude in terms of the root-mean-square of the cylinder displacement signal, rather than the mean peak height, as used in other studies. Assuming a sinusoidal displacement signal, this will result in the amplitude estimates being scaled down by a factor of $1/\sqrt{2}$. Unlike other studies, Okajima et al. [2003] and Blevins and Coughran [2009] found the second response branch to have a larger magnitude than that of the first, and observed the onset of the first branch to occur at a comparatively lower reduced velocity, $U_r/f^* \approx 1.25$. These differences may be related to Reynolds number effects, as the Re range in these studies was approximately an order of magnitude larger than those of the other works presented.

The response regime measured by Aguirre [1977] is quite similar to that measured in the current work, although the second response branch extends to a slightly higher reduced velocity. A similar trend is observed in the results of Okajima et al. [2003] and Jauvtis and Williamson [2003], and may be explained in terms of an increase in the response frequency (due to added mass effects which have not been accounted for in these two studies) which will act to increase the lock-in range. However, the increased range over which the second branch is observed in the work of Aguirre is likely to be attributable to the lower structural damping compared to the current system; Aguirre [1977] also showed that the extent of the second branch decreases with increasing damping.

Finally, the 2DOF cylinders examined by Jauvtis and Williamson [2003] and Blevins and Coughran [2009] both exhibited notably larger peak amplitudes compared to those found for cylinders free to move only in the streamwise direction, despite the relatively large damping employed in the latter study ($\zeta = 0.01$). It is well known that the ability of a cylinder to oscillate in the streamwise direc-

tion causes an increase in the transverse response amplitude [Dahl et al., 2006; Williamson and Jauvtis, 2004] compared to that of a single DOF cylinder. Therefore it is not surprising that this added DOF also increases the response amplitude in the streamwise direction.

Despite differences in the experimental conditions employed (structural damping, Reynolds number, number of DOFs etc.) the response regime measured in the current study shows strong similarities with previously published work, providing confidence that the results and discussion presented in this chapter are relevant to the general case of a cylinder experiencing VIV in the streamwise direction.

3.3 Cylinder Amplitude Response

The amplitude response of the cylinder and the dominant frequency of velocity fluctuations at various points in the wake are shown in Figures 3.2(a) and (b), respectively, as functions of reduced velocity. The blue and yellow shaded areas indicate the regions over which the S-I and SA modes were dominant respectively, while the A-II mode was observed for all other reduced velocities. The dominant frequency of velocity fluctuations in the wake was obtained from the transverse velocity signal extracted from the PIV fields at $(x/D, y/D) = (1, 0.5)$ and $(3, 0.5)$. For convenience, these signals are hereafter referred to as the 'near wake' and 'far wake' signals, respectively. The former provides an indication of the flow periodicity in the vicinity of the cylinder, i.e. the frequency at which the vortices are formed and shed, while the latter yields the frequency of the downstream wake once it has reached a stable configuration. Any change in the structure of

the wake between the near and far wake is likely to be indicated by a difference between the two frequencies. For all signals, the peak frequency was identified from the PSD of the velocity signals, which has a resolution of 0.39Hz, or $0.023 f_n$.

Figure 3.2(a) shows the cylinder amplitude response, presented in terms of the 'true' reduced velocity. The first and second response branches occur in the reduced velocity ranges $0.32 - 0.44$ and $0.52 - 0.6$, respectively, while the low amplitude region is centred at $U_r\mathrm{St}/f^* \approx 0.48$, which is slightly below the point at which the fluctuating drag force due to vortex-shedding is expected to coincide with the cylinder vibration frequency. Beyond the second response branch, $U_r\mathrm{St}/f^* > 0.6$, the cylinder vibration amplitude is reduced to $A/D \approx 0.01$, similar to that seen before the onset of the first branch.

The A-II mode was found to occur when the cylinder response was low (i.e. $U_r\mathrm{St}/f^* < 0.32$ and > 0.6), and during the peak of the first response branch, as was initially noted by Aguirre [1977]. The S-I mode was observed only at $U_r\mathrm{St}/f^* = 0.34$. This mode was found to occur over a larger reduced velocity range by Ongoren and Rockwell [1988]. However, this mode is caused directly by the cylinder motion [Naudascher, 1987]; as the amplitude in their study was considerably larger ($A/D = 0.13$) than that observed in free vibration, it is reasonable to expect the symmetric mode to occur for a narrower reduced velocity range in the wake of a freely oscillating cylinder. This finding is counter to the common claim that the entire first branch is associated with symmetric shedding, but is in agreement with the distribution of modes observed by Aguirre [1977]. Finally, the SA mode was observed for the low amplitude region at $U_r\mathrm{St}/f^* \approx 0.48$ and the second response branch.

Figure 3.2(b) shows that the far wake (closed symbols) becomes synchronised

to half the oscillation frequency ($f_{vs}/f_x = 0.5$) at $U_r\mathrm{St}/f^* = 0.48$, and remains locked in until $U_r\mathrm{St}/f^* = 0.6$, which corresponds to the low amplitude region and the second response branch. Unlike the case of the second branch and that of general VIV, the far wake does not become synchronised to the cylinder motion during the first response branch.

The frequency of the near wake fluctuations (open symbols) exhibits slightly more complex behaviour. For all reduced velocities outside the first response branch, the vortex-shedding frequency is approximately equal to that observed further downstream. However, when the S-I mode dominates ($U_r\mathrm{St}/f^* = 0.34$), the velocity fluctuations occur at the cylinder response frequency; for this mode the vortex-shedding is caused by the streamwise cylinder motion, and therefore occurs at the same frequency [Naudascher, 1987]. For the region of the first response branch over which the A-II mode is dominant, the near wake velocity fluctuations occur at $f_{vs}/f_x = 1$ for $U_r\mathrm{St}/f^* = 0.39$ and 0.5 for $U_r\mathrm{St}/f^* = 0.42$. This suggests that despite the A-II mode being dominant, the vortices are actually shed at the cylinder oscillation frequency, but quickly rearrange into an alternate structure like that seen at lower reduced velocities ($U_r\mathrm{St}/f^* < 0.32$) in which the shedding follows the Strouhal relationship. The effects of this vortex rearrangement on the frequency of the velocity fluctuations in the wake are discussed further in Chapter 4.

The variation in the frequency ratio of the cylinder with reduced velocity is shown in Figure 3.2(c). In general, the response frequency increases with reduced velocity, with the sharpest increases occurring during the regions of large cylinder vibration. Such variations in the frequency ratio are likely to be caused by changes in the added mass coefficient, which acts to reduce to effective or 'virtual' mass

of the system [Sarpkaya, 2004]. The frequency ratio appears to reach a steady value of approximately 1.36 beyond the second response branch.

Based on the observed characteristics of the cylinder response and wake structure described above, the response regime was divided into five regions, denoted R1-R5, which are summarised in Table 3.2. R1 occurs at reduced velocities before the first and after the second response branches, and is characterised by low amplitude cylinder oscillations, and a wake which is similar to that seen behind a stationary cylinder. R2 and R3 occur during the first response branch. The former is characterised by symmetric vortex-shedding, while the latter is associated with the A-II mode. The lock-in range is divided into R4 and R5. R4 contains the low amplitude region near $U_r\mathrm{St}/f^* = 0.5$, while R5 contains the second response branch.

Table 3.2: Reduced velocity ranges and dominant shedding mode observed for the five response regions shown in Figure 3.2.

Response Region	$U_r\mathrm{St}/f^*$	Wake Mode	Sample $U_r\mathrm{St}/f^*$
R1	$< 0.32, > 0.6$	A-II	0.2
R2	$0.32 - 0.37$	S-I	0.34
R3	$0.37 - 0.44$	A-II	0.42
R4	$0.44 - 0.53$	SA	0.49
R5	$0.53 - 0.6$	SA	0.55

Each region is discussed in more detail in the following sections using sample results for one reduced velocity, indicated in Table 3.2.

3.4 Region 1: $U_r\mathbf{St}/f^* = 0.2$

The raw displacement signal measured at $U_r\mathrm{St}/f^* = 0.2$ is shown in Figure 3.3(a), along with the spectra of the displacement and transverse velocity signals measured in the near and far wake (Figure 3.3(b)). As the absolute velocity was low in the location at which the near wake signal was measured for this reduced velocity, the near wake signal has been scaled up by 100 for clarity and economy of space. The cylinder exhibited a low amplitude and irregular response, which is most likely due to turbulent buffeting. The dominant frequencies of both velocity signals are well below half the oscillation frequency, indicating the absence of lock-in. The spectrum of the velocity signal measured in the far wake has a peak at the Strouhal frequency ($f/f_x = 0.2$), and a super-harmonic at twice this value. Both peaks are broad, indicating some unsteadiness in the vortex-shedding and disorganisation in the wake. The signal measured in the near wake also has a dominant frequency slightly below that of the far wake signal. Two super-harmonics are also visible, which are likely to be a result of the reorganisation of the wake in this region, as the small vortices formed in the shear layer coalesce into larger structures [Aguirre, 1977].

The phase-averaged vorticity fields for one shedding cycle are shown in Figure 3.4. The shear layers extend far into the wake, before they become saturated and roll up to form vortices at approximately $x/D = 1.7$ ($t/T = 5/16$ and $13/16$). The vortices are then cut-off from the shear layer at approximately $x/D = 2.5$ ($t/T = 7/16$ and $15/16$).

3.5 Region 2: $U_r\mathbf{St}/f^* = 0.34$

R2 is characterised by an increased response amplitude compared to R1, varying between $A/D = 0.02 - 0.07$ (Figure 3.5(a)). Some irregularity is still evident in the displacement signal. These amplitude fluctuations were not found to be repeatable, i.e. they are not a result of beating behaviour, as is also indicated by the absence of a second peak in the displacement spectrum shown in Figure 3.5(b).

The spectrum of the near wake velocity signal indicates that the vortex-shedding occurs at the cylinder response frequency. However, the spectrum of velocity fluctuations in the far wake has a peak near f_{St} and a super-harmonic at $2f_{\mathrm{St}}$ ($f_{vs}/f_x = 0.34$ and 0.69 respectively), indicating that the wake has become desynchronised with respect to the cylinder motion further downstream.

The phase-averaged vorticity fields for R2 are shown in Figure 3.6. In order to capture the wake structure which was present in the instantaneous vorticity fields, the near wake velocity signal was used as a reference for the phase-averaging process, instead of the far wake signal, as described in Section 3.1. The symmetric nature of the shedding can clearly be seen, as a vortex or shear layer on one side of the cylinder wake has a counterpart of opposite sign on the alternate side. As the cylinder moves downstream (a-d), the vorticity from the shear layers on either side of the cylinder accumulates to form two parallel vortices of opposite sign. These are shed from the cylinder as it moves upstream (e-h) and are convected downstream approximately parallel to the flow direction.

The symmetric structure of the S-I mode is known to rearrange downstream into an alternate pattern. This breakdown is described by Konstantinidis and

Balabani [2007] and Ongoren and Rockwell [1988] for the case of a cylinder experiencing forced excitation. As the flow field rearranges from the symmetric pattern to an alternate structure, the wavelength of the wake increases, causing a decrease in the local frequency of velocity fluctuations. The vortices in the S-I mode are shed at the oscillation frequency, while the A-II mode is essentially the von Kármán street found behind stationary cylinders [Aguirre, 1977]; therefore the fluctuations at f_x can be attributed to the S-I mode, and those near the Strouhal frequency to the A-II mode. As the phase-averaging process suppresses any information which is not correlated with the reference signal, the alternate structure which appears downstream will not be visible in the phase-averaged fields. Consequently, no large coherent structures are visible in Figure 3.6 for $x/D > 3$, despite being present in some instantaneous fields. This effect can also be observed in the vorticity distributions of the S-I presented by Konstantinidis and Balabani [2007] and Jauvtis and Williamson [2003].

3.6 Region 3: $U_r\mathbf{St}/f^* = 0.42$

The displacement signal in R3 is comparatively steady, with minor fluctuations in the non-dimensional amplitude between 0.06 and 0.09 (Figure 3.7(a)). The spectra shown in Figure 3.7(b) indicate a single narrow peak for cylinder displacement and multiple peaks for the fluctuating velocity. The far wake signal shows one large peak at the Strouhal frequency ($f/f_x = 0.42$), and a smaller one at $f/f_x = 1$. The first peak is near, but not equal, to $f_x/2$, indicating that the downstream wake continues to follow the Strouhal relationship, as found by Okajima et al. [2003]. The spectrum of the near wake signal has peaks at $f/f_x = 0.5, 1$

and the Strouhal frequency (0.42), as well as a smaller peak near 1.5. The peak near $f/f_x = 0.5$ indicates that while the far wake is not synchronised to the cylinder motion, the near wake is. It is therefore reasonable to expect that a significant component of the fluid forces also occurs at the response frequency, which explains the paradoxical occurrence of a large amplitude response region in the absence of synchronisation between the cylinder motion and far wake. The peaks in the near wake spectra at $f/f_x = 0.5$ and 1 were found to be of approximately equal height for both reduced velocities in R3. Thus, the change in the dominant frequency of near wake fluctuations in R3, which is apparent in Figure 3.2(b) is caused by a minor change in the spectra of the near wake signals, rather than a significant change in the structure of the wake.

The phase-averaged vorticity fields for this response region are shown in Figure 3.8; these were computed using the reference signal measured in the far wake, as explained earlier. The vorticity fields reveal an alternate shedding pattern and show that the A-II mode is dominant; however, the fields show some marked differences from those seen in R1. The vortices are now formed closer to the cylinder, at approximately $x/D = 1.3$. As the vortices are cut-off from the shear layer, they convect downstream parallel to the flow without nearing the centreline.

3.7 Region 4: $U_r\mathbf{St}/f^* = 0.49$

R4 is characterised by the onset of lock-in, with the velocity fluctuations in both the near and far wake occurring at half the cylinder response frequency. The displacement signal shown in Figure 3.9(a) is highly unsteady and shows a reduction in mean peak height, which varies between $A/D \approx 0 - 0.06$. Low-frequency fluc-

tuations, or riding waves, are also clearly present; for example, in regions such as $t = 1.7 - 1.8$s and $3.2 - 3.7$s the cylinder is clearly not oscillating about the mean position, calculated from the overall signal. The reason for this unsteadiness is not clear, as the periods in which the cylinder exhibits large or low amplitude vibrations do not correspond to changes in the shedding mode. As structures with low mass ratios are highly susceptible to added mass effects, it is likely that the cylinder in this case experiences significant unsteady modulations in its response frequency - and thus the effective reduced velocity - due to the complex coupling between its motion and added mass. This will affect the levels of energy transfer to and from the structure, and is likely to be the cause of the variable amplitude observed in this region.

These observations regarding the nature of the cylinder displacement signal are counter-intuitive; for transverse VIV and classical resonance, the synchronisation between the forcing and the structural response causes the response to increase in amplitude and become steadier [Govardhan and Williamson, 2000]. The fact that the exact opposite occurs in streamwise VIV illustrates the complex nature of the fluid-structure interaction involved.

The spectrum of the displacement signal (Figure 3.9(b)) has one large peak at $f/f_x = 1$, indicating that the fluctuations in amplitude are not the result of beating behaviour. Both the near and far wake velocity spectra have one peak, at $f_{\mathrm{St}} = f_x/2$. The peak is narrow compared to that seen for lower reduced velocities, reflecting the steadiness of the wake, in spite of the unsteadiness of the response amplitude. Unlike that seen for R1, R2 and R3, the two velocity spectra are very similar, indicating that there is a reduced spatial dependence of the frequency of velocity fluctuations in this response region.

The phase-averaged cylinder position (Figure 3.10(i)) shows a clear sinusoidal signal occurring at twice the shedding frequency. The amplitude of the phase-averaged signal is approximately equal to that seen in Figure 3.2; the phase-averaged displacement signal contains less scatter and shows no significant loss of amplitude as a result of the averaging process, which indicates that the cylinder motion and velocity fluctuations in the wake are now very closely correlated.

Despite the low response amplitude, the synchronised motion has a large effect on the wake, causing the SA mode to dominate, as can be seen in Figure 3.10. The shear layers roll up and vortices begin to form close to the cylinder ($x/D < 1$), which are convected downstream along the centreline. As the cylinder moves upstream ($t/T = 1/16 - 5/16$ and $9/16 - 12/16$), fluid is entrained into the near wake region that the cylinder has just vacated. This motion causes vorticity from the shear layers to be convected towards the centreline, which then forms a new vortex at the cylinder base. For R1 and R3, when the cylinder motion is not continuously synchronised to the cylinder motion, this fluid-entrainment effect is weaker, and the vortices are convected downstream further from the centreline, and thus the SA mode is not observed.

It is difficult to define the point at which vortex-shedding occurs - i.e. the specific phase at which the vortices are no longer connected to the cylinder by a shear layer - by visually examining the vorticity fields. Konstantinidis et al. [2005] proposed a method based on the magnitude of the phase-averaged transverse velocity, $\langle v \rangle / U_0$, across the wake centreline, whereby the shedding of a positive or negative vortex is said to occur when the transverse velocity reaches a maximum or minimum, respectively. By this definition, the newly formed positive vortex is shed at $t/T = 13/16$ and the negative vortex at $t/T = 6/16$, as the cylinder is

near its equilibrium position with a peak upstream velocity. This is in agreement with what can be observed qualitatively in Figures 3.10(c-d) and 3.10(g-h).

3.8 Region 5: $U_r\mathbf{St}/f^* = 0.53$

The displacement signal for R5, shown in Figure 3.11(a), is steady and has a peak amplitude in the range $A/D = 0.045 - 0.07$. The spectra of the displacement and wake velocity signals (Figure 3.11(b)) all exhibit only one narrow peak, with very little energy occurring at other frequencies. The vortex-shedding and downstream wake are locked in to the cylinder motion, with the velocity fluctuations occurring at $f/f_x = 0.5$.

As was also seen in R4, the phase-averaged displacement signal (Figure 3.12(i)) is clearly sinusoidal, with the amplitude matching that in the time-signal shown in Figure 3.11(a). The phase-averaged vorticity fields indicate that the shedding mode is SA, as in R4. However the fields exhibit some minor differences. Firstly, the vortices are formed and shed even closer to the cylinder. This may be a result of the greater fluid entrainment caused by the larger cylinder oscillations. Secondly, as the cylinder reaches its peak downstream position (and peak upstream acceleration) ($t/T = 3/16$ and $11/16$) a small region of vorticity is formed in the cylinder base, which has a sign opposite to that of the vortex already in this region. As the cylinder moves upstream ($t/T = 3/16 - 5/16$ and $11/16 - 13/16$), this region of counter-vorticity grows, causing the nearby vortex already formed to be cut off from the attached shear layer. Using the definition outlined in the previous section, the specific phases at which the positive and negative vortices are shed are $t/T = 13/16$ and $5/16$, respectively (Figures 3.12(c) and (g)), as

the cylinder is approaching its peak downstream position. Although the phase-averaged vorticity fields for R4 and R5 are qualitatively similar, there is a change in the phase of the vortex-shedding with respect to the cylinder motion. This change is similar to the change in phase between the fluid forcing and cylinder motion between $U_r \mathrm{St}/f^* = 0.5$ and the second response branch observed by Nishihara et al. [2005], which was proposed as the cause of the low amplitude response in the region. As far as the author is aware, no indication of this change in phase of shedding has previously been noted for free streamwise vibrations. Further information on the fluid forces is required to ascertain whether this change in phase induces a corresponding change in the phase of fluid forcing, such as to prevent any energy transfer to the structure.

3.9 Wake Velocity Profiles

The distributions of mean streamwise, $\bar{u}$, and fluctuating transverse velocity, v', along the centreline for the five regions described in Sections 3.4 - 3.8 are shown in Figure 3.13. The position of peak fluctuations along the centreline defines the vortex formation length, l_{vf}, while the position at which the mean streamwise velocity increases above zero defines the recirculation length, l_{rc}.

The mean velocity profile for R1 (Figure 3.13(a)) indicates that the recirculation length, in the absence of significant cylinder oscillations, is approximately 2.2D. The peak reversed flow occurs at $x/D = 1.53$, after which the mean velocity increases steadily. The S-I mode which occurs in R2 causes an increase in the extent of the recirculation region, as the symmetrically shed vortices combine to induce an upstream jet along the wake centreline. For $x/D > 1.5$, the mean

streamwise velocity is lower than that seen for any of the other response regions. R3 exhibits the same vortex-shedding mode as R1, except that the vortices are now formed closer to the cylinder. This wake contraction is apparent in the mean velocity profiles; the profiles for R1 and R3 are qualitatively similar, but the recirculation length for the latter is reduced to 1.44D.

The onset of the SA mode in R4 causes a further wake contraction, with the local streamwise velocity approaching the freestream value closer to the cylinder base. For R5, the SA mode is still dominant; however, the vortices reach the centreline closer to the cylinder (Figure 3.12). This closer vortex formation causes a further reduction in the recirculation length, which is now equal to 0.67.

The fluctuating transverse velocity profile for R1 (Figure 3.13(b)) increases in a roughly monotonic manner from the cylinder base to the formation length at $x/D = 2.63$, beyond which the fluctuations decrease steadily. Due to the symmetric arrangement of vortices observed during R2, the fluctuations across the centreline for this region are small. These increase for $x/D \gtrsim 2.5$, which is likely to be a result of the breakdown in the symmetric wake structure which occurs in this region of the wake.

For R3, the fluctuating velocity profile is qualitatively similar to that seen for R1. As in the case of the mean velocity profiles, contraction of the wake which occurs in R3 is also apparent in the fluctuating velocity distribution, with the vortex formation length now reduced to 1.45D. The onset of the SA mode in R4 produces a notable change in the fluctuating velocity profiles; as well as reducing the recirculation length, the convection of the vortices along the centreline observed for this mode also increases the levels of fluctuating transverse velocity along this line. This effect is clearly seen in the R4 fluctuating velocity profile;

compared to R3, the levels of fluctuating velocity have increased significantly for all measured points along the centreline.

In R5, the vortices approach the centreline very close to the cylinder base. As a result, the magnitude of the velocity fluctuations rises sharply at $x/D \approx 0.5$. The magnitude of the fluctuations is larger than that seen for R4 at all points outside the very near wake, which is likely to be caused by greater vortex strength, as will be discussed further in Section 3.11.

The estimated recirculation and vortex formation lengths discussed above are plotted in Figure 3.14 as a function of reduced velocity. The trends indicate that the wake lengths are largely consistent within most response regions. Within R1, the vortex formation lengths (open symbols) varies for $U_r \mathrm{St}/f^* < 0.32$, but becomes more stable at higher values. It is not clear why such variation is observed; this may be associated with increasing Reynolds number or changes in the strength of shed vortices, as will be shown in Section 3.11.

Figure 3.14 clearly indicates that the dominance of the symmetric shedding mode causes an increase in the recirculation and formation lengths. In contrast, regions of large cylinder response (R3 and R5) and lock-in (R4 and R5) correspond to a reduction in both lengths. These results are in agreement with the findings of Konstantinidis et al. [2003], for the wake of a fixed cylinder in pulsating flow.

3.10 Vortex Trajectories

In order to estimate the vortex trajectories as a function of streamwise position, $y_c(x)$, it was first necessary to identify the vortex cores. This was achieved using the swirling strength parameter, Λ_{ci}, as defined by Wu and Christensen [2006],

which utilises the standard λ-criterion to distinguish between vorticity due to coherent vortices and that due to shear layers. The swirling strength is given by:

$$\Lambda_{ci}(x,y) = \lambda_{ci}\frac{\omega_z(x,y)}{|\omega_z(x,y)|}, \tag{3.1}$$

where λ_{ci} is the imaginary component of the complex eigenvalue of the local velocity gradient tensor, which is defined in two dimensions as:

$$\mathbf{G^{2D}} = \begin{pmatrix} \frac{\partial u}{\partial x} & \frac{\partial u}{\partial y} \\ \\ \frac{\partial v}{\partial x} & \frac{\partial v}{\partial y} \end{pmatrix}. \tag{3.2}$$

The mean positive and negative swirling fields were calculated:

$$\overline{\Lambda_{ci}^{+}} = \frac{1}{N}\sum_{N}\Lambda_{ci}^{+}, \tag{3.3}$$

where the superscript '+' denotes a positive-only variable, in which all negative values are set to zero, and N is the number of fields summed. The centroid of the mean swirling strength parameter was used to estimate the position of the vortex core:

$$y_c^+(x) = \frac{\sum_y \overline{\Lambda_{ci}^+}(x,y)y}{\sum_y \overline{\Lambda_{ci}^+}(x,y)}. \tag{3.4}$$

The positions of the vortex cores identified using equation 3.4 were joined together to form the vortex trajectories. The paths of the negative vortices were estimated in a similar manner. Figure 3.15 shows the trajectories for each of the five response regions, overlaid on the mean swirling fields, obtained by averaging all values of Λ_{ci} (positive and negative).

The swirling motion of the vortices in the wake induce a negative streamwise velocity component, which can cause the local flow to be reversed if the vortices are sufficiently strong. As the vortices lose strength or approach the centreline, this effect is weakened or cancelled out by the competing effects of positive and negative vortices; the mean flow is no longer reversed, and the recirculation region is closed. Thus, it is the trajectories and strength of the vortices which control the extent of the recirculation region for each mode, which is indicated in Figure 3.15 by the thick black line.

It is interesting to note that the recirculation region for R1 (Figure 3.15(a)) is not connected to the cylinder, but starts at around $x/D = 0.7$. This can be explained in terms of the delayed shear layer roll-up and vortex formation compared to other response regions. The phase-averaged vorticity fields (Figure 3.4), and the mean swirling field, indicate that vortices are not formed for $x/D \lesssim 1.5$; as the magnitude of the reversed flow induced by the vortices will generally decrease with distance from the vortex core, it is reasonable to expect that vortices

which are formed further downstream of the cylinder will have a reduced effect on the flow nearest the cylinder. Thus, it appears that the flow nearest the base of the cylinder only becomes reversed when the vortices are formed reasonably nearby. The shear layers roll-up to form vortices at approximately $x/D = 1.7$ (Figure 3.4), which coincides with the point of greatest proximity between the positive and negative vortex trajectories. Beyond this point, vortices the move away from they centreline as they are convected downstream.

During the symmetric shedding in R2, the vortices convect downstream roughly parallel to the flow. As a result, the recirculation region is broader than that seen for the other response regions, in which the vortices move towards the centreline.

The vortex trajectories in R3 tend to closely follow the boundary of the recirculation region, similar to R1 and R2. They converge towards the centreline closer to the cylinder compared to R1, and the recirculation region is thus cut off sooner at $x/D = 1.44$.

In R4, the vortices convect towards the centreline quickly after formation. By $x/D = 1$, the vortices are approximately $0.2D$ away from the centreline, causing the recirculation region to close at this point. The vortices roughly maintain this level of separation as they move downstream.

In contrast, for the same vortex-shedding mode occurring in R5, the vortices actually cross the centreline and remain on the opposite side of the wake as they move downstream. The early crossing causes the recirculation region to contract, extending less than $0.2D$ from the cylinder base. The crossing is also apparent in the mean swirling field; beyond the point at which the trajectories cross the wake centreline, in contrast to that seen for other response regions, the positive swirling region occurs for $y/D > 0$ while negative swirling occurs for $y/D < 0$.

3.11 Vortex Strength

Vortex strength is conventionally expressed in terms of the circulation, Γ, computed by integrating the vorticity within or the velocity around some boundary. A consistent method is required to define this integration boundary, as this affects the final estimates. Previous researchers have chosen a boundary based on physical assumptions of the vortex shape [Konstantinidis et al., 2005], experimental constraints [Cantwell and Coles, 1983], or by fitting experimental data to a known model [Koopman, 1967].

In this work, the integration boundary was chosen by considering the phase-averaged swirling fields, which were calculated in the same manner as the phase-averaged vorticity. The position of a vortex was initially estimated by a peak in the swirling field, $\Lambda_{ci,peak}$. The contour of $\Lambda_{ci}(x, y) = 0.2\Lambda_{ci,peak}$ surrounding this point was identified, and a ray-casting algorithm was used to identify all the data points contained within. The value of 0.2 was chosen to reduce the influence of noise in the estimated vorticity and swirling fields. The vorticity within this boundary was summed to provide an estimate of the circulation. This method has the benefit of being based on the physical nature of the flow field, and requiring no *a priori* assumptions on the nature of the vortex.

For each reduced velocity, the swirling field was estimated from 16 phase-averaged velocity fields. The circulation of the vortices which had the strongest positive and negative values of the swirling parameter were estimated for each phase using the method outlined above. The centre of each such vortex was estimated using the centroid of the swirling field, (x_c, y_c), which was defined in a similar manner to equation 3.4:

$$x_c = \frac{\sum_x \sum_y \Lambda_{ci}(x,y)x}{\sum_x \sum_y \Lambda_{ci}(x,y)}, \tag{3.5}$$

$$y_c = \frac{\sum_x \sum_y \Lambda_{ci}(x,y)y}{\sum_x \sum_y \Lambda_{ci}(x,y)}. \tag{3.6}$$

The summations are performed over all values of Λ_{ci} within the vortex boundary defined. This method of estimating the vortex centre provided values very similar to those computed using the centroid of vorticity (within $0.05D$ in either direction for all cases). The estimated vortex strength for each phase-averaged field are shown in Figure 3.16(a-e) for R1-R5, as a function of the streamwise position at which the vortex centre was found. It should be noted that the scales used in Figures 3.16(a-e) are not the same.

The circulation of the shed vortices in R1 tends to increase with distance from the cylinder, appearing to reach a maximum near $x/D = 2.6$, which corresponds to the region of maximum transverse velocity fluctuations along the wake centreline (Figure 3.13(b)). No vortex centres are found for $x/D < 1.2$, as the vorticity in this region of the wake is due to the shear layers, rather than fully-formed vortices (see Figure 3.4), and the local swirling parameter is negligible. For R2, vortices are apparent in this near wake region, as the S-I mode now dominates and the vortices are formed very close to the cylinder, as seen in Figure 3.6(a-d). After a short increase, they maintain a low, roughly constant value of $|\Gamma|/U_0 D \approx 0.4$ until $x/D \approx 1.5$. Beyond this point no vortex peaks are

identified. As the alternate downstream structure of the wake is not apparent in the phase-averaged fields (as discussed in Section 3.5), the peaks in the swirling parameter will be small. This does not imply that the strength of the vortices in this region are negligible, as coherent vortices are apparent in Figure 3.6 as far downstream as $x/D = 2.5$. However, such vortices will be weaker than those occurring closer to the cylinder. Similar to R2, the strengths of the vortices in R3 in the vicinity of the cylinder are low, but increase as the vortices are shed downstream. The vortices reach a steady circulation of just below $|\Gamma|/U_0 D = 1$ at $x/D \approx 1$. Similar to R2, no vortex centres are found downstream of around $x/D > 1.75$.

In R4, as the SA mode dominates, the distance downstream at which vortices are observed extends to $x/D \approx 2.8$. The vortices again increase in strength in the region $x/D = 0.5 - 1$ before reaching an approximately stable value of $|\Gamma|/U_0 D \approx 1.3$. The trend in the evolution of the vortex strength in R5 is roughly similar to that in R4. However, the vortices continue to increase slightly in strength beyond $x/D \approx 1$, reaching a maximum value of $|\Gamma|/U_0 D \approx 2$ at $x/D = 2.7$.

The maximum values of vortex strength observed throughout the phase-averaged shedding cycle are summarised in Figure 3.17. In general, there is a good correspondance between the magnitude of circulation of the positive and negative vortices, indicating that the method provides a reasonably consistent method of estimating the vortex strength. The peak circulation is slightly variable within R1, as was also found for the recirculation and vortex formation lengths in Figure 3.14, which may be due to Reynolds number effects. The first response branch (R2 and R3) coincides with a reduction in the vortex strength. Although one

might expect the vorticity generated by the increased cylinder motion to increase the total circulation per vortex, the opposite effect is observed here. This may be explained by the increased frequency of vortex formation (now occurring at f_x) with respect to the natural formation frequency (f_{St}); there is now less time for each new vortex to entrain vorticity from the shear layers before being shed, reducing the total circulation of the shed vortices. As the wake becomes synchronised to the cylinder motion in R4, the shedding returns to the natural shedding frequency, and the vortex strength continues to increase linearly. The strength reaches a maximum in R5, with $|\Gamma|/U_0D = 2.09$, an increase of just under 90% based on the mean values before the onset of the first response branch. Post-lock-in, as the cylinder response falls, the vortex strength is also reduced, reaching a constant value which is slightly higher than that seen for $U_r\mathrm{St}/f^* < 0.32$.

3.12 Closure

The wake and structural response of a circular cylinder undergoing streamwise vortex-induced vibration were measured for a range of reduced velocities using PIV. The measurements of the cylinder response were compared to the results of previous studies in the literature, and the results contained within this chapter were deemed to be representative of the general case of a cylinder experiencing streamwise VIV. The variation in the amplitude response, frequency of velocity fluctuations in the wake and the dominant shedding mode were then summarised throughout the response regime, which was divided into five distinct regions. These were analysed individually in terms of the cylinder displacement and velocity signals extracted from the wake, as well as phase-averaged vorticity fields.

Finally, the effects of the cylinder vibration and shedding modes upon the wake were examined by comparing the regions in terms of velocity profiles and estimates of the vortex trajectories and strength.

The cylinder experienced two regions of comparatively high amplitude oscillations, separated by a low amplitude region at $U_r\mathrm{St}/f^* \approx 0.48$. The velocity fields were phase-averaged and the vorticity fields estimated in order to identify the dominant wake mode. The S-I and A-II wake modes were observed during the first response branch, at $U_r\mathrm{St}/f^* = 0.32 - 0.45$. The latter occurred at slightly higher reduced velocities and corresponded to a more regular displacement signal, with a higher amplitude. The velocity fluctuations in the far wake were not found to be synchronised to the cylinder motion during this region; however, synchronisation was observed in the near wake. This spatial dependence was caused by the reorganisation of vortices which are formed at the response frequency, but rearrange downstream into a more stable alternate structure.

Lock-in of both the near and far wake occurred for $U_r\mathrm{St}/f^* = 0.45 - 0.61$, which corresponded to both the low amplitude region at $U_r\mathrm{St}/f^* \approx 0.48$ and the second response branch. Both regions were characterised by the SA shedding mode; however, while the displacement signal was highly irregular at $U_r\mathrm{St}/f^* \approx 0.48$, it became very steady during the second response branch. A higher level of vorticity was also entrained from the shear layers into the near wake, causing a change in phase between the vortex-shedding and cylinder motion. This is likely to be linked to the change in phase between the fluid forcing and cylinder motion observed by Nishihara et al. [2005] for forced cylinder oscillations, and has not previously been reported in free vibrations.

The mean streamwise and fluctuating transverse velocity profiles were com-

pared and discussed in terms of the strength and trajectories of the shed vortices, the cylinder response and the irregular breakdown of symmetry in the S-I mode. Reductions in the vortex formation and recirculation lengths were found to occur at the onset of the first and second branches. The trajectories of the shed vortices were estimated using the modified swirling parameter, and the effect of the paths of the vortices upon the recirculation regime in the near wake was examined. The vortex strength was estimated for each reduced velocity, using the contours of the fluctuating swirling parameter to define the vortex boundary and region over which the vorticity was integrated. The increased shedding frequency which was observed during the first response branch caused a decrease in the circulation of shed vortices, but the vortex strength increased during the lock-in region of the far wake, with the maximum occurring during the second branch.

3.13 Figures

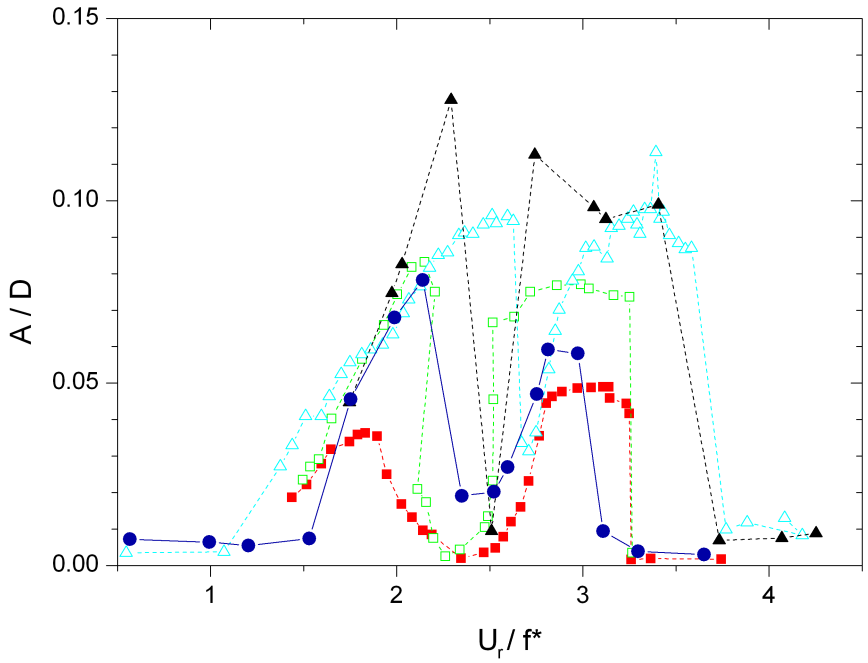

Figure 3.1: Variation of the cylinder amplitude response in the streamwise direction with the conventional reduced velocity ($U_r = U_0/f_n D$); present work (closed blue circles), Okajima et al. [2003] (closed red squares), Jauvtis and Williamson [2003] (closed black triangles), Aguirre [1977] (open green squares) and Blevins and Coughran [2009] (open light blue triangles). The amplitude measured by Okajima et al. [2003] is presented as the root-mean-square of the cylinder displacement signal, while for all other cases the amplitude represents the mean peak height of the signal. Details of the experimental studies are presented in Table 3.1.

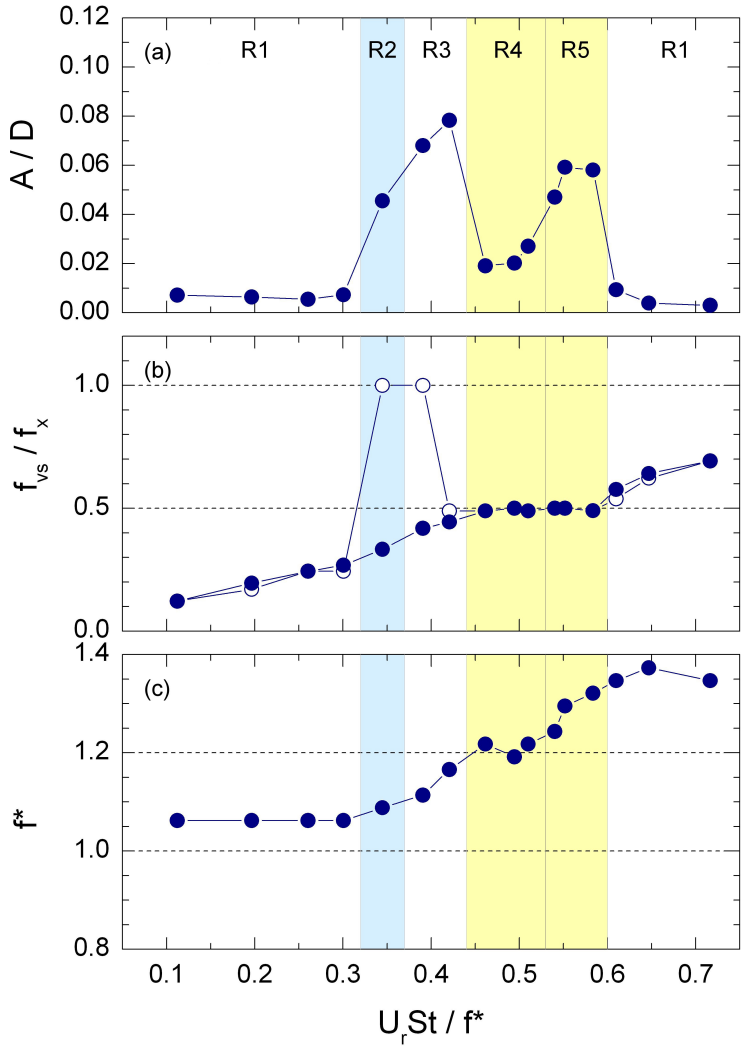

Figure 3.2: Variation of the cylinder amplitude response and wake frequency with reduced velocity: (a) amplitude response, (b) peak frequency of fluctuating velocity measured in the near wake (open circles) and far wake (closed circles) and (c) the variation in the cylinder frequency ratio. The wake frequencies are normalised by the cylinder response frequency, f_x, while in (c) the still water natural frequency is used to normalise the response frequency. The blue and yellow shaded regions indicate the reduced velocities over which the wake exhibited the S-I and SA modes, respectively, while the A-II mode was dominant for all other cases.

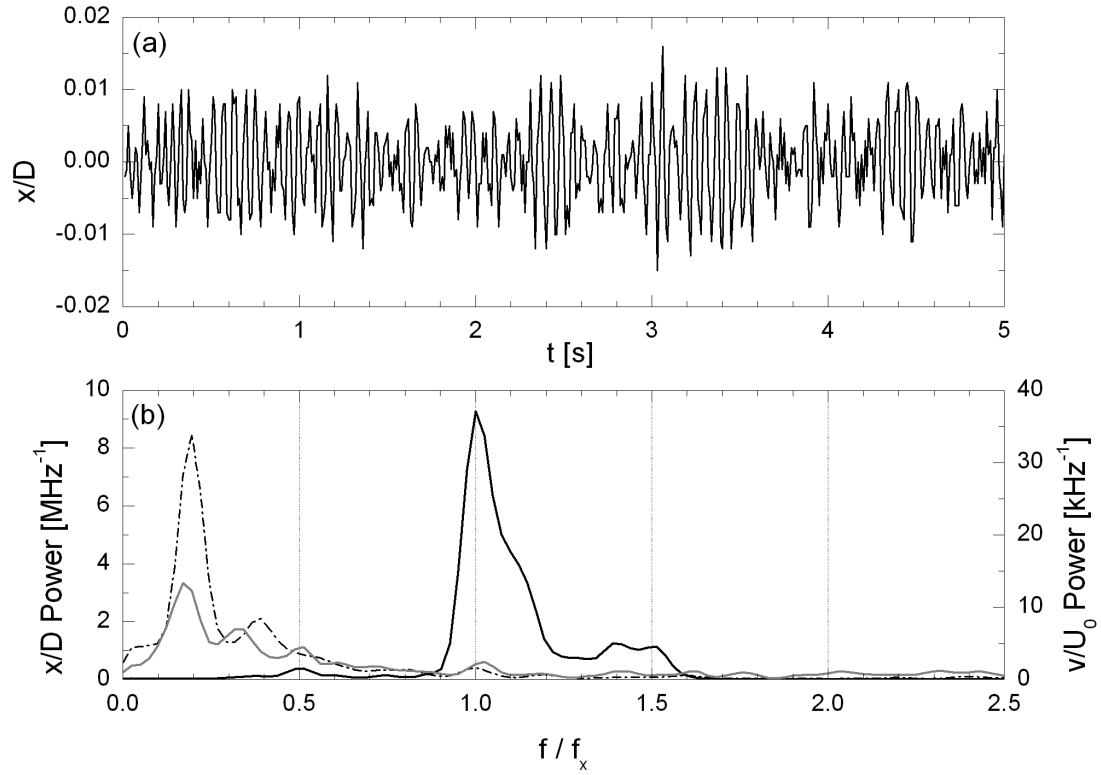

Figure 3.3: (a) Cylinder displacement signal and (b) spectra of cylinder displacement (solid black) and transverse velocity signal measured in the near wake (solid grey) and far wake (dashed black) for R1. For clarity and economy of space, the near wake signal has been scaled up by a factor of 100 for this reduced velocity.

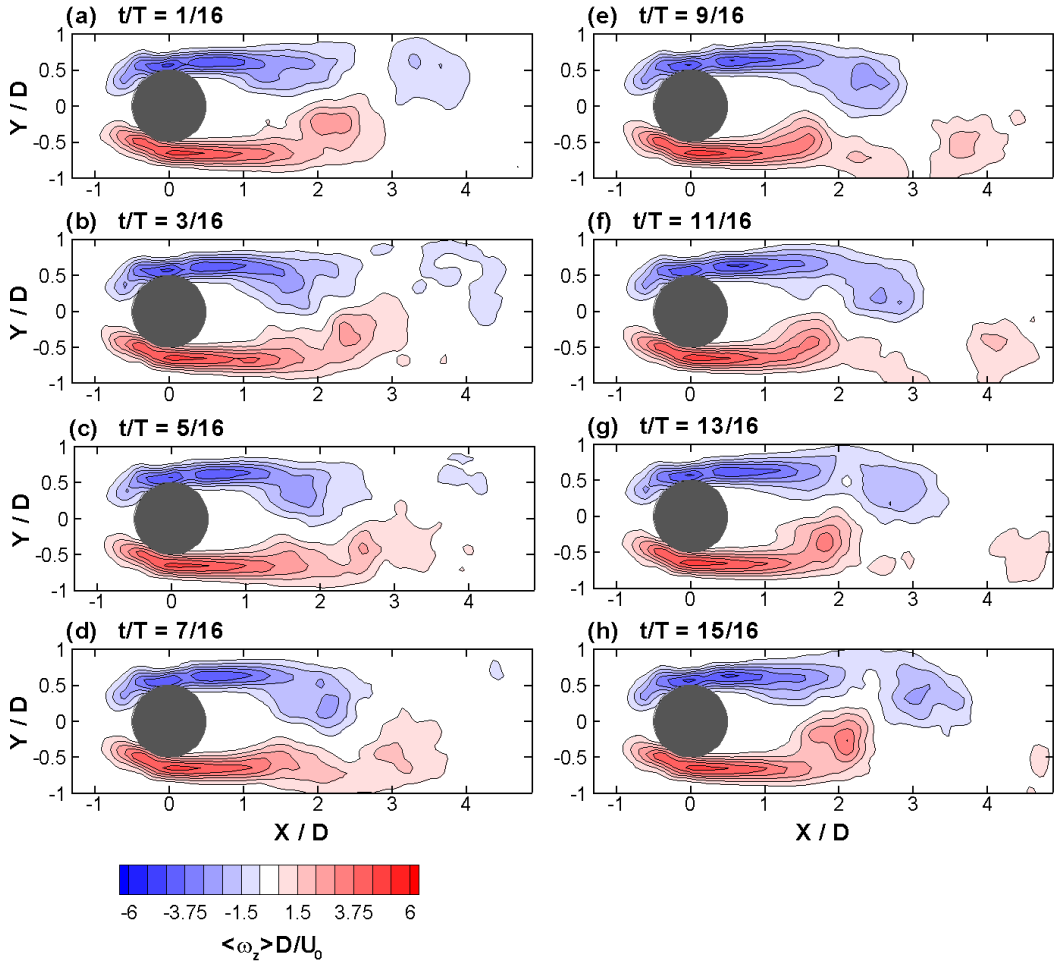

Figure 3.4: Phase-averaged vorticity fields over one shedding cycle for R1 ($U_r\mathrm{St}/f^* = 0.2$). The shedding cycle is not synchronised to the cylinder motion.

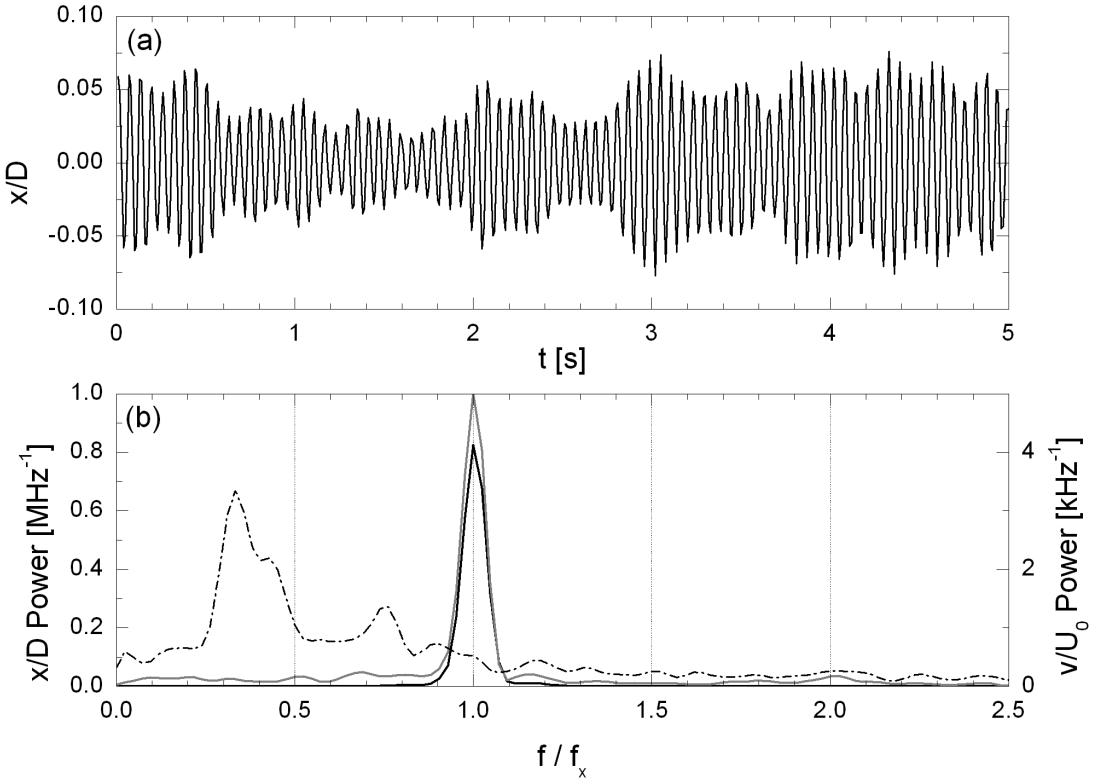

Figure 3.5: (a) Cylinder displacement signal and (b) spectra of cylinder displacement (solid black) and transverse velocity signal measured in the near wake (solid grey) and far wake (dashed black) for R2.

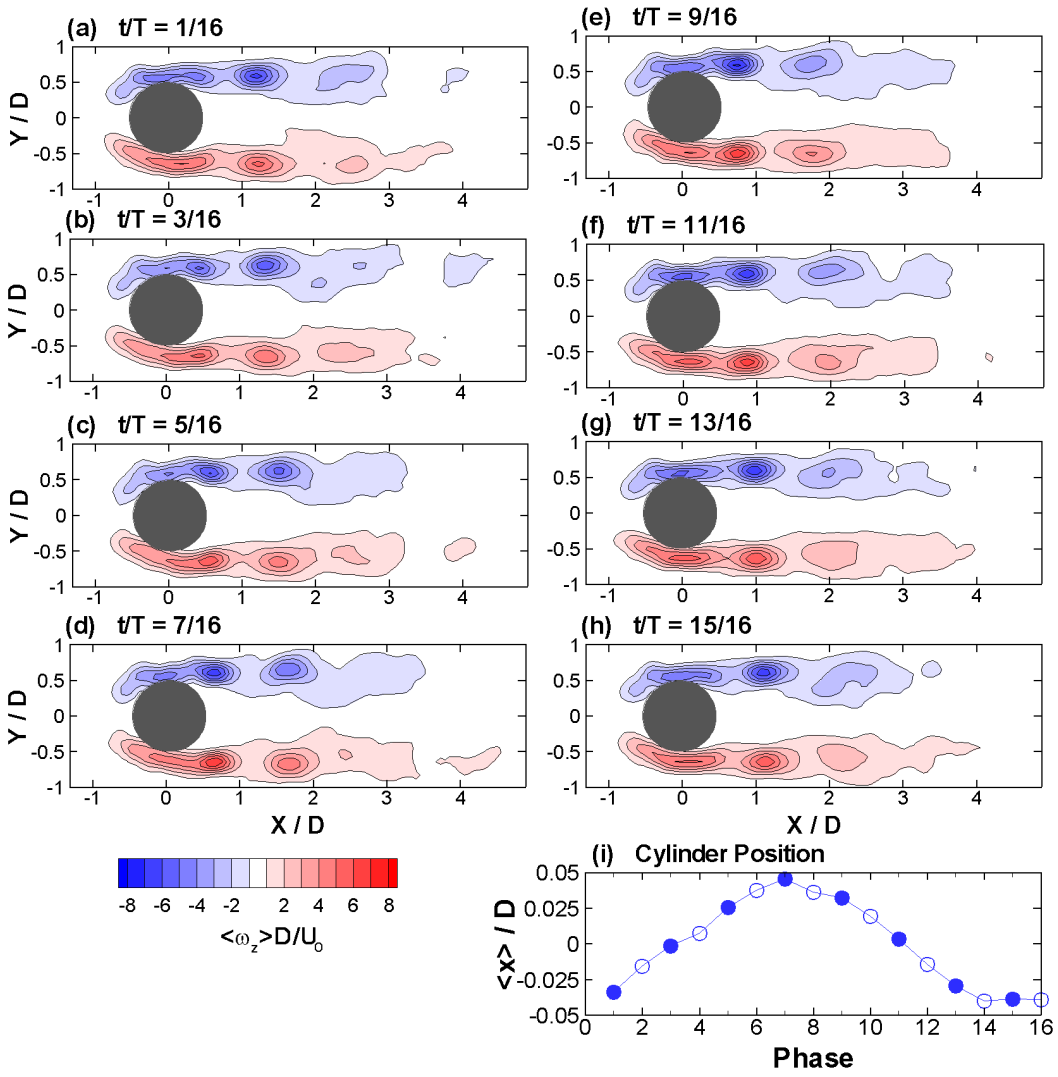

Figure 3.6: Phase-averaged vorticity fields over one shedding cycle for R2 ($U_r\mathrm{St}/f^* = 0.34$). The phase-averaged cylinder positions for each vorticity field are also shown (i). For this reduced velocity, the phase-averaged process was performed using a reference signal measured at $x/D = 1, y/D = 0.5$. The closed symbols in (i) indicate the phases for which the vorticity fields are shown.

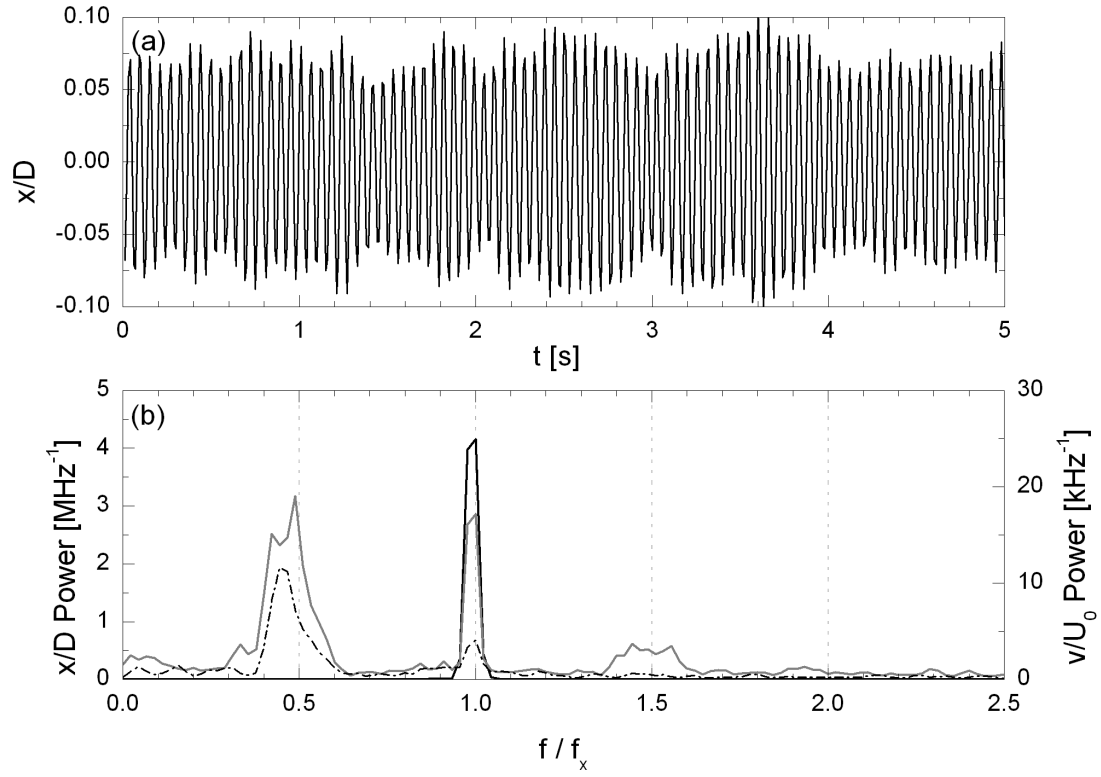

Figure 3.7: (a) Cylinder displacement signal and (b) spectra of cylinder displacement (solid black) and transverse velocity signal measured in the near wake (solid grey) and far wake (dashed black) for R3.

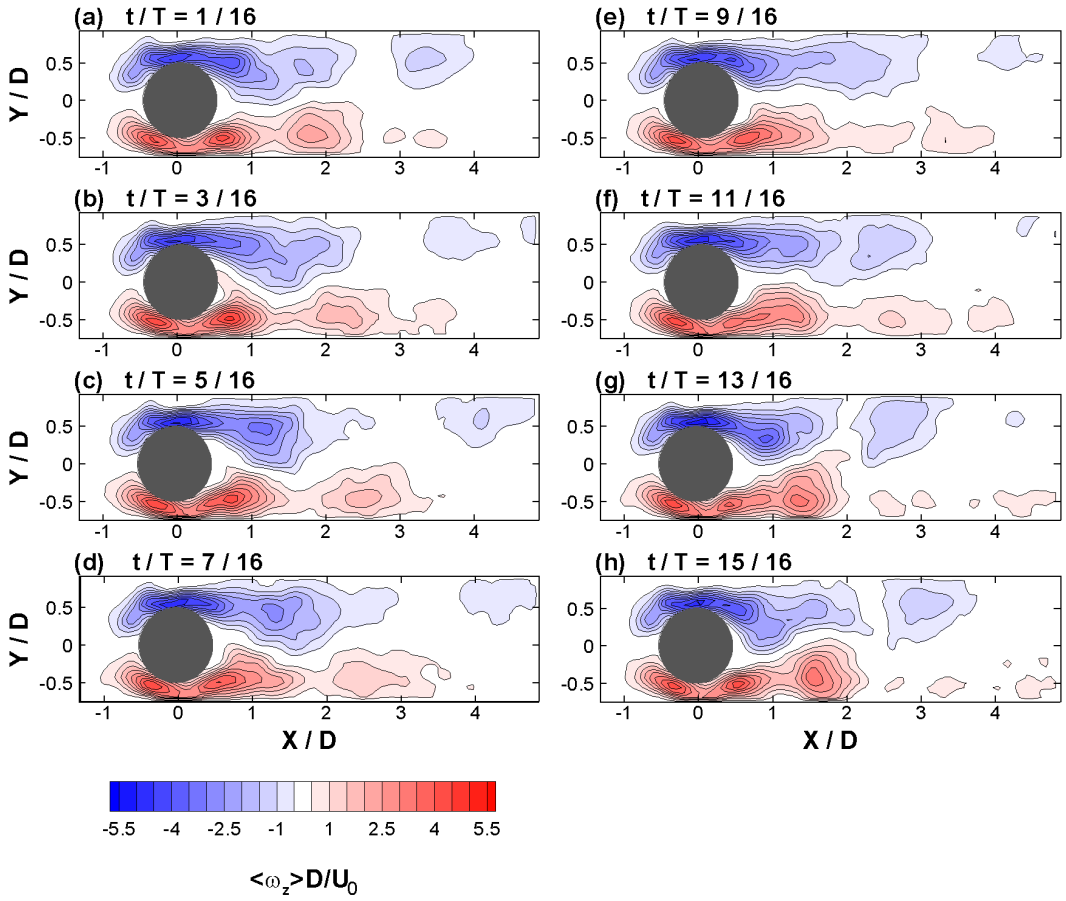

Figure 3.8: Phase-averaged vorticity fields over one shedding cycle for R3 ($U_r\mathrm{St}/f^* = 0.42$). The vorticity distributions are irregular, but the alternate nature of the vortex-shedding is clear in phases 5/16 and 13/16.

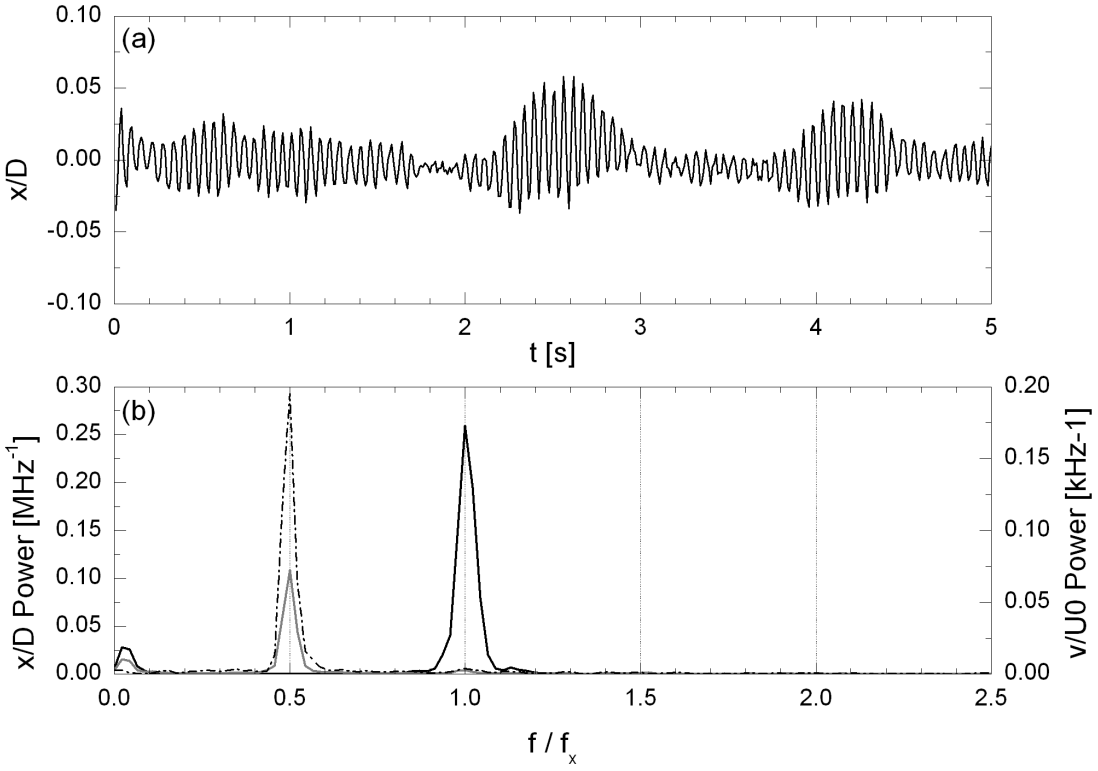

Figure 3.9: (a) Cylinder displacement signal and (b) spectra of cylinder displacement (solid black) and transverse velocity signal measured in the near wake (solid grey) and far wake (dashed black) for R4.

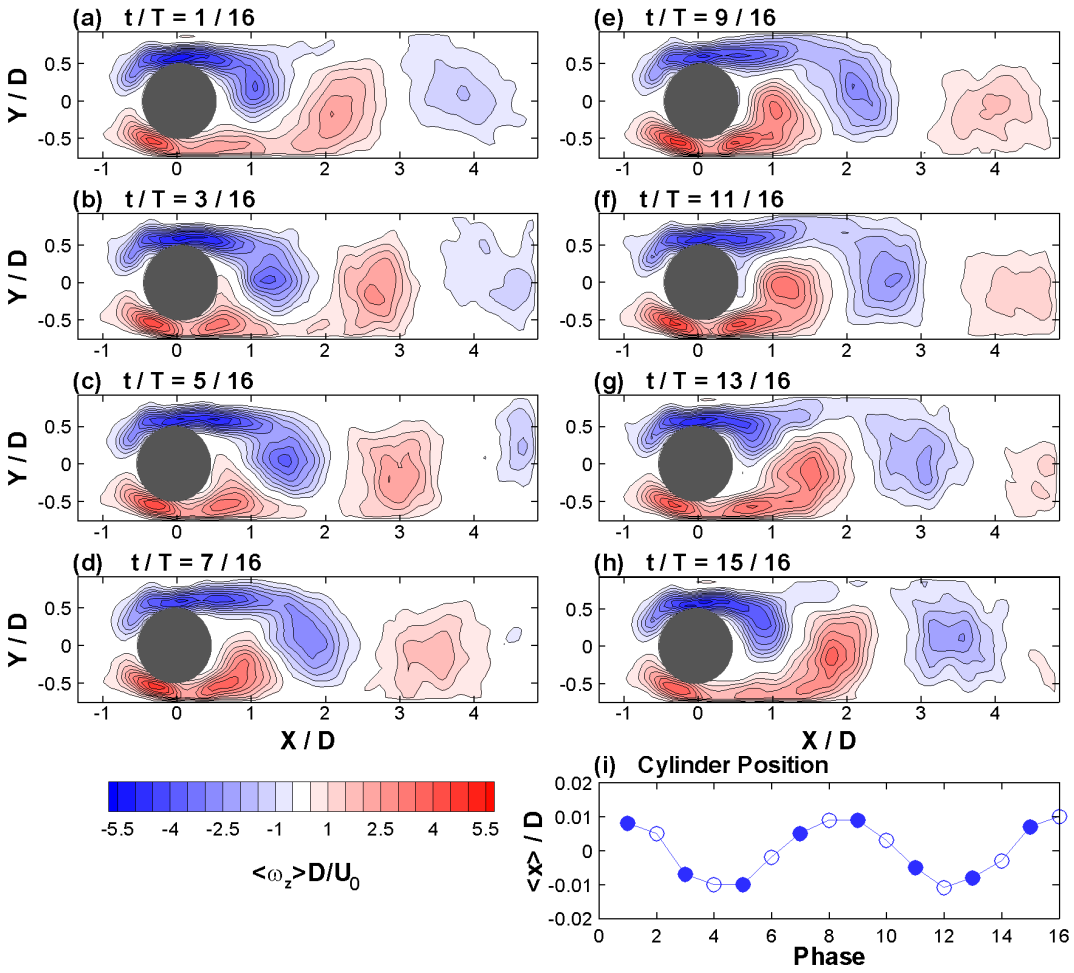

Figure 3.10: Phase-averaged vorticity fields over one shedding cycle for R4 ($U_r\mathrm{St}/f^* = 0.49$). The phase-averaged cylinder positions for each vorticity field are also shown (i). The closed symbols in (i) indicate the phases for which the vorticity fields are shown.

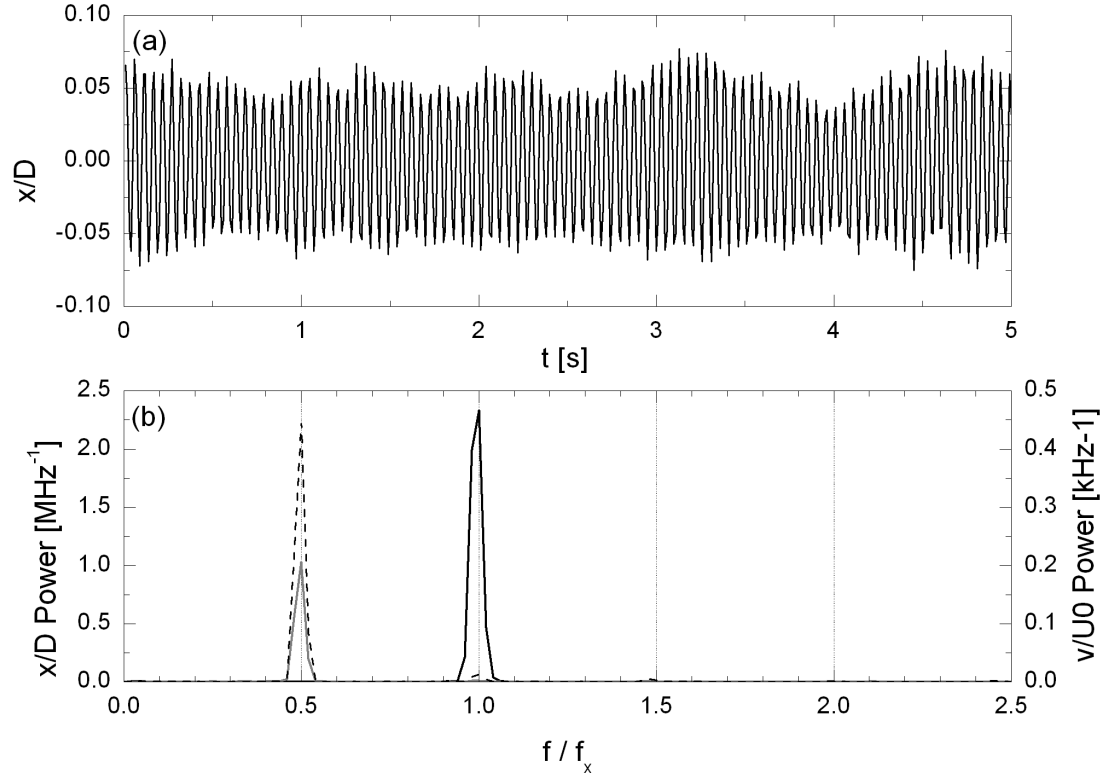

Figure 3.11: (a) Cylinder displacement signal and (b) spectra of cylinder displacement (solid black), transverse velocity signal measured in the near wake (solid grey) and far wake (dashed black) for R5.

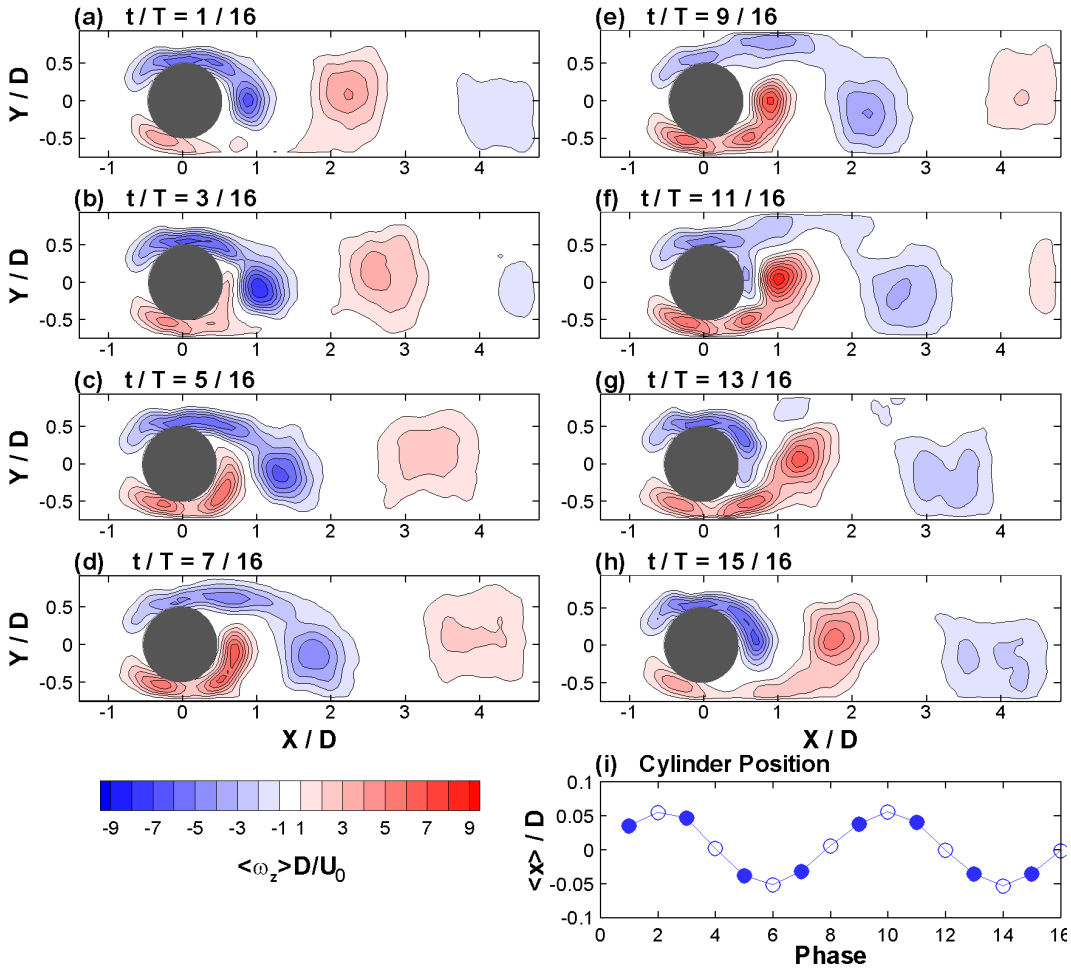

Figure 3.12: Phase-averaged vorticity fields over one shedding cycle for R5 ($U_r\mathrm{St}/f^* = 0.55$). The phase-averaged cylinder positions for each vorticity field are also shown (i). The closed symbols in (i) indicate the phases for which the vorticity fields are shown.

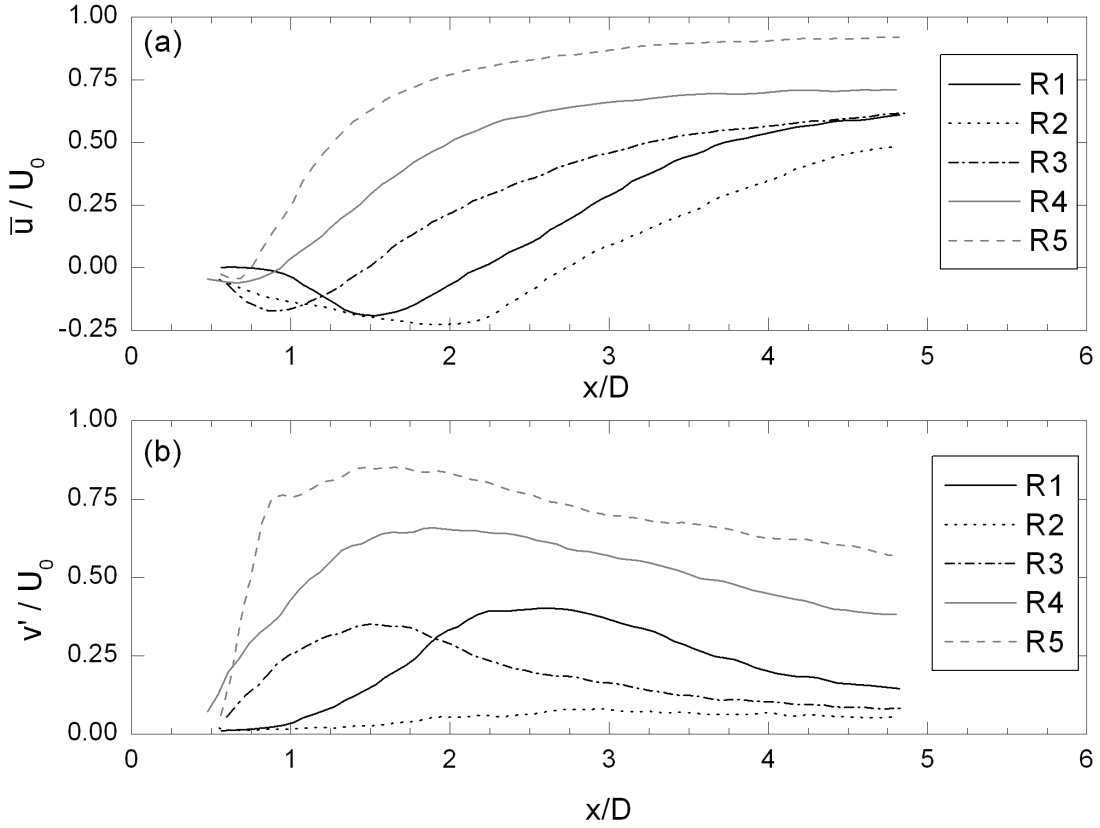

Figure 3.13: (a) Distributions of the mean streamwise velocity and (b) fluctuating transverse velocity along the centreline for R1-R5. The profiles have a resolution of 0.065D.

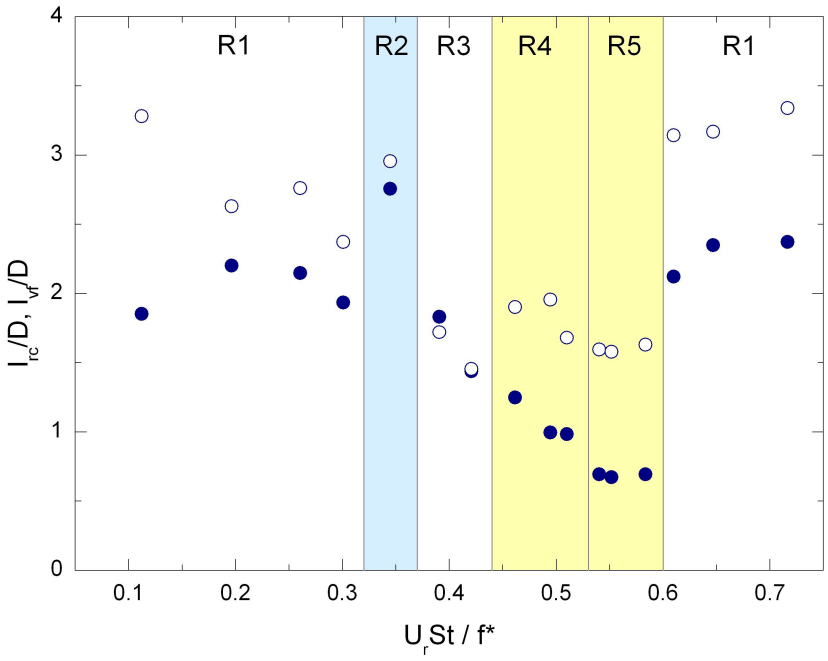

Figure 3.14: Variation in the recirculation length (closed symbols) and vortex formation length (open symbols) with reduced velocity.

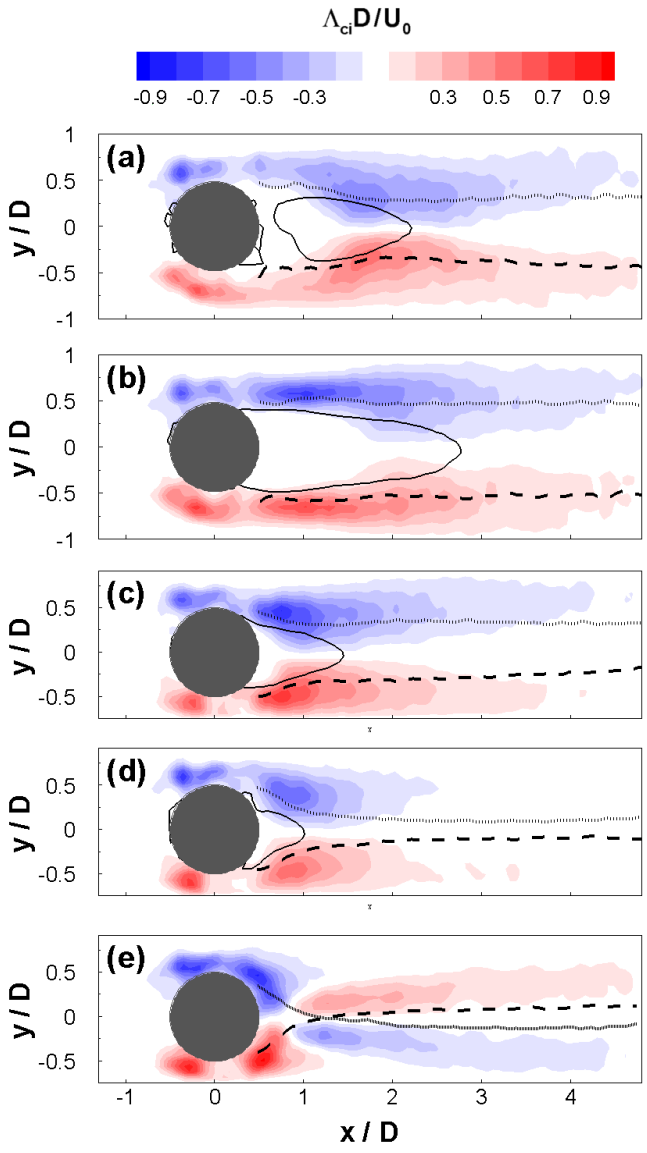

Figure 3.15: Estimated vortex trajectories for R1-R5 (a-e). The paths of the positive and negative vortices are shown using the dashed and dotted lines, respectively, while the solid line shows the boundary of the recirculation region. The paths are overlaid on the mean swirling field $\overline{\Lambda_{ci}}D/U_0$.

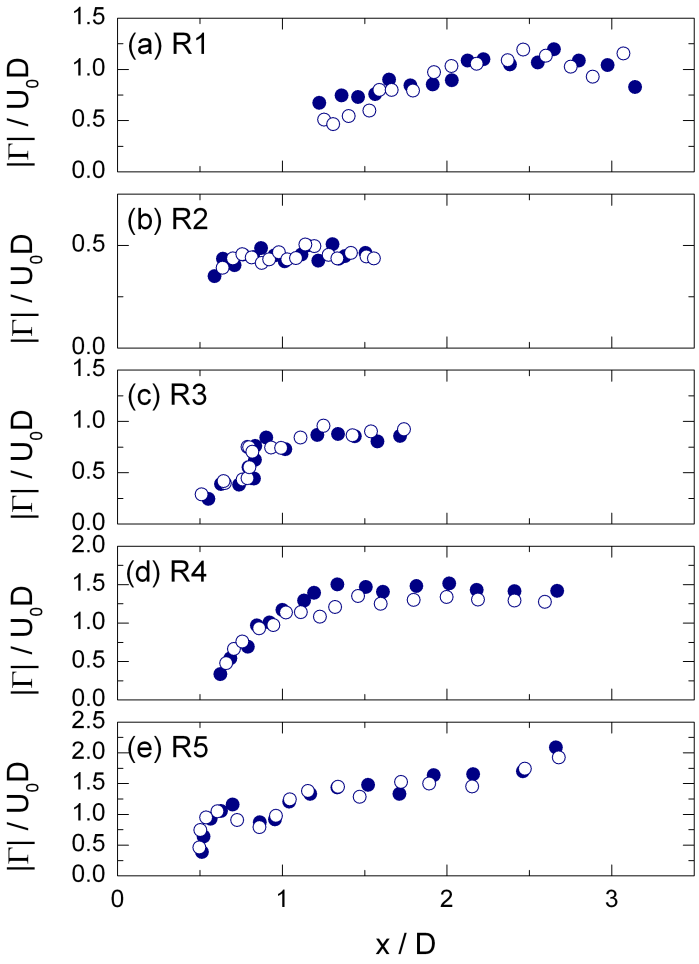

Figure 3.16: Variation of the maximum vortex strength with streamwise position for R1 - R5 (a-e). The closed and open symbols represent the absolute strengths of the positive and negative vortices, respectively. The scales used in each graph and not the same.

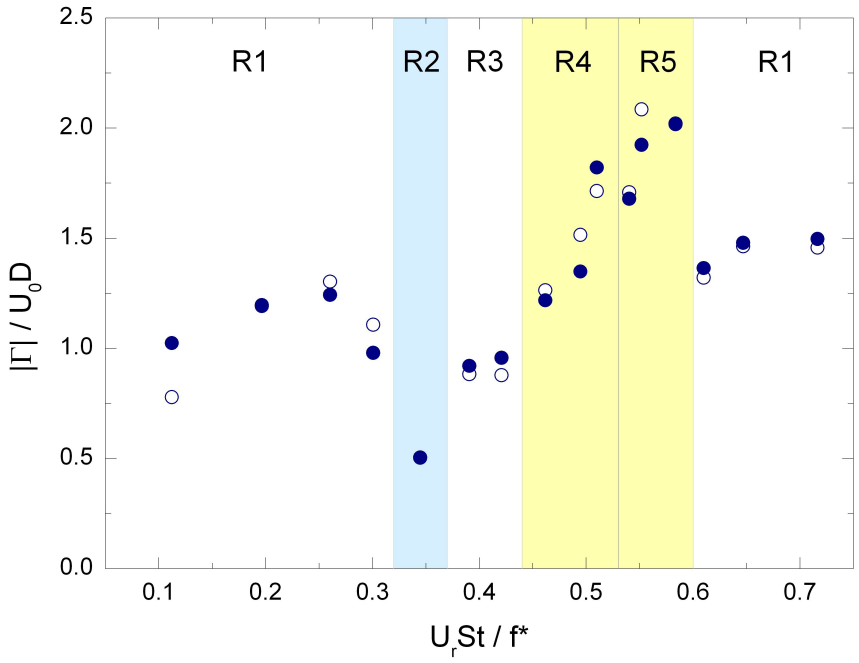

Figure 3.17: Variation of the maximum vortex strength with reduced velocity. The closed and open symbols represent the absolute strengths of the positive and negative vortices, respectively.

Chapter 4

Mode Competition in the First Branch[1]

4.1 Introduction

Chapter 3 described the wake modes which dominate throughout the response regime and the effect of each mode upon the cylinder response and various wake features. The first response branch was found to exhibit both the S-I mode (in which two vortices are shed simultaneously from either side of the cylinder per shedding cycle) and the A-II (in which the vortices are shed alternately). These

[1]The results in this chapter have also been been presented in:

N. Cagney and S. Balabani. Vortex modes and cylinder response in streamwise-only vortex induced vibration. In *IUTAM Symposium on Bluff Body Flows(BBVIV-7)*, Kanpur, India, 2012.

N. Cagney and S. Balabani. Mode competition in streamwise-only vortex induced vibrations. *Journal of Fluids and Structures* (Invited Paper, http://dx.doi.org/10.1016/j.jfluidstructs.2013.02.009i).

modes are sketched in Figure 1.4. The presence of both modes in this region is consistent with the results of Aguirre [1977]. However, Okajima et al. [2003] and Jauvtis and Williamson [2003], did not report the presence of the A-II mode in this region, indicating that some disagreement remains regarding the dominant wake mode in this reduced velocity range.

A number of studies in which a cylinder was forced to oscillate in the streamwise direction have observed mode competition between the S-I and A-II modes in this region. Konstantinidis et al. [2007] studied the wake of a fixed cylinder in sinusoidally perturbed flow (which is equivalent to a cylinder oscillating in the streamwise direction in steady flow) for a range of reduced velocities, $U_r \mathrm{St}/f^* = 0.25 - 0.33$, which is near the region over which the first response branch occurs. They noted that the wake alternated between the A-II and S-I modes. Similarly, Ongoren and Rockwell [1988] forced a cylinder to oscillate at various angles with respect to the freestream at relatively large amplitudes ($A/D = 0.13$), and noted that when the forcing occurred in the streamwise direction both wake modes occurred intermittently. Both studies also noted the tendency for the symmetrically shed vortices to rearrange downstream into an alternate pattern similar to that of the A-II mode. While the presence of mode competition has been observed in the wake of a cylinder experiencing forcing in the streamwise direction, as far as the author is aware, no studies have examined this phenomenon for the free vibration case. It is not known what effects such mode competition and the downstream breakdown of the S-I mode may have on the cylinder response.

In this chapter, the results of extended PIV measurements of the cylinder motion and associated wake are presented for two points of the response regime,

corresponding to the onset and the peak of the first response branch. Following the measurements described in Chapter 3, extensive PIV measurements of the cylinder response and wake at two values of reduced velocity were obtained in order to investigate any mode competition or transient behaviour in the wake. The cylinder and PIV system are the same as those described in Chapter 2 for Test Stage 1. These additional measurements were performed before the onset of the first response branch ($U_r\mathrm{St}/f^* = 0.275$) and at its peak ($U_r\mathrm{St}/f^* = 0.416$). The corresponding Reynolds numbers were Re = 980 and 1800. Three sets of 1000 image-pairs were acquired at 200Hz for each flowrate, which meant the combined data sets for each reduced velocity contained approximately 250 cylinder oscillation cycles. The PIV fields were estimated using a three-pass cross-correlation scheme, which had a final vector spacing of 16×16 pixels. The median test was applied after each pass and the erroneous vectors were replaced by their local median. Unlike the PIV fields presented in Chapter 3, the fields in this case were not smoothed. The estimated velocity fields spanned the domain $x/D = -1.17 - 4.34$, $y/D = -2 - 2.7$.

In order to compute properties such as the amplitude of the fluctuating velocity at a point or the cylinder response amplitude for either reduced velocity, the relevant signals were acquired for each of the three data set and abridged (forming one signal containing 3000 points). Thus, in this chapter, the cylinder displacement and velocity signals refer to the abridged data sets, rather than the signals acquired for only one data set.

The velocity fields acquired at both reduced velocities were analysed using POD (as outlined in Section 2.7). Due to computational constraints, it was not possible to apply the decomposition to all 3000 fields as a whole. Consequently,

each data set was decomposed separately. For both reduced velocities, the low order modes calculated in all three data sets were found to be approximately identical, indicating that the method had sufficiently converged. Figure 4.1 shows the cumulative relative kinetic energy of the POD modes for each data set. All six cases converge at approximately the same rate, with the first five modes accounting for over 50% of the total fluctuating kinetic energy.

An additional set of PIV measurements was acquired throughout the cylinder response regime, which was performed as part of Test Stage 2, as described in Chapter 2. The same cylinder and PIV system were used. However, the system had a higher natural frequency compared to the original tests. Thus, for the same approximate reduced velocity range, the corresponding Reynolds number range was higher; $\mathrm{Re} = 740 - 5400$, compared to $\mathrm{Re} = 450 - 3700$ in the original set of experiments discussed in Chapter 3. This allowed the effect of Reynolds number upon the cylinder amplitude response and the distribution of wake modes to be examined.

For each reduced velocity examined, 2000 image-pairs were acquired at 200Hz, which corresponded to approximately $250 - 300$ cylinder oscillation cycles.The cross-correlation scheme used to estimate the velocity fields is summarised in Table 2.2. These fields were also analysed using POD. Unlike the two large data sets acquired in the lower Reynolds number range, in this case it was possible to apply the decomposition to each set (of 2000 fields) without dividing the data sets into blocks.

The results presented in Sections 4.2 - 4.6 relate to the measurements performed in Test Stage 1 (i.e. at $U_r\mathrm{St}/f^* = 0.275$ and 0.416), while the discussion in Sections 4.7 and 4.8 relates to the measurements performed in the slightly

higher Reynolds number range in Test Stage 2.

4.2 Cylinder Response and Mode-switching

The cylinder amplitude response, calculated from the two extended PIV sets described in the previous section, are shown in Figure 4.2, superimposed upon the response regime discussed in the Chapter 3. Konstantinidis et al. [2007] and Ongoren and Rockwell [1988] observed mode competition between the S-I and A-II modes in the region $U_r\mathrm{St}/f^* = 0.25-0.33$. However, it is not clear whether such competition will occur in the wake of a freely vibrating cylinder in this region, nor what effects this may have upon the cylinder response. The instantaneous PIV measurements acquired at $U_r\mathrm{St}/f^* = 0.275$ indicated that the wake exhibited the A-II mode continuously, i.e. unlike the forced cases analysed by Konstantinidis et al. [2007], no mode competition was observed in this region. This is likely to be due to the different equivalent levels of A/D, as the A-II mode tends to dominate when the amplitude is low. However, the wake at $U_r\mathrm{St}/f^* = 0.416$ was found to be highly unstable, with both the S-I and A-II modes occurring intermittently. Sample instantaneous vorticity fields are shown in Figure 4.3. The alternate wake structure of the A-II mode is clear in 4.3(a), while two symmetrically shed vortices, characteristic of the S-I mode, are apparent in 4.3(b), which was acquired 0.5s later. The symmetric arrangement is not apparent downstream.

Konstantinidis et al. [2007] and Ongoren and Rockwell [1988] used PIV and hydrogen bubbles, respectively, to visualise the flow, and determined which wake mode was dominant in each snapshot by eye. This method has the disadvantage of being inherently subjective, which makes any statistical analysis of the

velocity fields for each mode unreliable. Furthermore, the turbulent and transient behaviour in the wake often makes the task of distinguishing between the two wake modes difficult. If the mode-switching behaviour in this region is to be examined quantitatively, a criterion is required which is capable of determining which mode is dominant as a function of time. POD was found to provide a suitable basis for such a criterion.

For flows which are dominated by convective structures such as shed vortices, the POD modes tend to occur in pairs which are 90° degrees out of phase [Ma et al., 2000; van Oudheusden et al., 2005]. The vorticity fields, estimated from the first four POD modes are shown in Figures 4.4(a-d), while samples of the corresponding temporal coefficients are shown in 4.4(e-f). The relation between modes 1 and 2 and modes 3 and 4 is immediately apparent in the vorticity fields; the vorticity distribution in (a) is very similar to that found in (b), while (c) and (d) also show strong similarities. The temporal coefficients oscillate with a variable amplitude (Figure 4.4(e-f)). The signals corresponding to modes 1 and 2 are 90° out of phase with each other, as are those of modes 3 and 4, further confirming the pairing between these modes.

The first two POD modes in this study were found to correspond to the basic alternate shedding wake pattern, and could be used to reconstruct the A-II mode. Figure 4.5(a) shows an instantaneous vorticity field, while 4.5(b) shows the same field reconstructed using the mean velocity field and modes 1 and 2; these modes clearly capture the alternate shedding pattern which characterises the A-II mode. Similarly, Figure 4.5(c) shows the same field, reconstructed using the mean field and modes 3 and 4, which capture the symmetric shedding of the S-I mode.

The correspondence between the various POD modes and the S-I and A-

II wake modes is also apparent from the power spectra of the POD amplitude coefficients. As the symmetrically shed vortices of the S-I mode are directly caused by the cylinder motion (as discussed in Section 3.5), this mode will occur at the cylinder response frequency. Similarly, the A-II mode is equivalent to the von Kármán wake observed behind a stationary cylinder, and will therefore occur at the Strouhal frequency. The power spectra of the temporal coefficients of the first four POD modes, shown in Figure 4.5, indicate that the coefficients for modes 1 and 2 fluctuate primarily at f_{St}, while modes 3 and 4 oscillate at f_x, further indicating the relation between the POD modes and the specific shedding modes.

Based on this correspondence between the first four POD modes and the S-I and A-II wake modes, a criterion is introduced to determine the dominant wake mode in a given PIV field; if the sum of the instantaneous amplitudes (calculated using the Hilbert transform) of the temporal coefficients of the first and second POD modes exceeds that of the third and fourth modes, the A-II mode is said to dominate, and when the opposite is true the S-I mode is said to occur. The criterion may be summarised as:

$$|\mathcal{H}(a_1)| + |\mathcal{H}(a_2)| > |\mathcal{H}(a_3)| + |\mathcal{H}(a_4)| \Rightarrow \text{A-II Mode} \tag{4.1}$$

$$|\mathcal{H}(a_1)| + |\mathcal{H}(a_2)| < |\mathcal{H}(a_3)| + |\mathcal{H}(a_4)| \Rightarrow \text{S-I Mode}, \tag{4.2}$$

where $\mathcal{H}$ denotes the instantaneous amplitude calculated using the Hilbert transform, and a_i denotes the temporal coefficient of the i^{th} POD mode.

Samples of the combined amplitude signals of modes 1 and 2 and modes 3 and 4 are presented in Figure 4.6. The shaded regions indicate time intervals at which the S-I mode is found to be dominant, based on the criterion described above. The snapshot and reconstructed vorticity fields shown in Figure 4.5 correspond to $t/T = 11.2$s, where $T = 1/f_x$. The points of mode transitions were found to occur unpredictably, i.e. they were not the result of beating behaviour due to the interaction of the competing effects of wake features occurring at f_x and f_{St}.

Given the correspondence between the various POD and wake modes, it would appear reasonable to simply analyse the velocity fields reconstructed using only modes 1 and 2 for the case of the A-II mode, and modes 3 and 4 for the S-I mode. However, Figure 4.1, indicates that the cumulative energy of the first four modes accounts for less than half the total fluctuating energy; therefore the reconstructed fields would neglect a significant amount of information contained in the measurements. It was instead decided to analyse the different wake modes directly from the instantaneous PIV fields. This approach had a number of advantages: (a) the results could readily be compared to those presented in Chapter 3 at different points in the response regime (e.g. the flow could be compared using phase-averaged velocity and vorticity fields, velocity profiles etc.), and (b) the results from each wake mode are less reliant on the specific form of the POD modes. This meant that the results for each wake mode were more dependent on the actual flow measurements, rather than on the mathematical decomposition (i.e. the form of the first four POD modes), which increases the generality of the findings presented.

This approach is also useful, as the effectiveness of the mode-detection criterion could be demonstrated using the phase-averaged vorticity fields calculated for the S-I and A-II wake modes. The ability of the criterion to divide the 3000 instantaneous fields into two sets which had significantly different phase-averaged fields would prove that the method is capable of accurately capturing the bimodal behaviour present. However, for this mode detection method to be validated in this manner, the process by which the phase-averaged field for both wake modes must be identical, i.e. the same reference signal must be used in both cases. Therefore, the only difference between the two final sets of phase-averaged fields will be the wake mode that the criterion determines to be dominant. As both wake modes are known to occur at different frequencies, the frequency content of the reference signal used in the phase-averaging process was required to be variable and dependent only on the wake; reference signals with a fixed frequency component (e.g. the cylinder displacement signal) would suppress information occurring at other frequencies, and may promote the appearance of a given mode in the final averaged fields. The transverse velocity signal, extracted from the wake at $(x/D, y/D) = (1, 0.5)$, shown in Figure 4.7(a), was found to have components occurring at both the Strouhal and cylinder response frequency (Figure 4.7(b)), and was thus likely to contain information of both the alternate and symmetric shedding modes. These velocity signals were extracted from each data set, low-pass filtered (with a cut-off frequency equal to twice the frequency at which the maximum of the power spectrum was found) and used as a reference signal in the phase-averaging process. The method of phase-averaging is summarised below:

(i) The transverse velocity at $(x/D, y/D) = (1, 0.5)$ was extracted

from the PIV fields for use as a reference signal.

(ii) This was used to calculate a phase angle (rounded to the nearest multiple of $\pi/4$) for each instantaneous PIV field.

(iii) The phase-averaged vorticity fields for the A-II mode were found by averaging all fields for each phase angle, ignoring any fields in which the S-I mode was deemed to be dominant using the criterion proposed.

(iv) Similarly, the phase-averaged vorticity fields for the S-I mode were found by averaging all fields for each phase angle, ignoring any fields in which the A-II mode was deemed to be dominant using the criterion proposed.

The vorticity distributions calculated from the phase-averaged velocity fields for the A-II and S-I modes are shown in Figures 4.8(a-d) and 4.8(e-f), respectively. Given the relatively low number of fields in which the S-I mode was detected, the averaging process divided the cycle into only 8 phases (compared to 16 in the results presented in Chapter 3) to reduce the irregularities in the final averaged fields. The symmetric and alternate structures of the S-I and A-II modes, respectively, are clearly visible.

The ability of the mode-detection criterion to extract such distinct averaged wake patterns from the same data set and using the same reference signal demonstrates its robustness. Given the unsteady and turbulent nature of the flow, the distinction between the S-I and A-II modes in an instantaneous field is inherently subjective; however, the distinct flow features apparent in the phase-averaged fields suggest that the criterion described above is effective in achieving this.

This method of mode-detection is applicable to both time-resolved and irregularly sampled data, but is limited to cases in which the POD mode-pairs can be found to correspond to distinct wake modes. Providing that such a correspondence is established, this approach has the advantage of being quantitative and objective. This allows the various wake and cylinder response characteristics of the S-I and A-II modes to be statistically analysed and compared, which could not be reliably performed if the modes were identified by eye, as had been performed previously [Konstantinidis et al., 2007; Ongoren and Rockwell, 1988].

The probability of occurrence of each mode is shown in Table 4.1, along with the probability that a given mode will continue to occur one cylinder oscillation cycle later and the associated cylinder response amplitude. The A-II mode was detected for 92% of the 3000 velocity fields; despite the intermittent presence of symmetric shedding, the alternate structure is clearly dominant at this reduced velocity.

Table 4.1: Probabilities of occurrence and associated response amplitude for each mode.

	S-I	A-II	All Modes
Number of fields	239	2761	3000
Probability of occurrence	8%	92%	100%
Probability of same mode occurring in next cycle	50.0%	94.3%	-
Mean peak height (A/D)	0.0764	0.0734	0.0737

The S-I mode tended to occur for a short number of cycles before the wake reverted to the alternate mode. A given instance of the S-I mode was found to have only a 50% probability of still being present in the following cylinder

oscillation cycle (measured as the cylinder was in its peak downstream position), compared to over 94% for the A-II mode, suggesting that the dominance of the symmetric shedding is quite unstable. Mode-switching did not result in significant variations in the cylinder response amplitude, as the difference between the mean peak height occurring for both modes was less than one standard deviation of the overall non-dimensional amplitude, (i.e. the difference in A/D measured in both cases was less than 0.007). This may be because the number of cycles for which the S-I mode occurred tended to be too small for changes in the level of fluid excitation to become apparent in the cylinder displacement signal. Alternatively, the wake mode may be variable along the cylinder axis; in which case variations in the fluid forcing along the cylinder axis will have a reduced effect on the total levels of excitation and overall vibrational amplitude. Regardless of the cause, this case of mode-switching differs from that observed for transverse VIV by Govardhan and Williamson [2000] and Morse and Williamson [2010], as it does not significantly affect the overall levels of fluid excitation (which would lead to a significant change in the amplitude response).

While this case of mode competition does not appear to significantly affect the levels of fluid excitation in the streamwise direction, it is likely to affect the response regime of a cylinder with freedom to move in both the transverse and streamwise direction, as is more commonly found in industry. The inherent symmetry of the S-I mode will mean that it is likely to induce a negligible lift force; however, the alternate shedding of the A-II mode will be associated with significant forcing in this direction [Cetiner and Rockwell, 2001]. Therefore, any switching between the S-I and A-II modes in this region is likely to lead to vibrations in the transverse direction, and may alter the overall nature of the two

degree-of-freedom cylinder response.

The incompatibility between the alternate shedding mode which occurs throughout the second response branch, and the symmetric shedding which dominates at lower reduced velocities has been considered to be the cause of the low amplitude region at $U_r\mathrm{St}/f^* \approx 0.5$ [Naudascher, 1987]. However, while these two wake structures compete in a complex and unsteady manner at $U_r\mathrm{St}/f^* \approx 0.416$, the results presented here indicate that such competition does not prevent positive energy transfer to the cylinder and comparatively large levels of vibration. Therefore, the mechanism proposed by Naudascher is unlikely to account for the true cause of the reduction in cylinder amplitude observed at $U_r\mathrm{St}/f^* \approx 0.5$, which still remains unclear.

4.3 Origins of Mode Competition

Some insight into the nature of the competition between the two wake modes may be gained from Figure 4.6. The amplitude of the POD modes associated with the S-I wake structure does not vary significantly compared to the amplitude of the POD modes associated with A-II shedding. Xu et al. [2006] showed that the two-dimensional vorticity field surrounding a cylinder oscillating in the streamwise direction can be expressed as the superposition of two components; an alternate structure similar to that surrounding a stationary cylinder in steady flow, and a symmetrical structure similar to that surrounding an oscillating body in fluid at rest. The former corresponds to the A-II mode (and POD modes 1 and 2), while the latter corresponds to the S-I wake mode (and POD modes 3 and 4). The equivalence between the wake modes and the low-order POD modes allows

the relative strength of the two vorticity field components described by Xu et al. to be measured as a function of time. Figure 4.6 can therefore be viewed as the time series of the components due to the cylinder motion (dotted line) and due to the alternate shedding structure (solid line).

As the amplitude of the cylinder vibration does not vary significantly at this reduced velocity (Figure 4.6), the component of the vorticity field caused by the cylinder motion (and the associated POD modes 3 and 4) should also be approximately constant, as can be seen in Figure 4.6. In contrast, the amplitude of modes 1 and 2 shows clear variations; at times the modes have a roughly constant amplitude of around 0.75m/s, e.g. $t/T = 9-14$ and $57-60$, while at other times the amplitude falls below 0.25m/s, e.g. $t/T = 45-50$ and $67-70$. Following the findings of Xu et al. [2006], this implies that the alternate shedding - as would occur for a fixed cylinder in crossflow - is intermittently interrupted. Although the effects of the streamwise cylinder motion upon the surrounding velocity and vorticity fields are always present, when the A-II shedding becomes disrupted, the cylinder motion effects become dominant and the S-I mode dominates in the wake.

Figure 4.9 presents the amplitude of the POD modes corresponding to the alternate shedding wake mode for one data set acquired at $U_r\mathrm{St}/f^* = 0.275$. As the cylinder response amplitude was negligible ($A/D = 0.006$), no POD modes were found to correspond to the S-I mode or the component of the vorticity field which is caused by the cylinder motion. Similar to that found at $U_r\mathrm{St}/f^* = 0.416$, the amplitude of the first two POD modes shows large, low frequency fluctuations, indicating that the alternate shedding structure is also being intermittently disrupted at this reduced velocity. Figures 4.10(a) and (b) show the instantaneous

vorticity fields computed at two instances corresponding to a maximum and a minimum in the amplitudes of the POD modes associated with the A-II mode, respectively. The well-known von Kármán wake (i.e. the A-II mode) is present in Figure 4.10(a) (albeit quite disorganised due to turbulence) when the amplitude of the associated POD modes is large. Figure 4.10(b) corresponds to a point at which the amplitude of these POD modes is low. The negative vortex at $x/D \approx 2.6$ and the positive vortex near $x/D \approx 4$ are considerably weaker that those in Figure 4.10(a), indicating that the alternate vortex shedding is now weaker than at $t/T = 2.9$. However, unlike the case for $U_r\mathrm{St}/f^* = 0.416$, this disruption of the alternate shedding mode does not lead to the appearance of the S-I mode. Even though the alternate shedding component of the vorticity field has become disrupted, the cylinder response amplitude is low, and does not induce a component due to the structural motion which is strong enough to cause the S-I mode to become dominant.

Mode competition in this region of the response regime can be said to be caused by the disruption of the alternate shedding wake mode. While this occurs both during and before the onset of the first response branch, it is only when the cylinder response amplitude is large (i.e. during the first branch) that a component of the vorticity field due to the cylinder motion is sufficiently strong to cause the appearance of the S-I mode.

4.4 Comparison of S-I and A-II Modes

The S-I and A-II shedding cycles during the first response branch have been examined separately in Sections 3.5 and 3.6, respectively, in terms of the cylinder

displacement signal and phase-averaged vorticity fields. However, the presence of both modes at the same point in the cylinder response regime allows the difference between the modes to be examined without being affected by differences in Reynolds number, reduced velocity and cylinder response amplitude.

The profiles of mean streamwise and fluctuating transverse velocity along the wake centreline ($y/D = 0$) were computed for both modes. The total set of 3000 fields was divided into two sub-sets, based on the wake mode identified as dominant in each field using the criterion described in Section 4.2. These sub-sets were processed separately to find estimates of the mean and fluctuating velocity fields for both modes. The resulting profiles are shown in Figure 4.11, normalised with respect to the freestream velocity. The same profiles, computed for the second and third response regions, R2 and R3 (discussed in Chapter 3) during which the wake exhibited the S-I and A-II, respectively, are also presented. These profiles have previously been discussed in Section 3.9. The reduced velocity and Reynolds number for each case are summarised in Table 4.2.

Table 4.2: Reduced velocity and Reynolds number for the measurements shown in Figure 4.11.

	$U_r\mathrm{St}/f^*$	Re
R2 (S-I)	0.345	1430
R3 (A-II)	0.421	1870
S-I	0.416	1800
A-II	0.416	1800

The mean streamwise velocity profile computed from the A-II fields matches that of R3 closely, which is to be expected, given the similarity between the values

of the cylinder response amplitude and reduced velocity in both cases. However, the corresponding profile for the fields exhibiting the S-I mode does not appear to match that measured in R2 as well, although the differences in the reduced velocity and cylinder response amplitude were larger in this case. The profiles indicate that the recirculation region has contracted at $U_r\mathrm{St}/f^* = 0.416$, when bimodal behaviour occurs and the S-I mode dominates, compared to that in R2, in which the same mode occurs.

Despite the strong similarities in the mean streamwise velocity profiles at R3 and the A-II fields at $U_r\mathrm{St}/f^* = 0.416$, the profiles of the fluctuating transverse velocity for both cases appear to be quite different. Although both exhibit similar trends qualitatively, the peak fluctuations are lower for R3. This is likely to result from the fact that no mode-detection was applied before computing the profile for R3; any instantaneous manifestations of the S-I mode will contaminate the estimates of the fluctuating velocity profiles. As the S-I mode is associated with low levels of transverse flow across the wake centreline, this 'contamination' acts to reduce the peak magnitude of v'/U_0. The fluctuating transverse velocity profile has a larger magnitude while the S-I mode dominates at $U_r\mathrm{St}/f^* = 0.416$ compared to R2. These fluctuations in R2 were attributed to the tendency for the symmetric structure of the wake to breakdown as the vortices were convected downstream (Section 3.5). The increased fluctuations at $U_r\mathrm{St}/f^* = 0.416$ are therefore likely to be a manifestation of the increased instability of the symmetrical arrangement of the vortices at this part of the response region, compared to $U_r\mathrm{St}/f^* = 0.345$, where the S-I mode was found to be most stable.

The fact that such distinct differences are apparent in the profiles of the mean and fluctuating velocities calculated from the fields which were found to exhibit

the S-I and A-II modes again demonstrates both the bimodal behaviour present at $U_r\mathrm{St}/f^* = 0.416$ and the effectiveness of the mode-detection criterion. It is also notable that in most cases these trends - large transverse velocity fluctuations while the A-II modes dominates and strong recirculation while the S-I modes occurs - are more pronounced after the mode-detection criterion has been applied, compared to the estimates for R2 and R3, for which no mode-detection was used. This suggests that the estimates of the mean and fluctuating - as well as the phase-averaged - velocity fields throughout the first response branch are affected by the intermittent appearance of both modes, and that this bimodal behaviour exists over a wide range of reduced velocity.

4.5 Effect of Mode-Switching on Vortex Strength

In Section 3.11, the first response branch was found to coincide with a decrease in the strength of the shed vortices, which was attributed to an increase in the frequency at which the vortices were formed. Similar to Section 3.11, the vortex strength was estimated using the phase-averaged swirling and vorticity fields in which the S-I and the A-II modes were detected. The maximum and minimum values of the vortex strength estimated throughout the shedding cycles of both modes are shown in Table 4.3, along with the corresponding values for R2 and R3.

For both the S-I and A-II modes, the peak vortex strength at $U_r\mathrm{St}/f^* = 0.416$ is approximately 33% higher that that found for R2 and R3, respectively. It is notable that the phase-averaged vorticity fields shown in Figure 4.8, which were computed at $U_r\mathrm{St}/f^* = 0.416$ using the mode detection criterion, are smoother

than those estimated for approximately the same reduced velocity for R3 (Figure 3.8). As in the case of the fluctuating transverse velocity profiles, the averaged fields for R3 may be contaminated by the intermittent appearance of the S-I mode. This increased variability in the instantaneous velocity fields reduces the amplitude of the averaged vorticity and swirling fields, and is likely to be the cause of the low estimates of the vortex strength found in R2 and R3, compared to those at $U_r\mathrm{St}/f^* = 0.416$ after the mode-detection algorithm has been applied.

Table 4.3: Maximum and minimum circulation of shed vortices, estimated using phase-averaged fields at $U_r\mathrm{St}/f^* = 0.416$ in which the S-I and A-II modes were detected, and those computed for R2 and R3.

Wake Mode	$U_r\mathrm{St}/f^*$	$\Gamma/U_0D(+)$	$\Gamma/U_0D(-)$
S-I (R2)	0.345	0.674	-0.674
S-I	0.416	0.880	-0.909
A-II (R3)	0.421	1.208	-1.215
A-II	0.416	1.642	-1.593

The estimated circulation of vortices throughout the S-I and A-II shedding cycles is shown in Figure 4.12 as a function of the corresponding streamwise position of the vortex core, which is given by the centroid of Λ_{ci} (Section 3.11). For both modes the vortices have a circulation of approximately $|\Gamma/U_0D| \approx 0.5$ as they are formed near $x/D \approx 0.6$, which then increases as they move away from the cylinder. While the symmetrically shed vortices appear to reach a peak value of around $|\Gamma/U_0D| \approx 0.9$, those shed alternately reach a peak strength of 1.64 at $x/D \approx 1.2$.

In Section 3.11 it was noted that the strength of the shed vortices decreases

at the onset of the first response branch, which was attributed to an increase in the shedding frequency. This gives vortices less time to entrain vorticity from the shear layers before being convected away from the cylinder. This mechanism of modulating the vortex strength implies that the strength should be inversely proportional to the shedding frequency. Figure 4.12(b) also shows the variation in the vortex strength through the S-I and A-II shedding cycles; however, the estimates of the strength have now been scaled by the shedding frequency, f_{vs}, (which is equal to the cylinder vibration frequency for the S-I mode and the Strouhal frequency for the A-II mode) over f_x. This scaled vortex strength is proportional to the total rate at which circulation of the vortices is created, or the non-dimensional time-derivative of the circulation which the wake mode transmits into the wake:

$$\left(\frac{f_{vs}}{f_x}\right)\left(\frac{|\Gamma|}{U_0 D}\right) \propto \frac{\partial|\Gamma|}{\partial t}\left(\frac{1}{U_0 D f_x}\right). \tag{4.3}$$

If the circulation contained within the shed vortices is linearly proportional to the formation period for each wake mode, the two trends in 4.12(a) should collapse. In fact, the trends do not fully do so, as can be seen in Figure 4.12(b); the symmetrically shed vortices have a slightly higher scaled strength, indicating that the shedding frequency does not entirely control the vortex strength. Clearly the circulation will be affected by the annihilation of counter-vorticity and other mechanisms, which have not been accounted for here. However, the trends exhibited by the vortices shed for both wake modes are quite similar in spite of the differences in the wake structure for the two modes; it is clear that

the shedding frequency plays an important role in determining the strength of the vortices shed.

4.6 Mode Breakdown

The S-I mode tends to occur for only a small number of cycles before the wake reverts to the A-II mode, as has been noted in previous sections. The relative instability of the symmetric mode is also apparent in the instantaneous vorticity fields, as symmetrically shed vortices tend to rearrange into an alternate pattern downstream. This can be seen in the sample vorticity field shown in Figure 4.13. Two vortices of opposite sign are clearly visible close to the cylinder. However, the wake quickly loses this symmetry downstream, and an alternate shedding pattern is apparent from $x/D \gtrsim 2$.

As the vortices convect downstream and rearrange into an alternate pattern, the frequency of local velocity fluctuations can be expected to change from f_x to f_{St}. This can be explained in terms of the transition from the S-I to the A-II arrangements increasing the wavelength of the wake, which causes a proportional decrease in the frequency of velocity fluctuations.

In order to investigate the effects of the wake transition in more detail, the distribution of the dominant frequency of transverse velocity fluctuations throughout the wake was measured. Time signals of the transverse velocity component were extracted at every PIV measurement location using all 3000 fields, and the dominant frequency of fluctuations was estimated from the respective PSDs. The resulting 'frequency map' is shown in Figure 4.14. Unlike other fields presented in this work, the frequency map is expected to be piecewise rather than smooth,

as the transitions between regions at which the primary fluctuations occur at f_{St} and f_x will occur as jumps, regardless of the spatial resolution of the measurements. As a result, unlike the vorticity distributions presented elsewhere, no interpolation is used in Figure 4.14 to evaluate the contours.

The map shows that for the majority of the measured wake, the fluctuations occur at the Strouhal frequency, which is to be expected, given the dominance of the A-II mode at this reduced velocity. The no-slip condition at the cylinder surface ensures that the fluctuations in the vicinity of the cylinder occur at f_x regardless of the wake mode. However, the f_x region is large, extending approximately two diameters into the wake on either side of the cylinder, roughly following the path of the shed vortices. The strength of the fluctuations occurring at f_x in this region suggests that the shear layers may roll up to form vortices at the cylinder response frequency, but these vortices tend to coalesce and reorganise such that they are convected into the wake in an alternate pattern, forming the A-II mode. This will not be visible in the phase-averaged A-II fields, as the averaging process will suppress any information which is not correlated to the reference signal, i.e. occurring at, f_{St}.

In order to confirm that the f_x region surrounding the cylinder is caused by the formation of vortices at this frequency, and is not simply due to the no-slip condition and the large amplitude cylinder motion, frequency maps were also calculated for the five response regions discussed in Chapter 3, and are shown in Figures 4.15(a-e). Sample phase-averaged vorticity fields, showing the dominant wake mode, are also included for reference (Figures 4.15(f-j)). The frequency maps indicate that, for all cases, there is a region near the cylinder at which the velocity fluctuations occur at the response frequency, f_x. However, it is only

during the first response branch (i.e. R2 and R3, Figures 4.15(b) and 4.15(c), respectively) that this region extends a significant distance from the cylinder. In the absence of mode competition or the intermittent appearance of the S-I mode, the region in which the transverse velocity fluctuations occur at f_x does not extend more than $0.5D$ from the cylinder surface, confirming that the large region in which the fluctuations occur at the frequency of the cylinder motion at $U_r\mathrm{St}/f^* = 0.416$ (Figure 4.14) is attributable to the shedding of vortices at this frequency.

In Section 3.3 it was noted that during the first response branch, the downstream velocity fluctuations are not synchronised to the cylinder motion, i.e. lock-in is not occurring. This finding is counter-intuitive, as for transverse VIV, no significant vibrations are observed outside of lock-in. However, as the fluid forces acting on the cylinder will be controlled by the pressure and velocity fields in the near wake where the fluid and cylinder motion are synchronised, it is likely that the fluctuating drag will also occur at the response frequency. This will result in positive energy transfer to the structure, which may explain the presence of relatively large amplitude vibrations in the *apparent* absence of lock-in.

The spatial dependence of the frequency of velocity fluctuations in the wake is also likely to be the cause of the conflicting reports in the literature regarding the vortex shedding frequency during the first response branch. Jauvtis and Williamson [2003] used measurements of the fluid forces to estimate the shedding frequency; as stated, the force information will relate primarily to the near wake or f_x region before vortex rearrangement has occurred. Consequently, their study found lock-in to occur during the first branch. Meanwhile, Okajima et al. [2003] based their estimates on velocity fluctuations in the far wake, six diam-

eters downstream of the cylinder, well beyond the point at which the vortices have rearranged; at this location the transverse velocity fluctuations have been shown to occur at the Strouhal frequency. As a result, their study found no sign of lock-in in this region. Aguirre [1977] estimated the shedding frequency using a stopwatch and counting the number of vortices shed; however, the subjective nature of the measurements makes it difficult to predict how his results would be affected by the wake rearrangement.

It is clear that the appearance of lock-in is, in some cases, dependent on the method used to estimate the vortex shedding frequency. If the shedding frequency is to be estimated based on one (or more) points in the wake (as is typical in LDA and hot-wire studies) the final estimation will depend on the choice of measurement site(s). This is particularly true for the first response branch, and other cases in which vortex rearrangement is likely, such as in the wakes of structures undergoing forced motion. While lock-in is generally presented as an objective, discrete phenomenon (i.e. lock-in is said to be clearly present or clearly absent), for some cases its manifestation might be more complex. In practice, its appearance may depend on the method by which the shedding frequency is estimated, and thus the comparison of various experimental studies may not be straightforward.

The results presented here highlight the role of the flow behaviour in the near wake, as opposed to the downstream wake structure, in determining the appearance of lock-in and the fluid forcing associated with vortex shedding, which is of importance to both the streamwise and general case of VIV.

4.7 Effect of Re on Mode-Switching

As detailed in Section 4.1, PIV measurements of the cylinder motion and the wake throughout the response regime were also carried out for a slightly higher Reynolds number range, Re = 750 − 5400, which had an increased spatial and temporal resolution, as outlined in Sections 2.4 and 4.1. By comparing these results to those presented in the preceding sections, the effects of Reynolds number upon the mode-switching behaviour in this region can be examined. As the S-I mode is induced by the streamwise motion of the cylinder [Naudascher, 1987; Ongoren and Rockwell, 1988], and the Reynolds number affects the amplitude of the cylinder response [Blevins and Coughran, 2009], it is reasonable to expect the region over which the S-I mode dominates to be affected.

The cylinder amplitude response for both sets of measurements are compared in Figure 4.16(a). Both response regimes align reasonably well. The differences in A/D measured in the low amplitude region at $U_r\mathrm{St}/f^* \approx 0.5$ and the second branch are discussed in Chapter 5. Within the first branch, the peak amplitude is slightly greater for the higher Reynolds number case, which is likely to be associated with the lower structural damping present in this experiment, as detailed in Table 2.1. One notable difference between the two response regimes measured is that for the higher Re case, the onset of the first response branch occurs at a lower reduced velocity, $U_r\mathrm{St}/f^* \approx 0.25$, compared to $U_r\mathrm{St}/f^* \approx 0.32$ for the lower Re case. Dickins [1976] and King [1974] did not observe VIV in the streamwise direction for Re < 1000 and 750, respectively, suggesting that there is a critical Reynolds number required for excitation due to the S-I mode. Figure 4.16(b) shows the variation in the cylinder response amplitude for both sets of measure-

ments as a function of Reynolds number. For both cases, the onset of the first response branch occurs at approximately Re $= 1200 - 1400$, despite differences in the actual reduced velocity, supporting the idea of a critical Re for excitation due to the S-I mode. While the critical Reynolds number appears to be approximately 1000, its exact value may be affected by other experimental parameters such as freestream conditions, blockage ratio etc. This Reynolds number effect is capable of altering the extent of the first branch considerably, and implies that the reduced velocity ranges over which the various response regions described in Chapter 3 will also depend on Re.

It is clear that the S-I mode is strongly affected by the Reynolds number. Therefore, it is likely that the mode-switching behaviour observed in the first branch will also be affected by Re. In order to study these effects, the velocity fields acquired at a higher Reynolds number range at $U_r\mathrm{St}/f^* = 0.404$ (Re $=$ 2630), were analysed using POD, and the mode detection criterion was applied. As in the low Re case, the first two POD modes were found to correspond to the A-II mode and fluctuated at the Strouhal frequency, while the third and fourth modes corresponded to the S-I wake and fluctuated at the cylinder response frequency. Using the mode detection criterion given by equations 4.1 and 4.2, the S-I and A-II modes were identified and averaged separately. The phase-averaged vorticity fields for both modes are shown in Figure 4.17. As in the lower Re case, the transverse velocity measured at $(x/D, y/D) = (1, 0.5)$ was used as a reference signal. The mode-detection criterion is again able to extract the symmetric and alternate arrangements of the S-I and A-II modes, respectively.

A sample of the amplitude of the POD modes corresponding to the A-II and S-I modes is shown in Figure 4.18. As in the case measured at Re $= 1800$ (Figure

4.6), the amplitude of the POD modes relating to the S-I structure does not vary significantly, while there are large scale fluctuations in the amplitude of the modes corresponding to the A-II mode, indicating again that the mode competition arises from the intermittent disruption of the alternate shedding pattern.

Table 4.4: Percentage of PIV fields which the mode-detection criterion determined to be dominated by the S-I and A-II modes, for two values of Reynolds number and reduced velocity.

Re	$U_r\mathrm{St}/f^*$	Probability of S-I	Probability of A-II
1800	0.416	8.7%	92.0%
2630	0.404	15.7%	84.3%

Table 4.4 lists the probability of occurrence of each wake mode for the sets of data measured at high and low Reynolds number. The probability of the appearance of the S-I mode has risen from approximately 8% at Re = 1800, to over 15.7% at Re = 2630. It appears that for the higher Re case, the amplitude of the first two POD modes has a greater tendency to drop off, i.e. the alternate shedding structure is more likely to become disrupted and the S-I mode more likely to dominate. This suggests that as well as affecting the reduced velocity range over which the S-I mode is dominant, the Reynolds number also affects the probability of this mode occurring for reduced velocities at which the A-II mode is dominant.

4.8 Effect of Reduced Velocity Upon Switching

The PIV measurements discussed in the previous section contained a large number of fields at each reduced velocity; it was thus possible to analyse each data set using POD. This allowed the mode-detection criterion to be applied to each set, and the dependence of the mode competition on the reduced velocity to be examined. While the pairing relationship between the first two modes and the alternate wake mode was present for all data sets examined, the relation between a POD mode-pair and the S-I mode was only observed for $U_r\mathrm{St}/f^* = 0.307 - 0.473$. The vorticity distributions calculated for the POD modes associated with S-I and A-II wake modes are shown in Figure 4.19. For brevity only one mode of each POD mode-pair is shown.

Even when the S-I mode was found to dominate ($U_r\mathrm{St}/f^* = 0.253 - 0.355$), the first two POD modes corresponded to the alternate shedding structure. Apparently, at these points, the fluctuating energy associated with the breakdown of the wake into an alternate structure is greater than that caused by the initial symmetric shedding pattern. It is also notable that despite the S-I mode appearing consistently in the instantaneous PIV fields acquired at $U_r\mathrm{St}/f^* = 0.253$, no POD mode-pair was found to completely capturing this shedding mode. Rather, features of the symmetric wake structure appeared in several POD modes, which occurred at a range of frequencies. This also serves as a reminder that the individual pairs of POD modes are not constrained to represent physical phenomena, and care must be taken when attempting to interpret them.

For the data sets in which the POD mode pairing was observed for both the S-I and A-II wake modes, the mode-detection criterion was applied, and the

percentage of fields which were found to exhibit the S-I mode could be calculated, as shown in Figure 4.20 as a function of reduced velocity. The S-I mode is apparent in the highest proportion of PIV fields in the range $U_r\mathrm{St}/f^* \approx 0.3-0.36$, which is the same range in which this wake mode was found to dominate in Chapter 3 and in the experiments of Ongoren and Rockwell [1988]. The green square point at $U_r\mathrm{St}/f^* = 0.416$ represents the percentage of fields in which the S-I mode was said to be dominant for the PIV measurements discussed in Sections 4.2 - 4.6 for Re = 1800. As noted in the previous section, the tendency for the S-I mode to dominate was found to be greater for the measurements performed at higher Reynolds numbers. It appears that throughout the first response branch the S-I and A-II modes compete in an unsteady manner which is dependent on both the reduced velocity and Reynolds number.

These results highlight the complexity of the distribution of wake modes during the first response branch. Rather than the symmetric shedding mode simply occurring for the entirety of the branch, as is commonly assumed [Jauvtis and Williamson, 2003; Okajima et al., 2003], the wake exhibits both the A-II and S-I modes intermittently, with the instantaneous mode being dependent on the reduced velocity and Reynolds number, as well as varying spatially throughout the wake. As the S-I mode induces zero fluctuating and mean lift acting upon the cylinder, while the A-II mode can cause strong forces in this direction [Cetiner and Rockwell, 2001], the tendency for the wake to switch between the two modes may have significant consequences for cylinders which are free to move in both the streamwise and transverse directions, although further work would be required to confirm that such switching would occur in the 2DOF case.

4.9 Closure

The transient variation in the dominant wake mode in the first response branch was examined for two Reynolds number ranges. PIV measurements of the velocity field in the wake were examined using POD and a criterion was developed which could determine the presence of either the A-II or the S-I mode in a given instantaneous field. The method was used to estimate phase-averaged vorticity fields for both modes at $U_r\mathrm{St}/f^* = 0.416$ using the same reference signal; the ability of the criterion to detect such distinct phase-averaged quantities was used to demonstrate the effectiveness and robustness of the approach. The A-II mode was found to be the dominant mode at this reduced velocity, occurring in over 92% of the instantanteous fields. The appearance of either mode was not found to have a statistically significant effect on the amplitude response of the cylinder.

Analysis of the temporal coefficients of the POD modes which corresponded to the A-II and S-I wake modes indicated that the mode switching was caused by the breakdown of the A-II mode; when the response amplitude was large (i.e. in the first branch) the structural motion induced a vorticity field component similar to the S-I mode which was capable of dominating when the alternate shedding pattern was disrupted. However, pre-lock-in, the disruption of the A-II mode was not associated with the appearance of the S-I mode as the response amplitude of the cylinder was too low.

The velocity fields in which the S-I mode was dominant were found to correspond to a large recirculation region and weak transverse velocity fluctuations across the wake centreline compared to the A-II mode. This finding is consistent with the velocity profiles presented for the response regions, R2 and R3 in Chap-

ter 3 when the same mode dominated. The A-II mode was associated with an increase in the strength of the shed vortices compared to the S-I mode. However, when the vortex strength was scaled by the shedding frequency, the circulation of the vortices shed in both modes was very similar. This supports the observation discussed in Chapter 3 that the shedding frequency controls the strength of the vortices.

It was found that in the first response branch the transverse velocity fluctuations over a significant region of the near wake occurred at the response frequency, while downstream they occurred at f_{St}. This spatial dependence of the frequency of the velocity fluctuations was used to explain the paradoxical appearance of VIV in the *apparent* absence of lock-in, as well as the cause of some of the conflicting results in the literature regarding the presence of lock-in in the region of the response regime. It was found that the Reynolds number had a significant effect on the wake mode. The S-I mode and the first response branch were not observed for Re $\lesssim$ 1000, while the measurements performed throughout the first branch indicated that the S-I mode occurred in a greater proportion of the instantaneous velocity fields when the Reynolds number was larger. The probability of the occurrence of the S-I mode was highest in the range $U_r\mathrm{St}/f^* \sim 0.3 - 0.36$, which was consistent with the point in the response regime presented in Chapter 3 at which this mode dominated.

4.10 Figures

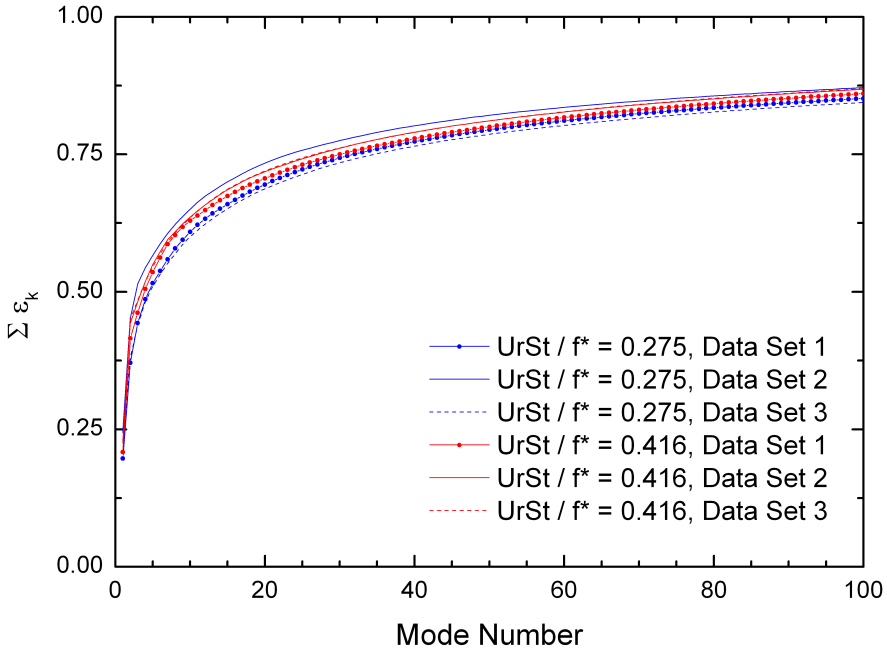

Figure 4.1: Cumulative fluctuating kinetic energy of the POD modes computed for the three data sets acquired at $U_r\mathrm{St}/f^* = 0.275$ and 0.416. Only the values for the first 100 modes are shown. The normalised fluctuating energy kinetic, ε_k, is given by the mode's corresponding eigenvalue, divided by the total sum of all the eigenvalues within that data set.

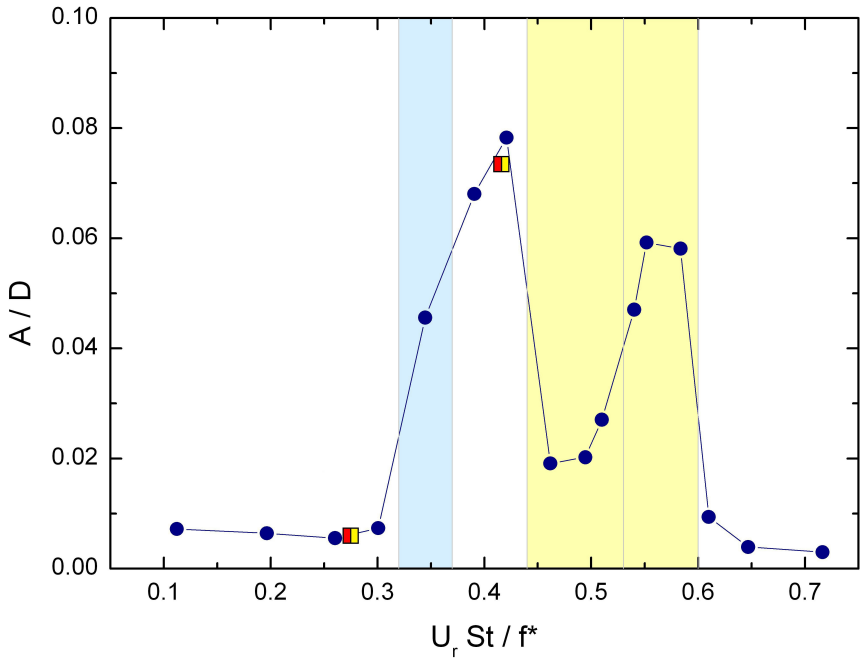

Figure 4.2: Cylinder amplitude response, as described in Section 3.3. The blue and yellow shaded regions indicate the reduced velocity ranges over which the S-I and SA modes were found to dominate, respectively, while the wake predominantly exhibited the A-II shedding mode in the white regions. The red and yellow squares denote the amplitude response for the extended PIV measurements discussed in this chapter.

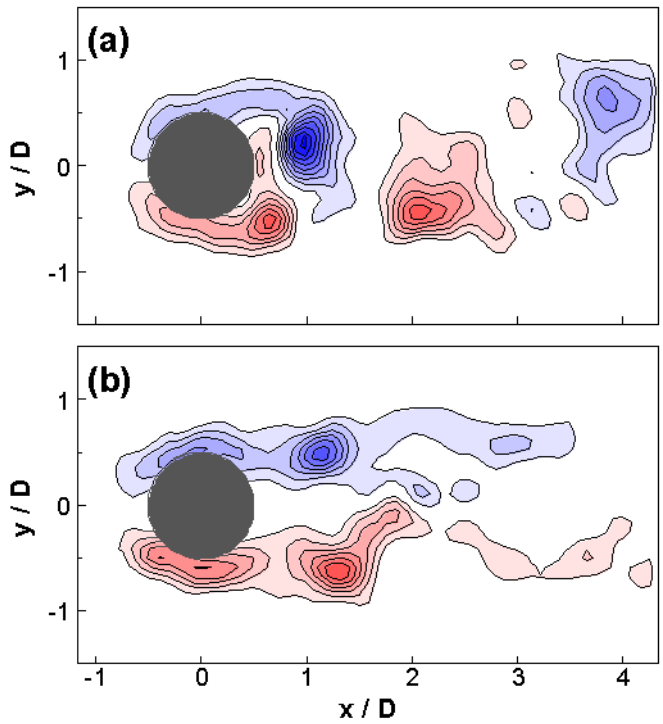

Figure 4.3: Instantaneous vorticity fields acquired 0.5s apart, at $U_r \mathrm{St}/f^* = 0.416$. The A-II mode is clear in (a), while the symmetric shedding (S-I) mode is dominant in (b). Contour levels for each case are $\omega_z D/U_0 = \pm 1, \pm 2, \ldots$

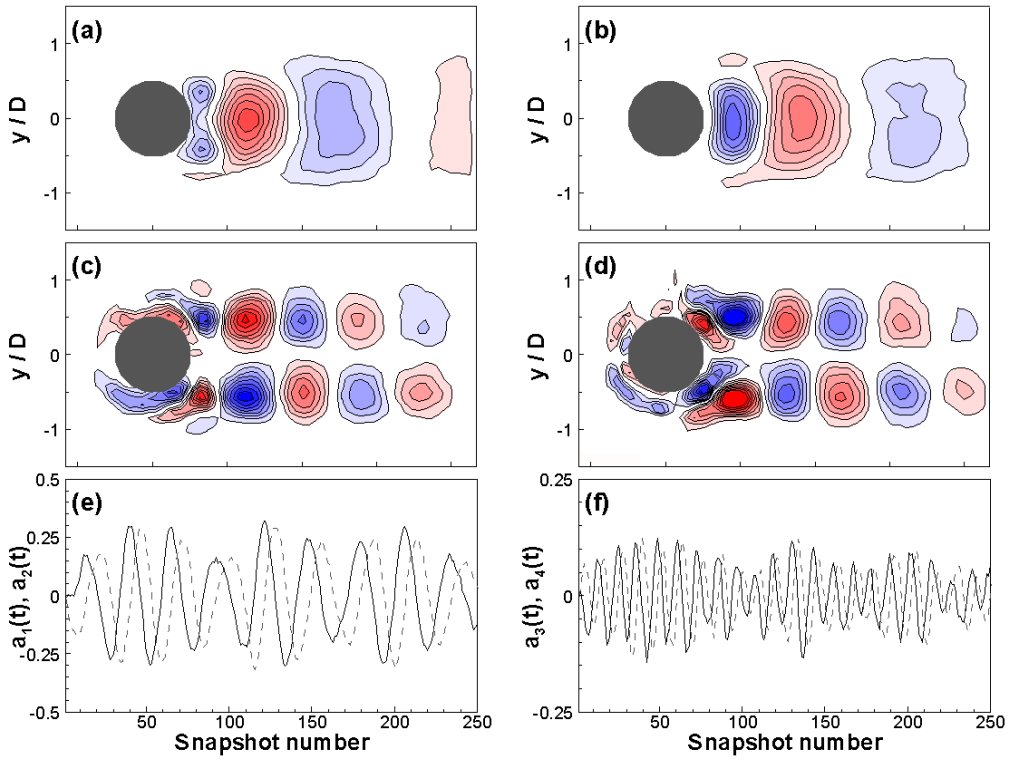

Figure 4.4: Vorticity distributions calculated from the velocity fields of the POD modes 1 to 4 (a-d). The vorticity fields in (a) and (b) are clearly symmetric, as is the case with the A-II mode, while the fields in (c) and (d) exhibit anti-symmetry, as is characteristic of the S-I mode. Contour levels are arbitrary. The spectra of the temporal coefficients of modes 1 and 2 are shown in (e), and those of modes 3 and 4 are shown in (f).

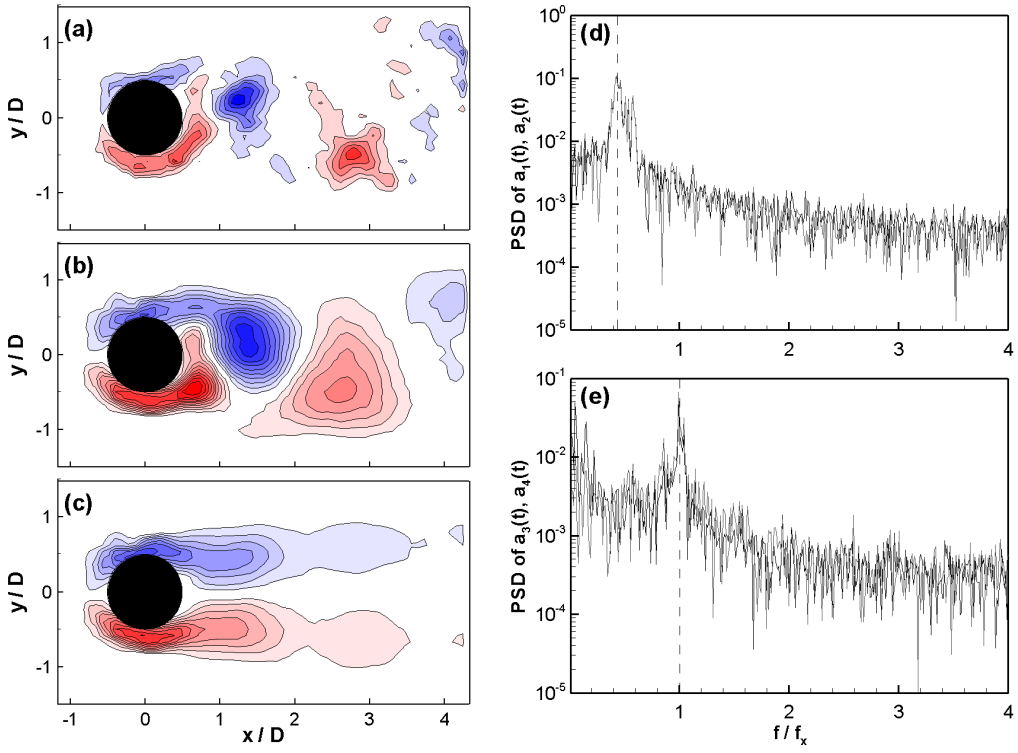

Figure 4.5: (a) Instantaneous vorticity field. (b) Vorticity distribution for same PIV snapshot shown in (a), reconstructed using mean velocity field and POD modes 1 and 2 only. The wake resembles the alternate shedding of the A-II mode. (c) Vorticity distribution of same snapshot shown in (a), now reconstructed using modes 3 and 4 only. Contour levels for each case are $\omega_z D/U_0 = \pm 1.5, \pm 3, \ldots$ The symmetric shedding (S-I) mode is clearly captured. (d-e) Power spectra of temporal coefficient of POD modes 1 - 4. The dashed lines in (d) indicates the Strouhal frequency, while that in (e) denotes the cylinder response frequency.

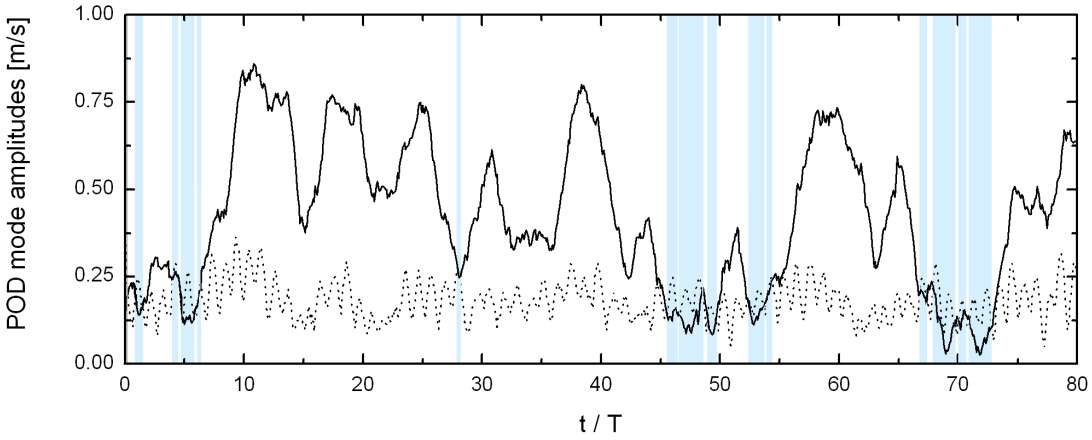

Figure 4.6: Combined amplitude of the temporal coefficients for the POD modes which relate to the A-II, ($|\mathcal{H}(a_1)| + |\mathcal{H}(a_2)|$, solid line) and S-I ($|\mathcal{H}(a_3)| + |\mathcal{H}(a_4)|$, dashed line) wake modes. The shaded regions indicate the times at which the criterion described above predicts the S-I mode to be dominant.

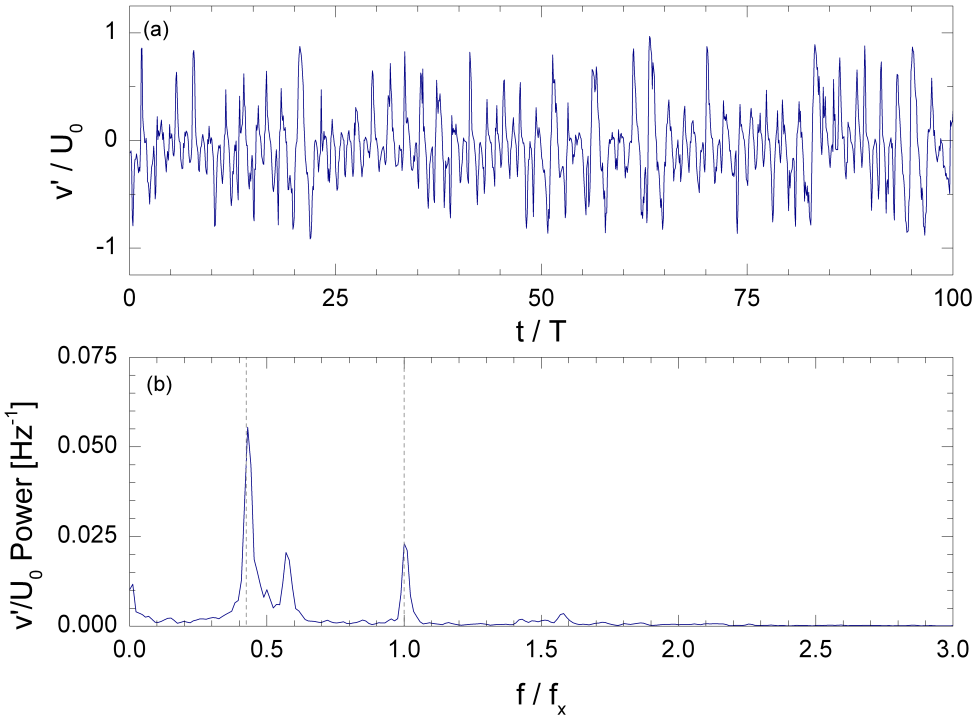

Figure 4.7: Sample of the time series (a) and the power spectrum (b) of the transverse velocity signal measured at $(x/D, y/D) = (1, 0.5)$, at $U_r\mathrm{St}/f^* = 0.416$. The dashed lines denote the Strouhal and cylinder response frequencies.

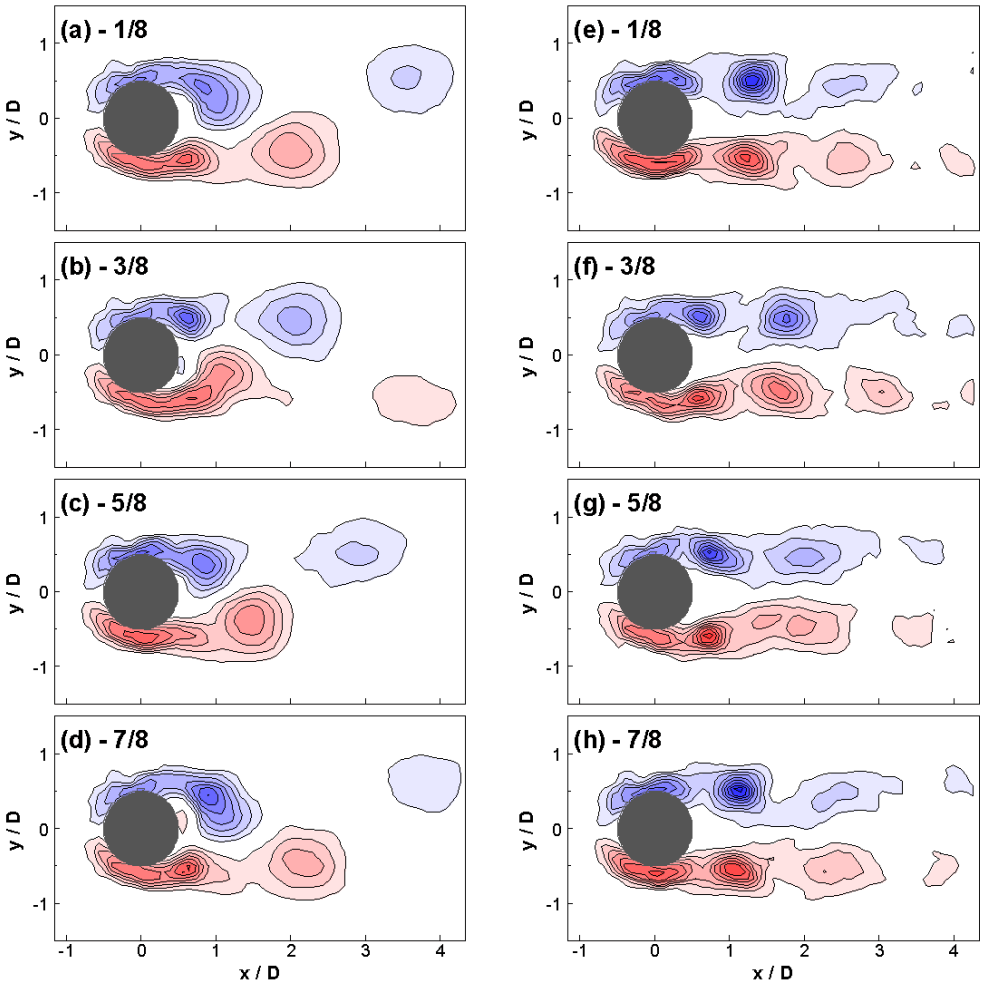

Figure 4.8: Vorticity distributions, calculated from phase-averaged velocity fields, for modes A-II (a-d) and S-I (e-h) (identified using the proposed mode detection criterion), at $U_r \mathrm{St}/f^* = 0.416$. Contour levels are $\omega_z D/U_0 = \pm 0.75, \pm 1.5, \ldots$

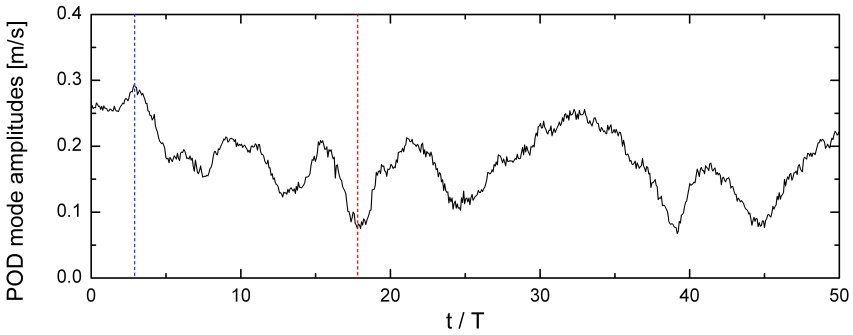

Figure 4.9: Combined amplitude of the temporal coefficients for the POD modes which relate to the A-II (solid line) wake mode, computed for $U_r\mathrm{St}/f^* = 0.275$. The dashed blue and red lines denote the times at which the instantaneous vorticity fields shown in Figure 4.10(a) and (b), respectively, were acquired.

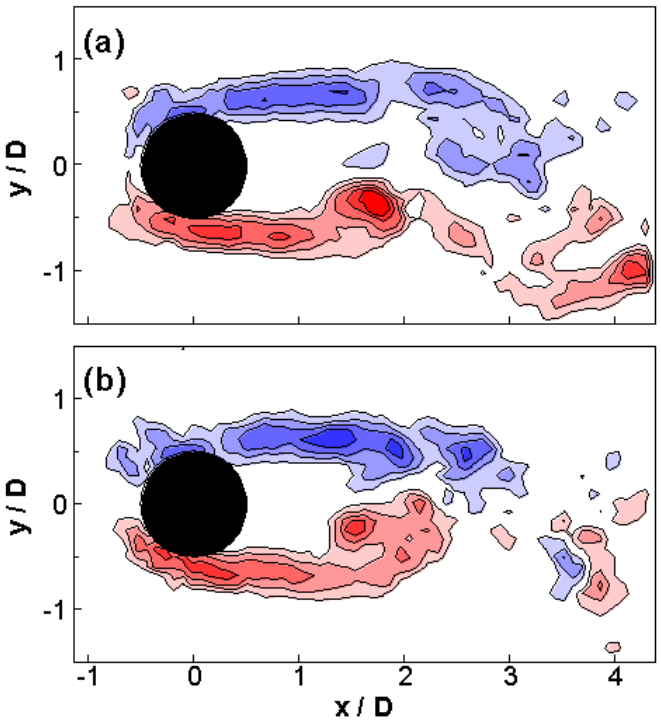

Figure 4.10: Instantaneous vorticity fields acquired at $U_r\mathrm{St}/f^* = 0.275$, at time intervals at which the combined amplitude of the POD modes associated with alternate vortex-shedding is comparatively large (a) and low (b). The magnitude of the POD modes is shown in Figure 4.9. Contour levels are $\omega_z D/U_0 = \pm 0.75, \pm 1.5, \ldots$

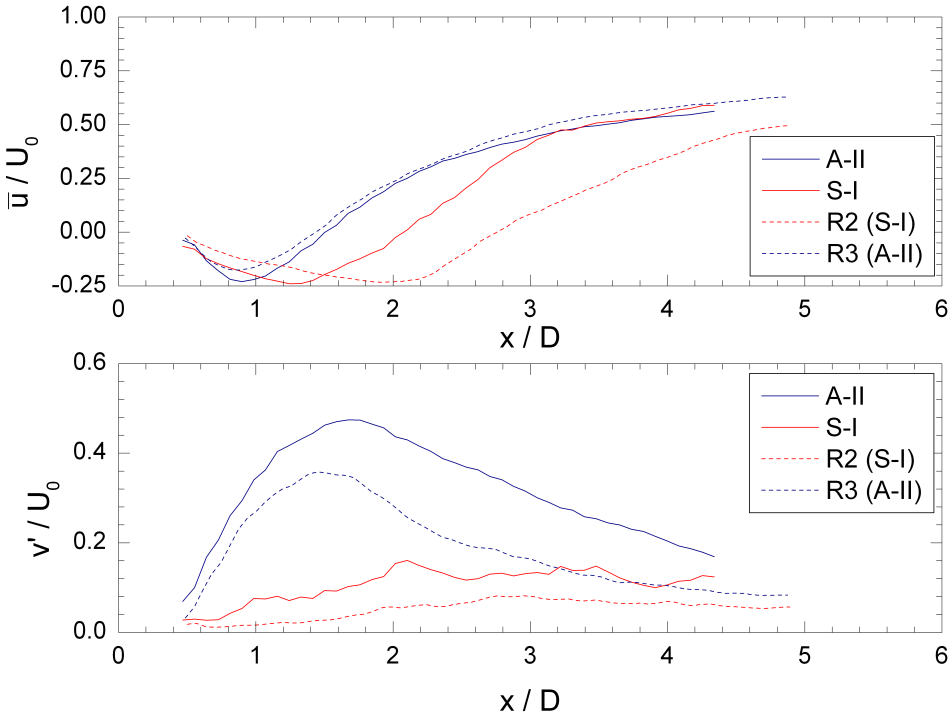

Figure 4.11: Distributions of the mean streamwise velocity (a) and fluctuating transverse velocity (b) along the wake centreline for the fields in which the wake was determined to be exhibiting the S-I (blue circles) and A-II (red squares) modes, as well as the profiles computed for R2 (blue line) and R3 (red line). R2 is associated with the S-I mode, while the A-II mode dominates for R3.

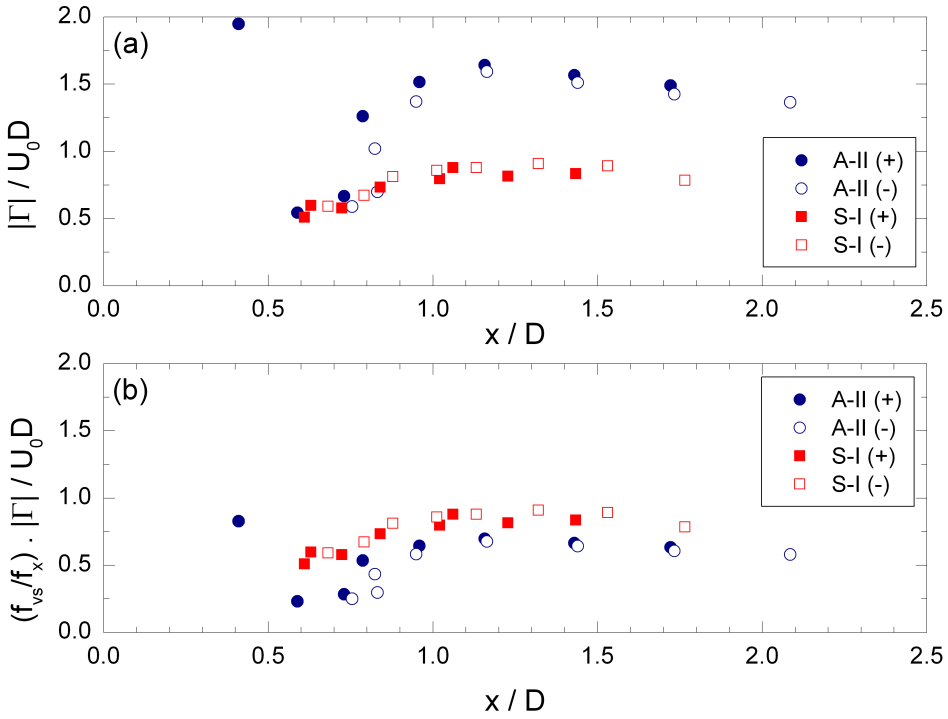

Figure 4.12: Variation of the peak vortex strength with streamwise position of the vortex core throughout the A-II and S-I wake cycles (a), and the variation in the vortex strength scaled by the normalised vortex shedding frequency (b). The strengths were estimated from phase-averaged fields calcalated at $U_r\mathrm{St}/f^* = 0.416$ using the mode-detection criterion outlined in Section 4.2.

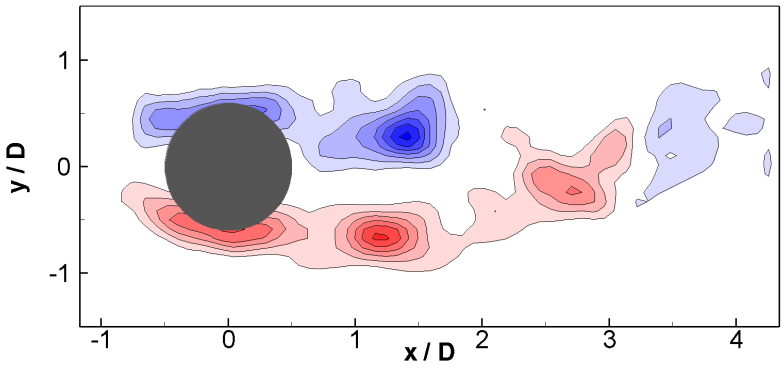

Figure 4.13: An instantaneous vorticity field demonstrating the breakdown of the S-I mode into an alternate structure downstream. Two vortices close to the cylinder are arranged symmetrically, but this symmetry has decayed by $x/D \approx 3$. Contour levels are $\omega_z D/U_0 = \pm 1, \pm 2, \ldots$

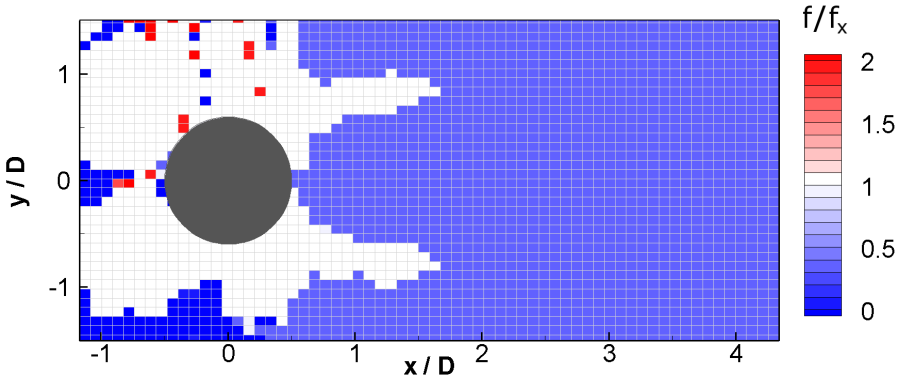

Figure 4.14: Distribution of dominant frequency of velocity fluctuations throughout the wake for $U_r \mathrm{St}/f^* = 0.416$. Frequencies are normalised with respect to the cylinder response frequency. The white regions indicate the areas in which the velocity fluctuations are synchronised to the cylinder response frequency. The resolution of the spectra used to estimate the distributions was 0.39Hz, i.e. $0.023 f_x$.

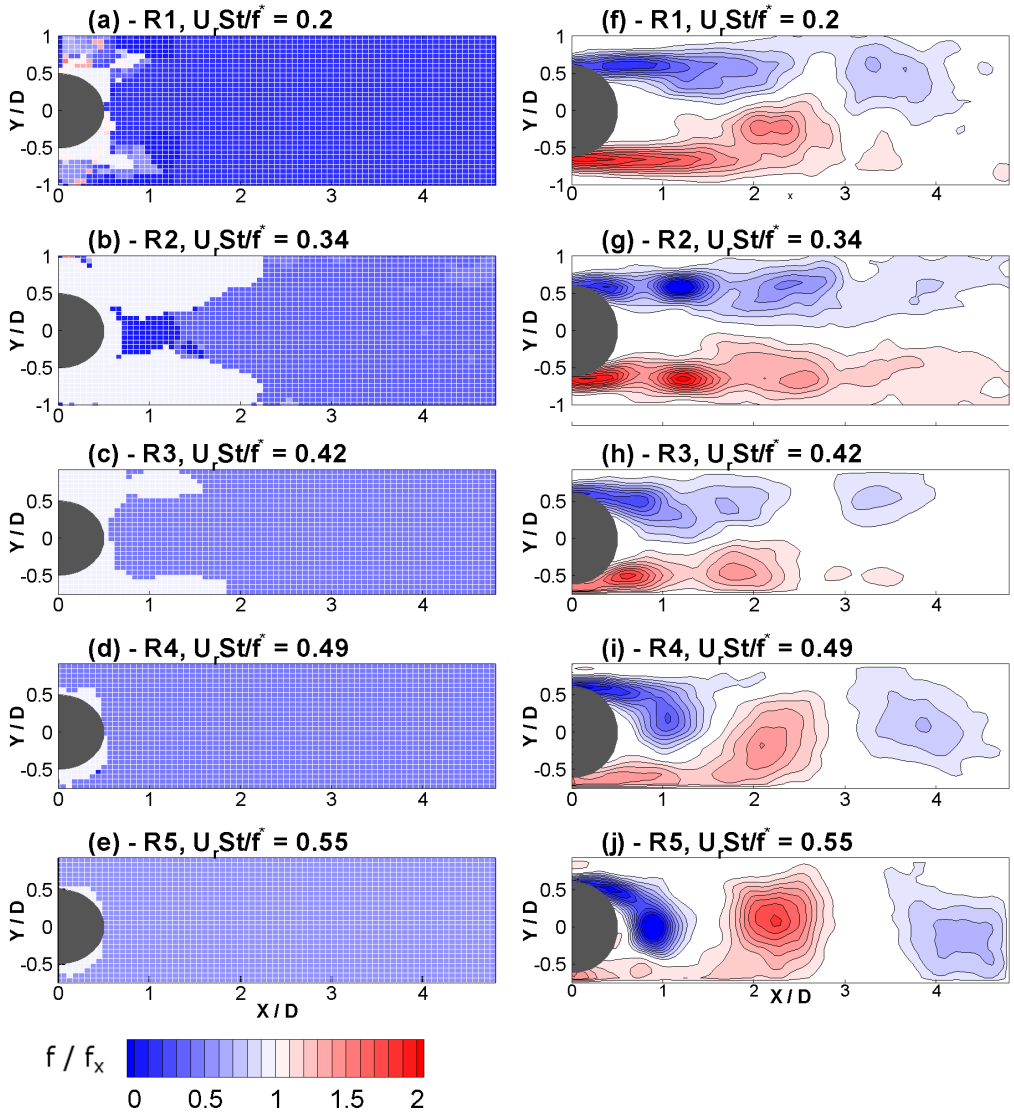

Figure 4.15: Distribution of the dominant frequency of velocity fluctuations throughout the wake for response regions R1-R5 (a-e). Frequencies are normalised with respect to the cylinder response frequency in each response region. The white regions indicate the areas in which the velocity fluctuations are synchronised to the cylinder response frequency, f_x. The resolution of the spectra used to estimate the distributions was 0.39Hz. Sample phase-averaged vorticity fields are shown in (f-i) for reference. Contour levels in (f-j) are $\omega_z D/U_0 = \pm 0.5, \pm 1, \ldots$

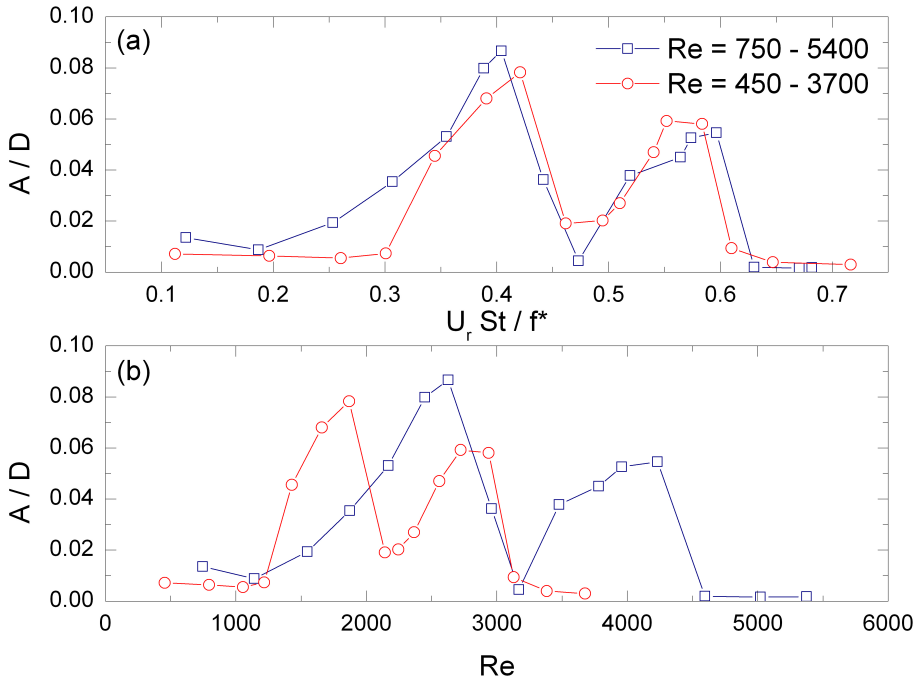

Figure 4.16: Cylinder amplitude response as a function of reduced velocity (a) and Reynolds number (b). Closed symbols indicate reduced velocities at which the S-I mode was either dominant or observed intermittently.

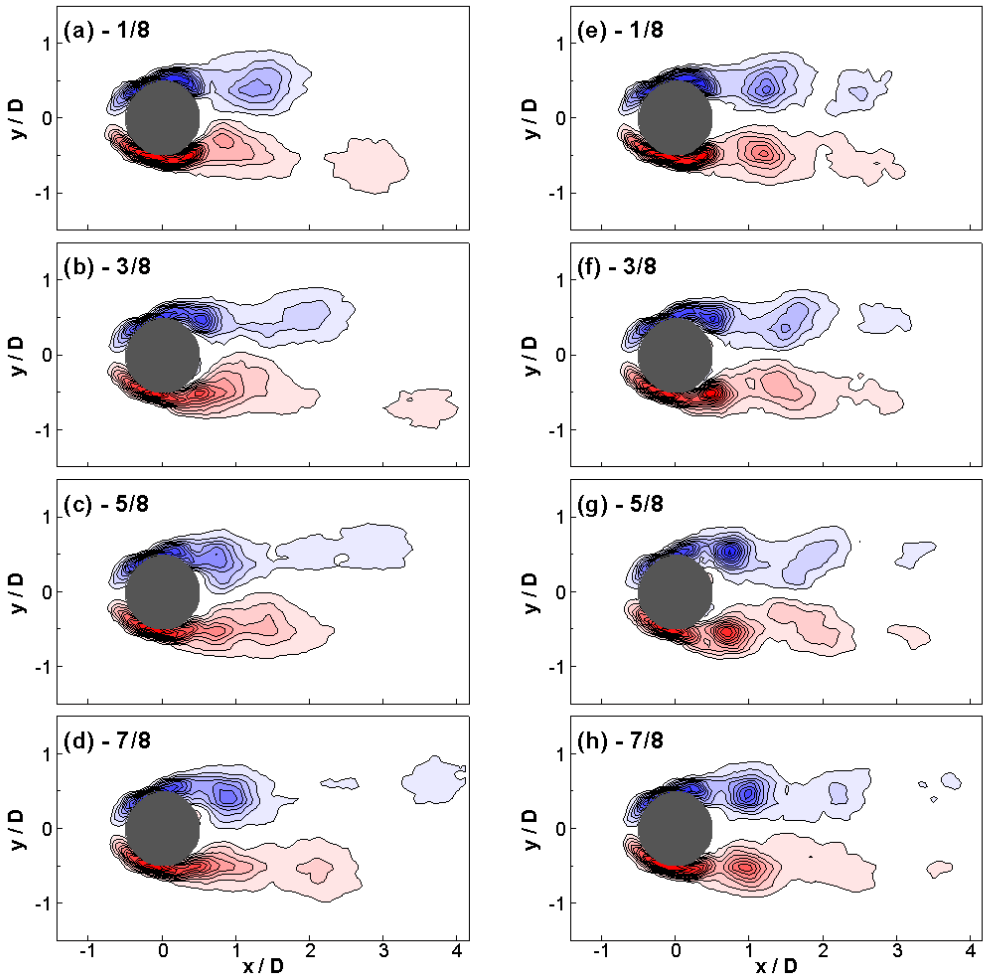

Figure 4.17: Vorticity distributions, calculated from phase-averaged velocity fields acquired at Re = 2630, $U_r \mathrm{St}/f^* = 0.404$, for modes A-II (a-d) and S-I (e-h), which were identified using the mode detection criterion proposed in Section 4.2. Contour levels are $\omega_z D/U_0 = \pm 0.75, \pm 1.5, \ldots$

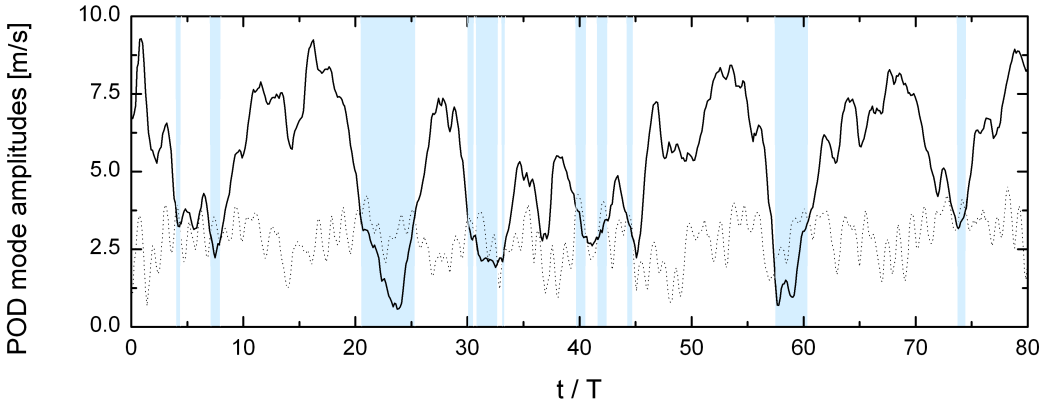

Figure 4.18: Samples of the combined amplitude of signals relating to the A-II (solid line) and S-I modes (dashed line), for the PIV measurements acquired at $\mathrm{Re} = 2630$, $U_r \mathrm{St}/f^* = 0.404$. The shaded regions indicate the times at which the criterion described above predicts the S-I mode to be dominant.

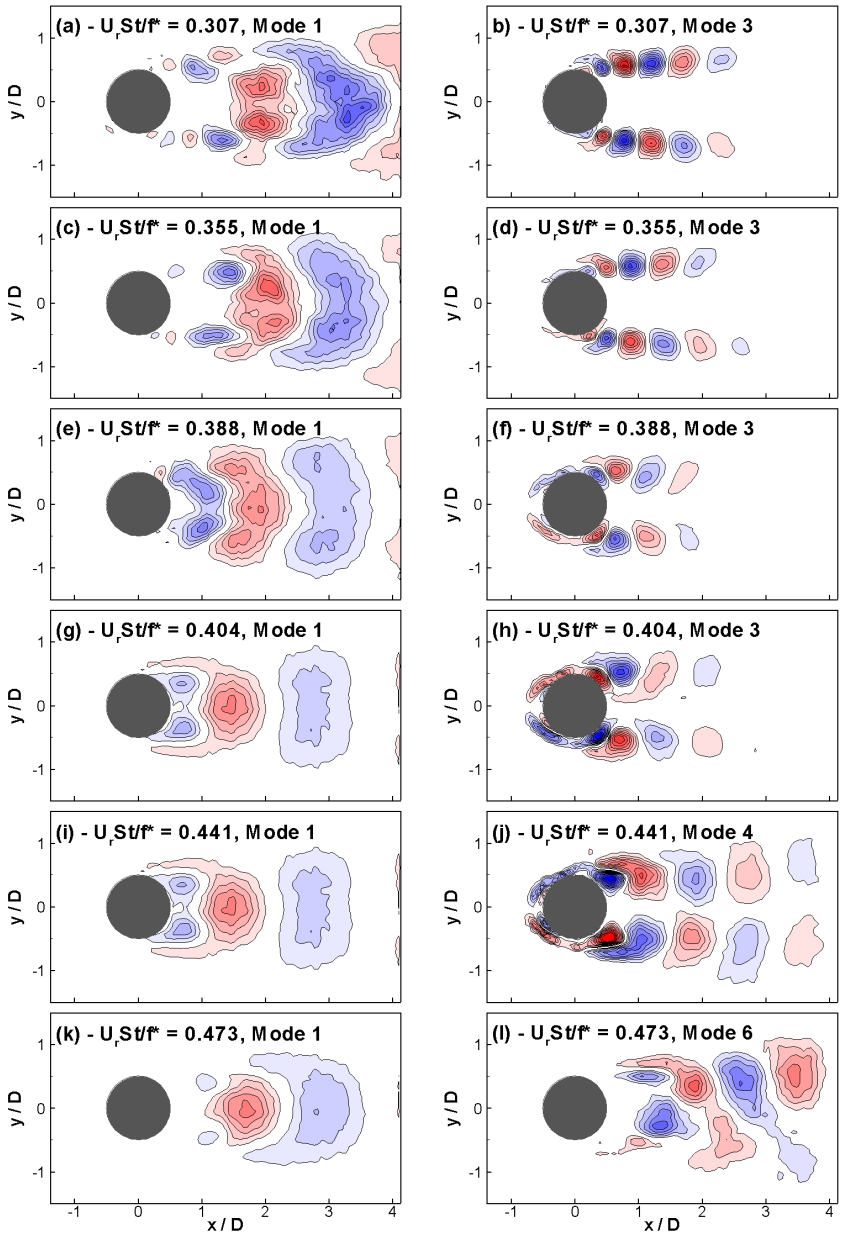

Figure 4.19: Vorticity distribution of the first POD-mode associated with the A-II mode (left column) and S-I mode (right column). Scales are arbitrary.

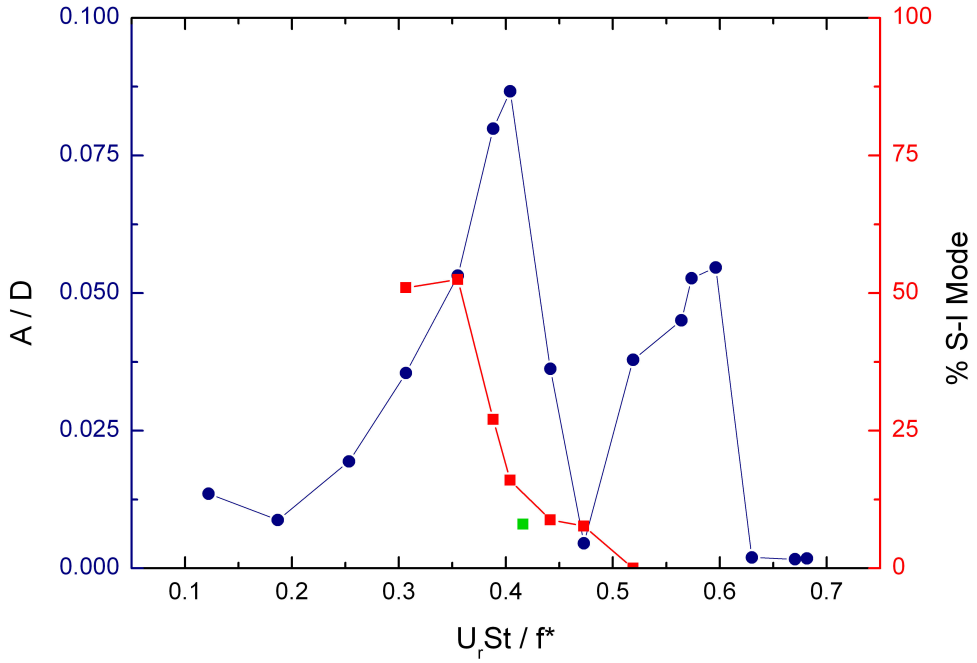

Figure 4.20: Cylinder amplitude response (blue circles) and percentage of the PIV fields in which the S-I mode was found to dominate (red squares). The green square denotes the percentage of fields in which the S-I modes dominated for Re = 1800.

Chapter 5

Mode Competition in the Second Branch[1]

5.1 Introduction

The wake modes which occur behind a cylinder free to move in the streamwise direction have been described in Chapter 3. The SA, A-II and S-I modes have been shown to dominate at various regions of the response regime, with the latter two modes competing in an unsteady manner throughout much of the first branch (Chapter 4). In general, the distribution of modes presented in the previous chapters agrees with the results of various studies in the literature. However, the A-IV mode has also been observed in the forced oscillation studies of Nishihara et al. [2005], Ongoren and Rockwell [1988] and Konstantinidis et al. [2007] within

[1]The results in this chapter have also been presented/published in:

N. Cagney and S. Balabani. Multiple manifestations of the second response branch in streamwise vortex-induced vibrations. (Submitted to *Physics of Fluids*.)

similar ranges of reduced velocity and oscillation amplitude, but was not observed in the results presented in Chapter 3, nor in the free vibration studies of Aguirre [1977]; Jauvtis and Williamson [2003] and Okajima et al. [2003].

The experiments discussed in the previous chapter were performed by incrementally increasing the reduced velocity throughout the response regime. However, no results were presented for the case of *decreasing* reduced velocity. Aguirre [1977] observed that the extent of the second branch varied depending on whether the reduced velocity was increasing or decreasing, i.e. the system exhibited hysteretic behaviour in this region.

In order to investigate the extent to which the amplitude response and wake modes of the current system are affected by hysteresis, and the conditions under which the A-IV mode may occur, additional sets of PIV measurements were acquired in which the reduced velocity was incrementally increased and decreased. These experiments were performed as part of Test Stage 2, as described in Chapter 2. The reduced velocity was varied between 0.122 and 0.682, which corresponded to a Reynolds number range of $\mathrm{Re} = 740 - 5400$. This is higher than that of the experiments described in Chapter 3 ($\mathrm{Re} = 450 - 3700$), and is thought to be the cause of some minor discrepancies between the two sets of data, which will be discussed throughout this chapter.

5.2 Hysteresis

Prior to performing detailed PIV measurements of the response regime using the current cylinder system, the amplitude response was measured for the cases of increasing and decreasing reduced velocity in order to ascertain the extent

to which the response regime is affected by hysteresis. The flowrate was first incrementally increased and then decreased, such that the reduced velocity varied between $U_r\mathrm{St}/f^* = 0.056$ and 0.766. At each flowrate 1000 images of the vibrating cylinder were acquired at 150Hz. A settling time of approximately three minutes was employed between changing the flowrate and acquiring the images. This is considerably lower than that used when acquiring the PIV measurements, for which a settling time of at least 10 minutes was employed. However, as the purpose of these experiments was only to identify regions of the response regime which are affected by hysteresis, the effects of the relatively short settling time were not considered to be significant.

The cylinder amplitude response for both cases (i.e. increasing and decreasing reduced velocity) are compared in Figure 5.1. The second branch measured for the two cases shows marked differences, both in terms of the peak amplitude response and the reduced velocity range over which it occurs. As the reduced velocity is decreased, the second branch occurs only in a narrow region of $U_r\mathrm{St}/f^* \approx 0.55 - 0.57$. However, when the reduced velocity is increased, the extent of the second branch is larger and the peak amplitude response is greater.

It is clear that the second response branch is strongly affected by hysteresis. Figure 5.1 indicates that the cylinder system is apparently capable of exhibiting various vibration amplitudes for the same values of reduced velocity and Reynolds number. In the following sections, this behaviour is investigated, focusing on the wake modes which dominate at the various levels of cylinder response amplitude in this region.

5.3 Amplitude Response and Wake Modes in the Higher Re Range

Following the preliminary investigation into the effects of hysteresis on the cylinder response regime, the wake and cylinder amplitude response were measured throughout the response regime using PIV for both increasing and decreasing reduced velocity, using the experimental procedure outlined in Section 2.4 (Test Stage 2). As noted in Section 4.7, the natural frequency of the cylinder system was larger than that used in the measurements described in Chapter 3. This meant that for approximately the same reduced velocity range, the Reynolds number range was higher. The current measurements were performed for $\mathrm{Re} = 740 - 5400$ (Test Stage 2), while the results presented in Chapter 3 were performed at $\mathrm{Re} = 450 - 3700$ (Test Stage 1). This change in the Reynolds number range is likely to have an effect on the cylinder response and wake characteristics observed. Therefore, before discussing the results of the current set of PIV measurements in terms of the hysteretic behaviour, the measured response regime is first compared to that presented in Chapter 3, for the lower Re range. Such a comparison was also presented in Section 4.7. However, in this section the comparison focuses on the low amplitude near $U_r\mathrm{St}/f^* \approx 0.47$ and the second response branch, as opposed to the mode competition between the S-I and A-II modes which occurs at lower reduced velocities.

Figure 5.2 compares the cylinder amplitude response and the correspond peak frequency of velocity fluctuations measured at $(x/D, y/D) = (3, 0.5)$ for Test Stages 1 and 2. The symbol colour indicates the wake mode which dominated at each reduced velocity. Symbols with two colours denote regions where mode

competition was observed. The white, yellow and blue symbols correspond to the A-II, SA and S-I modes, respectively, while the green points indicate the reduced velocities at which the wake exhibited the A-IV mode, in which two pairs of counter-rotating vortices were shed per wake cycle (Figure 1.4). In general the amplitude response measured in both cases are qualitatively similar. However, some differences are present in three regions:

(i) In Test Stage 2 (higher Re) the first branch occurs over the range $U_r\mathrm{St}/f^* \approx 0.25 - 0.45$, while in Test Stage 1 the cylinder response is negligible for $U_r\mathrm{St}/f^* \leq 0.3$.

(ii) The minimum amplitude response measured in the region between the first and second branches is smaller in Test Stage 2. Furthermore, the A-II is dominant in the wake, not the SA mode which is observed in this region in Test Stage 1.

(iii) The A-IV mode is dominant for much of the second response branch in Test Stage 2, and the velocity fluctuations occur at $f_{vs}/f_x = 0.5$ and 1, while in Test Stage 1 the SA mode is observed and the velocity fluctuations occur only at $f_{vs}/f_x = 0.5$.

The cause of the difference in the reduced velocity range over which the first branch occurs has been discussed in Section 4.7.

The amplitude response of the cylinder in Test Stage 2 at $U_r\mathrm{St}/f^* = 0.47$ is $A/D = 0.005$, which is lower than that measured for the lower Re case. The reason for this is not immediately clear, and cannot be attributed to the different structural properties of the two systems; in both cases the cylinder had the same

mass ratio, while the damping ratio was *lower* in Test Stage 2. It might be possible that the absence of such a very low amplitude region near $U_r\mathrm{St}/f^* = 0.47$ observed in Test Stage 1 is simply due to the experimental methodology. Since the cylinder response amplitude cannot be measured in real-time, and the vibrations are too small to estimate by eye ($A/D = 0.02$ corresponds to vibrations of less than 0.15mm), it is possible that as the flowrate and reduced velocity were incrementally increased the minima of the low amplitude region was simply 'missed', i.e. PIV measurements were acquired at reduced velocities above and below - but not at - this point. However, preliminary measurements of the response regime for the low Re case (not presented here) did not indicate that the amplitude was reduced below $A/D \approx 0.02$ in this region. In contrast, a decrease in amplitude below $A/D < 0.01$ was observed for all sets of measurements performed at the higher Re range (i.e. for the two measurements of the response amplitude for increasing and decreasing reduced velocity shown in Figure 5.1 and the three sets of PIV measurements discussed in Section 5.6, Figure 5.10). Based on this observation, it seems unlikely that the cylinder response regime discussed in Chapter 3 contained a region where $A/D \lesssim 0.01$ near $U_r\mathrm{St}/f^* = 0.47$ which was simply 'missed' in the lower Re measurements.

The SA mode was found to dominate at reduced velocities *above and below* $U_r\mathrm{St}/f^* = 0.47$; i.e. in the range $U_r\mathrm{St}/f^* = 0.46 - 0.495$, which contains the point at which the A-II mode was observed in the higher Re measurements. It is therefore reasonable to assume that the SA mode would also dominate at reduced velocities between these two values ($U_r\mathrm{St}/f^* = 0.46{-}0.495$) in the lower Re range. In this case, the difference between the two sets of PIV measurements cannot be attributed to the accidental omission of important measurements sites (i.e. in the

region $U_r\mathrm{St}/f^* = 0.47$). A more plausible explanation is that the wake mode, and consequently the amplitude response of the cylinder is affected by the Reynolds number, as was observed at the onset of the first response branch (Section 4.7).

The cylinder amplitude response measured for the lower Re case and that measured for various studies in the literature were shown in Figure 3.1. It is clear that the magnitude of the response amplitude between the two branches, as well as the reduced velocity range over which this occurs, are highly variable, and appear to be strongly affected by experimental conditions (Reynolds number, aspect ratio etc.). It is therefore plausible that the difference in the response amplitude measured in this region is due to the difference in the Reynolds number of the two sets of measurements.

The peak amplitude observed in the second response branch is slightly lower for the higher Re case. The variation in the dominant frequency of the velocity fluctuations, f_{vs}, measured at $(x/D, y/D) = (3, 0.5)$ (Figure 5.2(b)) indicates that there are also distinct changes in the wake. For the lower Re case, the fluctuations in the second branch occur consistently at $f_{vs}/f_x = 0.5$, while the measurements in the higher Re range indicate that the velocity signals in this region contain components at both $f_{vs}/f_x = 0.5$ and 1.

The variations in the dominant wake mode observed in both sets of measurements also show some differences. The most notable difference between the two sets of measurements is the presence of the A-IV mode for a substantial portion of the second branch $U_r\mathrm{St}/f^* \approx 0.54 - 0.6$, for the higher Re case. Two sample instantaneous vorticity fields showing the A-IV more are shown in Figure 5.3; a more detailed description of the wake mode will be presented in Section 5.5. In both fields in Figure 5.3 the wake is turbulent and the vorticity field is irregular;

however, vortex-pairs characteristic of the A-IV mode are clearly visible in the regions $(x/D, y/D) = (2-4, 1)$ and $(2-4, -1)$ in Figures 5.3(a) and 5.3(b), respectively.

The presence of the A-IV mode in the second branch is associated with a slight reduction in amplitude compared to the measurements performed in the low Re range, in which the SA mode was dominant. This is discussed further in Section 5.6. The A-IV mode has been observed in the wake of an externally excited cylinder [Griffin and Ramberg, 1976; Xu et al., 2006], and notably by Konstantinidis et al. [2007], who observed intermittent switching between the A-IV and SA modes in the wake of a fixed cylinder in oscillatory flow at similar values of reduced velocity and equivalent oscillation amplitude ($U_r\mathrm{St}/f^* = 0.55 - 0.57$, $A/D = 0.02-0.04$). The flow visualisation of Nishihara et al. [2005] also indicated the presence of such a mode in this reduced velocity range, at an amplitude of $A/D = 0.05$, although the distinct pairing formation of the vortices which is characteristic of the A-IV mode was not discussed in detail in their work. Despite having been observed in several forced oscillation studies, the A-IV mode has not previously been observed for the case of a freely oscillating cylinder. As this mode appears to be associated with distinct levels of cylinder vibration (i.e. slightly lower than those which occur when the SA mode dominates), the results presented here represent a new response branch in streamwise VIV.

The presence of the A-II mode in the wake and the reduction in amplitude in $U_r\mathrm{St}/f^* = 0.47$ in the higher Re measurements are discussed in more detail in the following section, while the formation process of the A-IV mode and its effect on the cylinder response are described in Section 5.5.

5.4 Low Amplitude Response Region, $U_r\mathrm{St}/f^* = 0.473$

The current set of PIV measurements revealed a greater reduction in the response amplitude in the region $U_r\mathrm{St}/f^* \approx 0.47$ compared to that found for the measurements performed at a lower Reynolds number (Chapter 3), as well as a change in the dominant wake mode. The reduced velocity, Reynolds number and cylinder response amplitude for both cases are compared in Table 5.1.

Table 5.1: Reduced velocities, Reynolds number, cylinder response amplitude and dominant wake mode observed in the low response region between the two branches for the measurements performed at different Reynolds number ranges.

Test Stage	$U_r\mathrm{St}/f^*$	Re	A/D	Wake Mode
1	0.495	2250	0.020	SA
2	0.473	3170	0.0045	A-II

The cylinder displacement signal and phase-averaged vorticity fields acquired in the lower Re range at $U_r\mathrm{St}/f^* = 0.495$ while the A-II mode was dominant were discussed in Section 3.7. The cylinder motion was found to be highly irregular, exhibiting low frequency fluctuations and a variable amplitude. A sample of the displacement signal measured in the higher Re system (Re = 3170) is shown in Figure 5.4(a), along with the corresponding power spectrum in Figure 5.4(b). The signal is highly unsteady with large fluctuations in amplitude, as was the case for $U_r\mathrm{St}/f^* = 0.495$ in the lower Re range. The spectrum contains one large peak at f_x, as well as some secondary peaks at slightly lower frequencies. Although the amplitude of the displacement signal is lower than that measured

at $U_r\mathrm{St}/f^* = 0.495$ for the lower Re case, the two signals are qualitatively similar (i.e. both have an irregular amplitude and low frequency fluctuations).

In Test Stage 1 at $U_r\mathrm{St}/f^* = 0.495$, the relatively low response amplitude ($A/D = 0.02$) was found to be sufficient to induce the SA mode, as the synchronised cylinder motion caused the vortices to form close to the cylinder and near the wake centreline. However, this is not the case for Test Stage 2, as indicated by the vorticity fields shown in Figure 5.5(a-h) for $U_r\mathrm{St}/f^* = 0.473$. The transverse velocity measured directly from the PIV velocity fields at $(x/D, y/D) = (3, 0.5)$ was used as a reference signal. In this case, the A-II mode is clearly visible in the vorticity fields; the shear layers roll up to form vortices at approximately $x/D = 1.5$, which are then shed into the wake, remaining at a distance of roughly half a diameter from the wake centreline, as can be seen in Figure 5.5(a) and 5.5(e). The corresponding phase-averaged cylinder displacement signal is shown in Figure 5.5(i). The amplitude is low and the signal appears to be slightly aperiodic, which is a result of the unsteadiness of the displacement signal with respect to the reference signal.

In previous chapters a method proposed by Konstantinidis et al. [2005] has been used to determine the point at which a vortex is shed from the cylinder, whereby a positive or negative vortex is said to be shed when the phase-averaged transverse velocity across the wake centreline reaches a maximum or minimum, respectively. Following this definition, the newly formed positive and negative vortices were found to be shed at $t/T = 4/16$ and $13/16$, respectively, as the cylinder is moving downstream at its peak velocity. These are approximately the same points at which the vortices were found to be shed for $U_r\mathrm{St}/f^* = 0.51$ when the SA mode was dominant (Section 3.7).

5.5 The A-IV Wake Mode

The A-IV mode has not previously been observed in the wake of a freely oscillating cylinder, in this work or in the published literature, and therefore the vortex-formation process has not been presented, and it is not known how this mode will affect the cylinder response. Measurements of the cylinder motion and the wake acquired at $U_r\mathrm{St}/f^* = 0.574$ while the A-IV mode was dominant are therefore presented below.

A sample of the cylinder displacement signal is shown in Figure 5.6(a), along with the power spectra of this signal and the transverse velocity signals extracted from the PIV fields at $(x/D, y/D) = (3, 0.5)$ and $(3, 0)$ in Figure 5.6(b). The displacement signal is reasonably steady, with fluctuations in amplitude between $A/D \approx 0.03 - 0.07$; the corresponding spectrum contains only one narrow peak at f_x. In contrast, the velocity signal measured at $(x/D, y/D) = (3, 0.5)$ has two peaks. One peak occurs at $f_x/2$, which is consistent with the results for the alternate shedding modes observed previously during lock-in (Sections 3.7 and 3.8). However, there is also a large peak at f_x (Figure 5.6(b)). Apparently the doubling of the number of vortices shed per cycle causes a corresponding increase in the frequency of velocity fluctuations in this region. The presence of more than one frequency component in the velocity signal measured at this point makes it unsuitable for use as a reference signal in the phase-averaging process. However, the transverse velocity signal measured at $(x/D, y/D) = (3, 0)$ contains only one relatively narrow peak at half the cylinder response frequency, $f_x/2$. As a result, this signal was used to compute the phase-averaged quantities while this mode dominated.

The resulting phase-averaged vorticity fields are shown in Figure 5.7(a-h), and the corresponding cylinder displacements in Figure 5.7(i). One shedding cycle corresponds to two cylinder oscillation cycles, similar to the case of the SA mode presented previously. In general, the vorticity fields appear disorganised and irregular compared to those found for other modes, and the non-dimensional magnitude of the vorticity is considerably lower ($|\langle\omega_x D/U_0\rangle| < 4$ throughout the wake for each phase).

Despite these irregularities, the distinct form of the A-IV mode is apparent; a pair of weak counter-rotating vortices are visible in the region $x/D = 2-4$ in phases $t/T = 1/16$ and $9/16$ (Figures 5.7(a) and (e), respectively). The vortices form very close to the cylinder, as in the case of the SA mode, but rather than being periodically shed, small regions of vorticity appear to separate from the vortex, as can be seen for the positive and negative vortices near $x/D = 1.5$ at $t/T = 3/16$ and $11/16$ (Figures 5.7(b) and (f)), respectively. In the subsequent phase-averaged fields shown ($t/T = 5/16$ and $13/16$ - Figures 5.7(c) and (g), respectively) the positive and negative vortices have been separated from the cylinder. However, a considerable region of vorticity of the same sign remains attached to the cylinder. Unlike the SA mode, at no point during this shedding cycle is the vorticity from either side of the cylinder fully shed from the structure; throughout all phases of the shedding cycle there remain significant levels of the positive and negative vorticity in the region $x/D = 0-1$.

The phase-averaged fields indicate that the positive vortices are cut-off from the cylinder at approximately $t/T = 1/16$ and $5/15$, while the negative vortices are cut-off at $t/T = 9/16$ and $13/16$, i.e. a vortex is shed every half-cycle of cylinder oscillation. This means that, for a pair of vortices of a given sign, the

first vortex is shed as the cylinder approaches its peak downstream position, and the second one as the cylinder nears it maximum upstream position. However, as the fluctuations across the wake centreline occur at $f_x/2$ - i.e. at half the frequency of vortex shedding - the criterion proposed by Konstantinidis et al. [2005] to determine at which point the shedding occurs is not fully applicable, and the estimates of the shedding phase remain subjective.

5.6 Multiple Stability Regions at $U_r\mathbf{St}/f^* = 0.52-0.6$

In order to examine the cause of the difference between the structural response and wake modes observed in Test Stages 1 and 2 in the region of the second branch, two additional sets of PIV measurements were acquired in this reduced velocity range. Some of the details of these measurements are given in Table 5.2. Apart from increasing or decreasing the flowrate to adjust the reduced velocity and the number of image-pairs acquired, the experimental details of these measurements are identical to those in Section 5.1 (i.e. Test Stage 2). Table 5.2 also lists the wake mode observed in the region $U_r\mathrm{St}/f^* \approx 0.56$. As all three sets correspond to a different wake mode in this region, the sets are henceforth referred to as the A-II, A-IV and SA sets accordingly.

Sample phase-averaged vorticity fields were calculated for each set in the region $U_r\mathrm{St}/f^* \approx 0.56$, which represent these three wake modes. The exact reduced velocities at which these averages were computed and the corresponding cylinder response amplitudes are listed in Table 5.3. In all cases, the transverse

Table 5.2: Experimental details regarding the three sets of PIV measurements (acquired in Test Stage 2) of the reduced velocity region surrounding the second response branch, including the reduced velocity range examined, the number of image-pairs acquired per data set and the wake mode observed in the region $U_r\mathrm{St}/f^* \approx 0.56$. For convenience, the three data sets are referred to using the mode observed here, e.g. the SA set, A-II set etc.

Notes	$U_r\mathrm{St}/f^*$	Image-pairs	Mode at $U_r\mathrm{St}/f^* \approx 0.56$
Increasing $U_r\mathrm{St}/f^*$	$0.122 - 0.682$	2000	A-IV
Increasing $U_r\mathrm{St}/f^*$	$0.468 - 0.648$	1000	SA
Decreasing $U_r\mathrm{St}/f^*$	$0.44 - 0.655$	1000	A-II

velocity measured at $(x/D, y/D) = (3, 0)$ was used as a reference signal. The averaged vorticity fields for the A-IV mode have been presented and discussed in the previous section (Figure 5.7), while those representing the SA mode (at $U_r\mathrm{St}/f^* = 0.566$) are shown in Figure 5.8. The vorticity patterns are quite similar to those discussed in Section 3.8 (Figure 3.12) which were computed at the same point in the response regime, but at a slightly lower Reynolds number. Finally, the phase-averaged fields for the A-II mode are shown in Figure 5.9; the reduced velocity is $U_r\mathrm{St}/f^* = 0.556$ and is reached by decreasing the flowrate. This point corresponded to negligible cylinder excitation. At this reduced velocity range the vortex-shedding is not synchronised to the cylinder motion.

The variation of the cylinder response amplitude and dominant frequency of transverse velocity fluctuations at $(x/D, y/D) = (3, 0.5)$ for the three sets of measurements are shown in Figure 5.10. The symbol colour indicates the dominant wake mode at each point. The wake exhibits a different mode in the region $U_r\mathrm{St}/f^* \approx 0.52 - 0.61$ for each data set. It is clear that these changes in the

Table 5.3: Reduced velocities, cylinder response amplitudes and wake modes corresponding to the phase-averaged vorticity fields shown in Figures 5.7, 5.8 and 5.9.

Mode	$U_r\mathrm{St}/f^*$	A/D	Figure
A-IV	0.564	0.0527	5.7
SA	0.566	0.0621	5.8
A-II	0.556	0.0052	5.9

wake mode correspond to significant changes in the cylinder response amplitude. When the A-II mode dominates, the cylinder response amplitude is low and the velocity fluctuations in the wake occur at the Strouhal frequency, indicating the absence of lock-in. This mode was observed in this region of the response regime when the reduced velocity was incrementally *decreased* from a high initial value. As $U_r\mathrm{St}/f^*$ is reduced to 0.56, the cylinder begins to oscillate and the SA mode becomes dominant. In contrast, when the reduced velocity is increased and the A-IV mode dominates, the second response branch extends to $U_r\mathrm{St}/f^* \approx 0.6$. The velocity fluctuations remain locked-in to the cylinder motion, at either f_x or $f_x/2$, over this range. The second branch has a peak amplitude of $A/D = 0.621$ when the SA mode is dominant. The maximum amplitude is slightly lower when the A-IV mode occurs, $A/D = 0.546$. In Chapter 4 it was shown that during the first branch the wake switched between the S-I and A-II modes. Similarly, the wake is capable of exhibiting two modes in the second branch; the SA and the A-IV. However, unlike the bimodal behaviour observed in the first response branch, the wake did not intermittently switch between modes; when the wake exhibited a given mode, this mode persisted, provided the reduced velocity and response

amplitude did not change significantly. The SA and A-IV modes were found to occur in the second branch both when the reduced velocity was increasing and decreasing (although they occurred over a considerably smaller range when the reduced velocity was decreasing, as the second branch was also shorter in this case). Therefore, it would appear that the presence of either mode is not caused by the hysteresis effects which are present in this region.

It is not clear why the A-IV mode was not observed in the low Re measurements presented in Chapter 3 (Test Stage 1). The appearance of either the A-II or the SA mode in the second branch appears to be unpredictable. Due to the computational requirements and processing times associated with PIV measurements, it was not possible to perform a large number of measurements of the dominant wake mode and the amplitude response in the second branch in order to estimate the probability of either mode occurring as the reduced velocity is increased or decreased. However, based on the results presented throughout this thesis and various preliminary studies (which are not presented here), the SA mode appears to be the more likely to occur than the A-IV mode. Thus it is possible that the A-IV mode was not observed in the low Re measurements as a result of the apparently random nature with which is appeared. However, this does not explain why this mode was not observed in the streamwise-only free vibration studies of Aguirre [1977] and Okajima et al. [2003]. Alternatively, the A-IV may only be possible within a certain range of Reynolds number, similar to the S-I mode which is only observed in the wake of a freely vibrating cylinder for Re $\gtrsim$ 1000 (Section 4.7). Further experiments in which the Reynolds number and reduced velocity could be varied independently would be required to verify this potential Re-dependency of the A-IV mode.

As far as the author is aware, the results presented here represent a unique case in the study of VIV; a point in the response regime of a freely oscillating body, at which *three* possible wake modes, each corresponding to a different level of response amplitude, are possible for the same flow conditions (Reynolds number, reduced velocity etc.). In the following section, the stability of each state is discussed.

5.7 Stability of Cylinder-Wake System

The previous section indicated that the response regime of a cylinder free to oscillate in the streamwise direction contains three possible states in the range $U_r\mathrm{St}/f^* \approx 0.52 - 0.61$, each corresponding to different wake modes and levels of amplitude response. Several previous studies have observed points in the response regime for transverse VIV in which two possible states have existed at a given point, perhaps the most common case being caused by hysteresis effects [Khalak and Williamson, 1997; Sarpkaya, 2004].

Morse and Williamson [2009] analysed the intermittent switching between the Upper and Lower response branches observed in transverse VIV using detailed measurements of the forces acting on a cylinder forced to oscillate in the transverse direction for a range of amplitudes and reduced velocities. By equating estimates of the fluid excitation and the energy dissipated from the cylinder due to damping, they showed that a sudden increase or decrease in the levels of excitation can cause a freely oscillating cylinder to change states (i.e. to change from oscillating at a large amplitude in the Upper branch to a reduced amplitude in the Lower branch, or *vice versa*). Such a system, which is capable of exhibiting multiple

states for a given set of parameters, but requires an external input of energy to switch between states, is known as a '*hard oscillator*' [Cecchi et al., 1993].

The distinction between a '*soft*' and a '*hard*' oscillator can be shown by observing the characteristic phase portraits of both systems, which are sketched in Figure 5.11. The horizontal and vertical axes represent the response variable and its temporal derivative (in this case displacement and velocity, respectively). The solid black line represents the path of steady state oscillations, while the origin (indicated by the black circle) corresponds to a static or non-responsive system. For the case of the soft oscillator (Figure 5.11(a)), the system will converge upon the steady state path if released from any point in the phase space - i.e. for any set of initial conditions. The convergence is shown in the phase-portraits using the blue arrows.

The behaviour of the hard oscillator is slightly more complex (Figure 5.11(b)). If the initial displacement and velocity of the system are within a certain region close to the origin (which is bounded by the 'unstable limit cycle', represented by the dotted black line) the system will converge on the origin - i.e. the oscillations will be damped out. However, if the system is perturbed such that its position in the phase portrait occurs outside this critical region, the system will exhibit steady oscillations (i.e. converge upon the steady state path, which is also known as the stable limit-cycle path). The steady state response of a soft oscillator is independent of its initial conditions and time history, while it is possible to induce permanent changes in the response of a hard oscillator by applying a transient perturbation.

Naudascher [1987] also discussed hard oscillator behaviour in the streamwise response of a plate, which had an aspect ratio of 5 and was aligned such that the

larger dimension was perpendicular to the flow. It was found that at certain points during lock-in the system acted as a hard oscillator. The structure exhibited reasonably steady vibrations; however, when the vortex shedding was disrupted by inserting a ruler into the wake, the vortex-shedding frequency reverted to the Strouhal frequency, lock-in ceased and the structural response amplitude was reduced.

The work of Naudascher [1987] indicates that it is possible to induce such a system to 'jump' between states by either modulating the wake or the levels of energy transfer to or from the system. It seems likely that the current system behaves as a hard oscillator in the region $U_r\mathrm{St}/f^* \approx 0.56$, where three potential cylinder-wake states have been observed.

In order to investigate the stability of the various states that the cylinder can exhibit during the second branch and ascertain whether the system behaves as a hard oscillator, phase-portraits were estimated for the three selected PIV data sets discussed in the previous sections (in which the wake exhibited the A-IV, SA and A-II wake modes) and listed in Table 5.3. The cylinder velocity, $\dot{x}$, was calculated from the displacement signal using the central-difference method. In order to remove any low-frequency fluctuations which were not associated with VIV, the displacement signals were first high-pass filtered, with a cut-off frequency of 5Hz. The cylinder diameter was used to normalise the displacement signals, while the cylinder velocity signals were normalised by the diameter and the Strouhal frequency.

The phase-portrait of the cylinder while the A-IV mode was dominant (at $U_r\mathrm{St}/f^* = 0.564$) is shown in Figure 5.12(a). Figure 5.12(b) shows a similar portrait for the case in which the SA mode was dominant ($U_r\mathrm{St}/f^* = 0.566$).

The white symbols denote the points at which the response amplitude was found to be increasing (i.e. the next peak in the displacement signal is larger than the previous one), while the black symbols denote points in which the amplitude was decreasing. The points are connected using cubic spline curves (grey lines) in order to represent the smooth trajectories followed by the system.

For both cases (Figures 5.12(a) and (b)), the points in the phase-portrait do not collapse on to a single line. Unlike the case of an ideal oscillator, structures oscillating in a fluid will experience modulations in their vibration frequency due to added mass effects. This will lead to changes in the levels of energy transfer and the instantaneous position of the stable limit-cycle (i.e. the response amplitude which the system will converge towards). Therefore, for structures which are affected by variations in the added mass, the stable limit-cycle will manifest itself as a stability *band*, rather than a path. The points at which the response amplitude is increasing and decreasing appear to be distributed evenly throughout the bands shown in Figures 5.12. This indicates that the width of the band is not simply caused by the cylinder responding to small perturbations away from a fixed stability path; if this was the case the majority of the points in the outer regions (i.e. higher amplitude regions) of the band would have a decreasing amplitude (as the cylinder amplitude decayed and the cylinder response converged on the stability path). Similarly, the points closer to the origin would have an increasing amplitude, as the amplitude increased and the system converged upon the stable path at the centre of the band. The even distribution of points of increasing and decreasing amplitude indicates that the band represents a range of stability limit-cycle paths which may occur.

The width of the band will depend on the variations in the amplitude of the

displacement and velocity signals. The band which is occupied by the cylinder when the A-IV move dominates is wider than that associated with the SA mode, indicating that the A-IV mode causes greater unsteadiness in the structural response.

The phase-portraits estimated for these two cases, and the measurements in which the wake exhibited the A-II mode at $U_r\mathrm{St}/f^* = 0.556$, are shown in Figure 5.13. It is notable that the paths corresponding to the times at which the A-IV and SA wake modes are dominant overlap slightly. This has significant implications for the nature of the stability of the system in this region. The paths followed by the cylinder through the phase-space when the SA or A-IV modes dominate are not separated by an unstable limit-cycle, i.e. a path or band in which no steady-state oscillations are possible. This implies that the transition between the two states (high amplitude cylinder response as the SA mode dominates, and slightly lower response as the A-IV mode occurs) is not governed by hard oscillator behaviour. In fact, the two responses may be said to occupy the same stability band.

Both wake modes cause the cylinder to follow a path through the phase-space in this relatively broad stability region, given by $(x/D)_{max} \approx 0.03 - 0.07$, $(\dot{x}/f_{St}D)_{max} \approx 0.3 - 0.7$. The cylinder tends to occupy a region of larger amplitude within this band when the SA mode dominates, and a slightly lower amplitude region when the A-IV mode occurs. This tendency for the two modes to cause the cylinder to occupy slightly different regions within the same stability band causes the *average* amplitude associated with each mode to be different. This can be seen in Figure 5.10, which shows the amplitude in terms of the mean peak height of the displacement signal, A/D.

Konstantinidis et al. [2007] observed the wake of a fixed cylinder in pulsating flow in this reduced velocity range, and found the wake to switch intermittently between the A-IV and SA modes. As the two modes were found to occur at approximately the same reduced velocity and response amplitude, it seems plausible that the wake of a freely oscillating cylinder should also be expected to switch intermittently between the two modes. However, it was found in the present study that the wake mode changed very rarely. For example, PIV measurements performed at $U_r\mathrm{St}/f^* = 0.55$ (while the SA mode was dominant) every ten minutes over the course of an hour ($\sim 50,000$ vortex-shedding cycles) did not indicate any change in the wake mode or the amplitude response. Similarly, the measurements which spanned the second response branch discussed in the previous section were acquired over the period of approximately an hour (as the time between measurements at the different reduced velocities was approximately 20 minutes), but at no point was the wake found to differ from that of the previous data set, unless it was accompanied by a significant change in the cylinder response amplitude or reduced velocity (Figure 5.10). Thus, both modes appear to be very stable.

The stability of both wake modes occurs in spite of the unsteadiness in the cylinder displacement signals in this region, as indicated by the width of the stability bands. If the stability of the wake modes is not caused by the cylinder motion, it must be caused by the wake itself. It is possible that the vortices shed as part of the SA mode exert an upstream influence which inhibits the formation of vortices in the near wake as part of the A-IV mode and *visa versa*; i.e. both wake modes are inherently self-sustaining. However, this does not explain why Konstantinidis et al. [2007] observed switching between the two modes in this region.

In contrast to the phase-portrait paths which occur when the SA and A-IV modes dominate, the paths followed by the cylinder when the A-II mode occurs do not overlap with any other path. This would suggest that the path followed by the cylinder when the A-II mode dominates may be separated from other paths by an unstable limit-cycle, i.e. the cylinder-wake system behaves as a hard oscillator in this region.

If the transition between the low and high amplitude response cases in the second branch is caused by hard oscillator behaviour, it will be possible to induce the system to jump between states by applying a suitable perturbation. As the experiments were performed in a closed-loop water tunnel which had no free surface, it was not possible to perturb the system by interfering directly with the wake or the cylinder. Instead, the perturbation was applied by tugging on or relieving the tension in the wires supporting the cylinder. This had the disadvantage of potentially causing a permanent change in the natural frequency of the system, which would lead to changes in the frequency ratio, $f^* = f_x/f_n$ (where f_n is the natural frequency measured in still fluid *before* the perturbation was applied) and the reduced velocity, $U_r\mathrm{St}/f^*$. Changes in the wake mode and the cylinder response amplitude will also affect the added mass coefficient and the cylinder response frequency. However, it is not possible to isolate the effects on the reduced velocity which are caused by the perturbation itself (adjusting the tension in the wires) and the effects of the changes to the cylinder-wake state (the variations in the added mass caused by the changes in the wake). In spite of the imperfections in the method used to perturb the system, it was found that the perturbations caused clear, identifiable changes to the state of the system.

In order to examine the response of the system to such perturbations, a series

of PIV measurements were performed in which the system was perturbed while the wake and cylinder response were recorded. The experimental details are similar to those presented in Section 5.1. The flowrate was adjusted such that the reduced velocity was in the range $U_r\mathrm{St}/f^* = 0.51-0.6$. A settling time of over ten minutes was employed to ensure that the system had reached a steady state. Subsequently, 2000 PIV image-pairs were captured at 200Hz. A few seconds after the image acquisition began the tension within the wires supporting the cylinder was adjusted (either by tugging or relieving the weights applied to control the stiffness of the system) and the response of the system was observed.

Three sample displacement signals are shown in Figures 5.14(a-c). The blue shaded regions indicate the segments of each set of measurements which were used to calculate the reduced velocity, amplitude response and dominant wake mode pre-perturbation, while the yellow regions indicate the same characteristics post-perturbation. These results are summarised in Table 5.4 for both the pre- and post-perturbation cases. The amplitude response of each set of measurements is shown in Figure 5.15, plotted together with the response regimes discussed in the previous section. It is clear that for the measurements in which the initial response amplitude was large (Cases 1 and 2 in Table 5.4, black symbols in Figure 5.15), the perturbations caused the system to jump to a state in which the structural response was negligible. The wake mode switched from the SA or A-IV, to the A-II. In the third perturbation measurement (grey symbols in Figure 5.15), the perturbation caused the system to jump from a state of low amplitude response in which the wake exhibited the A-II mode, to a state in which the A-IV mode dominated and the cylinder experienced significant levels of vibrations.

In all three cases, the perturbations induced the cylinder-wake system to jump

Table 5.4: Experimental parameters pre- and post-perturbation for the three sets of PIV measurements presented in Figure 5.15(a-c), in which the cylinder-wake system was perturbed by adjusting the tension within the support wires.

	$U_r\mathrm{St}/f^*$	A/D	$t[s]$	Mode
Case 1, Pre-pertubation	0.51	0.041	0 - 2.5	SA
Case 1, Post-pertubation	0.5534	0.005	5 - 10	A-II
Case 2, Pre-pertubation	0.549	0.039	0 - 1.25	A-IV
Case 2, Post-pertubation	0.625	0.002	5 - 10	A-II
Case 3, Pre-pertubation	0.592	0.003	0 - 1	A-II
Case 3, Post-pertubation	0.563	0.049	2.5 - 10	A-IV

between states, causing a change in the wake mode and the levels of cylinder vibrations. This confirms that the system behaves as a hard oscillator in this region.

5.8 Implications for Design of Systems Vulnerable to VIV

Some of the findings presented in this chapter have significant implications for the stability of structures which are susceptible to VIV in the streamwise direction.

In applications such as heat exchangers (including the Monju reactor which failed due to VIV in the streamwise direction [Okajima et al., 2001]) in which the flowrate and reduced velocity can be accurately controlled, it may be possible to increase the range over which the system can be operated safely. For example, by increasing and then decreasing the flowrate, it may be possible to operate in

the region $U_r\mathrm{St}/f^* \approx 0.56$ without causing the cylinder to experience significant vibration in the streamwise direction. In fact, is appears to be always beneficial to reach the operating condition (i.e. the reduced velocity) by *decreasing* the flowrate rather than simply increasing; the variations in the response amplitude for the cases of increasing and decreasing reduced velocity shown in Figures 5.1 and 5.10 indicate that in some regions the response amplitude is lower when the reduced velocity is decreased, but at no point does decreasing the velocity caused a comparative increase in the amplitude. The work of Khalak and Williamson [1997] and Sarpkaya [2004] suggests that this is also true for VIV acting in the transverse direction.

However, in many applications it is not possible to control the freestream velocity. In applications such as marine structures in tidal regions, the freestream velocity will either be increasing or decreasing depending on the time of day. The fact that the second response branch occurs over a very small range when the reduced velocity is decreasing suggests that the second branch may only occur to its maximum extent (i.e. $U_r\mathrm{St}/f^* = 0.52 - 0.6$) every second time that the reduced velocity is in this range (where the freestream velocity is given by the instantaneous value of the tidal velocity). This suggests that the levels of vibration and fatigue damage experienced by these structures in practice may be lower than those predicted from studies in which the reduced velocity was only increased.

The ability of perturbations to alter the levels of response amplitude of the structure also has significant implications for such applications. It has been shown that the system behaves as a hard oscillator in the second branch. Therefore it is possible to induce the system to switch from high to low amplitude response by

applying a suitable perturbation. It could then be possible to reduce the levels of structural response in the region of the second branch by means of active control; by restricting the structural motion or disrupting the vortex-shedding for a short number of cycles, the system will revert to the low amplitude response state (in which the A-II mode dominates), and will require a new perturbation to return to the large amplitude second branch. This method of control has the benefit of only requiring an energy input for a short period of time when the response amplitude became large ($A/D \gtrsim 0.04$), after which no further energy input would be required to maintain the low levels of vibration.

However, in many applications the freestream velocity cannot be accurately controlled, or the system is susceptible to random perturbations (e.g. significant freestream turbulence or wave-loading). In such cases these disturbances may cause the system to jump from a state of low response amplitude to one in which significant vibrations occurred, regardless of whether the reduced velocity had been increased or decreased.

The implications for industrial applications of the presence of multiple stability regions observed here will depend upon how significant a perturbation is required to induce a change in state, and to what degree these multiple stability regions are present for structures with two or more degrees-of-freedom. Further work is also required to ascertain to what extent the multiple-stabilty regions will be affected by experimental parameters such at the Re, aspect ratio, freestream turbulence, blockage ratio etc.

5.9 Wake Modes throughout the $U_r\mathrm{St}/f^* - A/D$ Plane

A summary of various studies in the literature which examine the wake of a cylinder forced to oscillate in the streamwise direction was presented in Figure 1.4, showing the distribution of the observed modes for various values of reduced velocity and forcing amplitude - i.e. throughout the $U_r\mathrm{St}/f^* - A/D$ plane. A similar 'mode map' is shown in Figure 5.16 for the region in which free streamwise oscillations are excited ($U_r\mathrm{St}/f^* < 0.75, A/D < 0.1$). The results from the PIV measurements discussed in this chapter and in Chapter 3 are also shown. The colour of each symbol denotes the dominant wake mode observed at each point, with symbols with two colours indicating points at which intermittent mode switching occurred. Based on the results of both free and forced streamwise studies, regions in which a given wake mode is expected to dominate are estimated and indicated using the shaded regions. The unshaded regions correspond to areas in which insufficient information was available to estimate the dominant mode.

Forced studies allow the effect of the cylinder motion upon the wake to be isolated and examined, and are useful in terms of characterising the various wake modes which may occur [Ongoren and Rockwell, 1988; Williamson and Roshko, 1988], but cannot fully capture the complex feedback mechanism between the cylinder motion and the fluid forcing. However, in general the distribution of modes observed in the free vibration experiments presented here is consistent with the findings of previous forced studies, suggesting that the results contained in the literature from forced studies may be extended to the case of cylinders undergoing free oscillations.

Table 5.5: Experimental details of the published studies from the literature presented in Figure 5.16.

Researcher	$U_r\mathrm{St}/f^*$	A/D	Symbol	Modes
Nishihara et al. [2005]	$0.23 - 0.92$	0.05	$\triangle$	A-II, S-I, SA
Griffin and Ramberg [1976]	$0.454 - 0.575$	$0.06 - 0.24$	$\star$	A-II, A-IV, SA
Kim et al. [2006]	0.5	0.02	$\Diamond$	SA
Konstantinidis et al. [2005]	$0.45 - 0.575$	$0.04 - 0.05$	$\square$	SA
Konstantinidis et al. [2007]	$0.535 - 0.575$	$0.01 - 0.03$	$\square$	A-IV, SA
Konstantinidis and Balabani [2007]	$0.25 - 0.33$	$0.02 - 0.04$	$\square$	A-II, S-I
Konstantinidis and Balabani [2008]	0.5	$0 - 0.09$	$\square$	A-II, SA

The A-II mode tends to dominate at low amplitudes and near $U_r\mathrm{St}/f^* = 0.4$. As the A-II mode is essentially the von Kármán street which occurs behind stationary cylinders, the regions of A-II shedding at low values of A/D correspond to points at which the cylinder vibrations were too small to significantly modify the wake mode from its natural state. The region of A-II shedding near $U_r\mathrm{St}/f^* = 0.4$ corresponds to the peak of the first response branch. As discussed in Section 4.6, when the S-I mode dominates during the first branch, the symmetrically shed vortices tend to rearrange into an alternate structure, causing the wake to revert to the A-II mode a number of diameters downstream of the cylinder. The dominance of the A-II mode in this region is therefore likely to be caused by the increased tendency for this rearrangement to take place.

This rearrangement, as well as the intermittent switching between the A-II

and S-I modes, makes it difficult to accurately define the boundaries between the regions of the $U_r\mathrm{St}/f^* - A/D$ plane over which of either mode is dominant. As noted in Section 4.8, the dominance of either of these modes is a probabilistic function which is dependent on the reduced velocity and Reynolds number. The mode map presented by Morse and Williamson [2009] for transverse oscillations contained a small region in which both the $2P$ and the $2P_0$ modes were possible. However, for the streamwise case the region over which the wake mode varies extends over a greater proportion of the response regime. As the switching between the two modes does not appear to cause any significant change in the levels of fluid excitation, mode-switching is not expected to affect the ability of such a map to predict the amplitude response of a freely oscillating cylinder using the method outlined by Morse and Williamson [2009] (which also requires the measurement of the fluid forces in the direction of the oscillations).

The SA mode dominates at $U_r\mathrm{St}/f^* \approx 0.52$. The mechanism of vortex-shedding for this mode (discussed in Sections 3.7 and 3.8) relies on the synchronisation between the cylinder motion and the vortex shedding, which occurs at this point. The SA mode is observed in the range $U_r\mathrm{St}/f^* = 0.45 - 0.6$. While this is roughly centred at the synchronisation point, $U_r\mathrm{St}/f^* = 0.5$, the region in which the SA mode is dominant appears to be asymmetrical, with a greater tendency to occur at higher reduced velocities, compared to $U_r\mathrm{St}/f^* < 0.5$.

The PIV measurements discussed in the previous sections indicate that a small region of A-IV shedding occurs at $U_r\mathrm{St}/f^* = 0.54 - 0.6$, $A/D \approx 0.04 - 0.06$. This mode has also been observed by Konstantinidis et al. [2007], Griffin and Ramberg [1976] and Nishihara et al. [2005] in the region, although this study represents the first time that the A-IV mode has been reported in the wake of a freely oscillating

cylinder.

It has briefly been discussed why this mode has not been observed in previous studies, most notably in the extensive experiments of Aguirre [1977]. It was noted that Reynolds number may play a role in determining the dominance of a given mode, as it does in the appearance of the first response branch and the S-I mode near $U_r \mathrm{St}/f^* \approx 0.3$ (Section 4.7), as well as in the extent of the lock-in range [Konstantinidis and Liang, 2011]. However, Morse and Williamson [2009] estimated a high amplitude mode map for a cylinder oscillating in the transverse direction at Reynolds numbers of Re = 4000 and 12000, and noted only minor differences between the two cases. In short, it is not clear how the Reynolds number may affect the map presented here, as it is compiled from a number of studies performed at different values of Re, while the Reynolds number for the free vibration experiments performed in this work will vary with reduced velocity. Similarly, it is not clear how the mode map will be affected by other parameters such as blockage ratio, the cylinder aspect ratio, freestream turbulence etc.

The fact that the small region of A-IV shedding has been noted in a number of studies (Griffin and Ramberg [1976]; Konstantinidis et al. [2007]; Nishihara et al. [2005] as well as the present work) which were performed using different experimental systems and at different values of Re, indicates that the appearance of this mode is reasonably robust.

It is possible, by superimposing the measured amplitude response of a freely vibrating system upon the mode map, to estimate the wake mode throughout the response regime. This requires information on the frequency of the cylinder oscillations, so that the response can be expressed in terms of the 'true' reduced velocity. As the results of many previous studies are given as a function of the

conventional reduced velocity, $U_r = U_0/f_n D$ (where f_n is the natural frequency of the system in a still fluid), it is sometimes difficult to directly relate these results to points on the mode map, and thus predict which mode will be dominant. It is notable that the amplitude response in the second branch for cylinders free to move in both the streamwise and transverse directions tends to be relatively large, $A/D \gtrsim 0.07$ [Blevins and Coughran, 2009; Jauvtis and Williamson, 2003]. The region of the mode map in which the A-IV mode appears to dominate occurs only for lower amplitudes, $A/D \approx 0.05$, suggesting that this mode may not occur for the case of cylinders with multiple degrees of freedom.

5.10 Closure

The effects of hysteresis on the response regime and the presence of multiple wake modes in the region of the second branch were examined. The experiments were performed at a slightly higher Re range compared to the results presented in Chapter 3. A preliminary investigation of the amplitude response of the cylinder indicated that the response regime was affected by hysteresis only in the second branch; the reduced velocity range over which lock-in and the second branch occurred was significantly shorted when $U_r \mathrm{St}/f^*$ was decreased.

Extensive PIV measurements were acquired throughout the response regime, and compared to the results presented in Chapter 3, which were performed at a slightly lower Reynolds number range. The high Re measurements indicated that the A-II mode was dominant in the low amplitude region between the first and second branches, and the value of A/D was lower. These differences were attributed to Reynolds number effects. The A-IV mode was observed for much

of the second branch. As far as the author is aware, this mode has not previously been recorded in the wake of a freely oscillating body. This mode was examined using phase-averaged vorticity fields, which indicated that - unlike the SA mode which has also been observed in the second branch - the vortices formed at the cylinder surface are never fully shed; instead, small regions of vorticity shear off, forming four small vortices in each shedding cycle.

Additional data sets acquired in the region of the second branch indicated that the response regime could be manifest in a number of ways; when the reduced velocity was decreased the second branch occurred over a small range of $U_r\mathrm{St}/f^*$ and the A-II mode was dominant outside of the range; while the reduced velocity was increased the second branch could occur in two forms, depending on whether the SA or the A-IV modes dominated in the wake. Both modes were found to be stable, occurring consistently in the wake for long periods of time, and it was unpredictable which mode the wake would exhibit as the reduced velocity was varied. The SA mode excited slightly larger cylinder vibrations. The results indicated that at $U_r\mathrm{St}/f^* \approx 0.56$ the wake was capable of exhibiting three modes (i.e. the A-II, SA and A-IV modes), with each mode corresponding to a different cylinder response amplitude, which is thought to represent a unique case in VIV. The stability of each state at $U_r\mathrm{St}/f^* \approx 0.56$ was estimated using phase-portraits of the cylinder response. The phase-portraits indicated that the cylinder behaved as a hard oscillator; this was confirmed by applying perturbations to the system (by adjusting the cylinder supports) which were capable of causing the cylinder to jump between a state of low amplitude response in which the A-II mode was dominant in the wake, to a high amplitude case in which the wake exhibited either the SA or A-IV modes, and *visa versa*. The phase portraits also indicated

that the cylinder occupied the same stability band when the SA or A-IV modes occurred in the wake.

The implications of the presence of hysteresis and the hard oscillator behaviour for the design of structures which are vulnerable to VIV were briefly discussed. Finally, the results regarding the variation in the dominant mode observed throughout the response regime were compared to the those of various forced oscillation studies in the literature.

5.11 Figures

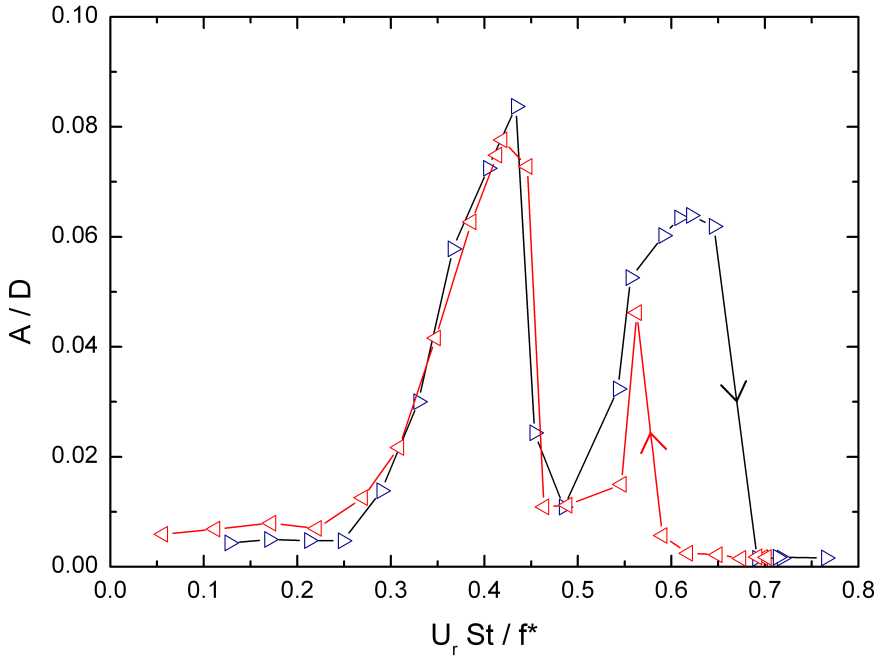

Figure 5.1: Cylinder amplitude response, found by incrementally increasing (blue triangles) and decreasing (red triangles) the reduced velocity.

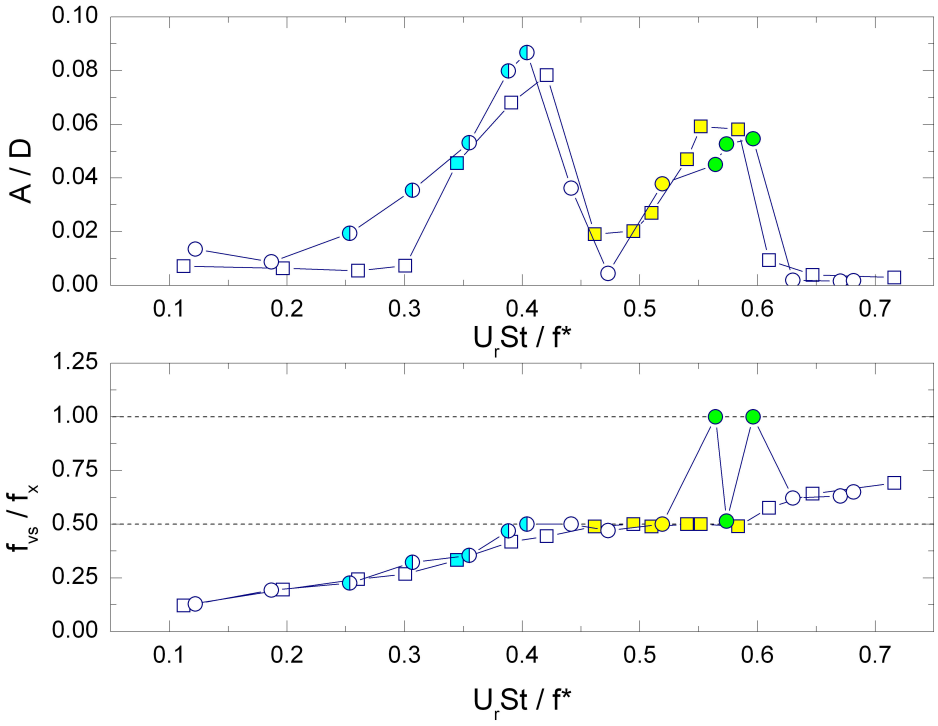

Figure 5.2: Comparison of the cylinder amplitude response (a) and dominant frequency of transverse velocity fluctuations measured at $(x/D, y/D) = (3, 0.5)$ (b), for the current measurements (Re $= 740 - 5400$, Test Stage 2, circles) and those presented in Chapter 3 (Re $= 450 - 3700$, Test Stage 1, squares). The colours within each symbol denote the dominant wake mode observed; white, A-II; blue, S-I; yellow, SA; and green, A-IV. Symbols with two colours represent points at which mode-competition was observed.

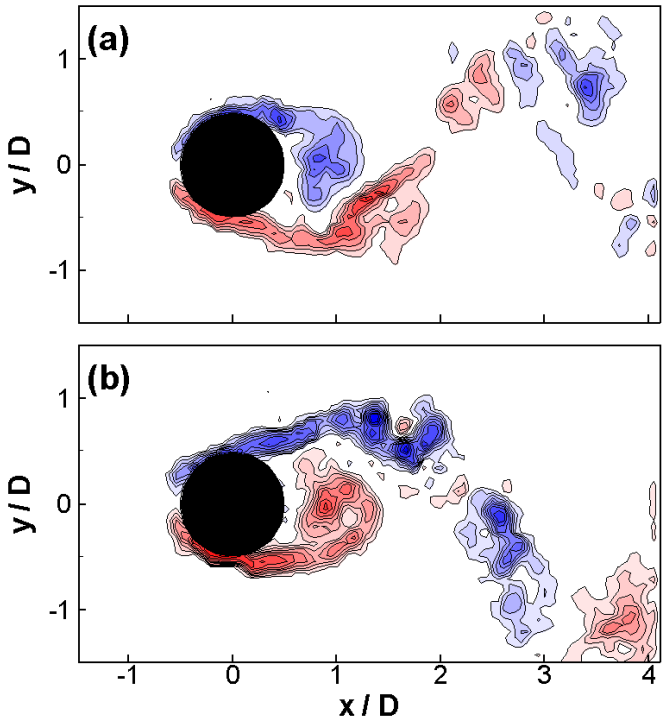

Figure 5.3: Sample vorticity fields acquired at $U_r\mathrm{St}/f^* = 0.564$ (Test Stage 2), showing the A-IV mode. The cylinder is in its most downstream position. Contour levels are $\omega_z D/U_0 = \pm 1.5, \pm 3, \ldots$

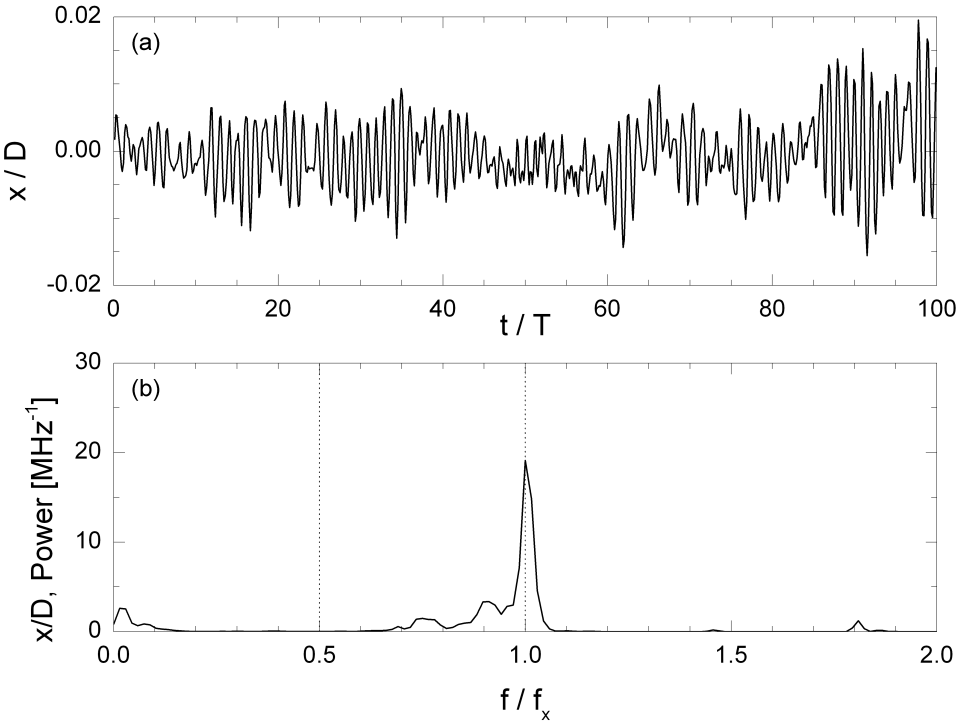

Figure 5.4: Sample of the cylinder displacement signal (a) and associated spectrum (b), measured for $U_r\mathrm{St}/f^* = 0.473$, which corresponds to the reduced amplitude region between the two response branches. The spectrum had a resolution of 0.39Hz, or $0.015f_x$.

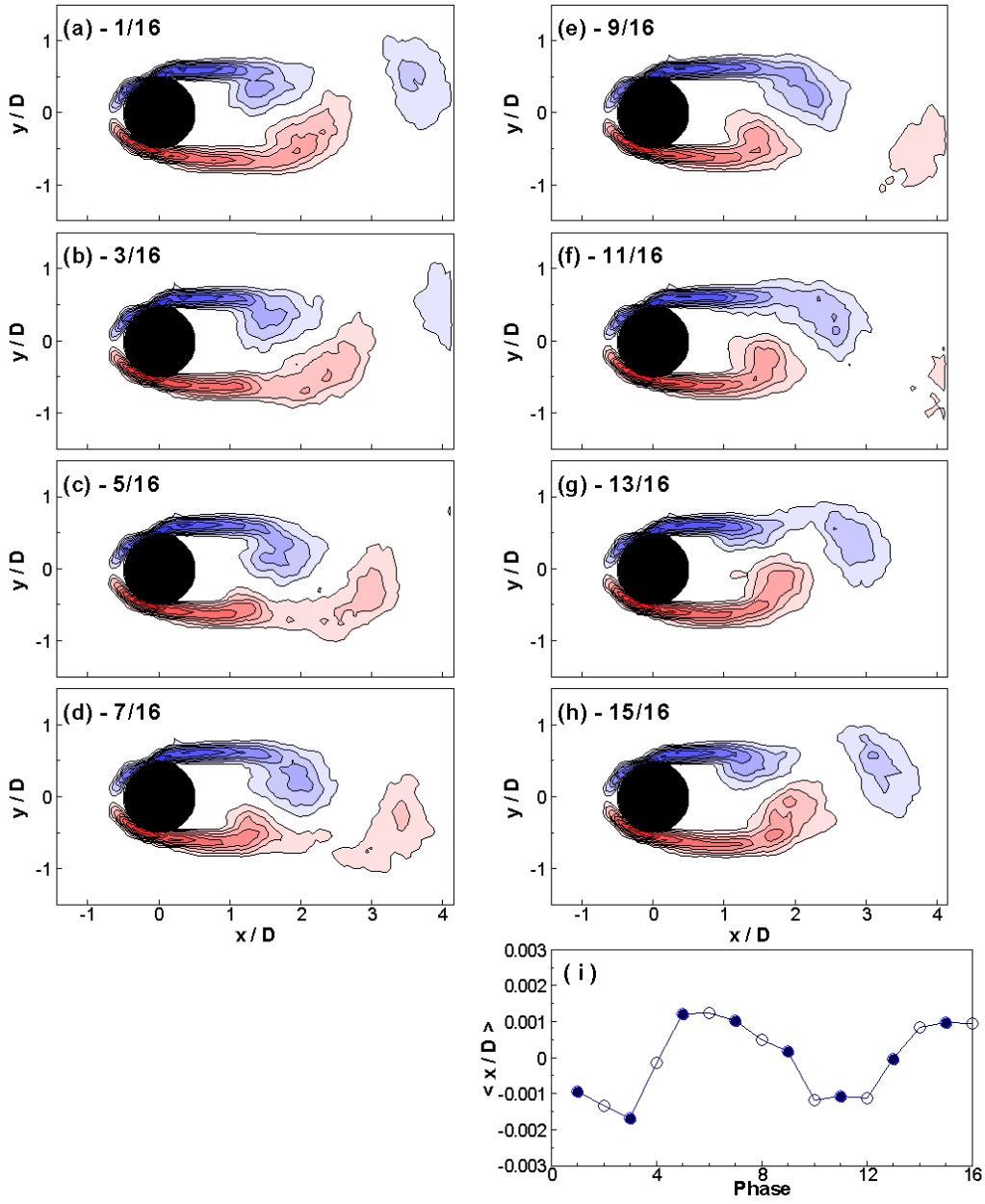

Figure 5.5: (a-h) Phase-averaged vorticity fields over one shedding cycle for $U_r\mathrm{St}/f^* = 0.473$, which corresponds to the low amplitude region between the two response branches. The A-II mode is clearly dominant. Contour levels are $\omega_z D/U_0 = \pm 1, \pm 2, \ldots$ The phase-averaged cylinder positions for each vorticity field are also shown in (i). The phase-averaging process was performed using the transverse velocity signal extracted from the PIV fields at $(x/D, y/D) = (3, 0.5)$ as a reference signal.

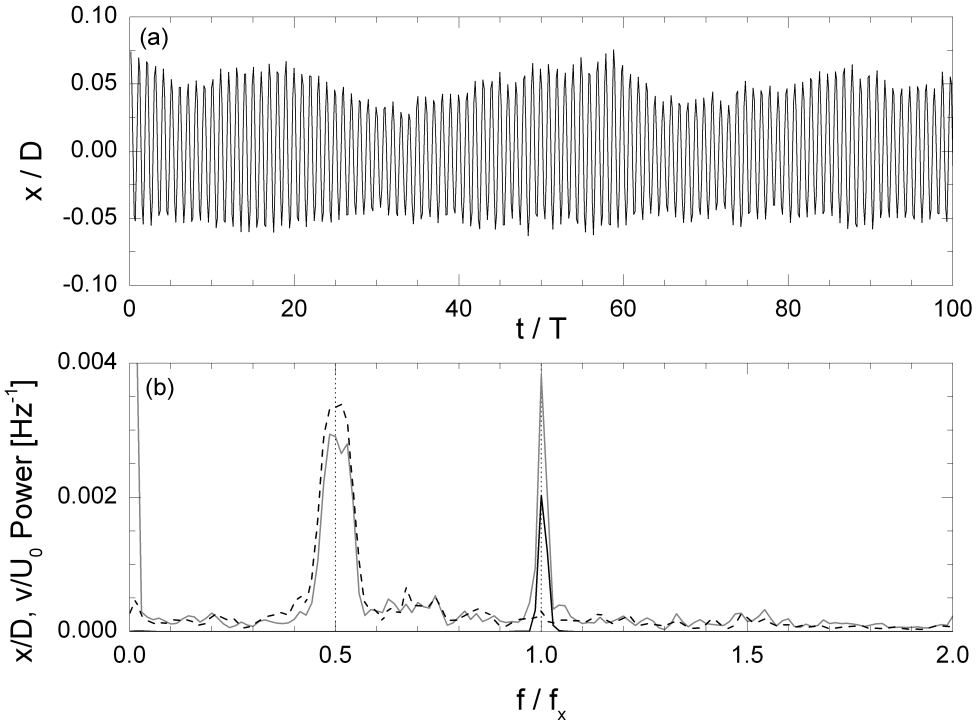

Figure 5.6: (a) A sample of the cylinder displacement signal and (b) spectra of cylinder displacement (solid black line) and transverse velocity signal measured in the wake at $(x/D, y/D) = (3, 0.5)$ (solid blue line) and $(x/D, y/D) = (3, 0.5)$ (dashed black line) for $U_r\mathrm{St}/f^* = 0.574$. This corresponds to the peak of the second response branch, while the A-IV mode is dominant. The displacement and velocity signals are normalised with respect to the cylinder diameter and freestream velocity respectively. The spectra have a resolution of 0.39Hz or $0.014f_x$.

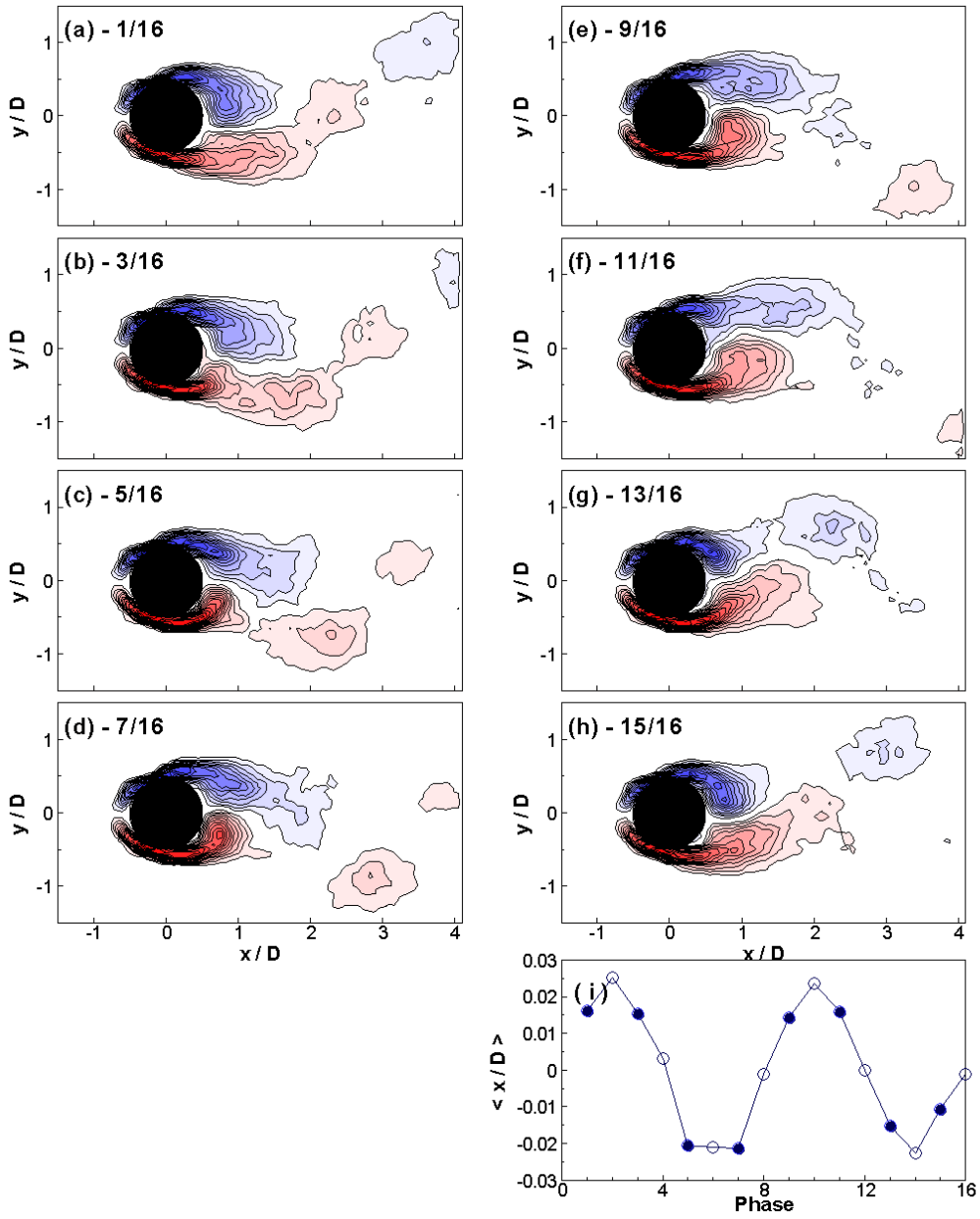

Figure 5.7: (a-h) Phase-averaged vorticity fields over one shedding cycle for $U_r\mathrm{St}/f^* = 0.574$, which corresponds to the peak of the second response branch. The A-IV mode is clearly dominant. Contour levels are $\omega_z D/U_0 = \pm 0.25, \pm 0.5,$ . . . The phase-averaging process was performed using the transverse velocity signal extracted from the PIV fields at $(x/D, y/D) = (3, 0)$ as a reference signal. The corresponding cylinder displacements are shown in (i).

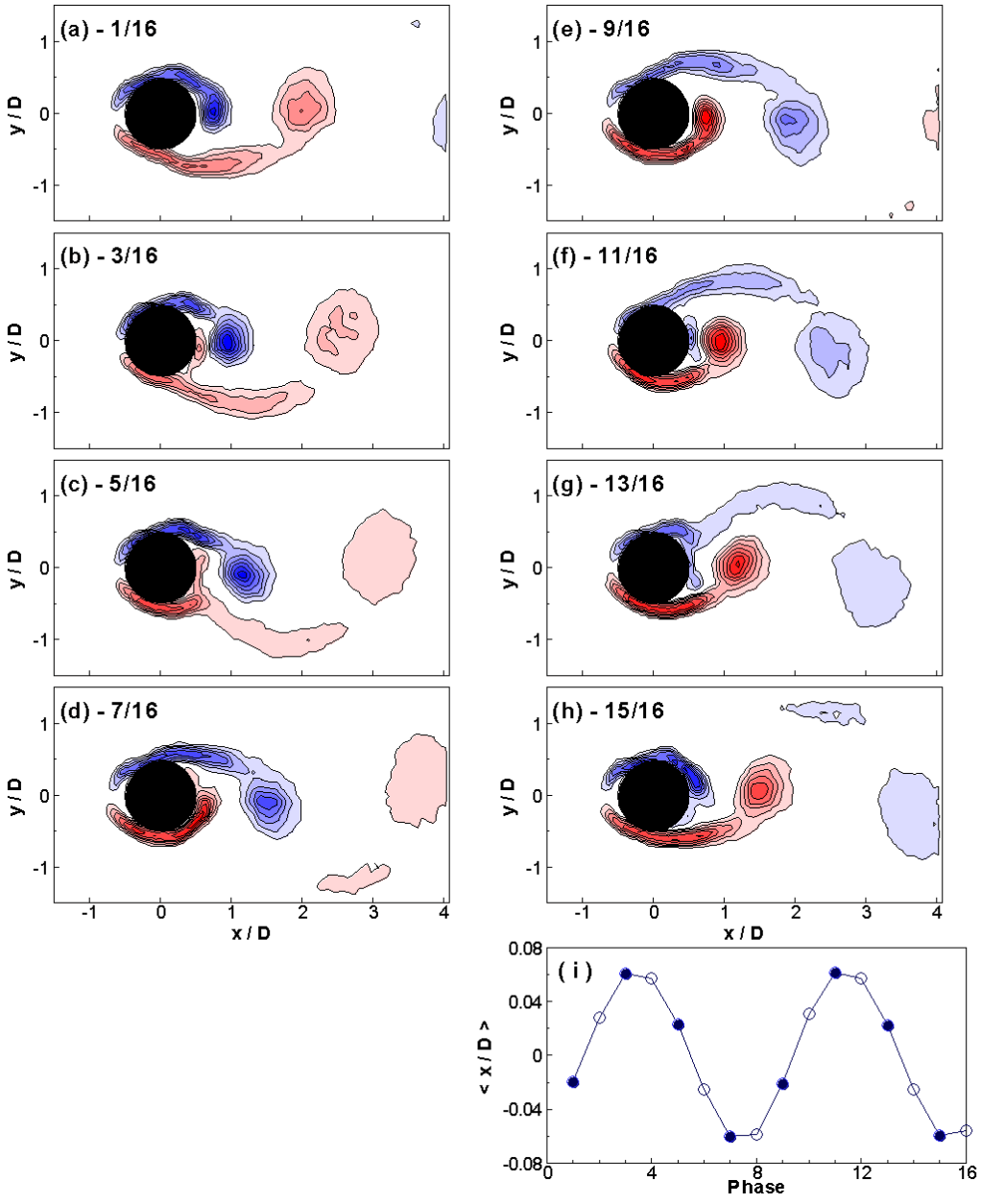

Figure 5.8: (a-h) Phase-averaged vorticity fields over one shedding cycle for $U_r\mathrm{St}/f^* = 0.565$, which corresponds to the peak of the second response branch. The fields are similar to those shown in Figure 3.12, which were calculated at the same region of the response regime, but at a slightly lower Reynolds number. The SA mode is clearly dominant. Contour levels are $\omega_z D/U_0 = \pm 1.5, \pm 3, \ldots$ The corresponding cylinder displacements are shown in (i).

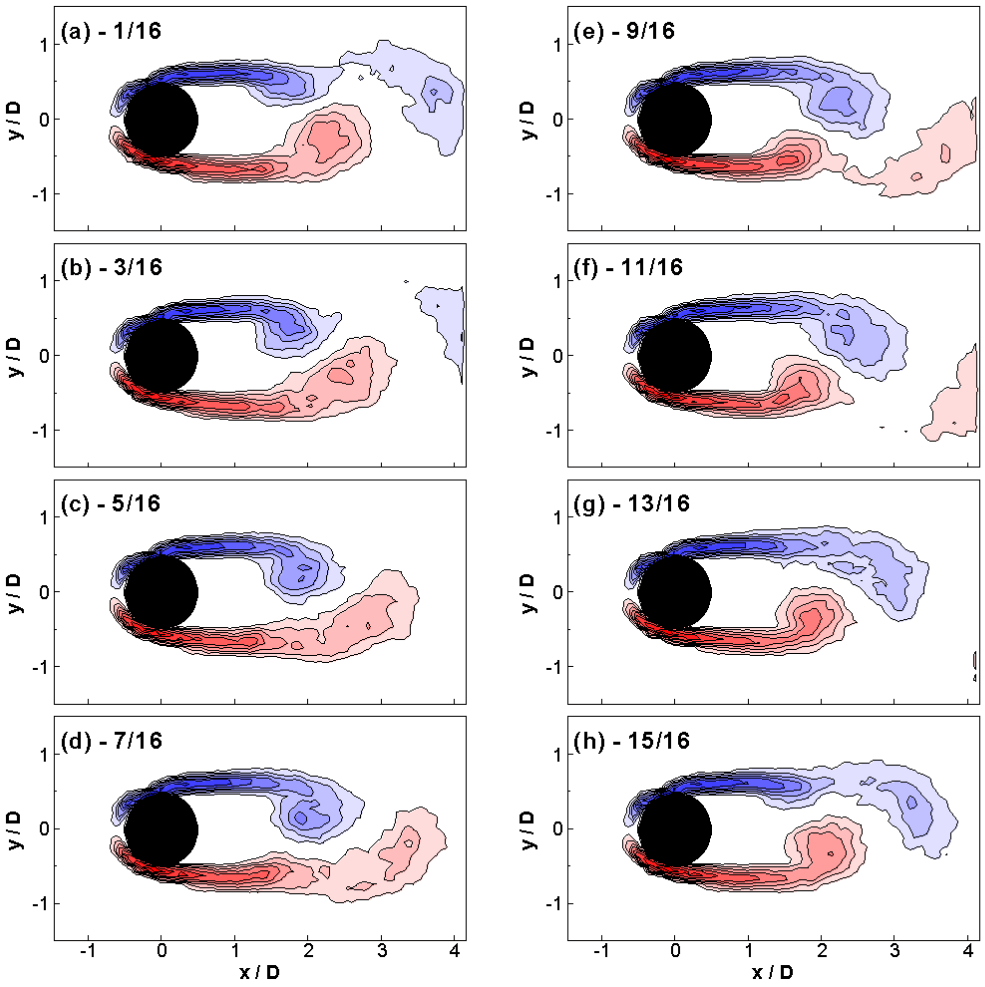

Figure 5.9: (a-h) Phase-averaged vorticity fields over one shedding cycle for $U_r\mathrm{St}/f^* = 0.556$, which was reached by decreasing the reduced velocity. The A-II mode is clearly visible. Contour levels are $\omega_z D/U_0 = \pm 1, \pm 2, \ldots$ The vortex shedding is not synchronised to the cylinder motion.

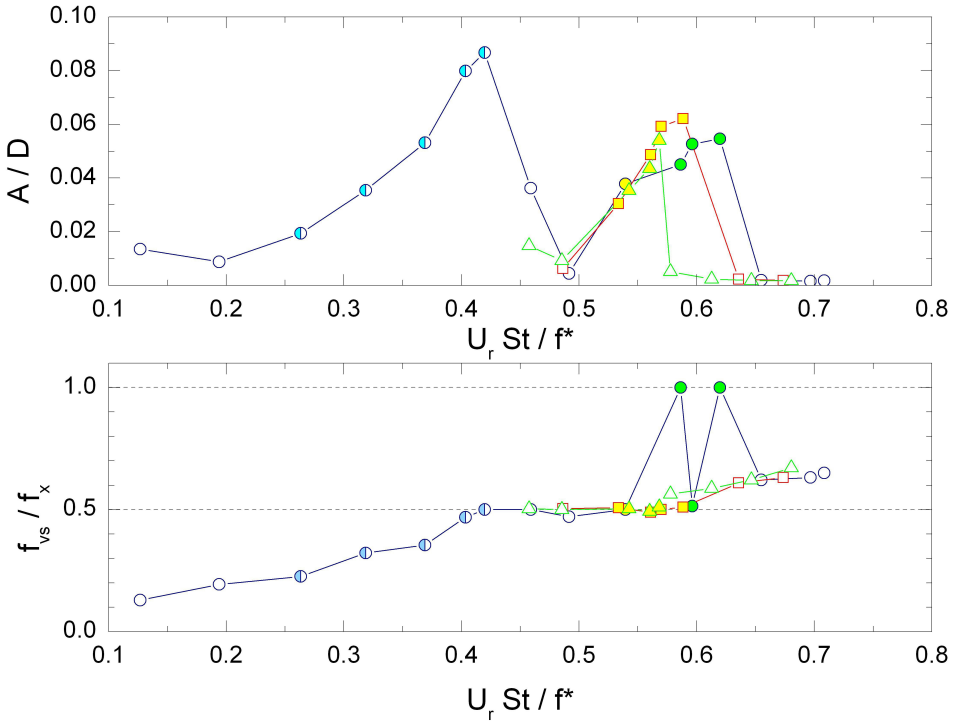

Figure 5.10: Variation of the cylinder amplitude response and wake frequency with reduced velocity: (a) amplitude response, (b) peak frequency of fluctuating velocity measured in $(x/D, y/D) = (3, 0.5)$, for three sets of PIV measurements listed in Table 5.2. The sets are referred to based on what wake mode dominates at $U_r\mathrm{St}/f^* \approx 0.56$: the A-IV set (circles), the SA set (squares), and the A-II set (triangles). The colours within each symbol denote the dominant wake mode observed; white, A-II; blue, S-I; yellow, SA; and green, A-IV. Symbols with two colours represent points at which mode-competition was observed. The reduced velocity was set by incrementally increasing (A-IV and SA sets) or decreasing (A-II set) the freestream velocity. In the latter case the cylinder response amplitude is greatly reduced over much of the second branch and the velocity fluctuations in the wake are not synchronised to the cylinder motion.

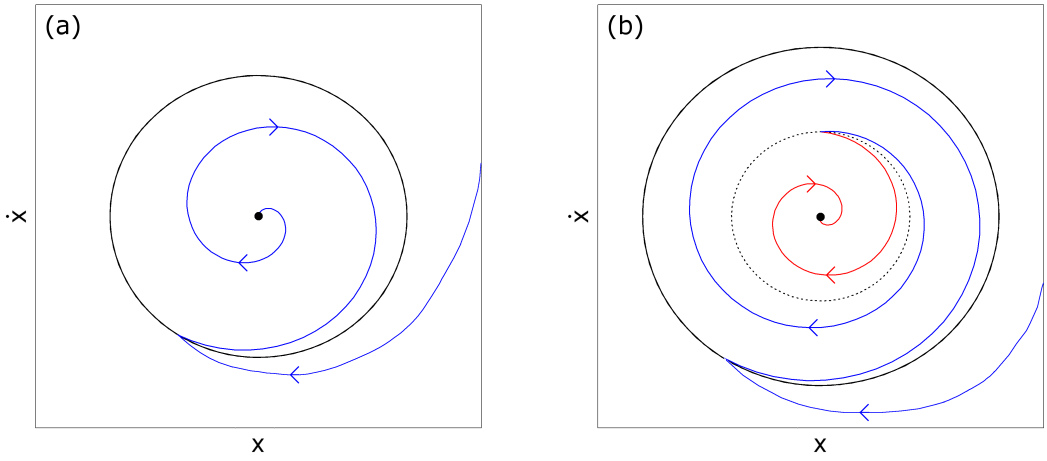

Figure 5.11: Sketches of the characteristic phase state portraits for a soft (a) and hard (b) oscillator. The solid black lines indicate paths followed by a body undergoing steady-state limit-cycle oscillations, while the blue and red arrows represent the system converging upon this path and the origin respectively. The origin corresponds to negligible response amplitude.

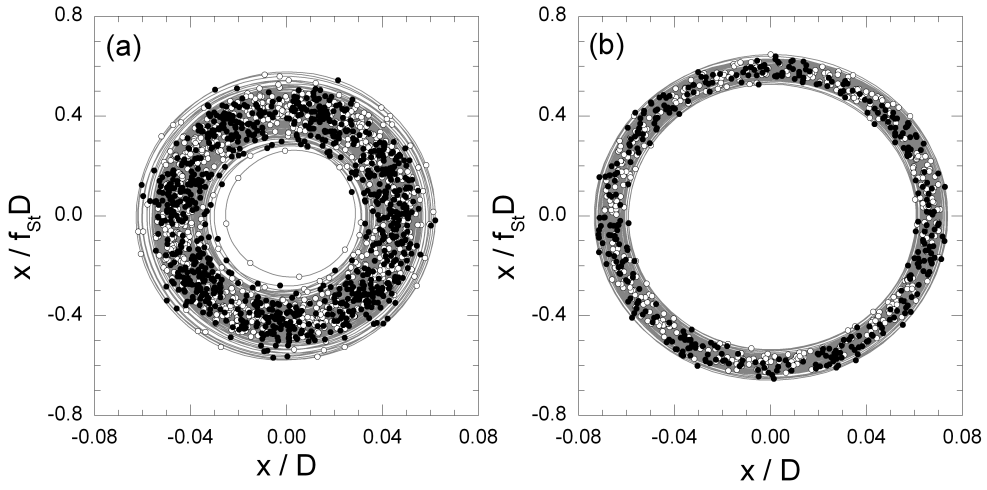

Figure 5.12: Phase-portraits of the cylinder response while the wake exhibited the A-IV mode at $U_r\mathrm{St}/f^* = 0.564$ (a), and the SA mode at $U_r\mathrm{St}/f^* = 0.566$ (b). The cylinder velocity was calculated from the displacement signal using the central-difference method. The white symbols indicates the points at which the amplitude of the displacement signal was increasing (i.e. the following peak was larger than the preceding peak), while the black points correspond to points at which the amplitude was found to be decreasing. For both modes, there is a broad band in which oscillations are possible.

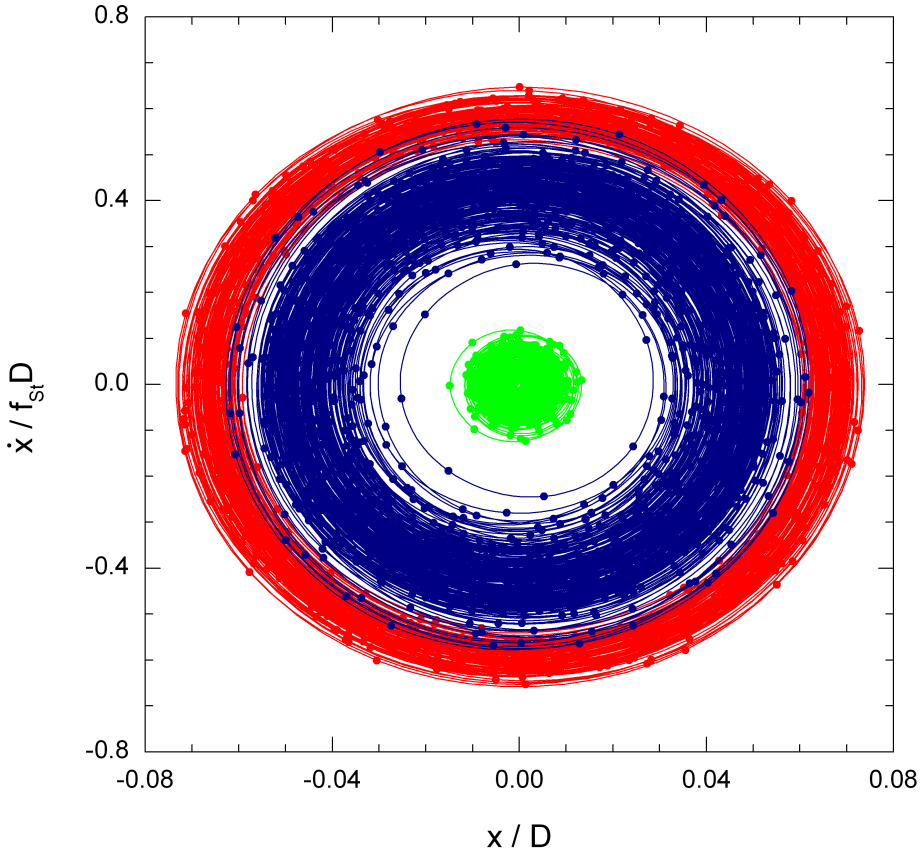

Figure 5.13: Phase-portrait of the cylinder response while the wake exhibited the A-IV mode ($U_r\mathrm{St}/f^* = 0.564$, blue), the SA mode ($U_r\mathrm{St}/f^* = 0.566$, red) and the A-II mode($U_r\mathrm{St}/f^* = 0.556$, green). The points in the displacement and velocity signals (circular symbols) were connected using splines to represent the trajectory of the system. The displacement signals were low-pass filtered with a cut-off frequency of 5Hz, and the first and last 100 data points were discarded to reduce any end-effects. The velocity signal was calculated from the displacement using the central difference method. Further experimental details for each case are given in Table 5.3.

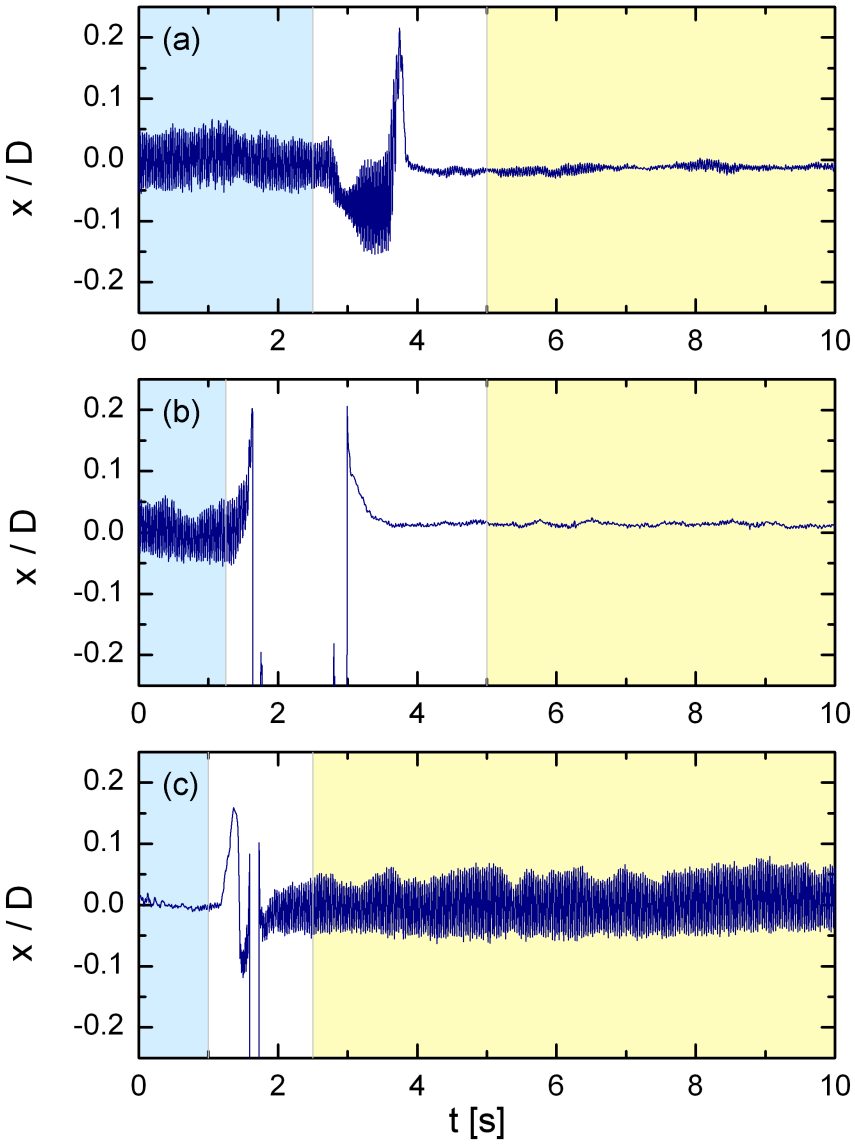

Figure 5.14: Displacement signals for measurements in which a perturbation was applied to the cylinder. The details of the measurements shown in (a)-(c) are presented in Table 5.4 (Cases 1-3, respectively). The blue and yellow regions indicate the segments of the PIV measurements which were used to estimate the cylinder response amplitude and frequency, and the dominant wake mode pre- and post-perturbation, respectively.

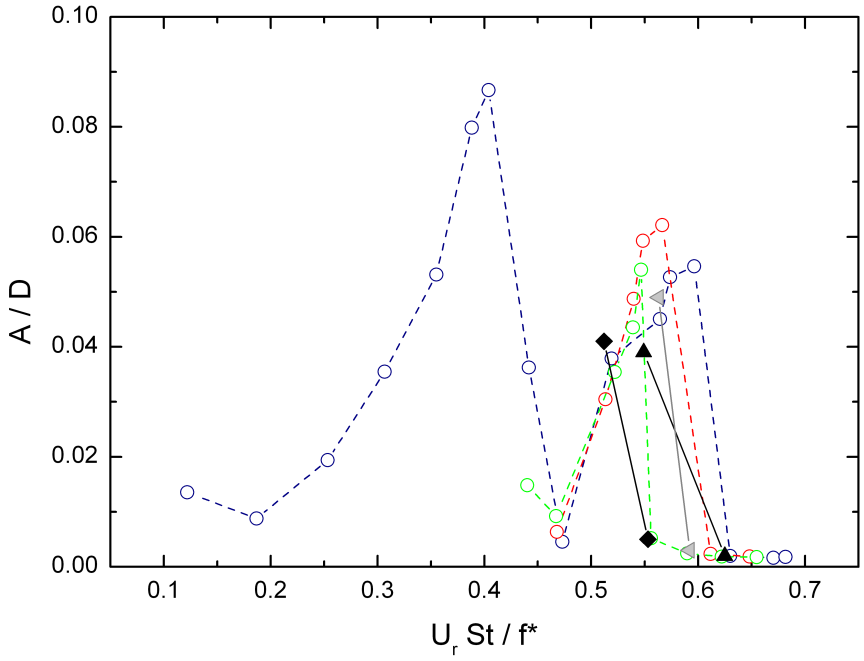

Figure 5.15: Amplitude response for the three sets of PIV measurements in which the cylinder was perturbed (closed symbols). The experimental details of the three sets of perturbed experiments are listed in Table 5.4. The results are superimposed upon the amplitude response measurements discussed in Section 5.6 (open symbols).

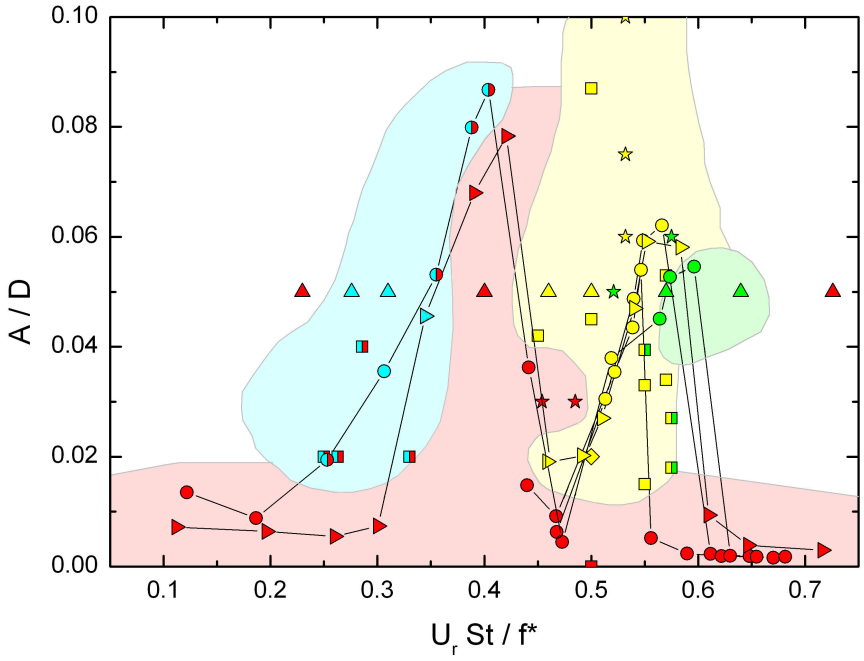

Figure 5.16: $U_r \mathrm{St}/f^* - A/D$ map showing the wake modes observed for various values of cylinder oscillation amplitude and reduced velocity in studies in the literature as well as the current work. The symbol colour denotes the wake mode observed: red (A-II), yellow (SA), green (A-IV) and blue (S-I), while unshaded regions correspond to areas where insufficient data was available to estimate the wake mode which may occur. Connected points correspond to the free vibration studies presented in this chapter (○) and in Chapter 3 (▷), while the scattered points are from studies in the literature, which are listed in Table 5.5. Split-colour symbols indicate points at which more than one wake mode was observed. The shaded regions are estimates of where each mode is expected to be dominant. The white regions indicate areas where no information on the wake is available.

Chapter 6

Estimation of Fluid Forces[1]

6.1 Introduction

The structural response and wake characteristics of a freely oscillating cylinder throughout the streamwise response regime have been described in the previous chapters. However, it is difficult to examine the effects of the wake modes on the response of the cylinder without knowledge of the associated fluid forcing. In particular, it remains unclear what causes the low amplitude response in the region $U_r\mathrm{St}/f^* \approx 0.5$, and what effects the multiple stability regions and wake modes observed in the second branch (described in Chapter 5) have on the levels of fluid forcing.

In order to investigate these questions, in this chapter, the forces acting on the cylinder are estimated throughout the response regime. Due to the nature

[1]The results in this chapter have also been presented in:

N. Cagney and S. Balabani. Unsteady fluid excitation in streamwise vortex-induced vibrations. In *10th International Conference on Flow-Induced Vibration (& Flow-Induced Noise)*, Dublin, Ireland, 2012. (http://www.fiv2012.com/site/view/46/)

of the cylinder supports (which were made of fishing wire) and the magnitude of the fluid forces acting on the structure (which were expected to be $\lesssim 0.1$N for all reduced velocities examined) it was not possible to measure the force directly using strain gauges. Two methods were used to estimate the forces; one based on the cylinder displacement signal and knowledge of the structural parameters, and a second method which utilised PIV measurements of the flow field surrounding the cylinder. Both methods were applied to the measurements discussed in Chapter 5 (i.e. those performed in Test Stage 2).

6.2 Displacement-Based Method

6.2.1 Derivation

Several researchers have modeled a cylinder free to move in the transverse direction as a simple harmonic oscillator in order to examine the dependence of the response amplitude on the magnitude and phase of the fluid forcing and structural parameters such as the mass ratio and damping (see, for example, reviews by Bearman [1984]; Sarpkaya [2004] and Williamson and Govardhan [2004], and the references cited therein). Khalak and Williamson [1999] showed that the same approach can also be used to derive information on the fluid force from the displacement signal *a posteriori*. The steady-state amplitude and phase of the fluid force in the direction of the cylinder motion can be expressed as a function of the vibration frequency and amplitude, the reduced velocity and various structural parameters. Khalak and Williamson found that the estimates were reasonably accurate when the mass ratio was low. Their analysis does not depend on the

direction in which VIV is occurring; it is equally applicable to oscillations in the streamwise direction, and is briefly summarised below, while a more comprehensive derivation can be found in the Appendix.

Table 6.1: Summary of the dimensionless groups used in derivation of the fluid forces from the cylinder displacement signal.

ζ_w	Combined structural and hydrodynamic damping ratio
$f^* = f_x/f_n$	Frequency ratio
U_r/f_nD	Conventional reduced velocity
$m^* = \frac{m}{\rho\pi D^2 L/4}$	Mass ratio
$C_a = \frac{\Delta m}{\rho\pi D^2 L/4}$	Added-mass coefficient
$\widetilde{C_D} = \lvert\widetilde{F_x}\rvert/\frac{1}{2}\rho U_0^2 DL$	Fluctuating drag coefficient

The derivation involves a number of dimensionless groups which are summarised in Table 6.1. The cylinder is assumed to have the characteristic equation of motion:

$$m_e\ddot{x} + c_e\dot{x} + kx = \widetilde{F_x}(t), \tag{6.1}$$

where m_e is the effective mass of the system ($m_e = m + \Delta m$, where m and Δm are the cylinder mass and added masses, respectively), c_e is the total damping coefficient of the system (structural and hydrodynamic), k is the stiffness of the system, and $\widetilde{F_x}(t)$ is the fluctuating drag force. The cylinder motion and fluid force signals are assumed to be sinusoidal, separated by a phase lag, $\phi_{x,D}$:

$$x(t) = A \sin\left(2\pi f_x t\right), \tag{6.2}$$

$$\widetilde{F_x}(t) = |\widetilde{F_x}| \sin\left(2\pi f_x t + \phi_{x,D}\right). \tag{6.3}$$

Only the component of the fluid forcing which occurs at the cylinder response frequency will affect the steady-state response amplitude. Therefore, the assumption in equation 6.3 that the forcing occurs at f_x is less restrictive than it may at first appear; the forcing signal may contain components occurring at a range of frequencies, but $|\widetilde{F_x}|$ relates only to the amplitude of the component occurring at f_x. Therefore, the analysis presented here is not restricted to cases in which the fluid forcing is locked-in to the cylinder motion, but is applicable throughout the response regime. However, outside of the lock-in range, the estimates of the fluctuating drag will relate to the fluid forces caused by turbulent buffetting and the cylinder motion, rather than those caused by the vortex-shedding.

Equation 6.2 can be differentiated to find expressions for the cylinder velocity and acceleration:

$$\dot{x}(t) = 2\pi f_x A \cos\left(2\pi f_x t\right), \tag{6.4}$$

$$\ddot{x}(t) = -4\pi^2 f_x^2 A \sin\left(2\pi f_x t\right). \tag{6.5}$$

Inserting these expressions and the relations for $x(t)$ and $\widetilde{F_x}(t)$ into equation 6.1, and utilising the non-dimensional groups summarised in Table 6.1, the steady-state cylinder response amplitude can be expressed as:

$$\frac{A}{D} = \frac{1}{4\pi^3} \frac{\widetilde{C_D} \sin\phi_{x,D}}{\left(m^* + C_a\right)\zeta_w} \left(\frac{U_r}{f^*}\right)^2 f^*, \tag{6.6}$$

where ζ_w is the damping coefficient measured in the fluid. This analysis can also describe the variation in the cylinder response frequency, using the concept of the 'effective added-mass coefficient', C_{ea} [Khalak and Williamson, 1999]. The standard added-mass coefficient, C_a, relates to the added-mass which occurs for a structure undergoing small amplitude oscillations, and controls the change in the natural frequency of a structure immersed in a fluid compared to that which occurs in a vacuum. C_{ea} describes the component of the added-mass of the system which is caused by the fluid forces in phase with the cylinder acceleration. It can be expressed in terms of the frequency ratio as;

$$f^* = \sqrt{\frac{m^* + C_a}{m^* + C_a + C_{ea}}}. \tag{6.7}$$

This expression can also be rearranged in order to calculate C_{ea} *a posteriori* from the displacement signal once the frequency ratio is known:

$$C_{ea} = (m^* + C_a)\left(\frac{1 - f^{*2}}{f^{*2}}\right). \tag{6.8}$$

Using equations 6.2, 6.3 and 6.7, the effective added mass can also be expressed in terms of the cylinder response characteristics and structural parameters:

$$C_{ea} = \frac{1}{2\pi^3}\frac{D}{A}\frac{\widetilde{C_D}\cos\phi_{x,D}}{(m^* + C_a)\,\zeta_w}\left(\frac{U_r}{f^*}\right)^2. \tag{6.9}$$

The above analysis is often used to indicate that the cylinder response amplitude is proportional to $\widetilde{C_D}\sin\phi_{x,D}$, while the effective added-mass coefficient, which controls the response frequency, is proportional to $\widetilde{C_D}\cos\phi_{x,D}$ (or C_L and $\phi_{y,L}$ in the case of transverse vibrations).

Khalak and Williamson [1999] combined equations 6.6 and 6.9 to produce expressions for the amplitude and phase of the fluid force:

$$\widetilde{C_D} = 2\pi^3\frac{A}{D}\left(\frac{f^*}{U_r}\right)^2\sqrt{C_{ea}^2 + \left(\frac{2\,(m^* + C_a)\,\zeta_w}{f^*}\right)^2}, \tag{6.10}$$

$$\phi_{x,D} = \tan^{-1}\left(\frac{2\,(m^* + C_a)\,\zeta_w}{f^* C_{ea}}\right). \tag{6.11}$$

They compared the estimates of the lift force acting on a transversely oscillating cylinder throughout the overall response regime found using Equation 6.10

to those directly measured using strain gauges, for two cylinders with mass ratios of 3.1 and 10.1, respectively. They found the method to be reasonably accurate for the low mass ratio cylinder, but the errors were quite large for the high m^* case; the errors in the maximum rms values of the lift force were approximately 6% and 33% respectively (see Figure 12 in Khalak and Williamson [1999]). They attributed this dependence of the accuracy on m^* to the difficulty in accurately measuring the frequency ratio of structures with high mass ratios, which are only weakly affected by the added-mass. In such cases f^* remains close to unity; small absolute errors in the measurement of f_x will therefore correspond to large relative errors in the measurements of C_{ea} using equation 6.8.

As the mass ratio of the present system is low ($m^* = 1.17$) and the changes in f^* were found to be relatively large (Figure 3.2(c)), this method can be expected to perform reasonably well.

The method also relies on the accurate measurement of other structural parameters, such as the structural damping and the natural frequency. The details of the tap tests used to evaluate these parameters were discussed in Section 2.3, and the results are summarised in Table 2.1. The natural frequencies measured in air and water were 33.16Hz and 23.703Hz, respectively, while the damping coefficient in water was $\zeta_w = 0.0198$.

The method also involves on the added mass coefficient, C_a, which can be shown theoretically to be equal to 1 [Khalak and Williamson, 1999]. By assuming the added mass effects to be negligible when the structure is vibrating in air, the added mass can be measured as:

$$C_a = m^* \left(\left(\frac{f_{n,a}}{f_n} \right)^2 - 1 \right), \tag{6.12}$$

where $f_{n,a}$ is the natural frequency measured in air. For the present system, this expression indicated $C_a = 1.11$, at low reduced velocities when the cylinder vibrations were small, which is close to the theoretical value of unity.

The steady-state response amplitude was taken as the mean peak height of the displacement signal (which was first band-pass filtered with cut-off frequencies of 10Hz and 40Hz), and the response frequency was measured using the Fast-Fourier Transform (FFT), which produced a finer frequency resolution than the PSD; for the displacement signals containing 2000 data point, the FFT has a resolution of 0.0988Hz or $0.0041 f_n$. The resolutions of the spectra of the signals containing 1000 points were half these values.

6.2.2 Results

The displacement-based method of force-estimation was applied to the three sets of PIV measurements discussed in Chapter 5. Each data set was found to contain a different wake mode in the region $U_r \mathrm{St}/f^* \approx 0.56$, and the sets are referred to as the A-IV, SA and A-II sets accordingly. The experimental details associated with each data set are summarised in Table 5.2.

The variation in the estimates of the amplitude and phase associated with the fluctuating drag coefficient with reduced velocity for each of the three data sets is shown in Figure 6.1. The variation in the amplitude response is also presented in Figure 6.1(a) for reference. The amplitude of the fluctuating drag is large

at low reduced velocities ($U_r\mathrm{St}/f^* \lesssim 0.44$ in the A-IV set). A local maximum occurs at $U_r\mathrm{St}/f^* = 0.39$, which approximately coincides with the peak of the first response branch. Nishihara et al. [2005] also observed large amplitude fluctuating drag forces acting on a cylinder undergoing forced streamwise vibrations ($A/D = 0.05$) at low values of $U_r\mathrm{St}/f^*$. This was also observed by Marzouk and Nayfeh [2009], who performed direct-numerical simulations (DNS) of a cylinder vibrating in the streamwise direction for a range of A/D and Re. By decomposing the signal into components in phase with the cylinder displacement and velocity, they showed that the large amplitude drag was caused by an increase in the inertial forces associated with the cylinder motion. Figure 6.1(c) shows that the phase lag between the forcing and the displacement is low for $U_r\mathrm{St}/f^* \lesssim 0.25$. This indicates that the fluid force acts in phase with the cylinder displacement and the inertial force acting on it (i.e. the d'Alembert force, $-m\ddot{x}$), as was found by Nishihara et al. [2005]. Equation 6.6 indicates that the amplitude response is proportional to $\sin\phi_{x,D}$. Therefore, the low $\phi_{x,D}$ value indicates that in spite of the large amplitude fluctuating drag in the region $U_r\mathrm{St}/f^* \lesssim 0.44$, the cylinder does not experience significant levels of fluid excitation, and the response amplitude remains low.

For $U_r\mathrm{St}/f^* \lesssim 0.22$ the A-II mode occurs consistently in the wake, and the vortices are shed at the Strouhal frequency. Despite the absence of lock-in, the cylinder experiences some excitation due to turbulent buffeting; therefore the cylinder response amplitude is non-zero, and Figure 6.1(c) indicates that the fluid forcing at f_x is not a damping force (which corresponds to $\phi_{x,D} < 0$). Post-lock-in, when the amplitude response is negligible (which occurs for $U_r\mathrm{St}/f^* \gtrsim 0.56-0.6$, depending on the data set), the phase lag is larger, indicating a drop in the flow-

induced inertial forces. As the inertial forces are low, and the A-II mode is not associated with significant fluid excitation, the total amplitude of the fluctuating drag also drops to a very low value (Figure 6.1(b)).

The phase lag between the drag and the cylinder motion does not vary significantly between the peak of the first branch and the low amplitude region at $U_r\mathrm{St}/f^* \approx 0.48$. This indicates that the sudden decrease in the amplitude response in this region is not caused by a change in $\phi_{x,D}$, as has been previously suggested [Nishihara et al., 2005]. In contrast, there is a dramatic change in $\widetilde{C_D}$ over this range. At $U_r\mathrm{St}/f^* = 0.47$ $\widetilde{C_D}$ has approximately the same amplitude as observed post-lock-in, when the amplitude response is also negligible. This indicates that the low amplitude observed in this region is caused by a reduction in the amplitude of the fluctuating drag force, rather than a change in its phase. This is discussed further in Section 6.3.7.

$\widetilde{C_D}$ is slightly larger when the A-IV mode dominates at $U_r\mathrm{St}/f^* \approx 0.56$ (blue symbols) compared to when the SA mode occurs (red symbols), although the difference is relatively small. However, the phase angle is larger when the SA mode dominates, indicating a slight increase in the fluid excitation. This coincides with an increased response amplitude (Figure 6.1(a)). This observation is similar to the change in the phase of the fluid forcing noted by Govardhan and Williamson [2000] between the regions of 2S and 2P vortex-shedding in transverse VIV. In both cases, the two possible modes induce similar levels of fluid forcing, but different levels of excitation to the structure. This leads to hysteretic behaviour in the cylinder response. The effect of the wake mode on the amplitude of the fluctuating drag is discussed further in Section 6.3.7.

6.3 Flow Field-Based Method

6.3.1 Derivation

The estimates of the fluid forces presented in the previous section were calculated *a posteriori* from the cylinder displacement signal, and contain no information derived from the flow. It is also possible to estimate the forces acting on the cylinder from measurements of the surrounding velocity field. This can be demonstrated by considering a body contained within a control volume, V, which is bounded by a surface, S, as shown in Figure 6.2. If the flow is incompressible, the force vector, $\mathbf{F}$, acting on the body is equivalent to the integral of the body forces acting within the control volume, and can be found by rearranging the integral form of the Navier-Stokes momentum equation:

$$\begin{aligned}\mathbf{F} = &-\frac{\mathrm{d}}{\mathrm{d}t}\int_V \mathbf{u}\mathrm{d}V \\ &+ \oint_S \mathbf{n}\cdot(-p\mathbf{I} - (\mathbf{u}-\mathbf{u_s})\,\mathbf{u} + \mathbf{T})\mathrm{d}S \\ &- \oint_{S_b(t)} \mathbf{n}\cdot(\mathbf{u}-\mathbf{u_s})\mathbf{u}\mathrm{d}S,\end{aligned} \tag{6.13}$$

where $\mathbf{n}$ is the unit vector normal to the control volume surface, S_b is the body surface, $\mathbf{u_s}$ is the velocity vector of the solid surface, p is the pressure field $\mathbf{T}$ is the viscous stress tensor. This tensor is defined as:

$$\mathbf{T} = \mu\left(\nabla\mathbf{u} + (\nabla\mathbf{u})^\top\right), \tag{6.14}$$

where μ is the dynamic viscosity of the fluid. In high Reynolds number flows the viscous forces are small and this term can often be neglected.

By assuming that the outer surface of the volume is fixed and the no-slip condition exists at the solid surface (i.e. $\mathbf{u} = \mathbf{u_s}$), equation 6.13 can be simplified to:

$$\begin{aligned} \mathbf{F} = &- \frac{\mathrm{d}}{\mathrm{d}t} \int_V \mathbf{u} \mathrm{d}V \\ &+ \oint_S \mathbf{n} \cdot (-p\mathbf{I} + \mathbf{T}) \mathrm{d}S. \end{aligned} \tag{6.15}$$

This expression for the fluid forces remains of little practical use in experimental studies, as the force still relies on the pressure field, which is difficult to measure experimentally. Various researchers have attempted to circumvent this difficulty by estimating the pressure term from measurements of the velocity field. Approaches have included a forward-marching integration algorithm to estimate the pressure along a contour line in a 2D flow field measured using PIV [Kurtulus et al., 2007] and the expression of the pressure field as a solution to the Poisson equation [de Kat and van Oudheusden, 2010]:

$$\nabla^2 p = \rho \nabla \left(\frac{\mathrm{D}\mathbf{u}}{\mathrm{D}t} + \nu \nabla^2 \mathbf{u} \right) \tag{6.16}$$

However, the forward-marching approach is highly vulnerable to noise [de Kat and van Oudheusden, 2010], while the solution of equation 6.16 requires a complex numerical implementation and the measurement of the velocity components and gradients in all three spatial directions [Charonko et al., 2010], which is difficult

to achieve experimentally.

Noca et al. [1997] used a series of algebraic manipulations to express the fluid forces as a function of only the velocity field and its spatial and temporal derivatives. In a subsequent paper [Noca et al., 1999], the fluid forces were presented in three formulations, the first of which was referred to as the 'Impulse Equation':

$$\begin{aligned}\frac{\mathbf{F}}{\rho} = &-\frac{1}{\mathcal{N}-1}\frac{\mathrm{d}}{\mathrm{d}t}\int_V \mathbf{x}\wedge\omega \mathrm{d}V \\ &+\oint_S \mathbf{n}\cdot\gamma_{\mathrm{imp}}\mathrm{d}S \\ &+\frac{1}{\mathcal{N}-1}\frac{\mathrm{d}}{\mathrm{d}t}\oint_{S_b(t)}\mathbf{x}\wedge(\mathbf{n}\wedge\mathbf{u})\,\mathrm{d}S,\end{aligned} \tag{6.17}$$

with

$$\begin{aligned}\gamma_{\mathrm{imp}} = &\frac{1}{2}u^2\mathbf{I}-\mathbf{u}\mathbf{u}-\frac{1}{\mathcal{N}-1}\omega(\mathbf{x}\wedge\mathbf{u}) \\ &+\frac{1}{\mathcal{N}-1}\Big(\mathbf{x}\cdot(\nabla\cdot\mathbf{T})\mathbf{I}-\mathbf{x}(\nabla\cdot\mathbf{T})\Big)+\mathbf{T},\end{aligned} \tag{6.18}$$

where $\mathbf{x}$ is the position vector, $[x, y, 0]^\top$, and $\mathcal{N}$ is the dimension of the control volume; $\mathcal{N} = 3$ for 3D measurements (e.g. Tomographic PIV), and $\mathcal{N} = 2$ for planar measurements. The formulations rely on the cross-product, which is only defined in three-dimensional space. Therefore, even if the flow is known to be entirely two-dimensional, the velocity, vorticity and position vectors are still treated as having three components. All measurements presented in this thesis are two-dimensional; therefore the control volume is 2D and $\mathcal{N} = 2$. The out-of-plane velocity, w, and all gradients in the z-direction are assumed to be zero. A

similar approach was used by Noca et al. [1999] when applying the method to two-component measurements of a 3D flow.

Using further algebraic manipulations, the force vector can be expressed as the 'Momentum Equation' (not to be confused with the Navier-Stokes momentum equation, from which it is derived), which does not rely on a surface integral at the body surface:

$$\begin{aligned}\frac{\mathbf{F}}{\rho} = &-\frac{\mathrm{d}}{\mathrm{d}t}\int_V \mathbf{u}\mathrm{d}V \\ &+ \oint_S \mathbf{n}\cdot\gamma_{\mathrm{mom}}\mathrm{d}S\end{aligned} \tag{6.19}$$

with

$$\begin{aligned}\gamma_{\mathrm{mom}} =&\frac{1}{2}u^2\mathbf{I} - \mathbf{uu} - \frac{1}{\mathcal{N}-1}\mathbf{u}(\mathbf{x}\wedge\omega) + \frac{1}{\mathcal{N}-1}\omega(\mathbf{x}\wedge\mathbf{u}) \\ &- \frac{1}{\mathcal{N}-1}\Big((\mathbf{x}\cdot\frac{\partial\mathbf{u}}{\partial t})\mathbf{I} - \mathbf{x}\frac{\partial\mathbf{u}}{\partial t}\Big) \\ &+ \frac{1}{\mathcal{N}-1}\Big(\mathbf{x}\cdot(\nabla\cdot\mathbf{T})\mathbf{I} - \mathbf{x}(\nabla\cdot\mathbf{T})\Big) + \mathbf{T}.\end{aligned} \tag{6.20}$$

A third formulation was also presented, which was referred to as the 'Flux Equation', and relied only on surface integrals. However, this was found to perform poorly compared to the Impulse and Momentum formulations, and is not discussed further here.

The control volume used in the present study was two-dimensional; therefore the volume and surface integrals become area and line integrals respectively. Furthermore, the resulting force vector is used to calculate the *sectional* force

coefficient vector $\mathbf{C_f} = [C_d, C_l, 0]^\top$ (which is denoted by lower case subscripts), rather than the *overall* force coefficient vector, $\mathbf{C_F} = [C_D, C_L, 0]^\top$ (upper case subscripts). The two vectors are related by:

$$\mathbf{C_F} = \frac{1}{L}\int_0^L \mathbf{C_f}(z)\mathrm{d}z \tag{6.21}$$

where L is the length of the cylinder. When the flow is fully two-dimensional both vectors are equal. However, when the flow becomes three-dimensional (as is the case in the experiments performed in this study), the variations in $\mathbf{C_f}$ along the cylinder span will act to reduce $\mathbf{C_F}$ due to destructive interference. Therefore the force estimates found using the formulations of Noca et al. will not be equal to those found using the displacement-based method presented in the previous section, regardless of the accuracy of either approach.

6.3.2 Validation

Before applying the formulations derived by Noca et al. to the PIV measurements presented in the previous chapter, the approach was applied to numerical data in order to estimate the accuracy of the method. The numerical data was provided by Lu and Papadakis [2011], who modeled a fixed cylinder in steady flow. Some of the conditions of the simulation are summarised in Table 6.2. The Reynolds number was 200, so the flow was laminar and two-dimensional. The simulations were therefore performed in a two-dimensional domain, with the velocity component and all gradients out of the plane equal to zero. The flow domain extended from $x/D = -16$ to 32 in the streamwise direction, and from $y/D = -16$ to 16

in the transverse direction. The computational mesh contained over $63,000$ cells, and was locally refined in the vicinity of the cylinder, as can be seen in Figures 6.3(a) and 6.3(b). A time-step of 8×10^{-3}s was employed, which corresponded to approximately 630 steps per vortex-shedding cycle. A more detailed description of the computational method can be found in Lu and Papadakis [2011]. The results of the simulation were found to closely match those of various experimental studies in the literature. However, in the present work the numerical data is used only to compare the estimates of the fluid forcing found using the formulations of Noca et al. to those found directly from the pressure and shear stresses acting on the cylinder. Therefore, it is of no importance whether the simulations are accurate.

Table 6.2: Boundary conditions and fluid and domain properties associated with the numerical data computed by Lu and Papadakis [2011]. The simulations model a fixed cylinder of diameter D in a freestream velocity U_0.

Freestream velocity	U_0	1 m/s
Cylinder diameter	D	1m
Fluid density	ρ	1000kg/m^3
Kinematic viscosity	ν	0.005m/s^2
Reynolds number	Re	200
Strouhal number	St	0.1976

The numerical data was used to acquire the velocity and acceleration fields surrounding the cylinder at eight points throughout the vortex-shedding cycle. These fields could then be used to create 'synthetic' PIV fields, similar to the PIV measurements described in Chapter 5, to which the force evaluation equations

will be applied later in this chapter. Each acceleration field was estimated by applying the central difference method to two velocity fields which were predicted by the simulations at times t and $t + \Delta t$ (where Δt is the numerical time-step, 8×10^{-3}s). The estimated acceleration field therefore corresponded to the time instant $t + \frac{\Delta t}{2}$. In order to evaluate the velocity field at the same instant, the velocity fields predicted at t and $t + \Delta t$ were averaged. A sample vorticity field calculated from the velocity field at one timestep is shown in Figure 6.4, which corresponds to the maximum in the lift force signal.

In order to replicate the spatial resolution of the PIV measurements, the numerical velocity and acceleration fields were interpolated onto a uniformly spaced grid, which was the same as that of the PIV measurements (i.e. it contained approximately 18 vectors per diameter, and had a streamwise and transverse span of $x/D = -1.38$ to 4.2 and $y/D = -1.66$ to 1.55, respectively) as shown in Figure 6.3(b). The fields were found using both linear and cubic spline interpolation; both methods were found to produce very similar fields and the choice of interpolation method did not have a noticeable effect on the accuracy of the force estimates. The following discussion relates to the fields found using linear interpolation.

The integration boundary used to apply the force-estimation algorithm is shown in Figure 6.5. The upstream and transverse boundaries lie along $x/D = -1$ and $y/D = \pm 1.25$, respectively, and the downstream position of the boundary is variable. The velocity gradients were found by applying the central-difference method to the interpolated data, i.e. the gradients were estimated from the synthetic PIV fields, rather than interpolating the exact values from the numerical simulations. The estimation of the gradients from the interpolated data (rather

than finding the gradients directly from the shape functions used in the simulations) is likely to introduce errors, but is more likely to replicate the errors that will occur when the method is applied to the PIV measurements.

Figure 6.6 shows the lift and drag coefficients measured directly from the pressure and shear stresses acting on the cylinder, and those estimated using the Impulse and Momentum Equations presented by Noca et al. (equations 6.17 and 6.19). In each case the viscous terms were neglected, and the downstream boundary of the control volume was fixed at $x/D = 1.11$. The force estimates found using both the Momentum and Impulse Equations appear to match the numerical estimates very closely. The mean errors of the drag and lift force estimates, ε_d and ε_l, respectively, are expressed by the mean of the absolute difference between the estimates of the force and the values found directly from the DNS data:

$$\varepsilon_d = \frac{1}{8}\sum_{i=1}^{8} |C_d(t_i) - C_{d,DNS}(t_i)|, \tag{6.22}$$

$$\varepsilon_l = \frac{1}{8}\sum_{i=1}^{8} |C_l(t_i) - C_{l,DNS}(t_i)|, \tag{6.23}$$

where C_d and C_l are the estimated force coefficients, $C_{d,DNS}$ and $C_{l,DNS}$ are the force coefficients found directly from the DNS measurements, and t_i is the time corresponding to each set of DNS data. It is useful to normalise the mean errors by the amplitudes of the fluctuating forces, which are estimated from the force

signals as:

$$\widetilde{C_{d,num}} = ((C_{d,DNS})_{max} - (C_{d,DNS})_{min})/2, \tag{6.24}$$

$$\widetilde{C}_{l,num} = ((C_{l,DNS})_{max} - (C_{l,DNS})_{min})/2, \tag{6.25}$$

in the drag and lift directions, respectively. The sub-script 'num' indicates that the amplitudes were estimated from the force signals calculated from the numerical data, in order to distinguish them from various other estimates of drag and lift coefficients discussed throughout this chapter.

The absolute and normalised values of ε_d and ε_l found using the Momentum and Impulse Equations are listed in Table 6.3. In all cases, the mean errors of the estimated coefficients were less than 4% of the amplitude of the force coefficient in that direction. These errors appear to be marginally lower than those found by Noca et al. [1999] when the authors applied the same formulations to numerical data of a transversely oscillating cylinder, despite the coarser spatial resolution used here. Both equations were applied to the numerical data for a range of conditions (which will be discussed in the following sections) and were found to produce approximately identical estimates of the fluid forcing. However, the Momentum equation has the advantage of not requiring any integrals to be evaluated around the cylinder surface when the cylinder is moving, which is the case in the present study. It was therefore decided to use the Momentum Equation

(equation 6.19), and the discussion and results presented in the following sections relate only to this formulation. The magnitude of the errors presented in Table 6.3 indicates that the force-evaluation algorithm is correctly implemented and, more generally, that under certain conditions it is capable of producing relatively high accuracy estimates of the fluid forces.

Table 6.3: Mean errors of the drag and the lift force estimates found using the Impulse and Momentum Equations.

Equation	ε_d	$\varepsilon_d/\widetilde{C}_{d,num}$	ε_l	$\varepsilon_l/\widetilde{C}_{l,num}$
Impulse	0.0028	0.0348	0.0511	0.0345
Momentum	0.0026	0.0320	0.0569	0.0373

In the following sections the sensitivity of the method to various conditions is examined with a view to estimating its accuracy when applied to the PIV measurements in this study. The following sections examine the effects of (a) the inclusion of viscous terms, (b) the choice of integration boundary, and (c) the effect of noise in the estimated velocity and acceleration fields. While a comprehensive review of all the errors associated with the method is beyond the scope of this work, the sources of error discussed in the following sections were thought to have the most significant effect of the performance of the Momentum Equation.

6.3.3 Effect of Viscous Terms

The estimates of the fluid forcing presented so far have neglected the viscous terms in the formulations of Noca et al. Figure 6.7 compares the fluid forces estimated

with the viscous terms both included and neglected. The inclusion of the viscous terms does not appear to have a significant effect on the accuracy of the lift force estimates. In contrast, the inclusion of the viscous terms dramatically reduces the accuracy of the estimates of the drag force. While Figure 6.7 suggests that the mean drag coefficient is roughly unchanged, the amplitude of the fluctuating drag signal has increased significantly, and the estimate of the signal no longer occurs at twice the frequency of the lift force.

The estimation of the viscous terms depends on the second derivative of the velocity field. The determination of spatial gradients from discrete measurements of a continuous variable is associated with errors, which tend to increase with the order of differentiation. The differentiation also tends to amplify the errors associated with noise in the original measurements, which may be the cause of the poor performance of the Momentum Equation when the viscous terms are included.

The viscous terms are proportional to the kinematic viscosity of the fluid, and are therefore likely to be very small for intermediate or high Reynolds number flows or flows in water. The previous discussion indicates that at low Reynolds number (Re = 200), the omission of the viscous terms does not prevent the Momentum Equation from producing accurate estimates of the fluid forcing. In the PIV measurements described in Chapter 5, the Reynolds number is larger and the kinematic viscosity is significantly lower ($\nu = 0.96 \times 10^{-6}\mathrm{m}^2/\mathrm{s}$ for water at $22°C$). Therefore the viscous terms are likely to have a significantly weaker effect on the force estimates and can safely be neglected in the present analysis.

6.3.4 Choice of Integration Boundary

If the equations used to estimate the fluid forces are fully closed, the estimates should be independent of the choice of integration boundary. However, as the measurements of the flow field are discrete and subject to errors, the estimates of the force will also contain errors, the magnitude of which may be affected by the choice of integration boundary. The integration boundary had fixed upstream and transverse positions of $x/D = -1$ and $y/D = \pm 1.25$ respectively, and a variable downstream position in the range $x_b/D = 1 - 4$, as shown in Figure 6.5. By varying x_b the effect of the choice of integration boundary on the accuracy of the estimates of the fluid forces could be examined.

The Momentum Equation was used to estimate the force coefficient at each of the eight points throughout the vortex-shedding cycle for a range of values of x_b. The variation in the normalised mean errors of the estimates are shown in Figure 6.8. The drag coefficient is most accurate when $x_b/D = 1.11$ (which corresponds to the estimates of the fluid forcing presented in Figures 6.6 and 6.7). The relative accuracy of the lift coefficient remains roughly constant at $\varepsilon_l/\widetilde{C}_{l_{num}} \approx 0.2$ for a wide range of x_b. For $x_b/D \gtrsim 1.3$ the relative errors in the estimates of the drag coefficient are larger than those of the lift. These errors increase significantly for $x_b/D \gtrsim 2.5$, exceeding the amplitude of the fluctuating drag force at $x_b/D \approx 3$. The cause of this sudden loss of accuracy for $x_b/D \gtrsim 2.5$ is not clear, as it does not coincide with any significant change in the wake structure or the density of the computational mesh (Figure 6.5).

It thus appears that the accuracy of the estimates of the lift coefficient is only weakly dependent on the integration boundary for $x_b/D = 1 - 4$, while the

drag estimates become significantly less accurate when the integration boundary is chosen far from the cylinder.

6.3.5 Effect of Measurement Noise

The discussion of the accuracy of the fluid force estimates in the preceding sections concerned the details of the implementation of the method, rather than the effects of the actual velocity measurements. In practice, the performance of the Momentum Equation is likely to be strongly dependent on the accuracy of the measurements of the flow field. In order to investigate this, various levels of noise were added to the velocity and acceleration fields and the effect upon the final estimates of the fluid forces was examined. The *rand* function in Matlab was used to generate the random noise, which was uniformly distributed in the range $(-\frac{R_f U_0}{100}, \frac{R_f U_0}{100})$, where R_f is the percentage of the maximum noise relative to the freestream velocity, U_0. The noise was added to the streamwise and transverse components of the velocity and acceleration fields.

The effect of the various levels of added noise on the vorticity fields calculated from a sample velocity field is shown in Figure 6.9. For the range of noise levels examined ($R_f = 0 - 10\%$), the dominant vortical structures in the wake remain distinct.

Figure 6.10 shows the drag and lift coefficients throughout the vortex-shedding cycle, computed for a range of added noise levels. At levels of 1.5% noise and above, the estimated drag coefficent bears little qualitative resemblance to that extracted directly from the numerical results. The estimated lift coefficients are also affected by the noise, but in this case all the signals shown are qualitatively

similar to the DNS-signal.

The variation in the absolute and normalised errors of the drag and lift signals with added noise is shown in Figure 6.11. The absolute errors of both components of the force signal are similar for a broad range of noise levels (Figure 6.11(a)). However, as the amplitude of the fluctuating drag is considerably lower than that of the lift, the normalised errors in the drag estimates are significantly higher (Figure 6.11(b)).

Figure 6.11 indicates that the mean errors in the lift signal do not exceed $\widetilde{C}_{l,num}$ for the majority of the noise levels examined. However, approximately 0.6% noise is sufficient to cause large relative errors ($\widetilde{\varepsilon_d}/C_{d,num} > 1$) in the estimates of the drag.

It is clear from the results presented here that the relative accuracy of the estimated drag signal is highly dependent on the accuracy of the velocity and acceleration measurements. The discussion in the preceding sections also indicates that the predictions of the drag are less robust than those of the lift in terms of the estimation of the viscous component of the force and the choice of integration boundary. In spite of these errors, the Momentum Equation is capable of estimating the fluid forces acting in both directions to a very high level of accuracy under certain conditions (Figure 6.6), which are similar to those of the PIV measurements acquired.

6.3.6 Application to PIV Measurements

The Momentum Equation was applied to each of the three sets of PIV measurements discussed in Chapter 5 and in Section 6.2.2. The implementation of

the Momentum Equation to the PIV measurements was identical to that of the numerical data. The acceleration fields were found using the central-difference method, i.e. the acceleration field at time t was found using the velocity fields measured at $t-\Delta t$ and $t+\Delta t$, where $\Delta t = 0.05$s (i.e. the inverse of the sampling rate, which was 200Hz). The downstream position of the integration boundary was varied in the range $x_b/D = 1-4$. The drag and lift signals were low-pass filtered with a cut-off frequency of 40Hz. The mean component of the filtered drag signal was subtracted to find the fluctuating drag. The amplitudes of the estimated fluctuating drag and lift coefficients expressed in term of the rms of the filtered signals, and denoted $\widetilde{C_{d,rms}}$ and $\widetilde{C_{l,rms}}$, respectively.

Selected results of the variation in the drag coefficient at $U_r\mathrm{St}/f^* = 0.253$, which corresponds to the low amplitude region before the onset of the first response branch, are shown in Figure 6.12. The amplitude of the fluctuating and mean drag coefficients (blue symbols in Figures 6.12 (a) and (b), respectively) show significant fluctuations as the integration boundary is varied in the range $x_b/D = 1-2.5$, but the values appear to converge beyond this point. In order to analyse the cause of these fluctuations further, the force signal is decomposed into an acceleration term, $\mathbf{C_{acc}}$ (equal to the volume integral in Equation 6.19, $-\frac{\mathrm{d}}{\mathrm{d}t}\int_V \mathbf{u}\mathrm{d}V$) and a convective term, $\mathbf{C_{con}}$ (equal to the surface integral in Equation 6.19, $\oint_S \mathbf{n}\cdot\gamma_{\mathrm{mom}}\mathrm{d}S$), which are indicated by the red and green symbols, respectively. The total force can thus be expressed as the sum of the acceleration and convective terms.

Figure 6.12(a) indicates that the variations in the amplitude of the estimated fluctuating drag force for $x_b/D < 2.5$ can be attributed to similar variations in the convective term. The amplitudes of the acceleration and convective terms

exhibit an approximately linear increase as x_b moves further from the cylinder, $x_b/D > 2.5$, while amplitude of the overall drag coefficient is approximately constant.

The fluctuations observed in the amplitude of the drag estimates for x_b values close to the cylinder may be due to errors in the PIV measurements, which are likely to be less accurate in the near wake, due to the high levels of shear and vorticity in this region. The accuracy of the estimates of the velocity and acceleration fields have been shown to have a significant effect on the performance of the Momentum Equation (Section 6.3.5). The estimates of the velocity fields (and the acceleration and vorticity fields and γ_{mom}) are more accurate when x_b is chosen further downstream, and the errors in the final force estimates are also lower.

The improved performance of the Momentum Equation at large values of x_b/D is counter to the trend observed during its application to the numerical data; in that case the equation performed very well for $x_b/D \approx 1$, but became less accurate as x_b increased (Figure 6.8). However, for the numerical case, the accuracy of the velocity measurements is likely to depend not on the local shear (as in the PIV measurements), but on the local mesh density (as interpolation errors were larger in regions of low mesh density). As the mesh density is high close to the cylinder (Figure 6.3), the synthetic PIV fields used to estimate the force are more accurate in this region, and the resulting force estimates are also more accurate.

It is also significant to note that although the amplitude of the fluctuating drag coefficient converges as x_b/D increases, the amplitudes of the acceleration and convective components do not. While the decomposition of the fluid force

into these two components is useful in terms of analysing the source of errors in the signals, it is apparent that the magnitude of the various components depends on the choice of integration boundary. Therefore, this decomposition cannot be used to determine the physical origin of the fluid forces acting on a body, as has been performed by previous researchers (e.g. Kurtulus et al. [2007]).

The convective term accounts for almost the entirety of the mean drag coefficient; as the freestream flow is steady, the time-averaged acceleration fields and their volume integral term will tend to zero. Therefore, the inaccuracies in estimating the convective term are responsible for the significant variations in the estimated values of $\overline{C_d}$ for $x_b/D < 2.5$ (Figure 6.12(b)).

The phase lag between the cylinder displacement and the drag force was found by comparing the phase angles of the FFT spectra occurring at f_x. Figure 6.12(c) shows the variation in phase lag with x_b. Similar to the amplitude of mean and fluctuating drag components, $\phi_{x,D}$ appears to converge after some minor fluctuations at $x_b/D < 2.5$.

In contrast to the drag coefficient, the amplitude of the estimated lift coefficient does not converge for $x_b/D \leq 4$ (Figure 6.13(a)). The value of $\widetilde{C_l}$ and the amplitude of the convective term in this direction show fluctuations as x_b is varied, but unlike the fluctuations shown in Figure 6.12(a) for the drag coefficient, these fluctuations are present throughout the entire x_b range examined. The amplitude of C_l also tends to gradually increase with x_b.

The variations in the phase lag between the transverse velocity measured at $(x/D, y/D) = (3, 0)$ and the estimated lift signal and its convective and acceleration terms are shown in Figure 6.13(b). The location at which the velocity is measured is arbitrary, but serves as a reference signal to show any variation in

the phase of the force signal estimated for various values of x_b. The phase lag of the acceleration term is largely independent of x_b, but that of the convective term and the overall lift signal are highly variable; both exhibit jumps of $\pm\pi$, and tend to gradually to increase with x_b.

In general, the estimates of the lift force do not converge within the range of x_b examined, and appear to be significantly less accurate than those of the drag. This is in contrast to what was observed when the method was applied to the numerical data. It appears that the freedom of the cylinder to move in the streamwise direction - even at low response amplitudes - significantly alters the wake and the performance of the Momentum Equation. Apparently the nature of the flow regime has a significant effect on the accuracy of the force estimates, as was found by Charonko et al. [2010], when estimating the pressure field from PIV measurements.

The trends discussed above for the selected set of PIV measurements at $U_r\mathrm{St}/f^* = 0.253$ were broadly observed over the range of reduced velocity examined, and can be summarised as:

(i) The amplitudes of the mean and fluctuating drag coefficients converged for $x_b/D \geq 2.5$.

(ii) The amplitude of the lift coefficient did not appear to converge for $x_b/D < 4$, but tended to increase steadily with x_b.

(iii) The phase of the lift signal calculated at various values of x_b was highly variable (measured with respect to an arbitrary reference signal occurring at the same frequency).

Based on these observations, it was decided to ignore all estimates of the fluid forces computed for $x_b/D < 2.5$, i.e. before the estimates of $\overline{C_d}$ and $\widetilde{C_d}$ had converged. While the amplitude of the fluctuating drag was found to converge quickly at $U_r\mathrm{St}/f^* = 0.263$ for $x_b/D > 2.5$, at other reduced velocities some fluctuations were still observed. In order to evaluate the convergence of the estimates of the fluctuating drag throughout the response regime, histograms of the estimates of $\widetilde{C}_{d,rms}$ for $x_b/D > 2.5$ were evaluated for each set of PIV measurements. Histograms measured for four selected reduced velocities are shown in Figure 6.14, which corresponded to a low reduced velocity before the onset of the first branch ($U_r\mathrm{St}/f^* = 0.253$), a point near the peak of the first branch ($U_r\mathrm{St}/f^* = 0.404$), the low amplitude region ($U_r\mathrm{St}/f^* = 0.473$) and the peak of the second branch ($U_r\mathrm{St}/f^* = 0.596$). For most cases (e.g. $U_r\mathrm{St}/f^* = 0.243, 0.404$ and 0.473, shown in Figures 6.14(a-c)), the estimates of $\widetilde{C_d}$ appear to have converged; although some scatter is present, the estimates are clearly centred about a mean value. However, for other cases - particularly while the A-IV mode dominated and post-lock-in, two cases in which the vortical structures in the wake were relatively weak or variable - there is a considerable degree of scatter ($U_r\mathrm{St}/f^* = 0.596$, Figure 6.14(d)).

The phase lag between the drag and the cylinder displacement signals also showed some scatter at certain reduced velocities. Histograms of the estimated phase lag are shown in Figure 6.15 for the same four reduced velocities presented in the previous figure. The cases in which there is significant scatter in the estimates of $\widetilde{C}_{d,rms}$ do not always coincide with large scatter in the estimates of $\phi_{x,D}$. For example, at $U_r\mathrm{St}/f^* = 0.596$, $\widetilde{C}_{d,rms}$ shows significant scatter, while $\phi_{x,D}$ is clearly centred at approximately ± 0.1 rad (Figures 6.14(d) and 6.15(d),

respectively). The opposite trend is apparent at $U_r\mathrm{St}/f^* = 0.473$, in which case $\widetilde{C_d}$ is well-ordered and $\phi_{x,D}$ shows significant scatter (Figures 6.14(c) and 6.15(c), respectively).

Averaging the force signals estimated for integration boundaries in the range $x_b/D = 2.5-4$ may appear to be a suitable method of tackling the fluctuations in the properties of the signals estimated in this range (i.e. to find one drag and one lift signal for each reduced velocity). However, due to the variation in the phase angles of the signals, this method is not appropriate. While the different signals calculated at a given reduced velocity may have an average amplitude which can readily be identified, the signals may also occur at different phases; which implies that averaging might reduce the amplitude due to destructive interference.

An alternative approach to averaging the force signals would be to average the amplitudes of the components of the fluids forces found for each value of x_b/D in the range $2.5-4$. The standard deviation of the estimates of the amplitude of the fluctuating drag coefficient, $\sigma(\widetilde{C_{d,rms}})$, was used to define the errors associated with the method of force estimation. The final estimate of the fluctuating drag coefficient was thus given by:

$$\widetilde{C_{d,rms}} = \frac{1}{N_b} \sum_{x_b/D=2.5}^{4} \widetilde{C_{d,rms}}(x_b) \pm 1.645\sigma(\widetilde{C_{d,rms}}), \tag{6.26}$$

where N_b is the number of downstream integration boundaries at which the Momentum Equation was applied in the range $x_b/D = 2.5 - 4$ ($N_b = 27$ in this study), and $\widetilde{C_{d,rms}}(x_b)$ is the amplitude of the fluctuating drag coefficient computed at a given value of x_b. If the fluctuations are normally distributed, the

factor of 1.645 in Equation 6.26 indicates a 95% confidence that the true estimate of the $\widetilde{C_{d,rms}}$ lies within the specified error range. The amplitude of the mean drag coefficient was calculated in a similar manner.

This approach was not used to estimate the amplitude of the lift coefficient, as the estimates were not observed to converge at any reduced velocity examined. Nor was this method applied to the phase angles of the lift or the drag signals, as the mean is not a statistically valid representation of variables which are defined in a modular space (in this case the phase angle is defined in the range $(-\pi, \pi)$, and $\phi_{x,D} = \phi_{x,D} \pm 2\pi$). Therefore the method outlined above provides estimates only of the amplitude of the mean and the fluctuating drag.

6.3.7 Results

Figure 6.16 shows the variation of the fluctuating and mean drag coefficients throughout the response regime. The amplitude response of the cylinder is also shown for reference. The shaded regions denote the dominant wake mode.

The amplitude of the fluctuating drag coefficent is very large at low reduced velocities. This trend was also seen in the estimates derived from the displacement-based method (Figure 6.1), as well as in the results of Nishihara et al. [2005] and Marzouk and Nayfeh [2009]. The fluctuating forcing amplitude decreases slightly near $U_r\mathrm{St}/f^* \approx 0.22$, before increasing again as the cylinder response amplitude becomes larger in the first branch. $\widetilde{C_{d,rms}}$ has a local maximum at $U_r\mathrm{St}/f^* = 0.388$, which is near the peak of the first branch ($U_r\mathrm{St}/f^* = 0.404$). As the reduced velocity increases further, the A-II mode becomes fully dominant ($U_r\mathrm{St}/f^* \gtrsim 0.41$) and the response amplitude is reduced, which coincides

with a decrease in $\widetilde{C_{d,rms}}$. The amplitude of the fluctuating drag coefficient is recovered during the second branch when the SA and A-IV modes occur, but it remains lower than that observed in the first branch. Post-lock-in, the wake reverts to the A-II mode and $\widetilde{C_{d,rms}}$ falls to approximately 0.6, which is close to the value observed during the low amplitude response region at $U_r\mathrm{St}/f^* \approx 0.48$. As the force-estimation method could not be used to find accurate measurements of the phase difference between the cylinder displacement and the drag signals, it is not possible to examine the hypothesis that the low amplitude region at $U_r\mathrm{St}/f^* \approx 0.48$ is caused by a change in $\phi_{x,D}$ in this region, which prevents energy transfer to the cylinder [Konstantinidis et al., 2005; Nishihara et al., 2005]. However, Figure 6.16(b) indicates that $\widetilde{C_{d,rms}}$ is very low in the region, which is consistent with the results found using the displacement-based method (Section 6.2.2). Both approaches indicate that the reduction in the amplitude response near $U_r\mathrm{St}/f^* \approx 0.48$ may be explained by the simultaneous reduction in $\widetilde{C_{d,rms}}$. As far as the author is aware, this represents the first time that the drag force acting on a cylinder free to move in the streamwise direction has been examined, and the results presented here provide an explanation for the counter-intuitive reduction in the cylinder amplitude response at the onset of lock-in which has not previously been hypothesised.

In Chapter 3 it was noted that there was a change in the phase of the vortex-shedding with respect to the cylinder motion between the low amplitude region and the second branch, which had previously been proposed as a cause of the reduction in A/D at $U_r\mathrm{St}/f^* \approx 0.5$ [Konstantinidis et al., 2005; Nishihara et al., 2005]. This hyposthesis is not inconsistent with the results presented in Figure 6.16; it is possible that there is a change in both the amplitude *and* phase of the

fluctuating drag force in this region. However, the estimates of $\phi_{x,D}$ presented in Figure 6.1 do not reveal a significant change in the phase of the force near $U_r\mathrm{St}/f^* \approx 0.48$, and the estimates of $\widetilde{C_{d,rms}}$ and $\widetilde{C_D}$ found using both methods indicate that the reduction in the fluctuating forcing in this region is sufficient to reduce the vibration amplitude.

The estimated mean drag coefficient is shown in Figure 6.16(c). The uncertainty in the estimation of $\overline{C_d}$ is considerably larger than that of the fluctuating drag. Pre-lock-in, as the A-II mode dominates, the mean drag is in the range $\overline{C_d} = 0.65 - 0.95$. The mean drag decreases as the S-I mode occurs in the wake at $U_r\mathrm{St}/f^* \approx 0.22 - 0.4$, reaching a minimum of $\overline{C_d} = 0.505$ at $U_r\mathrm{St}/f^* = 0.355$. There is a sudden rise in $\overline{C_d}$ at the peak of the first branch, which approximately coincides with the region in which the A-II mode becomes fully dominant $U_r\mathrm{St}/f^* \gtrsim 0.42$. The mean drag coefficient increases further in the second branch. It is slightly larger when the A-IV mode dominates (and the response amplitude is larger), reaching a maximum value of 1.55 at the peak of the branch. Post-lock-in, the mean drag coefficient falls to approximately 1.2.

Anderson [1991] measured the mean (overall) drag coefficient for a stationary cylinder for a range of Reynolds numbers, which is indicated by the solid red line in Figure 6.16(c). Pre- and post-lock-in the cylinder response amplitude is low and the system may be viewed as equivalent to the stationary cylinder case. The estimated values are slightly larger post-lock-in, but tend to be close to those measured by Anderson when the cylinder response amplitude is low, suggesting that the estimates of $\overline{C_d}$ are reasonably accurate.

The fluctuating drag estimated using the displacement- and flow-based methods are compared in Figure 6.17(a). It should be noted that the amplitudes

estimated using both methods are not equivalent; the flow-based method estimates the *sectional* force coefficients, which will tend to be lower than the *overall* force coefficients predicted by the displacement-based method. The methods used to determine the two forms of the drag coefficient in this study are also different; the overall drag found from the displacement signal represents only the component of the force acting at the cylinder response frequency, while the value of $\widetilde{C_{d,rms}}$ found from the PIV measurements is the root-mean-square of the fluctuating drag signal which occurs in the range $0 - 40$Hz (as the signals are low-pass filtered with a cut-off frequency of 40Hz). Therefore, regardless of the accuracy of either method of force-estimation, the trends of $\widetilde{C_d}$ and $\widetilde{C_D}$ found throughout the response regime are unlikely to collapse. However, both methods produce the same trend regarding the variation of the fluctuating drag coefficient, as can be seen in Figure 6.17(a). The values of $\widetilde{C_d}$ found using the Momentum Equation appear to have a fixed offset with respect to the overall drag coefficient. Figure 6.17(b) shows the two sets of estimates with a fixed value $C_{d,o} = 0.467$ subtracted from the fluctuating sectional drag coefficient. The choice of $C_{d,o}$, which was taken as the value of $\widetilde{C_{d,rms}}$ found at the maximum reduced velocity examined, is arbitrary, and serves only to highlight the qualitative similarity in the trends exhibited by both sets of estimates. The estimates found using the flow-based method are still larger during the second response branch, which is to be expected as the sectional forces tend to be larger than the overall coefficients.

Although the results of the two methods are not directly comparable, it is clear that both methods predict qualitatively similar trends in the fluctuating drag coefficient throughout the response regime. This suggests that both methods are capable of capturing the physics of the fluid forces in the drag direction.

6.4 Effect of Wake Mode on the Drag Coefficient

The variation in the amplitude of the overall fluctuating drag coefficient, estimated from the displacement signal, throughout the three sets of PIV measurements was presented in Section 6.2.2. Although the response amplitude in the second branch was larger when the SA mode dominated, it was found that $\widetilde{C_D}$ was slightly larger when the A-IV mode occurred. The difference in the response amplitude was attributed to a change in the phase of the fluctuating drag signal with respect to the cylinder displacement signal, such that there was an increase in the amount of energy transferred to the structure. The A-II mode was found to correspond to lower levels of fluid forcing in the drag direction.

The variation in A/D, $\widetilde{C_{d,rms}}$ and $\overline{C_d}$ with reduced velocity in the range $U_r\mathrm{St}/f^* = 0.45 - 0.7$ is shown in Figure 6.18 for each of the three sets of PIV measurements acquired in Test Stage 2. The colour within each symbol denotes the wake mode observed at each point. Figure 6.18(b) indicates that in the region $U_r\mathrm{St}/f^* \approx 0.56$ the amplitude of the fluctuating drag caused by the A-IV mode is significantly larger than that induced by the SA mode. The relative difference in the estimated sectional fluctuating drag coefficients of the two modes in this region is greater than the corresponding difference between the overall fluctuating drag coefficient, $\widetilde{C_D}$, shown in Figure 6.1(b). This apparent discrepancy may be explained in terms of the three-dimensionality within the wake; if the A-IV mode is associated with greater three-dimensionality than the SA mode, the overall fluctuating drag coefficient will be significantly lower than the sectional coefficient (due to greater destructive interference along the cylinder span), and the

difference between the overall and the sectional fluctuating drag coefficients will be more pronounced for the A-IV mode than for the SA mode. This hypothesis of the increased three-dimensionality of the A-IV mode is supported by the tendency for this mode to be disorganised and irregular (Section 5.5). However, further measurements are required to quantify the degree of three-dimensionality present (e.g. using stereoscopic-PIV).

The maximum reduced velocity at which the second branch occurs (i.e. the point lock-in ceases and the A-II mode dominates in the wake) varies depending on the measurement set. However, for all cases post-lock-in the fluctuating drag coefficient drops to approximately $\widetilde{C_{d,rms}} = 0.47 - 0.55$, regardless of which mode was observed at lower reduced velocities.

In contrast to the fluctuating drag coefficient, the mean drag is largest when the SA mode dominates, reaching at peak of $\overline{C_d} = 1.78$ at $U_r\mathrm{St}/f^* = 0.548$. The maximum value of $\overline{C_d}$ found when the A-IV mode occurs is 1.55 ($U_r\mathrm{St}/f^* = 0.596$). Post-lock-in the mean drag falls to approximately $\overline{C_d} = 1 - 1.15$, regardless of the mode which was observed in the second branch. This is approximately equal to the value found in the low amplitude region at $U_r\mathrm{St}/f^* \approx 0.48$. It appears that this region at $U_r\mathrm{St}/f^* \approx 0.48$ and the post-lock-in region ($U_r\mathrm{St}/f^* \gtrsim 0.6$) are equivalent not just in terms of the dominant wake mode (A-II) and the amplitude response, but also in the amplitudes of the mean and fluctuating drag coefficient.

6.5 Performance of the Momentum Equation Applied to PIV Data

Some general observations may be made on the effectiveness of the Momentum Equation derived by Noca et al. [1999] when applied to PIV data, based on the results presented in the previous sections.

The method was found to be highly accurate when it was applied to low Reynolds number DNS data (Figure 6.6); however, the magnitude of the errors grew rapidly when noise was added to the velocity fields. Therefore the Momentum Equation is likely to be highly sensitive to the accuracy of the PIV measurements. The uncertainty in the instantaneous PIV measurements performed in Test Stage 2 is of the order of 7.3% of the freestream velocity (Section 2.6.4); Figure 6.10 indicates that when this level of noise was added to the numerical data the errors in the estimates of the fluid forces became very large.

In spite of the sensitivity of the method to the accuracy of the PIV measurements, the variation in $\widetilde{C_{drms}}$ found using the Momentum Equation is consistent with the variation in the overall fluctuating drag coefficient found using the cylinder displacement signal (Figure 6.17). This is in fact quite surprising, given the magnitude of the errors associated with the PIV measurements and the lack of information regarding the three-dimensionality of the velocity fields. Although it was not possible to directly measure the forces acting on the cylinder and thus ascertain the exact accuracy of the estimates, the similarity between the results found using both methods suggests that the Momentum Equation is at least capable of capturing the general trends in the variation of the amplitude of the fluid forcing throughout the response regime. The method can therefore be applied to

PIV measurements in certain cases, although care must be taken when analysing the results. For example, the accuracy of the method was not found to be the same in both directions. While the amplitude of the mean and fluctuating drag was found to be roughly independent of the choice of integration boundary (providing it was reasonably far from the cylinder ($x_b/D \gtrsim 2.5$), the amplitude of the lift coefficient was not found to converge (for $x_b/D < 4$) and the estimates in this direction were not deemed to be accurate.

The method has the benefit of being applicable in many situations in which the direct measurement of the forces using gauges would be difficult or impossible. In the present system, the use of fishing wires to support the cylinder makes the use of strain gauges impractical. Furthermore, the absolute forces acting on the cylinder are very low; assuming the overall force coefficient is equal to the sectional value estimated in the PIV plane, the total mean drag force occurs in the range $\overline{F_x} = 10^{-2} - 10^{-1}$N, while the total fluctuating drag occurs in the range $\widetilde{F_x} = 10^{-3} - 10^{-1}$N. Even if it was possible to measure the forces using gauges, the very small magnitude of the fluids would make their measurement highly susceptible to noise.

In summary, the Momentum Equation can provide a very useful means to estimate the fluid forces acting on a body, particularly in cases in which the use of gauges is impractical. However, the accuracy of the measurements will depend on a wide range of parameters (accuracy and spatial resolution of the flow measurements, three-dimensionality etc.), and in many cases it will first be necessary to perform a sensitivity study to confirm that the force estimates are physically representative.

6.6 Closure

The forces acting on a freely oscillating cylinder throughout its response regime were estimated using two approaches, based on the cylinder displacement signal and PIV measurements of the surrounding velocity fields, respectively. The displacement-based method indicated that the fluctuating drag was largest at low reduced velocities, but acted in phase with the displacement signal and provided little excitation to the cylinder. In the second branch, the A-IV mode was found to cause larger amplitude fluctuating drag force than the SA mode, despite being associated with lower levels of cylinder vibration.

A method of estimating the fluid forcing using the 'Momentum Equation' derived by Noca et al. [1999] was applied to numerical and PIV data. The former case indicated that the method was capable of achieving highly accurate estimates of both the lift and the drag coefficients, but was very sensitive to errors in the velocity measurements. When the method was applied to the PIV measurements (described in Chapter 5), it was found to provide consistent estimates of the amplitude of the fluctuating and mean drag coefficient when the integration boundary was reasonably far downstream ($x_b/D \gtrsim 2.5$). However, the estimates of the lift force were not found to converge for any reduced velocity or integration boundary examined. The estimates of the amplitude of the fluctuating and mean drag force were not directly comparable to those found using the displacement signals, but were found to be qualitatively in agreement. The fluctuating sectional drag coefficient in the second branch was found to be significantly higher when the A-IV mode dominated, compared to when the SA mode was observed.

All three sets of PIV measurements indicated that the fluctuating drag force

in the region $U_r St/^* \approx 0.48$ was approximately equal to that which occurred post-lock-in when the cylinder response was negligible. The estimates of the amplitude of the fluctuating drag coefficient indicate that the region of the low amplitude response near $U_r \mathrm{St}/f^* \approx 0.48$ is caused by a local reduction in $\widetilde{C_d}$, rather than a local change in $\phi_{x,D}$, as was proposed by Nishihara et al. [2005]. This potential cause of the low amplitude region has not previously been identified and is supported by the results found using the displacement-based method.

Finally, the effectiveness of the Momentum Equation in terms of estimating the fluid forcing using PIV measurements was briefly discussed. The method was found to be capable of producing accurate estimates of the fluid forcing, but was highly sensitive to errors in the velocity field measurements, and care was required when interpreting the physical significance of the estimates.

6.7 Figures

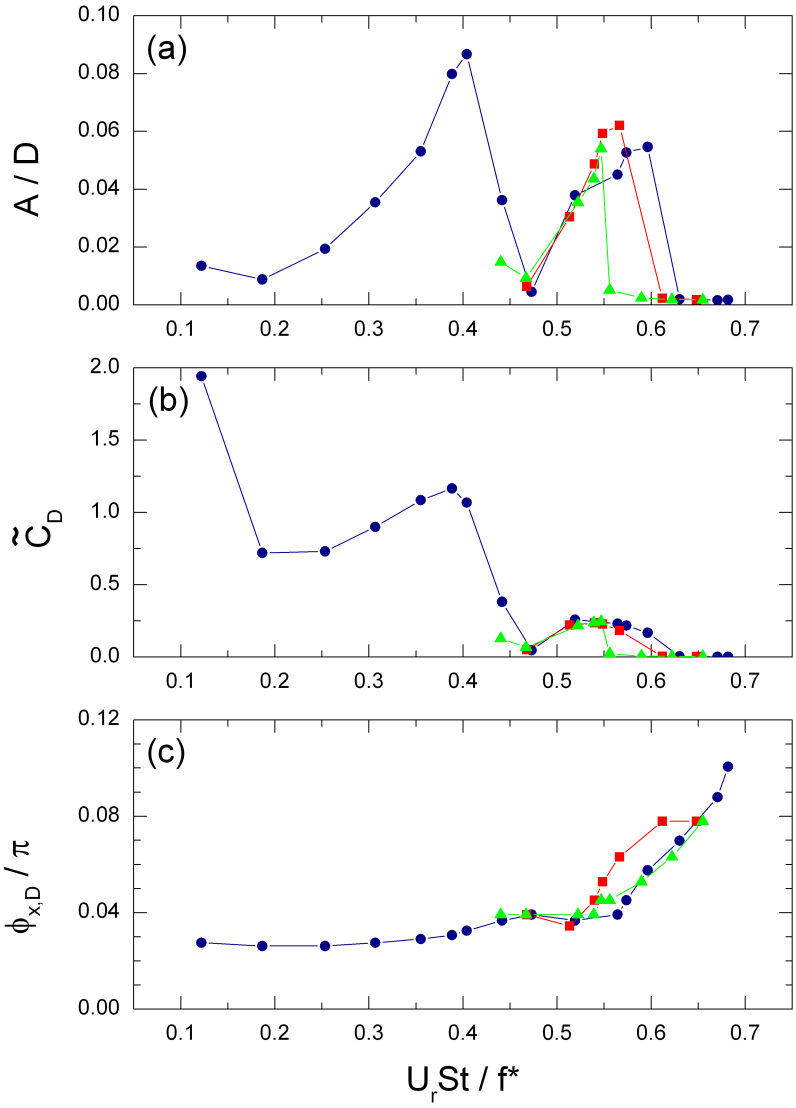

Figure 6.1: Amplitude response of the cylinder (a), amplitude of the fluctuating drag coefficient (b) and phase angle between the fluctuating drag and the cylinder displacement (c) for the three sets of PIV measurements discussed in Chapter 5. The results in (b) and (c) were calculated using Equations 6.10 and 6.11, respectively. The points correspond to the A-IV (blue), SA (red) and A-II (green) data sets.

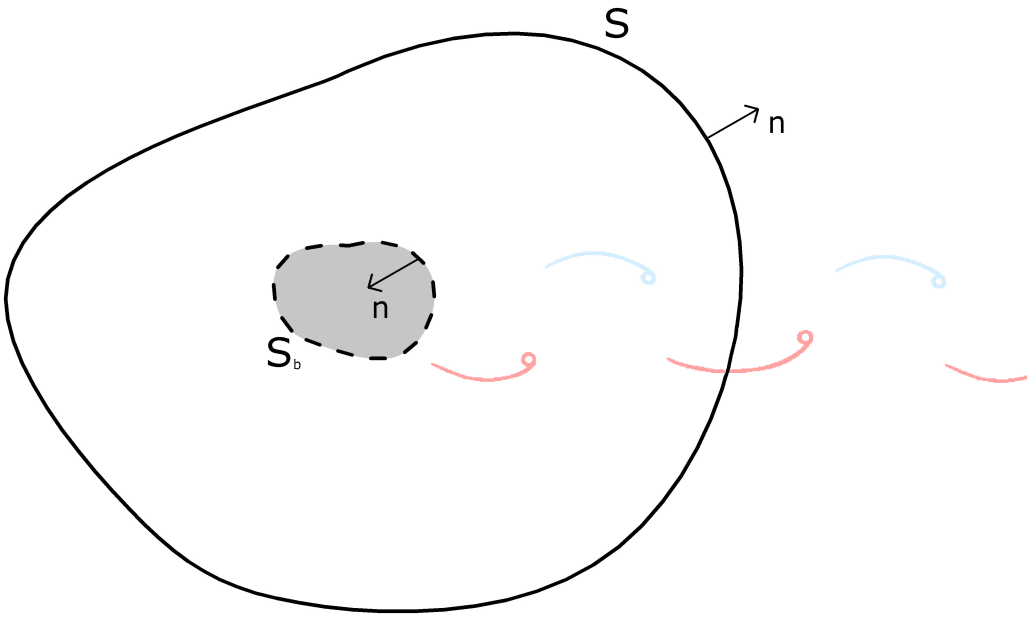

Figure 6.2: Integration boundary, S (solid black line), surrounding a solid body for the estimation of the fluid forces using Equation 6.13 and the formulations derived by Noca et al. [1999]. The body is of arbitrary shape, and is bounded by S_b (dashed black line).

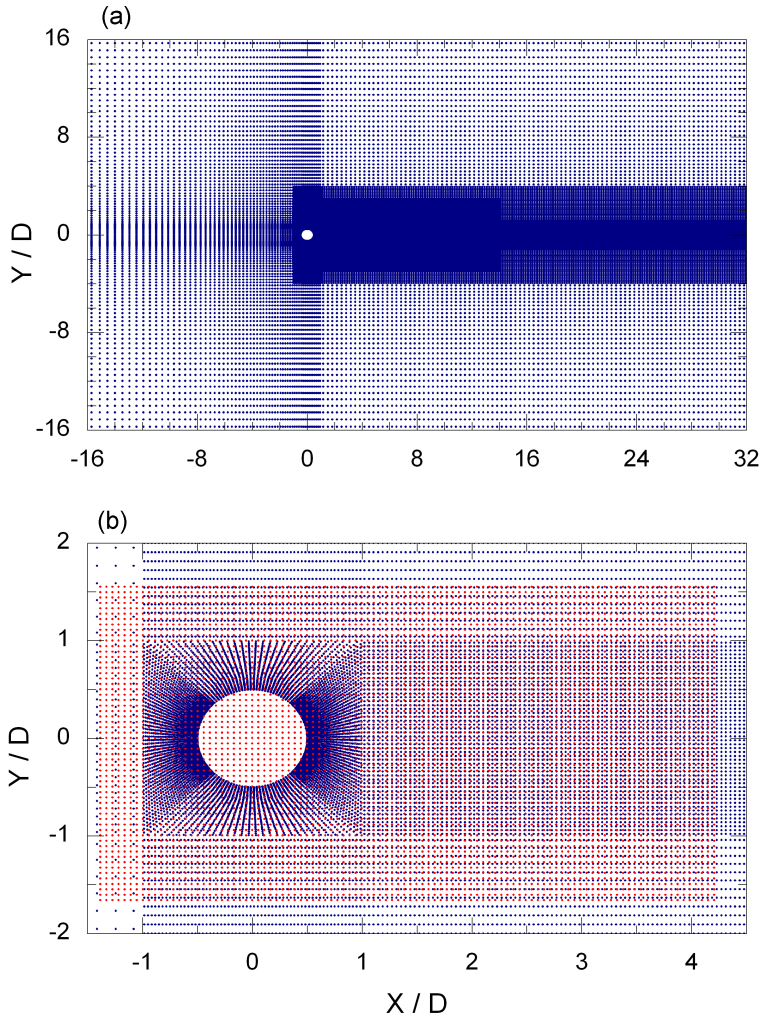

Figure 6.3: Computational mesh (blue symbols) used by Lu and Papadakis [2011] in the entire fluid domain (a) and in the near wake (b). The red symbols indicate the points at which the velocity and acceleration values were interpolated to form synthetic PIV fields.

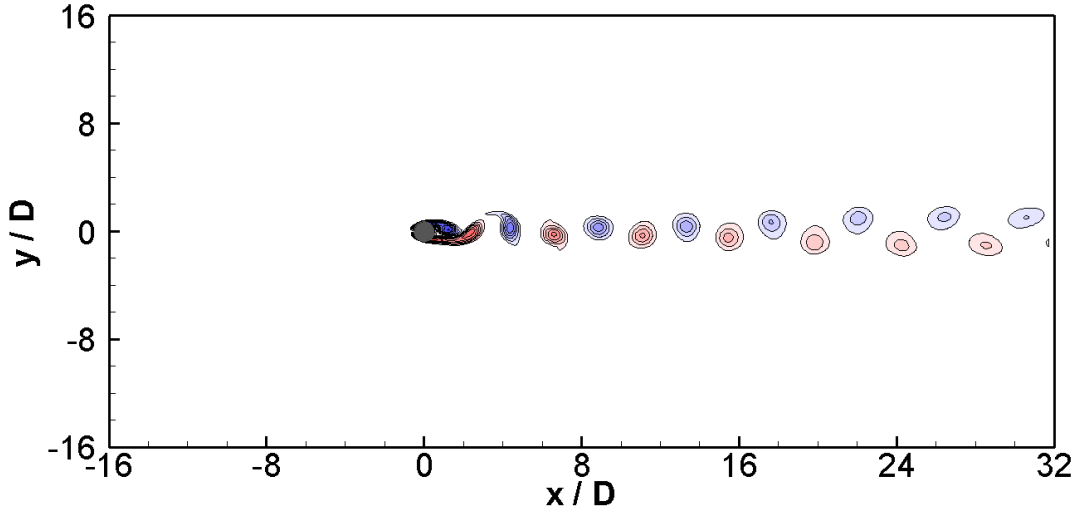

Figure 6.4: Sample vorticity field calculated using the numerical data of Lu and Papadakis [2011]. The field corresponds to the maximum drag coefficient. The cylinder is stationary and the freestream velocity is steady. Contour levels are $\omega_z D/U_0 = \pm 0.5, \pm 1, \ldots$

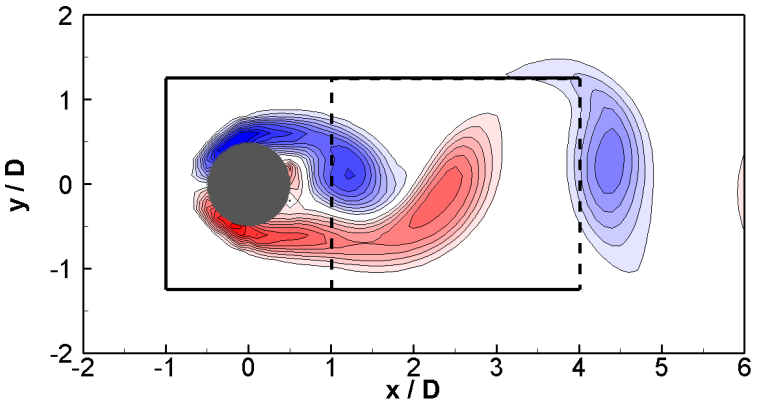

Figure 6.5: Integration boundary used to estimate the fluid forces. The boundary contains fixed paths at $x/D = -1$ and $y/D = \pm 1.25$ (solid lines), while the downstream segment of the path is variable, occurring in the range $x_b/D = 1 - 4$ (dashed lines). The boundary is superimposed upon the vorticity field shown in Figure 6.4.

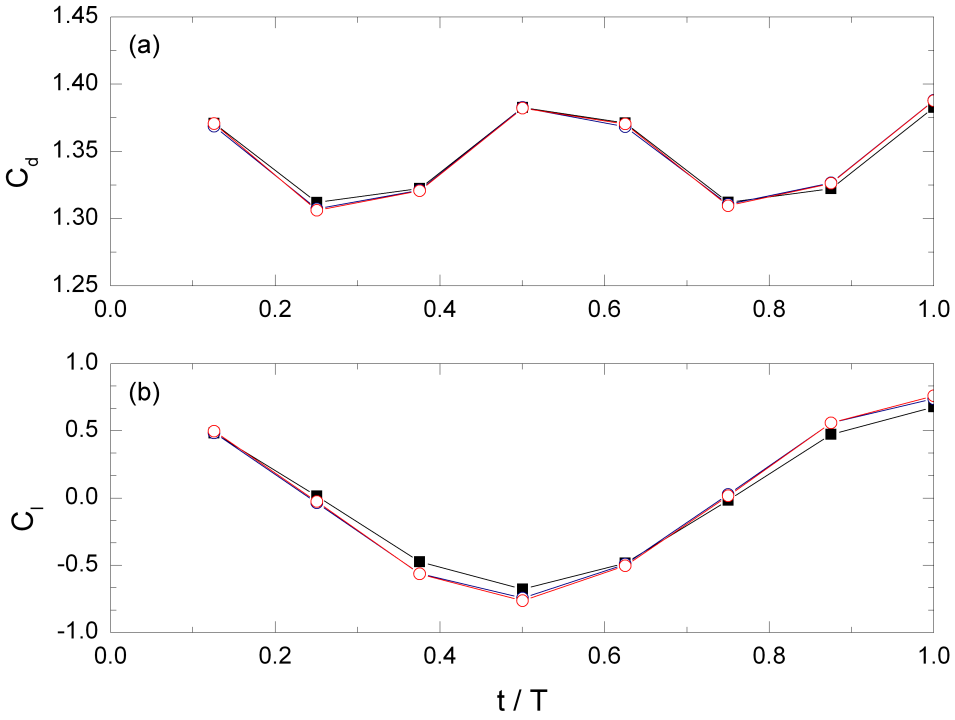

Figure 6.6: Drag (a) and lift (b) coefficients estimated directly from the numerical simulations (solid black squares), and by using the Impulse Equation (blue circles) and the Momentum Equation (red circles). The estimates found using both equations are approximately equal, and closely match the numerical value. The viscous terms were neglected when computing the estimates. The downstream position of the integration boundary was fixed at $x_b/D = 1.11$ in all cases.

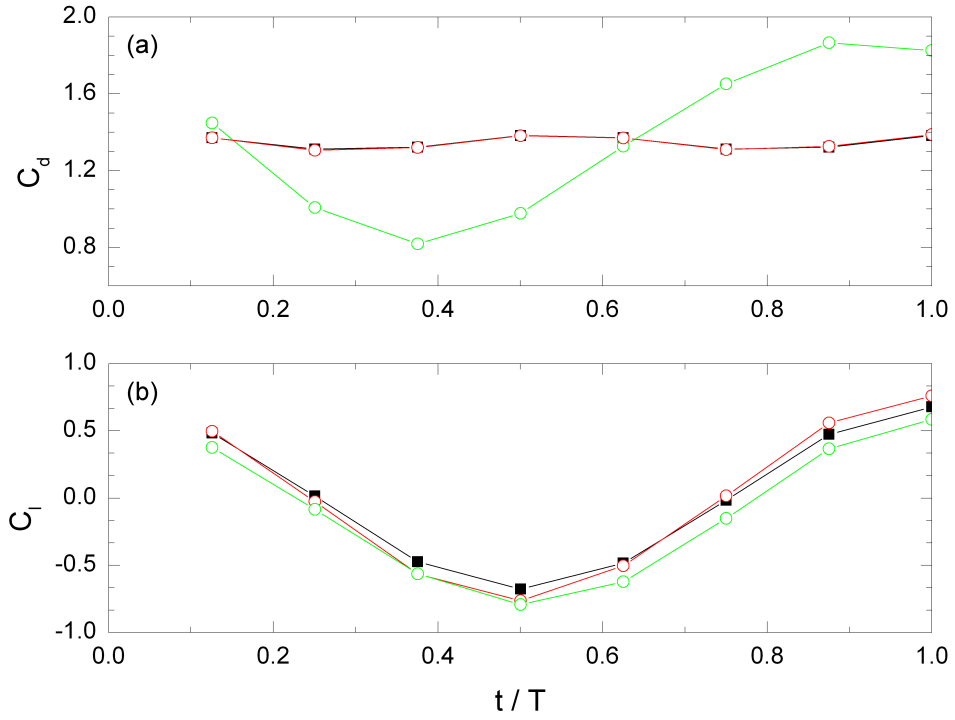

Figure 6.7: Drag (a) and lift (b) coefficients estimated directly from the numerical simulations (solid black squares), and by using the Momentum Equation in which the viscous terms were neglected (red circles) and included (green circles). The downstream position of the integration boundary was fixed at $x_b/D = 1.11$ in all cases.

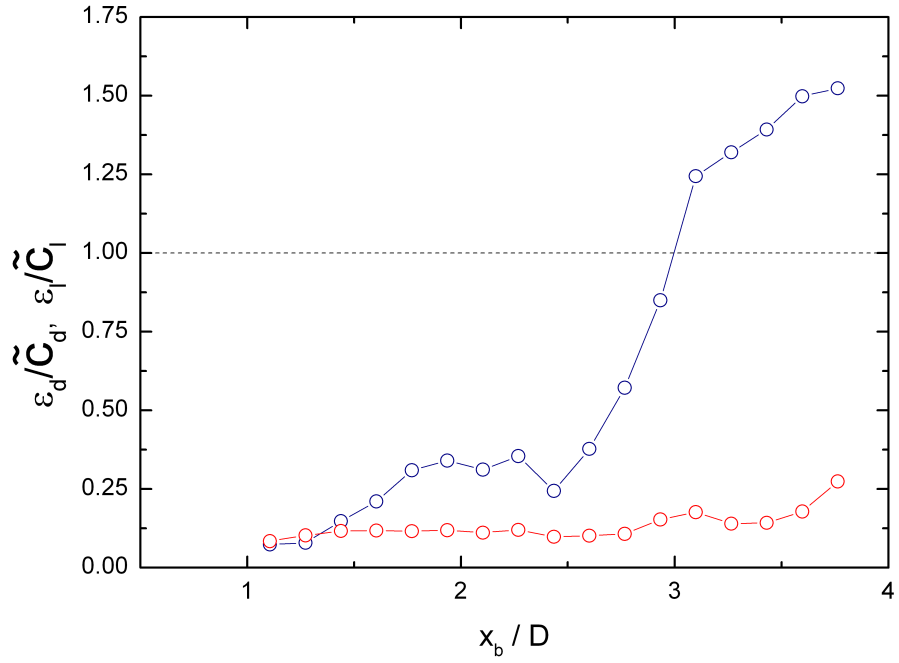

Figure 6.8: Variation in the mean errors of the estimates of the drag (blue circles) and lift coefficient (red circles) with the position of the downstream segment of the integration boundary, x_b. The errors are normalised by the fluctuating amplitude of the fluid forces in the relevant direction, as defined in equations 6.22 and 6.23.

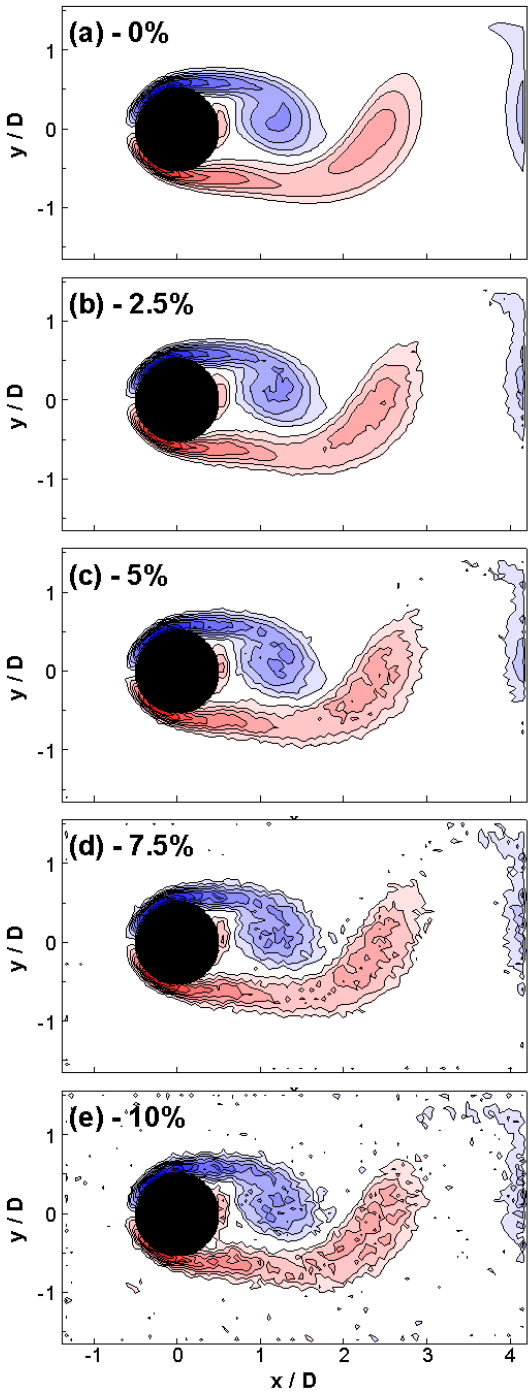

Figure 6.9: Vorticity fields estimated from a DNS velocity field (acquired at $t/T = 0.125$), for various levels of added noise: (a) 0%; (b) 2.5%; (c) 5%; (d) 7.5%; (e) 10% of the freestream velocity. Contour levels are $\omega_z D/U_0 = \pm 1, \pm 2, \ldots$

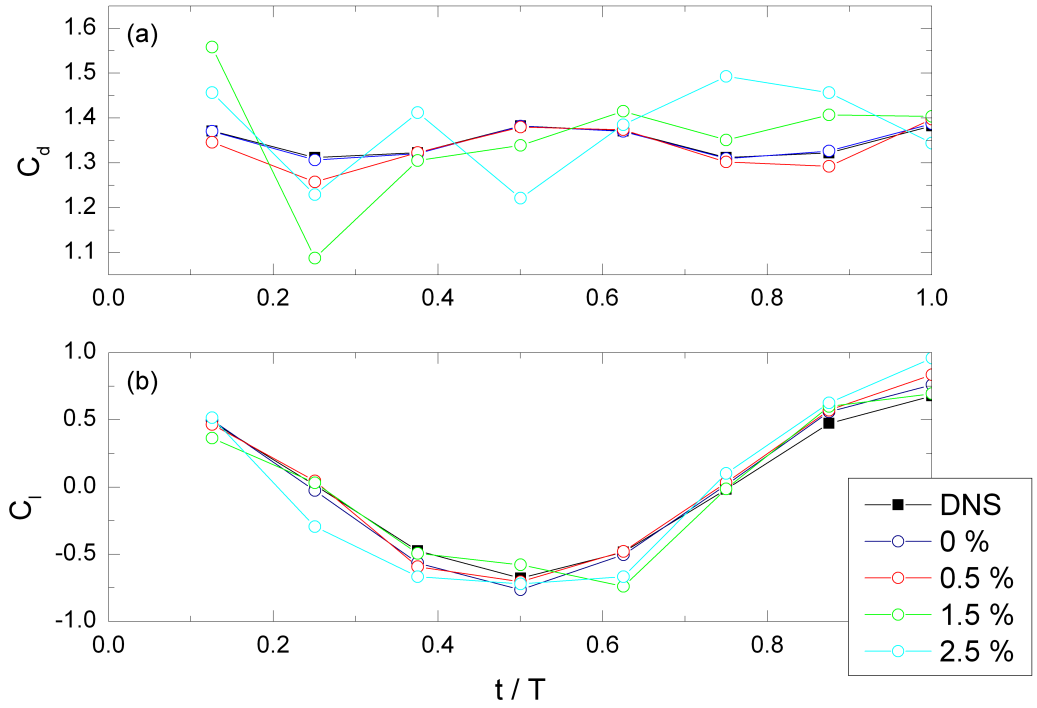

Figure 6.10: Drag (a) and lift (b) coefficients estimated directly from the numerical simulations, and using the Momentum Equation after various levels of noise were added to the velocity and acceleration fields.

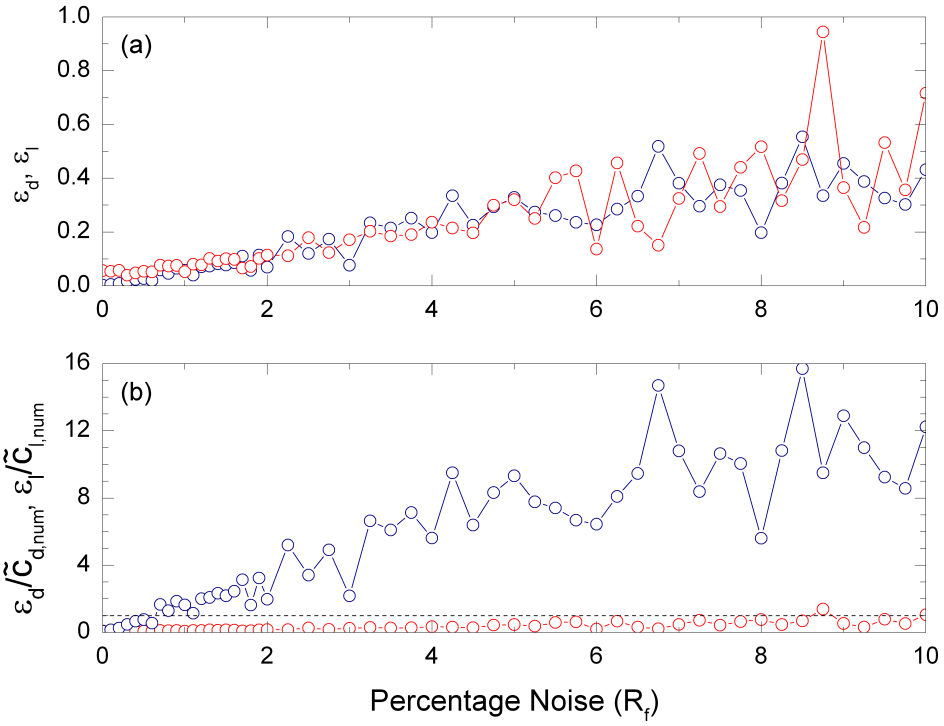

Figure 6.11: Variation in the absolute (a) and relative (b) mean errors of the estimates of the drag (blue circles) and lift (red circles) with the level of noise added to the velocity and acceleration fields. In (b), the errors in the drag and lift are normalised with respect to the amplitude of the fluctuating drag and lift respectively (Equations 6.22 and 6.23).

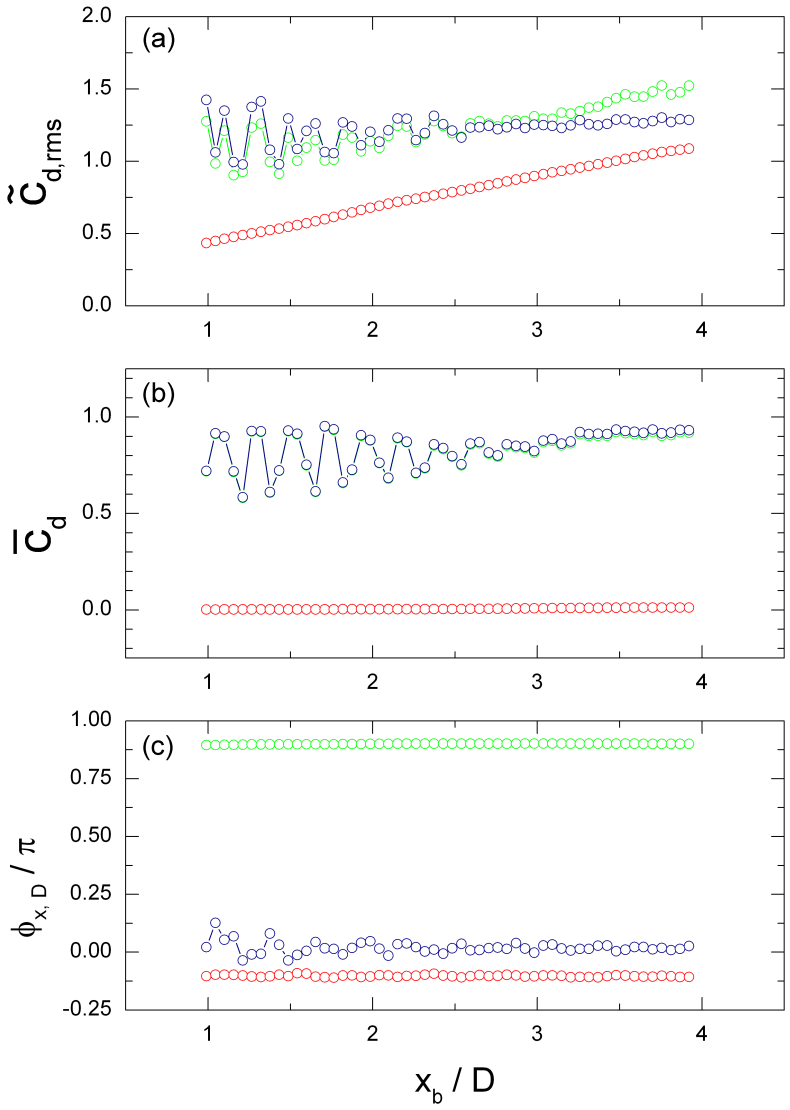

Figure 6.12: Amplitude of the fluctuating (a) and mean (b) drag coefficients and phase lag between the drag force and the cylinder displacement (c), shown as functions of the downstream position of the integration boundary. The blue symbols represent the overall force estimates, while the red and green symbols represent the components due to the acceleration and convective terms of the Momentum Equation, respectively. The estimates of $\widetilde{C_{d,rms}}$, $\overline{C_d}$ and $\phi_{x,D}$ all appear to have converged for $x_b/D \gtrsim 2.5$.

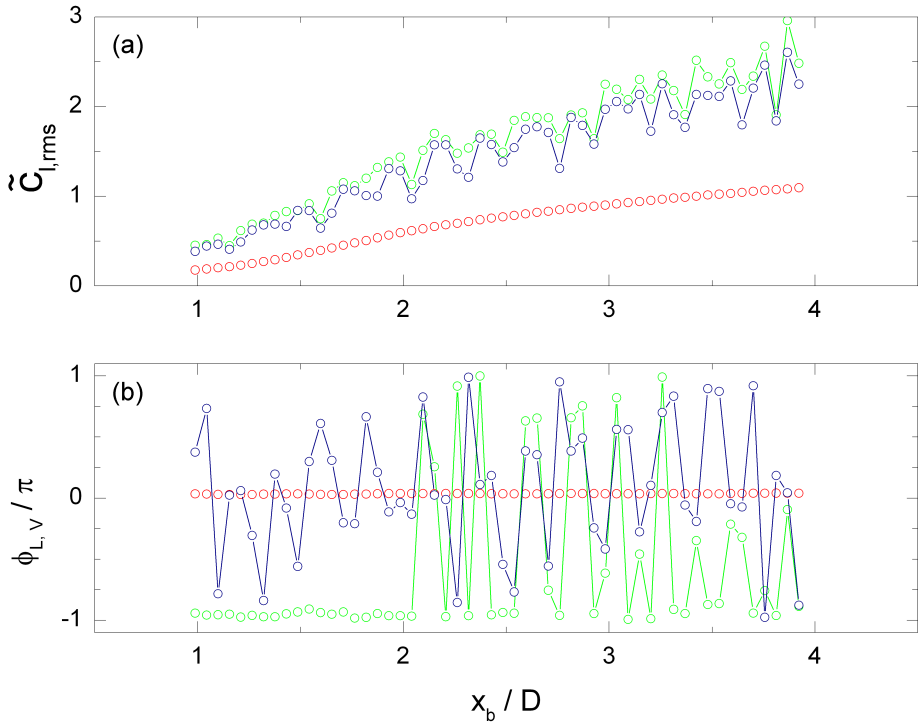

Figure 6.13: Amplitude of the lift drag coefficient (a) and the phase lag between the estimated lift force and the transverse velocity measured at $(x/D, y/D) = (3, 0)$ (b), shown as functions of the downstream position of the integration boundary. The blue symbols represent the overall force estimates, while the red and green symbols represent the components due to the acceleration and convective terms of the Momentum Equation respectively.

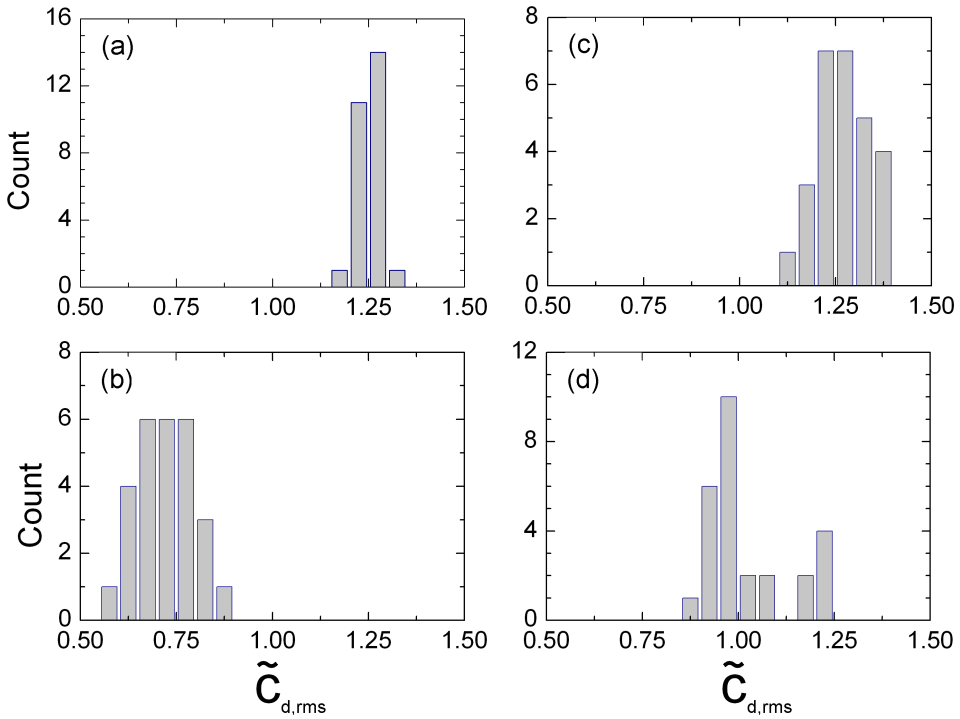

Figure 6.14: Histograms showing the variation in the fluctuating drag coefficient estimated for $x_b/D = 2.5 - 4$, at $U_r\mathrm{St}/f^* = 0.253$ (a), 0.404 (b), 0.473 (c) and 0.596 (d). These points correspond to pre-lock-in, the peak of the first response branch, the low amplitude response region between the two branches and the peak of the second response branch respectively.

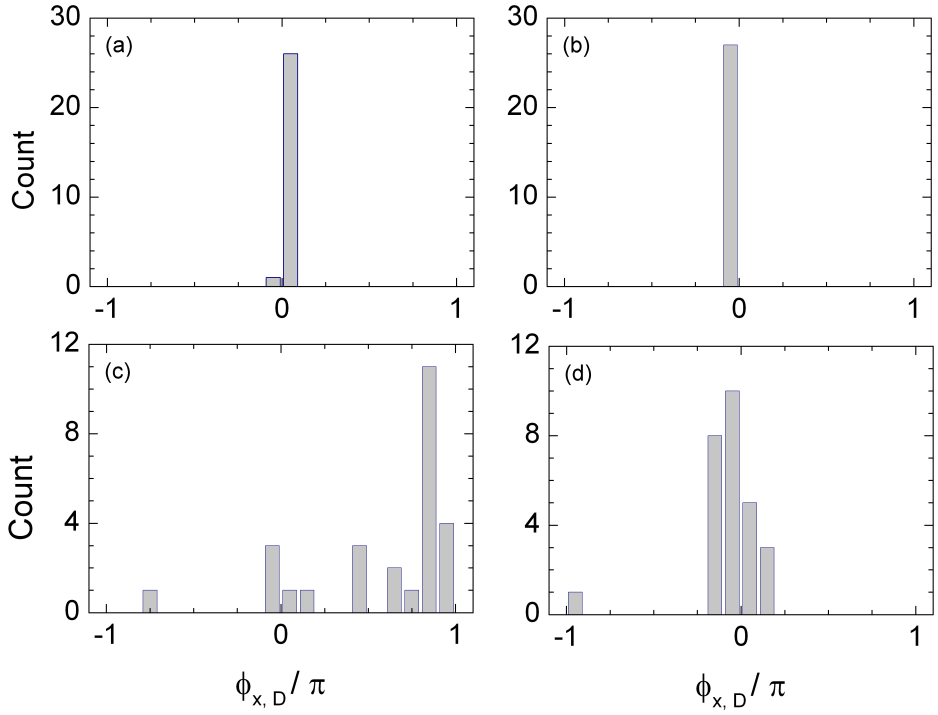

Figure 6.15: Histograms showing the variation in the phase difference between the cylinder displacement signal and the drag signal estimated at $x_b/D = 2.5 - 4$, for $U_r\mathrm{St}/f^* = 0.253$ (a), 0.404 (b), 0.473 (c) and 0.596 (d). These points correspond to pre-lock-in, the peak of the first response branch, the low amplitude response region between the two branches and the peak of the second response branch respectively.

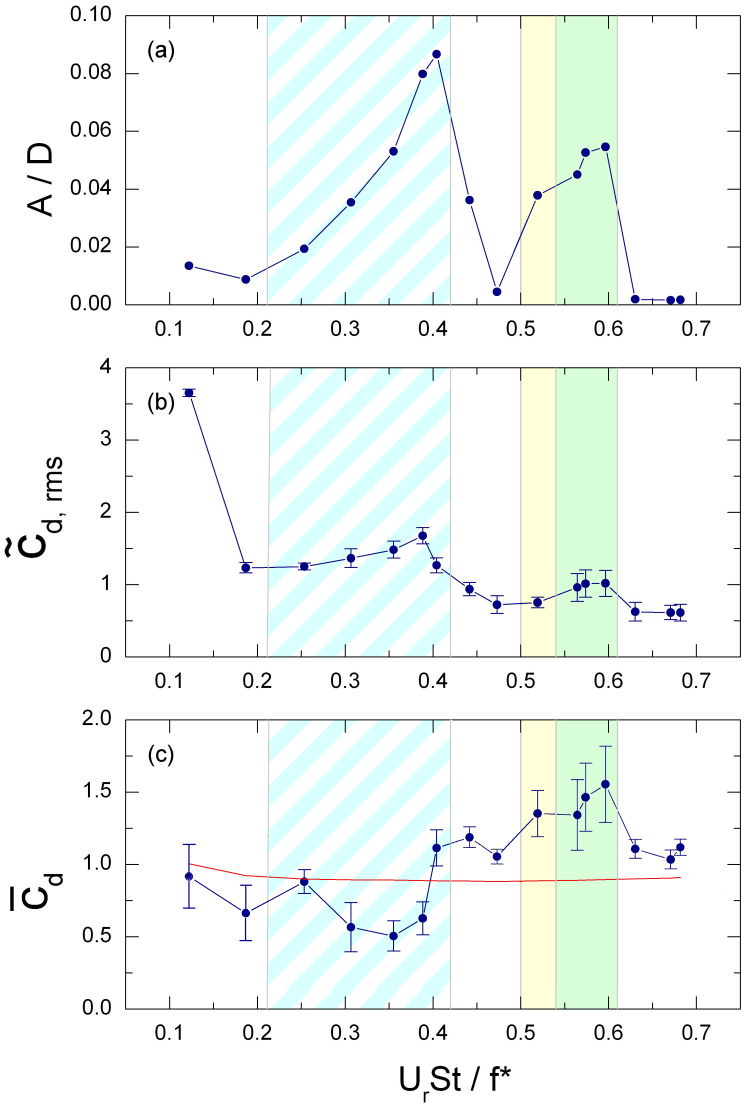

Figure 6.16: Cylinder amplitude response (a) and estimated amplitude of the fluctuating (b) and mean (c) drag coefficients throughout the response regime. The red line in (c) indicates the overall mean drag coefficient for a stationary cylinder, as measured by Anderson [1991]. The shaded regions denote the dominant wake mode; A-II (white), S-I (blue), SA (yellow) and A-IV (green), while the hatched regions indicate points at which mode competition was observed.

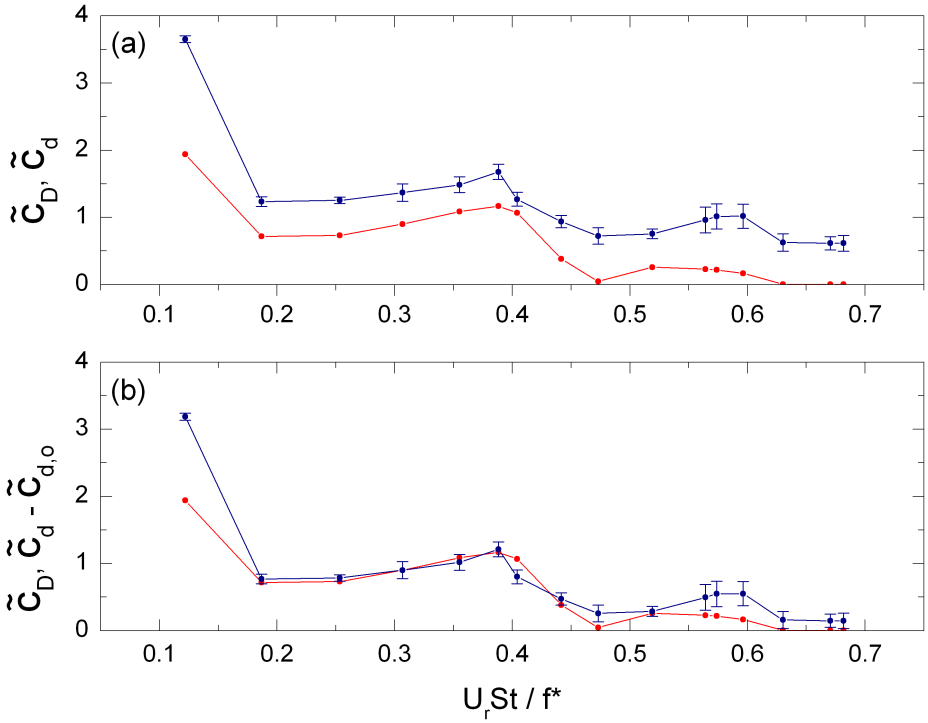

Figure 6.17: Comparison of the amplitude of the sectional fluctuating drag coefficient, $\widetilde{C_{d,rms}}$ calculated using the Momentum Equation (blue symbols) and the fluctuating overall drag coefficient, $\widetilde{C_D}$, found from the cylinder displacement signal using Equation 6.10 (red symbols), throughout the response regime (a). The similarity between the two trends can clearly be seen in (b) when an arbitrary offset ($\widetilde{C_{d,o}} = 0.467$) is subtracted from the sectional coefficient.

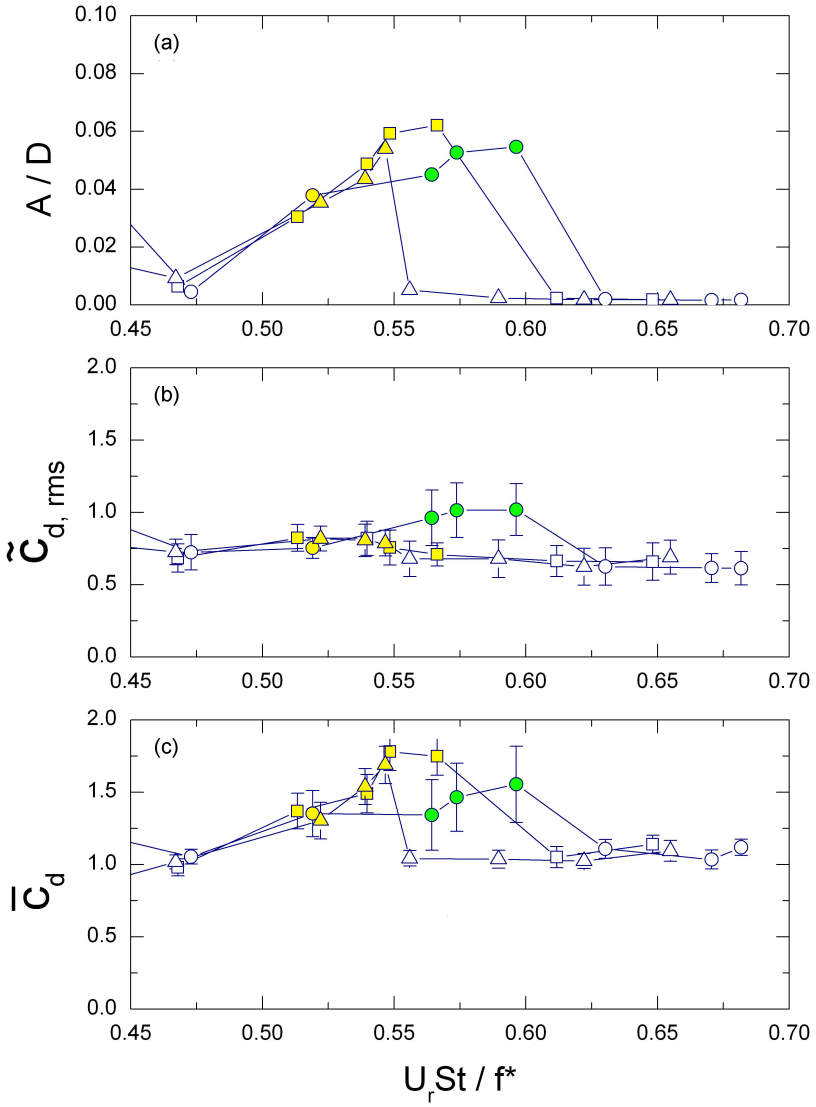

Figure 6.18: Variation in the cylinder response amplitude (a), estimated fluctuating drag coefficient (b) and mean drag coefficient (c) with reduced velocity for each of the three sets of PIV measurements; the A-IV set (circles), the SA set (squares) and the A-II set (triangles). The experimental details of each set are summarised in Table 5.2. The colours within each symbol denote the dominant wake mode observed at this point; A-II (white), SA (yellow), and A-IV (green).

Chapter 7

Conclusions and Recommendations for Future Work

7.1 Present Contribution

The aim of this study was to characterise the structural response and wake characteristics of a cylinder free to move in the streamwise direction. The literature review presented in Chapter 1 indicated that, despite streamwise VIV having a significant effect on a wide range of industrial applications, the streamwise response regime of a cylinder was not fully understood. No previous studies had performed quantitative measurements of the wake or the fluid forces associated with a freely oscillating cylinder, nor had the presence or the effects of mode competition in free vibrations been examined.

Experiments were performed in which the wake and the structural motion of a cylinder free to move in the streamwise direction were examined simultaneously. A test-section was designed which allowed the cylinder to move only parallel to the flow. The cylinder displacement and the surrounding velocity field were measured

using time-resolved Particle-Image Velocimetry, in the Reynolds number range 400 - 5500.

7.2 Main Findings

The variation in the cylinder response and the dominant wake mode was examined for a range of reduced velocity. The response regime was characterised by two branches of approximately equal magnitude, separated by a low amplitude region at $U_r St/f^* \approx 0.48$, which was in agreement with previous studies in the literature. The first response branch occurred over the range $U_r St/f^* \approx 0.32 - 0.45$ and was characterised by the presence of the S-I and A-II modes in the wake. The SA mode was observed throughout the low amplitude region and the second branch, which occurred for $U_r St/f^* \approx 0.45 - 0.61$. The response regime was divided into five distinct regions based on the dominant wake mode and the cylinder response amplitude. The regions were discussed and compared in terms of the cylinder displacement signals, phase-averaged vorticity fields, velocity profiles in the wake and estimates of the strength and trajectories of the shed vortices. The role of the trajectories of the vortices on the recirculation region was examined. There was a decrease in the strength of the vortices in the first branch, as the vortex-shedding frequency was higher than the Strouhal frequency, $f_{vs} > f_{\mathrm{St}}$; however the opposite trend was observed in the second branch, where the presence of lock-in caused the shedding frequency to be lower than the Strouhal frequency, $f_{\mathrm{St}} > f_{vs}$.

The wake was found to switch intermittently between the S-I and A-II modes during the first branch. A criterion was developed using Proper-Orthogonal De-

composition which was capable of determining which mode was dominant in a given instantaneous field. The mode competition did not have a significant effect on the structural response. The appearance of the S-I mode was found to be affected by the Reynolds number, and was observed in the greatest proportion of instantaneous fields in the range $U_r St/f^* \approx 0.3 - 0.36$. The breakdown of the S-I mode and the resulting variation in the dominant frequency of velocity fluctuations throughout the wake were examined, and used to explain some of the conflicting results in the literature regarding the presence of lock-in in the first branch.

Further measurements of the response regime indicated that the amplitude response was affected by hysteresis in the region of the second branch, and that this branch could occur in multiple forms, depending on which wake mode dominated. Three wake modes were observed at $U_r St/f^* \approx 0.56$; the A-II, A-IV and SA. The SA and A-IV modes occurred when the amplitude response of the cylinder was large, with the SA mode exciting slightly larger amplitude vibrations. The A-II mode was observed at $U_r St/f^* \approx 0.56$ when the reduced velocity was decreased and the response amplitude was negligible. The A-IV mode has not previously been identified in the wake of a freely oscillating structure. Similarly, previous VIV studies have not observed a point in the response regime in which *three* wake modes and cylinder response states were possible for the same values of reduced velocity and Reynolds number. The stability of each state was discussed using phase-portraits of the cylinder response, which indicated that the system behaved as a hard oscillator in this region. This was confirmed by experiments in which perturbations were applied to the system which induced it to change state. Finally, the variation in the dominant wake mode throughout the response regime

was compared to the results of various published studies of a cylinder undergoing forced oscillations.

The fluid forces acting on the cylinder throughout the response regime were estimated using two methods, based on measurements of the cylinder displacement signal and the velocity field in the wake, respectively. The trends in estimates of the amplitude of the unsteady drag coefficient found using both methods were consistent, and the results were related to the various wake modes. The low amplitude region was found to coincide with a decrease in the amplitude of the unsteady drag coefficient, which may explain the counter-intuitive reduction in vibrations at this point. The phase angle between the unsteady drag force and the cylinder motion was not found to change significantly in this region, as has been hypothesised by previous researchers. The amplitudes of the fluctuating drag coefficient associated with the SA and A-IV modes in the second response branch were approximately equal, and the difference in the cylinder response excited by the two modes was attributed to a change in the phase of the fluid forcing. Finally, the accuracy of the method of estimating the fluid forces from the measurements of the velocity field was analysed using both numerical and PIV data, and the effectiveness of the technique was discussed.

7.3 Recommendations for Further Work

This work provides a comprehensive description of the wake and structural dynamics associated with a cylinder undergoing streamwise VIV. However, there are some areas which remain unclear and require further work to be fully understood.

Firstly, it is unclear what causes the appearance of either the SA or the

A-IV modes in the second response branch, and why the A-IV mode has not been reported in previous studies. It is possible that the appearance of either mode is determined by transient conditions, e.g. the rate at which the reduced velocity is varied. A specially designed test facility in which the rate of change of the freestream velocity could be accurately controlled would allow the potential effects of transient conditions to be examined.

While there have been a number of studies of cylinders forced to oscillate in the streamwise direction, no study has attempted to characterise the dominant wake mode and the fluid forces *throughout* the $U_r\mathrm{St}/f^* - A/D$ plane, as Morse and Williamson [2009] performed for the transverse case. This may also be useful in determining the cause of the multiple response branches near $U_r\mathrm{St}/f^* \approx 0.56$, as well as examining the effects of both the reduced velocity and the vibration amplitude on the mode competition between the S-I and A-II modes, and its effect on the fluid excitation.

In practice, most structures which are susceptible to VIV will be free to move in both the streamwise and transverse directions, and it is not clear how the freedom to move in the transverse direction will affect the results presented throughout this thesis. In particular, it is not known whether the A-IV mode may appear in the wake of multi-DOF cylinder nor how this mode would affect the transverse response. Similarly, it would be interesting to examine the effects of mode-competition and the breakdown on the S-I mode in the first branch; as the A-II mode induces a larger lift force than the S-I mode [Nishihara et al., 2005], the competition between the two modes is likely to have a significant effect on the transverse and overall response of the structure.

Appendix

This appendix describes in detail the derivation of equations 6.10 and 6.11, which are used to express the amplitude and phase of the unsteady drag signal, respectively, in terms of the structural parameters and the characteristics of the measured displacement signal.

The equation of motion of a cylinder in fluid which is free to move in the streamwise direction is given by:

$$m_e\ddot{x} + c_e\dot{x} + kx = \widetilde{F_x}(t), \tag{1}$$

where m_e is the effective mass of the cylinder ($m_e = m + \Delta m$), c_e is the total damping coefficient of the system (i.e. structural and hydrodynamic), and $\widetilde{F_x}(t)$ is the unsteady fluid force in the streamwise direction. Dividing by the effective mass, equation 1 can be expressed in terms of the damping coefficient, $\zeta_w = c_e/2\sqrt{km_e}$, and the natural frequency, $f_n = \frac{1}{2\pi}\sqrt{k/m_e}$ (both measured in still fluid);

$$\ddot{x} + 2\zeta_w(2\pi f_n)\dot{x} + (2\pi f_n)^2 x = \frac{\widetilde{F_x}(t)}{m_e}. \tag{2}$$

Replacing the right-hand-side of equation 2 with the non-dimensional unsteady drag coefficient, mass ratio and added mass coefficient, gives:

$$\ddot{x} + 2\zeta_w(2\pi f_n)\dot{x} + (2\pi f_n)^2 x = \frac{\widetilde{C_D}(t)}{(m^* + C_a)}\frac{2}{\pi}\frac{U_0^2}{D}. \tag{3}$$

The cylinder displacement and unsteady drag coefficient signals are assumed to be sinusoidal, with fixed amplitudes, separated by a phase lag, $\phi_{x,D}$:

$$x(t) = A\sin\left(2\pi f_x t\right), \tag{4}$$

$$\widetilde{C_D}(t) = |\widetilde{C_D}|\sin\left(2\pi f_x t + \phi_{x,D}\right). \tag{5}$$

The cylinder velocity and acceleration can be found by differentiation:

$$\dot{x}(t) = 2\pi f_x A\cos\left(2\pi f_x t\right), \tag{6}$$

$$\ddot{x}(t) = -4\pi^2 f_x^2 A \sin\left(2\pi f_x t\right). \tag{7}$$

Inserting the expressions for $x(t)$, $\dot{x}(t)$, $\ddot{x}(t)$ and $\widetilde{C_D}(t)$ into equation 3 gives;

$$\begin{aligned} 4\pi^2\left(f_n^2 - f_x^2\right) A \sin\left(2\pi f_x t\right) + 8\pi^2 \zeta_w f_n f_x A \cos\left(2\pi f_x t\right) = \\ \frac{2}{\pi}\frac{U_0^2}{D}\frac{|\widetilde{C_D}|}{(m^* + C_a)}\Big(\sin\left(2\pi f_x t\right)\cos\left(\phi_{x,D}\right) + \cos\left(2\pi f_x t\right)\sin\left(\phi_{x,D}\right)\Big) \end{aligned} \tag{8}$$

.

By letting $t = 0$, equation 8 can be rearranged to express the non-dimensional cylinder response amplitude;

$$\frac{A}{D} = \frac{1}{4\pi^3}\frac{\widetilde{C_D}\sin\phi_{x,D}}{(m^* + C_a)\,\zeta_w}\left(\frac{U_r}{f^*}\right)^2 f^*. \tag{9}$$

Equation 8 can also be used to form an expression for the effective added mass coefficient, by setting $t = 1/4f_x$;

$$C_{ea} = \frac{D}{A}\frac{\widetilde{C_D}\cos\phi_{x,D}}{2\pi^3}\left(\frac{U_r}{f^*}\right)^2. \tag{10}$$

The effective added mass coefficient can also be measured *a posteriori* by examining the frequency ratio. As the natural frequency in still fluid will be a function of the mass ratio and the added mass coefficient, $f_n \propto (m^* + C_a)^{-1/2}$,

while the response frequency will also be affected by C_{ea}, $f_x \propto (m^*+C_a+C_{ea})^{-1/2}$, the frequency ratio can be expressed as:

$$f^* = \sqrt{\frac{m^* + C_a}{m^* + C_a + C_{ea}}}. \tag{11}$$

This can be rearranged to give an expression for the effective added mass coefficient:

$$C_{ea} = (m^* + C_a)\left(\frac{1 - f^{*2}}{f^{*2}}\right). \tag{12}$$

Both A/D and f^* can be measured from the displacement signal, and $(m^* + C_a)$ can be found from the natural frequency measured in still air and in water (as discussed in Section 6.2.1). As C_{ea} can also be measured using equation 12, the only unknowns in equations 9 and 10 are the amplitude and the phase of the unsteady drag coefficient. The unknowns can be isolated by rearranging equations 9 and 10;

$$|\widetilde{C_D}| \sin(\phi_{x,D}) = 4\pi^3 \frac{A}{D} \frac{(m^* + C_a)\zeta_w}{f^*} \left(\frac{f^*}{U_r}\right)^2, \tag{13}$$

$$|\widetilde{C_D}| \cos(\phi_{x,D}) = 2\pi^3 \frac{A}{D} C_{ea} \left(\frac{f^*}{U_r}\right)^2 \tag{14}$$

By combining these expressions, $|\widetilde{C_D}|$ and $\phi_{x,D}$ can be expressed as;

$$\widetilde{C_D} = 2\pi^3 \frac{A}{D} \left(\frac{f^*}{U_r}\right)^2 \sqrt{C_{ea}^2 + \left(\frac{2\left(m^* + C_a\right)\zeta_w}{f^*}\right)^2}, \tag{15}$$

$$\phi_{x,D} = \tan^{-1}\left(\frac{2\left(m^* + C_a\right)\zeta_w}{f^* C_{ea}}\right). \tag{16}$$

References

M. S. Adaramola, O. G. Akinlade, D. Sumner, D. J. Bergstrom, and A. J. Schenstead. Turbulent wake of a finite circular cylinder of small aspect ratio. *Journal of Fluids and Structures*, 22:919–928, 2006.

J. E. Aguirre. *Flow induced, in-line vibrations of a circular cylinder*. PhD thesis, Imperial College of Science and Technology, 1977.

J. D. Anderson. *Fundamentals of Aerodynamics*. McGraw-Hill, 1991.

B. J. Armstrong and F. H. Barnes. The effect of a perturbation on the flow over a bluff body. *Physics of Fluids*, 29(7):2095–2102, 1986.

G. R. S. Assi, J. R. Meneghini, J. A. P. Aranha, P. W. Bearman, and E. Casaprima. Experimental investigation of flow-induced vibration interference between two circular cylinders. *Journal of Fluids and Structures*, 22:819–827, 2006.

C. Barbi, D. P. Favier, C. A. Maresca, and D. P. Telionis. Vortex shedding and lock-on of a cylinder in oscillatory flow. *Journal of Fluid Mechanics*, 170: 527–544, 1986.

P. W. Bearman. Vortex shedding from oscillating bluff bodies. *Annual Review of Fluid Mechanics*, 16:195–222, 1984.

M. M. Bernitsas, K. Raghavan, Y. Ben-Simon, and E. M. H. Garcia. VIVACE (Vortex Induced Vibration Aquatic Clean Energy): A new concept in generation of clean and renewable energy from fluid flow. *Journal of Offshore Mechanics and Arctic Engineering*, 130, 041101:1–15, 2008.

G. Berzook, P. Holmes, and L. Lumley. The Proper Orthogonal Decomposition in the analysis of turbulent flows. *Annual Review of Fluid Mechanics*, 25:539–575, 1993.

R. D. Blevins. *Flow-Induced Vibrations*. Van Nostrad Reinhold, 1977.

R. D. Blevins and C. S. Coughran. Experimental investigation of vortex-induced vibrations in one and two dimensions with variable mass, damping, and Reynolds number. *Journal of Fluids Engineering*, 131 (101202):1–7, 2009.

M. Brankovic and P. W. Bearman. Measurements of transverse forces on circular cylinders undergoing vortex-induced vibration. *Journal of Fluids and Structures*, 22:829–836, 2006.

B. Cantwell and D. Coles. An experimental study of entrainment and transport in the turbulent near wake of a circular cylinder. *Journal of Fluid Mechanics*, 136:321–374, 1983.

J. Carberry, J. Sheridan, and D. Rockwell. Controlled oscillations of a cylinder: forces and wake modes. *Journal of Fluid Mechanics*, 538:31–69, 2005.

G. A. Cecchi, D. L. Gonzalez, M. O. Magnasco, G. B. Mindlin, O. Piro, and A. J. Santillan. Periodically kicked hard oscillators. *Chaos*, 3 (1):51–62, 1993.

O. Cetiner and D. Rockwell. Streamwise oscillations of a cylinder in a steady current. Part 1. Locked-on states of vortex formation and loading. *Journal of Fluid Mechanics*, 427:1–28, 2001.

J. R. Chaplin, P. W. Bearman, Y. Cheng, E. Fontaine, J. M. R. Graham, K. Herfjord, F. J. Huera-Huarte, M. Isherwood, K. Lambrakos, C. M. Larsen, J. R. Meneghini, G. Moe, R. J. Pattenden, M. S. Triantafyllou, and R. H. J. Willden. Blind predictions of laboratory measurements of vortex-induced vibrations of a tension riser. *Journal of Fluids and Structures*, 21:25–40, 2005.

J. J. Charonko, C. V. King, B. L. Smith, and P. P. Vlachos. Assessment of pressure field calculations from particle image velocimetry measurements. *Measurement Science and Technology*, 21 (105401):1–14, 2010.

J. M. Dahl, F. S. Hover, and M. S. Triantafyllou. Two-degree-of-freedom vortex-induced vibrations using a force assisted apparatus. *Journal of Fluids and Structures*, 22:807–818, 2006.

R. de Kat and B. W. van Oudheusden. Instantaneous planar pressure from PIV: analytic and experimental test-cases. In *15th International Symposium on Applications of Laser Techniques to Fluid Mechanics*, 2010.

W. R. Dickins. *Self-induced vibration of a cylinder in-line with a fluid flow*. PhD thesis, University of London, 1976.

C. Feng. The measurements of vortex-induced effects in flow past a stationary

and oscillating circular and D-section cylinders. Master's thesis, University of British Columia, 1963.

F. Flemming and C. H. K. Williamson. Vortex-induced vibrations of a pivoted cylinder. *Journal of Fluid Mechanics*, 552:215–252, 2005.

A. L. C. Fujarra, C. P. Pesce, F. Flemming, and C. H. K. Williamson. Vortex-induced vibration of a flexible cylinder. *Journal of Fluids and Structures*, 15: 651–658, 2001.

R. D. Gabbai and H. Benaroya. An overview of modeling and experiments of vortex-induced vibration of circular cylinders. *Journal of Sound and Vibration*, 282:575–616, 2005.

R. Govardhan and C. H. K. Williamson. Modes of vortex formation and frequency response of a freely vibrating cylinder. *Journal of Fluid Mechanics*, 420:85–130, 2000.

O. M. Griffin and S. E. Ramberg. Vortex shedding from a cylinder vibrating in line with an incident uniform flow. *Journal of Fluid Mechanics*, 75:257–271, 1976.

W. Hanke, M. Witte, L. Miersch, M. Brede, J. Oeffner, M. Michael, F. Hanke, A. Leder, and G. Dehnhardt. Harbor seal vibrissa morphology suppresses vortex-induced vibrations. *The Journal of Experimental Biology*, 213:2665 – 2672, 2010.

N. Jauvtis and C. H. K. Williamson. Vortex-induced vibration of a cylinder with two degrees of freedom. *Journal of Fluids and Structures*, 17:1035–1042, 2003.

N. Jauvtis and C. H. K. Williamson. The effect of two degrees of freedom on vortex-induced vibration at low mass and damping. *Journal of Fluid Mechanics*, 509:22–63, 2004.

A. Khalak and C. H. K. Williamson. Investigation of relative effects of mass and damping in vortex-induced vibration of a circular cylinder. *Journal of Wind Engineering and Industrial Aerodynamics*, 69-71:341–350, 1997.

A. Khalak and C. H. K. Williamson. Motions, forces and mode transitions in vortex-induced vibrations at low mass-damping. *Journal of Fluids and Structures*, 13:813–851, 1999.

W. Kim, J. Y. Yoo, and J. Sung. Dynamics of vortex lock-on in a perturbed cylinder wake. *Physics of Fluids*, 18(7):074103 1–22, 2006.

R. King. *Vortex excited structural oscillations of a circular cylinder in flowing water*. PhD thesis, Loughborough University of Technology, 1974.

E. Konstantinidis and S. Balabani. Symmetric vortex shedding in a near wake of a circular cylinder due to streamwise perturbations. *Journal of Fluids and Structures*, 23:1047–1063, 2007.

E. Konstantinidis and S. Balabani. Flow structure in the locked-on wake of a circular cylinder in pulsating flow: Effect of forcing amplitude. *International Journal of Heat and Fluid Flow*, 29:1567–1576, 2008.

E. Konstantinidis and C. Liang. Dynamic response of a turbulent cylinder wake to sinusoidal inflow perturbations across the vortex lock-on range. *Physics of Fluids*, 23 (075102):1–21, 2011.

E. Konstantinidis, S. Balabani, and M. Yianneskis. The effect of flow perturbations on the near wake characteristics of a circular cylinder. *Journal of Fluids and Structures*, 18:367–386, 2003.

E. Konstantinidis, S. Balabani, and M. Yianneskis. The timing of vortex shedding in a cylinder wake imposed by periodic inflow perturbations. *Journal of Fluid Mechanics*, 543:45–55, 2005.

E. Konstantinidis, S. Balabani, and M. Yianneskis. Bimodal vortex shedding in a perturbed cylinder wake. *Physics of Fluids*, 19:011701 1–4, 2007.

G. H. Koopman. The vortex wakes of vibrating cylinders at low Reynolds number. *Journal of Fluid Mechanics*, 28 (3):501–512, 1967.

D. F. Kurtulus, F. Scarano, and L. David. Unsteady aerodynamic forces estimation on a square cylinder by TR-PIV. *Experiments in Fluids*, 42:185–196, 2007.

A. Leonard and A. Roshko. Aspects of flow-induced vibration. *Journal of Fluids and Structures*, 15:415425, 2001.

B. Levy, Y. Z. Liu, and L. L. Shi. Cactus spines and grooved cross-section, VIV reducers or self-defense mechanisms? In *IUTAM Symposium on Bluff Body Flows*, 2011.

L. Lu and G. Papadakis. Investigation of the effect of external periodic flow pulsation on a cylinder wake using linear stability analysis. *Physics of Fluids*, 23:094105, 1–14, 2011.

X. Ma, G. S. Karamanos, and G. E. Karniadakis. Dynamics and low dimensionality of a turbulent near wake. *Journal of Fluid Mechanics*, 410:29–65, 2000.

O. A. Marzouk and A. H. Nayfeh. Reduction of loads on a cylinder undergoing harmonic in-line motion. *Physics of Fluids*, 21:083103 1–13, 2009.

T. L. Morse and C. H. K. Williamson. Prediction of vortex-induced vibration response by employing controlled motion. *Journal of Fluid Mechanics*, 634: 5–39, 2009.

T. L. Morse and C. H. K. Williamson. Steady, unsteady and transient vortex-induced vibration predicted using controlled motion data. *Journal of Fluid Mechanics*, 649:429–451, 2010.

A. Nakamura, A. Okajima, and T. Kosugi. Experiments on flow-induced in-line oscillation of a circular cylinder in a water tunnel (2nd report, influence of aspect ratio of a cantilevered circular cylinder). *JSME International Journal Series B Fluids and Thermal Engineering*, 44 (4):705–711, 2001.

E. Naudascher. Flow-induced streamwise vibrations of structures. *Journal of Fluids and Structures*, 1:265–298, 1987.

T. Nishihara, S. Kaneko, and T. Watanabe. Characteristics of fluid dynamic forces acting on a circular cylinder oscillating in a streamwise direction and its wake patterns. *Journal of Fluids and Structures*, 20:505–518, 2005.

F. Noca, D. Shiels, and D. Jeon. Measuring instantaneous fluid dynamic forces

on bodies, using only velocity fields and their derivatives. *Journal of Fluids and Structures*, 11:345–350, 1997.

F. Noca, D. Shiels, and D. Jeon. A comparison of methods for evaluating time-dependent fluid dynamic forces on bodies, using only velocity fields and their derivatives. *Journal of Fluids and Structures*, 13:551–578, 1999.

A. Okajima, T. Kosugi, and A. Nakamura. Experiments on flow-induced in-line oscillation of a circular cylinder in a water tunnel (1st report, the difference of the response characteristics when a cylinder is elastically supported at both ends and cantilevered). *JSME International Journal*, 4 (4):695–704, 2001.

A. Okajima, A. Nakamura, T. Kosugi, H. Uchida, and R. Tamaki. Flow-induced in-line oscillation of a circular cylinder. *European Journal of Mechanics B/Fluids*, 23:115–125, 2003.

A. Ongoren and D. Rockwell. Flow structure from an oscillating cylinder Part 2. Mode competition in the near wake. *Journal of Fluid Mechanics*, 191:225–245, 1988.

M. P. Païdoussis. Real-life experiences with flow-induced vibration. *Journal of Fluids and Structures*, 22:741–755, 2006.

M. Raffel, C. Willert, S. Wereley, and Kompenhans. *Particle Image Velocimetry*. Springer, 2nd edition, 2007.

T. Sarpkaya. Hydrodynamic damping, flow-induced oscillations and biharmonic response. *Journal of Offshore Mechanics and Arctic Engineering*, 117:232–238, 1995.

T. Sarpkaya. A critical review of the intrinsic nature of vortex-induced vibrations. *Journal of Fluids and Structures*, 19:389–447, 2004.

Y. Tanida, A. Okajima, and Y. Watanabe. Stability of a circular cylinder oscillating in uniform flow or in a wake. *Journal of Fluid Mechanics*, 61:769–784, 1973.

M. Tatsuno. Vortex streets behind a circular cylinder oscillating in the direction of flow. *Bulletin of the Research Institute for Applied Mechanics of Kyushu University*, 36:25–37, 1972.

M. Van Dyke. *An album of fluid motion.* Parabolic Press (Stanford, CA), 1982.

B. W. van Oudheusden, F. Scarano, N. P. van Hinsberg, and D. W. Watt. Phase-resolved characterization of vortex shedding in the near wake of a square-section cylinder at incidence. *Experiments in Fluids*, 39:86–98, 2005.

K. Vikestad, J. K. Vandiver, and C. M. Larsen. Added mass and oscillating frequency for a circular cylinder subjected to vortex-induced vibrations and external disturbance. *Journal of Fluids and Structures*, 14:1071–1088, 2000.

P. D. Welch. The use of Fast Fourier Transform for the estimation of power spectra: A method based on time averaging over short, modified periodograms. *IEEE Transactions on Audio Electroacoustics*, AU-15:70–73, 1967.

J. Westerweel and F. Scarano. Universal outlier detection for PIV data. *Experiments in Fluids*, 39:1096–1100, 2005.

J. Westerweel, G. E. Elsinga, and R. J. Adrian. Particle image velocimetry for

complex and turbulent flows. *Annual Review of Fluid Mechanics*, 45:409–436, 2013.

C. H. K. Williamson. Three-dimensional vortex dynamics in bluff body wakes. *Experimental Thermal and Fluid Science*, 12:150–168, 1996.

C. H. K. Williamson and R. Govardhan. Vortex-induced vibrations. *Annual Review of Fluid Mechanics*, 36:413–455, 2004.

C. H. K. Williamson and N. Jauvtis. A high-amplitude 2T mode of vortex-induced vibration for a light body in XY motion. *European Journal of Mechanics B/Fluids*, 23:107–114, 2004.

C. H. K. Williamson and A. Roshko. Vortex formation in the wake of an oscillating cylinder. *Journal of Fluids and Structures*, 2:355–381, 1988.

Y. Wu and K. T. Christensen. Population trends of spanwise vortices in wall turbulence. *Journal of Fluid Mechanics*, 568:55–76, 2006.

S. J. Xu, Y. Zhou, and M. H.. Wang. A symmetric binary-vortex street behind a longitudinally oscillating cylinder. *Journal of Fluid Mechanics*, 556:27–43, 2006.